CHARACTERIZATION OF LUNAR ACCESS RELATIVE TO CISLUNAR ORBITS

A Thesis

Submitted to the Faculty

of

Purdue University

by

Rolfe J. Power

In Partial Fulfillment of the

Requirements for the Degree

of

Master of Science in Aeronautics and Astronautics

December 2019

Purdue University

West Lafayette, Indiana

THE PURDUE UNIVERSITY GRADUATE SCHOOL
STATEMENT OF THESIS APPROVAL

Professor Kathleen C. Howell, Chair

School of Aeronautics and Astronautics

Professor Carolin Frueh

School of Aeronautics and Astronautics

Professor David A. Spencer

School of Aeronautics and Astronautics

Approved by:

Professor Gregory Blaisdell

Associate Head of Graduate Program of Aeronautics and Astronautics

To Mom & Dad.

ACKNOWLEDGMENTS

First, I would like to thank my wife, Shannon. Through the months while writing this document and the months leading up to it, you supported me and gave me the encouragement I needed at every turn. Without you, this journey would have been substantially more difficult, and, thus, I am forever grateful. I also want to thank my parents. Whether it was driving me to practice, struggling with me attempting to put together a diorama, or supporting me through my college education, your encouragement to pursue all aspects of life – especially education – made me into the person I am today. Your love and support have made all the difference in my life and I am truly blessed to have parents like you. To my sisters, Caroline and Jacque, I want to say thank you for being my oldest of friends; having you by my side through the years has been one of my greatest motivators.

I am exceptionally grateful to my advisor, Professor Kathleen C. Howell. Throughout my time here at Purdue and as both a teacher and an advisor, you have continued to inspire me and your passion for the subject has built and grown my own. Your guidance through this process has been my most valuable resource and, without it, I would not have been able to reach this point. As I move forward in my studies, I look forward to learning more from your insights and am excited for what that will bring.

I would like to thank my committee members, Professors Carolin Frueh and David Spencer. I appreciate the feedback you have provided and the time taken to review this document. I would also like to thank the School of Aeronautics and Astronautics and Purdue University for financial support of my studies. I also extend my gratitude to Dr. Diane Davis for her guidance and feedback. Finally, I would like to thank my peers in the Multi-Body Dynamics Research Group who have given me more feedback than I can list here.

TABLE OF CONTENTS

Page

LIST OF TABLES vii

LIST OF FIGURES viii

ABSTRACT xix

1 INTRODUCTION 1
1.1 Previous Contributions 1
1.2 Document Overview 2

2 BACKGROUND 5
2.1 The N-Body Problem 6
2.2 The Circular Restricted Three-Body Problem 7
2.2.1 Assumptions in the CRTBP 8
2.2.2 Derivation of the Equations of Motion 10
2.2.3 Equilibrium Solutions 17
2.2.4 The Jacobi Integral 20
2.2.5 Zero Velocity Surfaces 21
2.2.6 Linear Variational Equations Relative to the Collinear Lagrange Points 27
2.2.7 The State Transition Matrix 35
2.3 Differential Corrections 39
2.3.1 Single Shooting 43
2.3.2 Multiple Shooting 50
2.4 Continuation Methods 53
2.4.1 Natural Parameter Continuation 53
2.4.2 Pseudo-Arclength Continuation 54
2.5 Periodic Solutions in the CRTBP 55
2.6 Invariant Manifold Theory 58
2.6.1 Hyperbolic Manifolds Associated with the Collinear Lagrange Points 60
2.6.2 Poincaré Maps for Dynamical Systems Analysis 61
2.6.3 Stability and Invariant Manifolds for Periodic Orbits 64

3 MOTIVATING APPLICATION: LUNAR IMPACT CHARACTERISTICS OF 9:2 LSR NRHO 66
3.1 Background and Definitions 67
3.1.1 Definition of Lunar Impact Characteristics 69

Page
3.2 Lunar Impact Trajectories . . . 73
3.2.1 Application: Impact Trajectories at the Shackleton Crater . . . 84

4 LUNAR ACCESS CHARACTERISTICS OF PERIODIC ORBITS IN THE LUNAR REGION . . . 94
4.1 The Stability Index . . . 94
4.2 Stability of Periodic Orbit Families in the Lunar Region . . . 99
4.2.1 Definition of Lunar Region Periodic Families of Interest . . . 100
4.2.2 Earth-Moon Distant Retrograde Orbits . . . 100
4.2.3 Earth-Moon Low Prograde Orbits . . . 101
4.2.4 Earth-Moon Lyapunov Orbits . . . 104
4.2.5 Earth-Moon Halo Orbits . . . 107
4.2.6 Earth-Moon Vertical Orbits . . . 111
4.2.7 Earth-Moon Axial Orbits . . . 114
4.2.8 Earth-Moon Butterfly Orbits . . . 117
4.2.9 Earth-Moon Period-4 Halo Orbits . . . 120
4.2.10 Summary of Earth-Moon Periodic Orbit Stability Characteristics 124
4.3 Lunar Access Characteristics . . . 124
4.3.1 Definition of Lunar Orbit Insertion Characteristics . . . 124
4.3.2 Lunar Impact Characteristics of Planar Orbit Families . . . 125
4.3.3 Low Lunar Orbit Access Characteristics of Planar Orbit Families 138
4.3.4 Lunar Impact Characteristics of Spatial Orbit Families . . . 145
4.3.5 Low Lunar Orbit Access Characteristics of Spatial Orbit Families 189

5 APPLICATION: LUNAR ACCESS FROM 9:2 LSR NRHO USING INTERMEDIATE PERIODIC ORBITS . . . 201
5.1 Shackleton Crater Impact Trajectories . . . 201
5.2 Transfers from 9:2 LSR NRHO to LLO . . . 213

6 CONCLUDING REMARKS . . . 222
6.1 Summary . . . 222
6.2 Recommendations for Future Work . . . 224

REFERENCES . . . 226

LIST OF TABLES

Table Page

2.1 Eccentricities of Common Systems 9

4.1 Investigated Subset of Lunar Region Periodic Orbits 100

LIST OF FIGURES

Figure Page

2.1 Schematic of CRTBP System Configuration 11

2.2 Collinear Lagrange Point Search Regions 18

2.3 CRTBP Lagrange Points 20

2.4 Zero Velocity Curves (ZVCs) in the Earth-Moon System at Various Jacobi Constant Values 24

2.5 ZVC in the Earth-Moon System When $J = J_{L_1}$ 25

2.6 ZVS in the Earth-Moon System when $J > J_{L_1}$ 26

2.7 ZVS in the Earth-Moon System when $J < J_{L_{4/5}}$ 26

2.8 Schematic for a Mapping of the Variations for a General Trajectory in the CRTBP 36

2.9 Initial guess for planar single shooting problem 45

2.10 Updated trajectory for fixed-time single shooting algorithm 46

2.11 Corrected trajectory for fixed-time and variable-time single shooting algorithms 48

2.12 Corrected trajectory for fixed-time and variable-time single shooting algorithms 49

2.13 Multiple Shooting Schematic 50

2.14 Linear Approximation Versus Nonlinear Propagation for Planar Periodic Orbits Around Earth-Moon L_1 for a) 0.5 km, b) 10 km, and c) 25 km . . . 56

2.15 Converged Periodic Orbit Around Earth-Moon L_1 Compared to the Initial Guess from Linear Variational Equations 58

2.16 Lyapunov Orbit Families for Earth-Moon L_1, L_2, and L_3 59

2.17 Vertical Orbit Families for Earth-Moon L_1, L_2, and L_3 59

2.18 Global Invariant Manifolds for Earth-Moon L_1 61

2.19 Schematic of Poincaré Map Adapted from Palis et. al [9] and Perko [8] . . 62

Figure Page

2.20 One-Sided ($\dot{y} > 0$) Planar CRTBP Poincaré Map at $J = 3.44$ in the Earth-Moon System 63

2.21 Stable (blue) and Unstable (red) Manifolds for L_2 Lyapunov Orbit (black) in the Earth-Moon System 65

3.1 9:2 LSR NRHO in the Earth-Moon System 67

3.2 Latitude, Longitude, and Range Definition with Respect to P_2 in CRTBP Rotating Frame 68

3.3 Location of VNB Unit Vectors in Yaw-Pitch Grid 69

3.4 Latitude, Longitude, and Range Definition with Respect to P_2 in CRTBP Rotating Frame 70

3.5 Quadrant Definitions Around P_2 in xy-Plane 71

3.6 (a) Minimum and Maximum Theoretical Impact Speeds and, (b) the Difference Between The Maximum and Minimum Values 72

3.7 Impact Angle Definition Diagram 73

3.8 Impacting Departure Conditions for $\Delta v = 15$ m/s Colored by Time of Flight 74

3.9 Sample Impact Trajectories for 15 m/s Magnitude Departures Corresponding to Marked Locations in Figure 3.8 76

3.10 Impacting Departure Conditions for $\Delta v = 15$ m/s Colored by Impact Speed 77

3.11 Impacting Departure Conditions for $\Delta v = 15$ m/s Colored by Impact Angle 77

3.12 Impacting Departure Conditions for $\Delta v = 15$ m/s Colored by Latitude At Impact 78

3.13 Impacting Departure Conditions for $\Delta v = 15$ m/s Colored by Longitude At Impact 79

3.14 Impacting Departure Conditions for $\Delta v = 1$ m/s Colored by Time of Flight 80

3.15 Sample Impact Trajectories for 1 m/s Magnitude Departures Corresponding to Marked Locations in Figure 3.14 80

3.16 Impacting Departure Conditions for $\Delta v = 1$ m/s Colored by Impact Speed 81

3.17 Impacting Departure Conditions for $\Delta v = 1$ m/s Colored by Impact Angle 82

3.18 Impacting Departure Conditions for $\Delta v = 1$ m/s Colored by Latitude At Impact 83

3.19 Impacting Departure Conditions for $\Delta v = 1$ m/s Colored by Longitude At Impact 83

Figure Page

3.20 Latitudes and Longitudes of Shackleton Crater at Selected Epochs in 2023 85

3.21 Longitudes and Latitudes of the Shackleton in 2023 with Selected Epochs Marked 86

3.22 Locations of Shackleton Crater in 2023 (in Red) Overlaid on Latitude and Longitude of Impact Conditions Originating from the 9:2 LSR NRHO with a 15 m/s Departure Maneuver 87

3.23 Locations of Shackleton Crater in 2023 (in Red) Overlaid on Latitude and Longitude of Impact Conditions Originating from the 9:2 LSR NRHO with a 15 m/s Departure Maneuver 88

3.24 Example Low and High Impact Angle Trajectories from 9:2 LSR NRHO to Shackleton Crater Area 89

3.25 Corrected Trajectories from NRHO to Shackleton Crater for All Selected Epochs 91

3.26 TOF Values for Corrected Transfers from NRHO to Shackleton Crater . . 92

3.27 $\Delta\mathbf{v}$ Magnitudes for Corrected Transfers from NRHO to Shackleton Crater 93

4.1 Stability Indices for Earth-Moon L_2 Northern Halo Family 96

4.2 Earth-Moon L_2 Northern Halo Family where Red Orbits Possess Unstable Manifolds and Blue Orbits Possess a Four-Dimensional Center Manifold . . 97

4.3 Time Constants of Earth-Moon L_2 Northern Halo Family 98

4.4 Trajectory Arc on Unstable Manifold Originating from Periodic Orbit with Low Time Constant ($\kappa_\tau = 0.8$) Propagated for 2 Revolutions 98

4.5 Trajectory Arc on Unstable Manifold Originating from Periodic Orbit with High Time ($\kappa_\tau = 1.8$) Constant Propagated for 13 Revolutions 99

4.6 Simply Symmetric Planar Distant Retrograde Orbits (DROs) and Corresponding Stability Indices 101

4.7 Low Prograde Orbits (LPOs) 102

4.8 Jacobi Constant as a Function of Lunar Periapse Radius for Earth-Moon Low Prograde Orbits 102

4.9 Stability Characteristics of Earth-Moon Lunar Prograde Orbit Family . . 103

4.10 Low Prograde Orbits (LPOs) Where Red Indicates Unstable Orbits and Blue Indicates Stable Orbits 104

4.11 Earth-Moon Lyapunov Orbit Families 105

Figure Page

4.12 Jacobi Constant Value Versus Lunar Periapse Radii for Earth-Moon L_1 and L_2 Lyapunov Orbit Families 105

4.13 Stability Characteristics of Earth-Moon Lyapunov Orbit Families 106

4.14 Northern Halo Orbit Families in the Earth-Moon System 107

4.15 Stability Characteristics of Earth-Moon Northern Halo Orbit Families . . 108

4.16 L_1 Halo Orbit Family Colored by Stability where Red Indicates Unstable and Blue Indicates Stable 109

4.17 L_2 Halo Orbit Family Colored by Stability where Red Indicates Unstable and Blue Indicates Stable 110

4.18 Vertical Orbit Families in the Earth-Moon System 111

4.19 Jacobi Constant Versus Lunar Periapse Radius for Earth-Moon Vertical Orbit Families 112

4.20 Stability Characteristics of Earth-Moon Vertical Orbits 113

4.21 Axial Orbit Families in the Earth-Moon System 114

4.22 Jacobi Versus Lunar Periapse Radius for Earth-Moon Axial Families . . 115

4.23 Stability Characteristics of Earth-Moon Axial Orbit Families 116

4.24 Northern Butterfly Orbit Family in the Earth-Moon System 117

4.25 Jacobi Versus Lunar Periapse Radius for Earth-Moon Northern Butterfly Orbits 118

4.26 Stability Characteristics of Earth-Moon Butterfly Orbit Families 119

4.27 P4HO1 Family in the Earth-Moon System 120

4.28 P4HO2 Family in the Earth-Moon System 121

4.29 Jacobi Constant Versus Periapse Radius for the P4HO1 Family in the Earth-Moon System 121

4.30 Jacobi Constant Versus Periapse Radius for the P4HO2 Family in the Earth-Moon System 122

4.31 Stability Characteristics of Earth-Moon Period-Four Halo Orbit Families 123

4.32 Planar Orbit Families where Red Indicates Unstable Orbits with $\kappa_\tau \leq 1.5$ and Blue Indicates $\kappa_\tau > 1.5$ 126

Figure Page

4.33 Time of Flight Versus Impact Longitude for Unstable Manifolds Associated with Earth-Moon Low Prograde Orbits Colored by Jacobi Constant Value with Selected Points 127

4.34 Selected Trajectories from Figure 4.33 where the Blue Trajectories are the Periodic Orbits and the Red Trajectories are on the Manifolds 128

4.35 Impact Speed and Angle for Unstable Manifolds Associated with Earth-Moon LPO Family 130

4.36 Impact Evolution for LPO Unstable Orbit Manifolds Example 131

4.37 Time of Flight Versus Impact Longitude for Unstable Manifolds Associated with Earth-Moon L_1 Lyapunov Orbits Colored by Jacobi Constant Value 132

4.38 Example Demonstrating Quadrant III Avoidance of Large Lyapunov Impacting Manifolds 133

4.39 Example of Complex Geometry from L_1 Earth-Moon Lyapunov Orbit Unstable Manifold Impacting at $\varphi = 225°$ After 37 Days 134

4.40 Impact Speed and Angle for Unstable Manifolds Associated with Earth-Moon L_1 Lyapunov Family 134

4.41 Impacting Trajectory Examples for 15 Day TOF from Earth-Moon L_1 Lyapunov Orbits 135

4.42 Time of Flight Versus Impact Longitude for Unstable Manifolds Associated with Earth-Moon L_2 Lyapunov Orbits Colored by Jacobi Constant Value 136

4.43 Example Demonstrating Quadrant I Avoidance of L_2 Lyapunov Impacting Manifolds 137

4.44 Impact Speed and Angle for Unstable Manifolds Associated with Earth-Moon L_2 Lyapunov Family 137

4.45 Lunar Periapse Locations for Unstable Manifolds Associated with the LPO Family in the Earth-Moon System 139

4.46 Sample Geometries of LPO Unstable Manifold Periapses from Figure 4.45 140

4.47 Lunar Periapse Locations for Unstable Manifolds Associated with the LPO Family in the Earth-Moon System 140

4.48 Lunar Periapse Locations for Unstable Manifolds Associated with the L_1 Lyapunov Family in the Earth-Moon System 141

Figure Page

4.49 Lunar Periapse TOF Versus Altitude for the Unstable Manifolds Associated with the Earth-Moon L_1 Lyapunov Family 142

4.50 Lunar Periapse Locations for Unstable Manifolds Associated with the L_2 Lyapunov Family in the Earth-Moon System 143

4.51 Lunar Periapse TOF Versus Altitude for the Unstable Manifolds Associated with the Earth-Moon L_2 Lyapunov Family 144

4.52 L_1 and L_2 Halo Orbit Families where Red Indicates Unstable Orbits with $\kappa_\tau < 1.5$ and Blue Indicates $\kappa_\tau > 1.5$ 146

4.53 Unstable L_1 Halo Orbits with Manifold Structures Impacting the Moon Within 43 Days 146

4.54 Time of Flight and Longitude of Impact Conditions for Unstable Manifolds Associated with L_1 Halo Orbits 147

4.55 Example Impacting Trajectories from L_1 Halo Orbits Corresponding to Marked Points in Figure 4.54 148

4.56 Time of Flight as a Function of Latitude of Lunar Impact Conditions of Unstable Manifolds Associated with L_1 Halo Orbits 149

4.57 Latitude Versus Longitude of Impact Conditions of Unstable Manifolds Associated with the L_1 Halo Orbit Family 149

4.58 Latitude Versus Longitude for Impacts of Unstable Manifolds Associated with the L_1 Halo Orbits 151

4.59 Unstable L_2 Halo Orbits with Manifold Structures Impacting the Moon Within 43 Days 152

4.60 Time of Flight and Longitude of Impact Conditions for Unstable Manifolds Associated with L_2 Halo Orbits 152

4.61 Example Impacting Trajectories from L_2 Halo Orbits Corresponding to Marked Points in Figure 4.60 153

4.62 Time of Flight as a Function of Latitude of Lunar Impact Conditions of Unstable Manifolds Associated with L_2 Halo Orbits 153

4.63 Latitude Versus Longitude of Impact Conditions of Unstable Manifolds Associated with the L_2 Halo Orbit Family 154

4.64 Latitude Versus Longitude for Impacts of Unstable Manifolds Associated with the L_2 Halo Orbits 155

4.65 L_1 and L_2 Vertical Orbit Families where Red Indicates Unstable Orbits with $\kappa_\tau < 1.5$ and Blue Indicates $\kappa_\tau > 1.5$ 156

Figure Page

4.66 Unstable L_1 Vertical Orbits with Manifold Structures Impacting the Moon Within 43 Days . . . 157

4.67 Time of Flight and Longitude of Impact Conditions for Unstable Manifolds Associated with L_1 Vertical Orbits . . . 158

4.68 Example Impacting Trajectories from L_1 Vertical Orbits Corresponding to Marked Points in Figure 4.67 . . . 159

4.69 Latitude of Impact for L_1 Vertical Impacting Manifolds . . . 160

4.70 Latitude Versus Longitude of Impact Conditions of Unstable Manifolds Associated with the L_1 Vertical Orbit Family . . . 161

4.71 Latitude Versus Longitude for Impacts of Unstable Manifolds Associated with the L_1 Vertical Orbits . . . 162

4.72 Unstable L_2 Vertical Orbits with Manifold Structures Impacting the Moon Within 43 Days . . . 163

4.73 Time of Flight and Longitude of Impact Conditions for Unstable Manifolds Associated with L_2 Vertical Orbits . . . 163

4.74 Example Impacting Trajectories from L_2 Vertical Orbits Corresponding to Marked Points in Figure 4.73 . . . 164

4.75 Latitude Versus Longitude of Impact Conditions of Unstable Manifolds Associated with the L_2 Vertical Orbit Family . . . 165

4.76 Latitude Versus Longitude for Impacts of Unstable Manifolds Associated with the L_2 Vertical Orbits . . . 166

4.77 L_1 Axial Orbits Where Red Indicates Axial Orbits with Impacting Manifolds and Blue Indicates Axial Orbits without Impacting Manifolds . . . 168

4.78 Time of Flight as a Function of Longitude of Lunar Impact Conditions of Unstable Manifolds Associated with L_1 Axial Orbits . . . 168

4.79 Example Impacting Trajectories from L_1 Axial Orbits Corresponding to Marked Points in Figure 4.78 . . . 169

4.80 Time of Flight as a Function of Latitude of Lunar Impact Conditions of Unstable Manifolds Associated with L_1 Axial Orbits . . . 170

4.81 Example Impacting Trajectories from L_1 Axial Orbits Corresponding to Marked Points in Figure 4.80 . . . 171

4.82 Latitude Versus Longitude of Impact Conditions of Unstable Manifolds Associated with the L_1 Axial Orbit Family . . . 172

Figure Page

4.83 Latitude Versus Longitude for Impacts of Unstable Manifolds Associated with the L_1 Axial Orbits . . . 173

4.84 L_2 Axial Orbits Where Red Indicates Axial Orbits with Impacting Manifolds and Blue Indicates Axial Orbits without Impacting Manifolds . . . 174

4.85 Time of Flight as a Function of Longitude of Lunar Impact Conditions of Unstable Manifolds Associated with L_2 Axial Orbits . . . 174

4.86 Example Impacting Trajectories from L_2 Axial Orbits Corresponding to Marked Points in Figure 4.85 . . . 175

4.87 Time of Flight as a Function of Latitude of Lunar Impact Conditions of Unstable Manifolds Associated with L_2 Axial Orbits . . . 176

4.88 Latitude Versus Longitude of Impact Conditions of Unstable Manifolds Associated with the L_2 Axial Orbit Family . . . 177

4.89 Latitude Versus Longitude for Impacts of Unstable Manifolds Associated with the L_2 Axial Orbits . . . 178

4.90 Earth-Moon Northern Butterfly Orbits with Sufficiently Fast Manifold Departure . . . 179

4.91 Unstable Northern Butterfly Orbits with Manifold Structures Impacting the Moon Within 43 Days . . . 180

4.92 Time of Flight and Longitude of Impact Conditions for Unstable Manifolds Associated with Northern Butterfly Orbits . . . 181

4.93 Example Impacting Trajectories from Northern Butterfly Orbits Corresponding to Marked Points in Figure 4.92 . . . 182

4.94 Time of Flight as a Function of Latitude of Lunar Impact Conditions of Unstable Manifolds Associated with Northern Butterfly Orbits . . . 183

4.95 Latitude Versus Longitude of Impact Conditions of Unstable Manifolds Associated with the Northern Butterfly Orbit Family . . . 183

4.96 Latitude Versus Longitude for Impacts of Unstable Manifolds Associated with the Northern Butterfly Orbits . . . 184

4.97 P4HO2 Orbits where Red Indicates $\kappa_\tau < 1.5$ and Blue Indicates Otherwise 186

4.98 Unstable P4HO2 Orbits with Manifold Structures Impacting the Moon Within 43 Days . . . 186

4.99 Time of Flight and Longitude of Impact Conditions for Unstable Manifolds Associated with P4HO2 Orbits . . . 187

Figure Page

4.100Example Impacting Trajectories from P4HO2 Orbits Corresponding to Marked Points in Figure 4.99 188

4.101Time of Flight and Latitude of Impact Conditions for Unstable Manifolds Associated with P4HO2 Orbits 188

4.102Latitude Versus Longitude of Impact Conditions of Unstable Manifolds Associated with the Northern P4HO2 Orbit Family 189

4.103Latitude Versus Longitude for Impacts of Unstable Manifolds Associated with the P4HO2 Orbits 190

4.104Time of Flight and Altitude for Periapse Conditions on Manifolds Associated with the L_1 Halo Orbit Family 191

4.105Inclinations and Altitudes of Periapse Conditions on Manifolds Associated with the L_1 Halo Orbit Family 192

4.106Time of Flight and Altitude for Periapse Conditions on Manifolds Associated with the L_2 Halo Orbit Family 192

4.107Inclinations and Altitudes of Periapse Conditions on Manifolds Associated with the L_2 Halo Orbit Family 193

4.108Time of Flight and Altitude for Periapse Conditions on Manifolds Associated with the L_1 Vertical Orbit Family 194

4.109Inclinations and Altitudes of Periapse Conditions on Manifolds Associated with the L_1 Vertical Orbit Family 194

4.110Time of Flight and Altitude for Periapse Conditions on Manifolds Associated with the L_2 Vertical Orbit Family 195

4.111Inclinations and Altitudes of Periapse Conditions on Manifolds Associated with the L_2 Vertical Orbit Family 195

4.112Time of Flight and Altitude for Periapse Conditions on Manifolds Associated with the L_1 Axial Orbit Family 196

4.113Inclinations and Altitudes of Periapse Conditions on Manifolds Associated with the L_1 Axial Orbit Family 197

4.114Time of Flight and Altitude for Periapse Conditions on Manifolds Associated with the L_2 Axial Orbit Family 197

4.115Inclinations and Altitudes of Periapse Conditions on Manifolds Associated with the L_2 Axial Orbit Family 198

4.116Time of Flight and Altitude for Periapse Conditions on Manifolds Associated with the L_2 Butterfly Orbit Family 198

Figure Page

4.117 Inclinations and Altitudes of Periapse Conditions on Manifolds Associated with the L_2 Butterfly Orbit Family . . . 199

4.118 Time of Flight and Altitude for Periapse Conditions on Manifolds Associated with the P4HO2 Orbit Family . . . 200

4.119 Inclinations and Altitudes of Periapse Conditions on Manifolds Associated with the P4HO2 Orbit Family . . . 200

5.1 Latitude and Longitude of Impacts for Spatial Periodic Orbits in the Lunar Region Excluding L_2 Vertical, L_2 Axial, and P4HO1 Families Separated Into Northern, Southern, and Axial/Vertical Groups . . . 203

5.2 Shackleton Crater Locations Overlaid on Unstable Manifold Impact Locations Associated with the Southern Lunar Region Orbits . . . 204

5.3 Candidate Trajectories Selected from Southern Family Impact Conditions in Figure 5.2 . . . 204

5.4 Views Down x-Axis of Candidate Trajectories Selected from Southern Family Impact Conditions in Figure 5.2 . . . 205

5.5 Converged Transfers from P4HO2 Orbit To Shackleton Crater Locations in 2023 Yielding Low Impact Angle Trajectories . . . 206

5.6 Converged Transfers from L_2 Halo Orbit To Shackleton Crater Locations in 2023 Yielding High Impact Angle Trajectories . . . 206

5.7 Required Departure Δv of Impact Trajectories at Epochs Associated with Shackleton Crater Locations . . . 207

5.8 Time of Flight Along Impact Trajectories at Epochs Associated with Shackleton Crater Locations . . . 208

5.9 Impact Angle of Trajectories at Epochs Associated with Shackleton Crater Locations . . . 208

5.10 Poincaré Map For Connections Between the 9:2 LSR NRHO in Red and the Selected P4HO2 Orbit in Blue . . . 210

5.11 Corrected Transfer from 9:2 LSR NRHO to P4HO2; Δv = 140.4 m/s, TOF = 60.6 days . . . 211

5.12 Complete Transfer From 9:2 LSR NRHO to Shackleton Crater Location Using Intermediate P4HO2; Δv_{max} = 145.9 m/s, TOF_{Avg} = 115.0 days (Maneuver Locations Marked with Red Dots) . . . 212

5.13 Corrected Transfer from 9:2 LSR NRHO to L_2 Halo; Δv = 307.0 m/s, TOF = 34.5 days . . . 213

Figure Page

5.14 Complete Transfer From 9:2 LSR NRHO to Shackleton Crater Location Using Intermediate L_2 Halo; Δv_{max} = 316.8 m/s, TOF_{Avg} = 82.3 days (Maneuver Locations Marked with Red Dots) 214

5.15 Difference in Jacobi Constant from 9:2 LSR NRHO Versus Λ for Periodic Orbit Apse Conditions 215

5.16 Manifold from L_2 Northern Halo Yielding Apse Condition Selected in Figure 5.15. TOF = 37.3 Days 216

5.17 Manifold from L_2 Northern Halo Yielding Apse Condition Selected in Figure 5.15 Corrected to $i = 90°$, Altitude = 100 km. Δv = 77 m/s, TOF = 37.4 Days 218

5.18 Poincaré Map For Connections Between the 9:2 LSR NRHO in Red and the Selected Halo Orbit in Blue 219

5.19 Transfer from NRHO to L_2 Northern Halo. Δv = 164.0 m/s, TOF = 65.6 Days 220

5.20 Transfer from NRHO to LLO with $i = 90°$, Altitude = 100 km. Δv = 914.8 m/s (Including 673.8 m/s Insertion into LLO), TOF = 110.2 Days 221

ABSTRACT

Power, Rolfe J. MSAAE, Purdue University, December 2019. Characterization of Lunar Access Relative to Cislunar Orbits. Major Professor: Kathleen C. Howell.

With the growth of human interest in the Lunar region, methods of enabling Lunar access including surface and Low Lunar Orbit (LLO) from periodic orbit in the Lunar region is becoming more important. The current investigation explores the Lunar access capabilities of these periodic orbits. Impact trajectories originating from the 9:2 Lunar Synodic Resonant (LSR) Near Rectilinear Halo Orbit (NRHO) are determined through explicit propagation and mapping of initial conditions formed by applying small maneuvers at locations across the orbit. These trajectories yielding desirable Lunar impact final conditions are then used to converge impacting transfers from the NRHO to Shackleton crater near the Lunar south pole. The stability of periodic orbits in the Lunar region is analyzed through application of a stability index and time constant. The Lunar access capabilities of the Lunar region periodic orbits found to be sufficiently unstable are then analyzed through impact and periapse maps. Using the impact data, candidate periodic orbits are incorporated in the the NRHO to Shackleton crater mission design to control mission geometry. Finally, the periapse map data is used to determine periodic orbits with desirable apse conditions that are then used to design NRHO to LLO transfer trajectories.

1. INTRODUCTION

Recent years have seen an explosion in interest pertaining to operations on and around the Moon. Manned missions seek to establish a permanent presence in the Lunar region, enabling scientific discovery for decades to come. Many of these mission concepts leverage multi-body orbits presenting complex dynamical environments within which mission design and operations must take place. Furthermore, fundamental to many of these applications is access to the Lunar surface or Low Lunar Orbit (LLO) for sample recovery, surface operations, and observation. NASA's Gateway mission will leverage a Near Rectilinear Halo Orbit (NRHO) to establish a human outpost in cislunar space and a key mission objective for the program is Lunar surface and LLO access [1, 2]. Consequently, design methodologies for Lunar access from the NRHO are required including access to both the Lunar surface and LLO. The highly dynamic multi-body environment in the Lunar region presents challenges to the design process in developing low-cost transfers with geometries that meet mission criteria. The current analysis is performed within the Circular Restricted Three Body Model (CRTBP) enabling the incorporation of the Earth's gravitational influence. This investigation explores the Lunar access capabilities of the periodic orbits in the vicinity of the Moon both in general as well as in the context of facilitating transfer design from the NRHO to the Lunar surface or LLO. Such transfer design scenarios are explored leveraging intermediate periodic orbits to for NRHO to Lunar surface/LLO transfers.

1.1 Previous Contributions

In 1609, Johannes Kepler published *Astronomia Nova* defending the heliocentric model of the solar system and refuting the previously dominant Ptolemaic system [3].

In this book, Kepler presented the first two of his three laws of planetary motion with the third law published in 1619. Later in the 17^{th} century, Newton published *Principia* in 1687 presenting the foundation of classical mechanics, proving the phenomena observed by Kepler [4], and giving a solution to the two-body problem using the newly postulated laws of motion. Thus, the analytic study of the N-body problem, i.e., the motion of N massive bodies moving under the influence of their mutual gravitational attractions, was ignited. The analysis of a restricted three-body problem first gained traction with Euler's formulation using a synodic coordinate system in 1772 leading to the Jacobi integral of the motion [5]. The same year, Lagrange discovered the five equilibrium solutions aptly denoted the *Lagrange points*. In 1878, Hill demonstrated the forbidden regions created via the Jacobi integral allowing for the bounding of motion without explicitly solving for particular solutions. One of the greatest contributions in the study of the restricted three-body problem was the completion of Poincaré's *Méthodes Nouvelles* in 1899 emphasizing the "qualitative aspects of celestial mechanics" [5]. Poincaré's work in the three-body problem marked a new era in the analysis of dynamical systems and gave rise to Dynamical Systems Theory (DST) and led to the study of chaos theory.

1.2 Document Overview

The Lunar access characteristics of periodic orbits in the Lunar vicinity are determined in the context of a mission design scenario. The motivation for Lunar access and the incorporation of intermediate periodic orbits is developed. Periodic orbits in the Circular Restricted Three Body Problem are characterized by stability and the Lunar access capabilities of the unstable periodic orbits are determined. These Lunar access capabilities are the impact locations on the Lunar surface, impact conditions such as speed and angle, and the altitudes and inclinations of the apse conditions. The obtained access characteristics are then used to design Lunar impact trajectories and transfers to Low Lunar Orbit (LLO). The current investigation is organized as

- **Chapter 2:** This chapter presents the necessary background information regarding the Circular Restricted Three Body Problem (CRTBP), corrections, and dynamical systems theory. The equations of motion for the CRTBP are derived and the resulting integral of the motion is determined. Forbidden regions leveraging the integral of the motion are described and visualized. Linear variational equations are investigated with respect to the equilibrium solutions of the CRTBP. Furthermore, parallel shooting corrections methods are introduced along with numerical continuation schemes for the construction of families of solutions. Finally, periodic solutions within the CRTBP are detailed along with their associated manifold structures.

- **Chapter 3:** This chapter presents a motivating example for the investigation of the Lunar access characteristics of periodic orbits in the Lunar region. The 9:2 Lunar Synodic Resonant (LSR) Near Rectilinear Halo Orbit (NRHO) planned for use in NASA's Gateway program is introduced along with Shackleton crater presenting a possible impact destination. Impact characteristics of trajectories originating from the 9:2 NRHO are obtained via application of small maneuvers across the orbit are analyzed graphically. Trajectories impacting at Shackleton crater at epochs spanning 2023 are designed using the obtained impact data.

- **Chapter 4:** This chapter presents the stability and Lunar access characteristics of periodic orbits in the lunar region. The Lunar periodic orbits of interest are identified and displayed. Furthermore, the stability index and time constant are introduced as methods of assessing the stability of a periodic orbit and the speed that manifold structures depart. These metrics are used to determine periodic orbit families with unstable manifold structures and which of these structures present sufficiently fast departure rates. The impact locations and characteristics of these manifold structures are determined as well as the apse altitudes and inclinations with respect to the Moon.

- **Chapter 5:** This chapter revisits the application presented in Chapter 3, i.e., the impact trajectory design from the 9:2 LSR NRHO to the Shackleton crater locations. However, the design is performed using the unstable intermediate periodic orbits analyzed in Chapter 4. Candidate intermediate orbits are determined based on the impact characterization determined in Chapter 4 and transfers to the intermediate orbit from the NRHO are found via Poincaré maps. Additionally, transfers are found to a 100 km polar LLO using intermediate orbits between the NRHO and LLO leveraging the apse characterizations with respect to the Moon developed in Chapter 4.

- **Chapter 6:** This chapter presents a summary of this investigation including the usage of intermediate periodic orbits to facilitate NRHO to the Lunar surface and LLO as well as the general characteristics of Lunar access among periodic orbits in the Lunar region. Furthermore, recommendations regarding future work are offered.

2. BACKGROUND

Fundamental to any investigation into the motion of spacecraft is the establishment of a dynamical model that allows for the mathematical representations describing the motion. Various models have been developed in the gravitational problem that differ in terms of the number of primary bodies, the restrictions on the motions of those bodies, and the gravitational force fields. A low-fidelity but fundamental model is the two-body model. The two-body model predicts the movement of a point mass relative to another point mass and influenced by their mutual gravitational interaction. The relative formulation delivers an analytical solution that has been extensively studied and applied successfully for preliminary analysis in many spacecraft missions. While effective in many cases, the two-body model does not accurately predict motion in regions of space where the influence of a third body cannot be ignored nor represented by a small perturbation. Unfortunately, the incorporation of even a single additional body into the model precludes any known closed-form analytical solutions. Multi-body models that include three or four gravitational bodies require numerical analysis but benefit from application of dynamical systems theory. The N-Body problem incorporates as many bodies as may influence the behavior in the Newtonian gravity model. However, due to the complexities in the N-Body problem, the analysis offers fewer general conclusions than simpler models. The Circular Restricted Three-Body Problem (CRTBP), however, provides significant insight given a set of reasonable assumptions. A simplified multi-body formulation enables the application of powerful concepts from Dynamical Systems Theory (DST) to the mission design problem.

2.1 The *N*-Body Problem

In the *Principia*, Isaac Newton introduced the relationship between the force applied to a body and the resulting change in the body's state [4]. The law of motion from Newton stated, in modern terms, that the force applied to a particle is equal to the time rate of change of its momentum, i.e.

$$\mathbf{F} = \frac{d}{dt}\left(M\mathbf{R}'\right) \tag{2.1}$$

where $\mathbf{F}$ is the net force applied to the particle, M is the mass of the particle, $\mathbf{R}$ is the particle's position vector, and the prime symbol represents the time derivative with bold symbols denoting vector quantities. Assuming that the mass is constant, Equation (2.1) becomes the familiar

$$\mathbf{F} = M\mathbf{R}'' \tag{2.2}$$

where $\mathbf{R}''$ is the generic acceleration of the particle as viewed by an inertial observer. This inertial derivative may also be expressed in the more descriptive Leibniz notation as

$$\mathbf{R}'' = {}^{I}\frac{d^2\mathbf{R}}{dt^2}$$

where the superscript I denotes a derivative with respect to an inertial observer. The explicit notation for the frame of differentiation as well as the dependent variable becomes valuable as multiple frames and independent variables are incorporated.

In the *Principia*, Newton also introduced the Universal Law of Gravitation describing two massive particles that interact gravitationally. Using this law, the force exerted on a particle with mass M_2 by a second particle with mass M_1 is expressed as

$$\mathbf{F}_{12} = -G\frac{M_1 M_2}{R_{12}^3}\mathbf{R}_{12} \tag{2.3}$$

where G is the universal gravitational constant (approximately $6.674 \times 10^{-11}\ m^3 \cdot kg^{-1} \cdot s^{-2}$) and $\mathbf{R}_{12}$ is the position vector locating M_2 with respect to M_1. Equations (2.1) and (2.3) are combined to develop the set of ordinary differential equations describing the motion of N particles (or bodies that are centrobaric such that they can be represented as particles for modeling the gravity force) interacting gravitationally. Formally, given N centrobaric masses M_i where $i = 1, 2, 3, \ldots, N$ the differential equations describing the motion of the bodies are

$$M_i \mathbf{R}'' + G \sum_{j=1, j \neq i}^{N} \frac{M_i M_j}{R_{ji}^3} \mathbf{R}_{ji} = \mathbf{0} \quad \text{where} \quad i = 1, \ldots, N. \tag{2.4}$$

For every body added to the general N-body problem, as described in Equation (2.4), six dimensions are added to the phase space. Therefore, the closed-form analytical solution to Equation (2.4) requires $6N$ first integrals of the motion. However, in 1890, Poincaré proved that no more than 10 algebraic integrals – with respect to the time, position, and velocity coordinates only – exist [6]. Therefore, even with only two bodies, no closed-form solution is available as 12 first integrals are required. A solution does exist as an infinite series, but is impractical to apply to spacecraft mission design [6]. While the all-encompassing nature of the N-body problem offers a higher-fidelity model for gravitational interactions at the scale of interest for spaceflight, it fails to yield the rich analytical insight offered by models with fewer bodies and more assumptions. Therefore, a trade-off exists between the fidelity of the model and the ease of the analysis. The Circular Restricted Three-Body Problem (CRTBP) provides a middle ground in this trade offering higher fidelity analysis while possessing desirable structure.

2.2 The Circular Restricted Three-Body Problem

In terms of the multi-body problem, the fidelity scale ranges from two to N bodies. Both extremes are employed extensively to great effect, but a satisfactory model offers

the ability to leverage dynamical structures not obviously available in the ephemeris model and predict motion with greater accuracy than the two-body model. The Circular Restricted Three-Body Problem (CRTBP) yields significant structures and insight while representative of a common configuration for the bodies.

2.2.1 Assumptions in the CRTBP

In the gravitational problem, when $N = 2$, a relative formulation yields a Keplerian solution, but no closed-form analytical solution to the N-body problem exists when $N \geq 3$. Therefore, to explore more complex motion beyond the two-body problem, one more body is added to offer new behaviors. Yet, the motion of three bodies under Newton's Law of Universal Gravitation delivers a system representing an 18-dimensional phase space; with only 10 known integrals, the differential equations are not solvable. The complexity is reduced, however, by introducing two additional assumptions to yield the circular restricted three-body problem.

The first of the fundamental assumptions in the CRTBP pertains to the relative masses of the three bodies. For spaceflight applications, the three-body problems of interest most often involves Sun-Planet-Spacecraft (e.g., Sun-Earth-Spacecraft) or Planet-Moon-Spacecraft (e.g., Mars-Phobos-Spacecraft) configurations. Therefore, a reasonable assumption for many applications is a third body (the spacecraft) with a mass that is negligible in comparison to the masses of the other two bodies, labelled primaries. Thus,

$$M_3 << M_1, M_2 \tag{2.5}$$

where M_3 is the mass of the spacecraft and M_1 and M_2 are the masses of the primaries. The validity of this assumption is dependent on the system, of course. The consequence of this assumption is that the third body does not affect the motion of the two primary bodies. The two primary bodies form an isolated two-body system whose solution for motion is a conic orbit.

The second fundamental assumption constrains the motion of the two primary bodies. The systems of interest include primaries that are commonly in elliptical orbits with respect to one another (in the two-body approximation). For convenience, the two primary bodies are assumed to be moving on circular orbits about their mutual barycenter. A key outcome of this assumption is the removal of time from the equations of motion forming an autonomous dynamical system. Various eccentricities for primary bodies in the solar system are listed in Table 2.1. Most of the planetary systems possess relatively low eccentricities with the obvious exception of Sun-Mercury. Furthermore, the Moon, as well as Phobos and Titan, moves in relatively circular orbits about their respective primaries. Therefore, the assumption of circular orbits for many primary systems is representative for numerous scenarios in modern spaceflight.

Table 2.1.: Eccentricities of Common Systems

System	**Eccentricity**
Sun-Mercury	0.2056
Sun-Venus	0.0068
Sun-Earth	0.0167
Sun-Mars	0.0934
Sun-Jupiter	0.0483
Sun-Saturn	0.0560
Sun-Uranus	0.0473
Sun-Neptune	0.0086
Sun-Pluto	0.2482
Earth-Moon	0.0549
Mars-Phobos	0.0151
Saturn-Titan	0.0288

The circular restricted three-body problem balances the relative simplicity of the two-body problem and the higher fidelity of the complete N-body problem. Dynamical structures unavailable in either the two-body or ephemeris models arise and are successfully leveraged for trajectory design in multi-body regimes.

2.2.2 Derivation of the Equations of Motion

The derivation of the equations of motion originates with the application of Newton's Law of Motion, Equation (2.2), or an equivalent form (e.g., Lagrangian or Hamiltonian treatments). The CRTBP assumptions are then applied to the resulting equations of motion to yield a dimensional set of the governing equations of motion in the CRTBP. The dimensional equations of motion are then nondimensionalized to produce a set of equations of motion characterized by a single system parameter.

Newton's Law of Universal Gravitation is applied to the three bodies constructing second order differential equations governing their motions that are simplified through the CRTBP assumptions. Application of Equations (2.2) and (2.3) to the general three body problem yields

$$\begin{aligned}
\mathbf{R}_1'' &= -G\frac{M_2}{R_{21}^3}\mathbf{R}_{21} - G\frac{M_3}{R_{31}^3}\mathbf{R}_{31}, \\
\mathbf{R}_2'' &= -G\frac{M_1}{R_{12}^3}\mathbf{R}_{12} - G\frac{M_3}{R_{32}^3}\mathbf{R}_{32}, \\
\mathbf{R}_3'' &= -G\frac{M_1}{R_{13}^3}\mathbf{R}_{13} - G\frac{M_2}{R_{23}^3}\mathbf{R}_{23}.
\end{aligned}$$

However, the assumption that $M_3 << M_1, M_2$ eliminates the M_3 terms from the equations governing the acceleration of M_1 and M_2 producing

$$\mathbf{R}_1'' = -G\frac{M_2}{R_{21}^3}\mathbf{R}_{21}, \tag{2.6}$$

$$\mathbf{R}_2'' = -G\frac{M_1}{R_{12}^3}\mathbf{R}_{12}, \tag{2.7}$$

$$\mathbf{R}_3'' = -G\frac{M_1}{R_{13}^3}\mathbf{R}_{13} - G\frac{M_2}{R_{23}^3}\mathbf{R}_{23}. \tag{2.8}$$

Notice, Equations (2.6) and (2.7) decouple from Equation (2.8) and form an isolated two-body problem. This decoupling renders the barycenter of M_1 and M_2 an inertially fixed point. Because the assumption of circular motion has not been applied, the inertial nature of the M_1-M_2 barycenter holds in the case of elliptical motion as well.

However, assuming the initial conditions of the system are such that M_1 and M_2 are in circular orbits about their mutual barycenter, the system is depicted in Figure 2.1. The primaries, P_1 and P_2, are in circular orbits about their mutual barycenter, B. The differential equation for the motion for the third body (Equation (2.8)) is, therefore, analyzed independently. Figure 2.1 also demonstrates the addition of a rotating reference frame with the $\hat{\mathbf{x}}$ axis oriented along the P_1-P_2 line. Because the primary system orbit is assumed to be circular, this rotating reference frame will rotate with $\dot{\theta} = \bar{N}$ where $\bar{N}$ is the mean motion of the system.

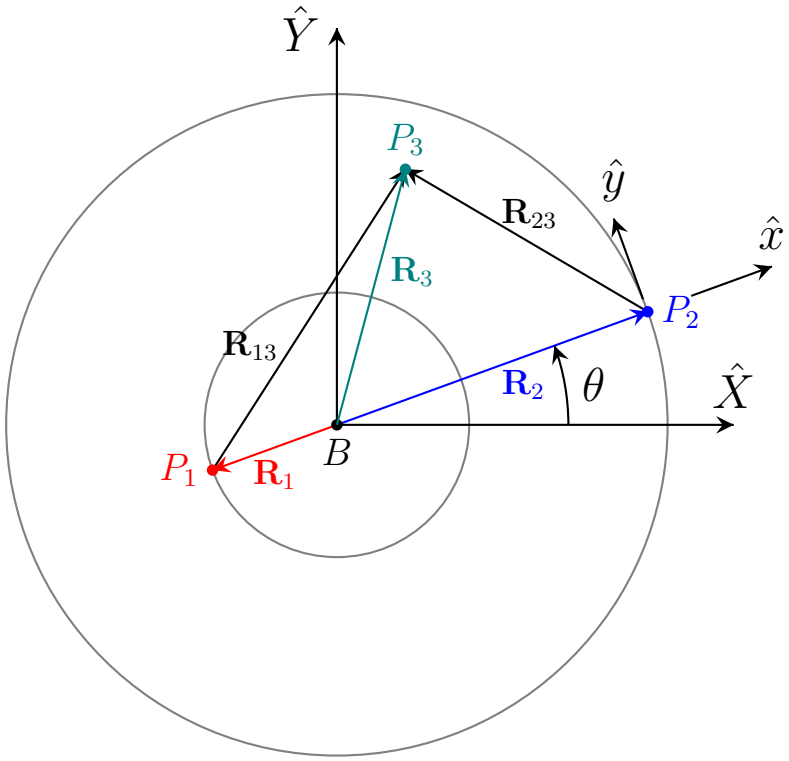

Figure 2.1.: Schematic of CRTBP System Configuration

While a particular system is the focus for a specific application, generalization of the equations of motion to multiple systems proves to be beneficial for analysis. As formulated in Equation (2.8), the equations of motion are parameterized by the masses of the three primaries and the radius of the circular paths for the primaries P_1 and P_2. Additionally, the problem has three fundamental dimensions:

mass, length, and time. Therefore, the system is nondimensionalized to yield a set of differential equations with a single nondimensional parameter. To achieve this nondimensionalization, three characteristic quantities are introduced; m^*, l^*, and t^* are the characteristic mass, characteristic length, and characteristic time, respectively. These characteristic quantities are defined as

$$m^* = M_1 + M_2, \tag{2.9}$$

$$l^* = R_1 + R_2, \tag{2.10}$$

$$t^* = \sqrt{\frac{l^{*3}}{Gm^*}}. \tag{2.11}$$

Additionally, as $\mathbf{R}_3$ is the vector quantity of interest, the definition $\mathbf{R} = \mathbf{R}_3$ simplifies the notation. To nondimensionalize Equation (2.8) with dimension $\left[\text{length}/\text{time}^2\right]$, both sides are multiplied by a factor t^{*2}/l^* yielding

$$\frac{t^{*2}}{l^*} \cdot {}^I\frac{d^2\mathbf{R}}{dt^2} = -\frac{GM_1}{Gm^*} \cdot \frac{l^{*3}}{R_{13}^3} \cdot \frac{\mathbf{R}_{13}}{l^*} - \frac{GM_2}{Gm^*} \cdot \frac{l^{*3}}{R_{23}^3} \cdot \frac{\mathbf{R}_{23}}{l^*}. \tag{2.12}$$

In the current form, Equation (2.12) is dimensionless. However, further notational simplification aids practical application. Let a nondimensional time, τ, be defined as

$$\tau = \frac{t}{t^*}, \tag{2.13}$$

so a k^{th} order derivative with respect to dimensional time, t, is written in terms of τ as

$$\frac{d^k x}{d\tau^k} = t^{*k}\frac{d^k x}{dt^k}. \tag{2.14}$$

Furthermore, let $\mathbf{r}$, $\mathbf{r}_{13}$, and $\mathbf{r}_{23}$ be the nondimensional forms of $\mathbf{R}$, $\mathbf{R}_{13}$, and $\mathbf{R}_{23}$, respectively, i.e.,

$$\mathbf{r} = \frac{\mathbf{R}}{l^*}, \tag{2.15}$$

$$\mathbf{r}_{13} = \frac{\mathbf{R}_{13}}{l^*}, \tag{2.16}$$

$$\mathbf{r}_{23} = \frac{\mathbf{R}_{23}}{l^*}. \tag{2.17}$$

Combining the definitions of τ, $\mathbf{r}$, $\mathbf{r}_{13}$, and $\mathbf{r}_{23}$ with Equation (2.12) yields

$$^I\frac{d^2\mathbf{r}}{d\tau^2} = -\frac{M_1}{m^*} \cdot \frac{\mathbf{r}_{13}}{r_{13}^3} - \frac{M_2}{m^*} \cdot \frac{\mathbf{r}_{23}}{r_{23}^3}. \tag{2.18}$$

Defining the nondimensional mass parameter, μ, as $\mu = M_2/m^*$ further simplifies the equation to

$$^I\frac{d^2\mathbf{r}}{d\tau^2} = -\frac{(1-\mu)\,\mathbf{r}_{13}}{r_{13}^3} - \frac{\mu \mathbf{r}_{23}}{r_{23}^3}. \tag{2.19}$$

Equation (2.19) is a nondimensonal set of ordinary differential equations that are parameterized by a single nondimensional parameter, μ, allowing for the analysis of different CRTBP systems simultaneously on the condition that they share a common μ value.

Due to the introduction of a rotating reference frame, the kinematic expression for the inertial acceleration is derived incorporating the angular velocity of the working frame with respect to the inertial frame. The position vector, $\mathbf{r}$, is written in terms of the rotating coordinate frame formed by the orthonormal triad $\hat{\mathbf{x}}$, $\hat{\mathbf{y}}$, and $\hat{\mathbf{z}}$:

$$\mathbf{r} = x\hat{\mathbf{x}} + y\hat{\mathbf{y}} + z\hat{\mathbf{z}} \tag{2.20}$$

where the measure numbers x, y, and z are nondimensional lengths. This frame rotates with respect to the inertial frame with a constant dimensional angular velocity, $\bar{N}$, equal to the mean motion of the P_1-P_2 two-body system. The mean motion has

dimensions of [1/time], and is, therefore, transformed into the nondimensional mean motion, n, as

$$n = \bar{N}t^* = \sqrt{\frac{Gm^*}{l^{*3}}} \cdot \sqrt{\frac{l^{*3}}{Gm^*}} = 1. \tag{2.21}$$

Because the application of Newton's Laws of Motion require the acceleration to be inertial, a kinematic expansion on the left side of Equation (2.19) is performed to write the equation in terms of the dependent variables x, y, and z and their derivatives. Consequently, the inertial derivative of $\mathbf{r}$ is then

$$\begin{aligned} {}^{I}\frac{d\mathbf{r}}{d\tau} &= {}^{R}\frac{d\mathbf{r}}{d\tau} + n\hat{\mathbf{z}} \times \mathbf{r} \\ &= (\dot{x} - ny)\,\hat{\mathbf{x}} + (\dot{y} + nx)\,\hat{\mathbf{y}} + \dot{z}\hat{\mathbf{z}} \end{aligned}$$

where the superscript R denotes the derivative taken with respect to the rotating frame and the dot above a variable represents the derivative with respect to the nondimensional time, τ. The second derivative again yields the kinematic expression for acceleration:

$${}^{I}\frac{d^2\mathbf{r}}{d\tau^2} = \left(\ddot{x} - 2n\dot{y} - n^2x\right)\hat{\mathbf{x}} + \left(\ddot{y} + 2n\dot{x} - n^2y\right)\hat{\mathbf{y}} + \ddot{z}\hat{\mathbf{z}}. \tag{2.22}$$

The circular orbits of the two primaries allow simple expressions for $\mathbf{r}_{13}$ and $\mathbf{r}_{23}$ in the rotating frame. A key advantage of the rotating frame application is that the quantities $\mathbf{r}_{13}$ and $\mathbf{r}_{23}$ have no explicit dependence on time. This property allows the CRTBP equations of motion to be autonomous. Specifically, $\mathbf{r}_{13}$ and $\mathbf{r}_{23}$ are expressed as

$$\mathbf{r}_{13} = (x + \mu)\,\hat{\mathbf{x}} + y\hat{\mathbf{y}} + z\hat{\mathbf{z}}, \tag{2.23}$$

$$\mathbf{r}_{23} = (x - 1 + \mu)\,\hat{\mathbf{x}} + y\hat{\mathbf{y}} + z\hat{\mathbf{z}}. \tag{2.24}$$

The nondimensional equations of motion for the Circular Restricted Three-Body Problem (CRTBP) are, therefore, written

$$\ddot{x} - 2n\dot{y} = n^2 x - \frac{(1-\mu)(x+\mu)}{r_{13}^3} - \frac{\mu(x-1+\mu)}{r_{23}^3}, \tag{2.25}$$

$$\ddot{y} + 2n\dot{x} = n^2 y - \frac{(1-\mu)y}{r_{13}^3} - \frac{\mu y}{r_{23}^3}, \tag{2.26}$$

$$\ddot{z} = -\frac{(1-\mu)z}{r_{13}^3} - \frac{\mu z}{r_{23}^3}. \tag{2.27}$$

Numerical integration of Equations (2.25) - (2.27) results in trajectories reflecting the motion of P_3 in the rotating frame under the assumptions of the CRTBP. Importantly, Equations (2.25) - (2.27) are autonomous and independent of a particular epoch. Coupled and nonlinear, the equations of motion for the CRTBP lack a closed form analytical solution but do possess useful properties such as a first integral.

The equations of motion in the CRTBP from Equations (2.25) - (2.27) expose multiple symmetries to be exploited in the analysis. Given a solution to the equations of motion, $\mathbf{\Gamma}_0(\tau)$, where

$$\mathbf{\Gamma}_0(\tau) = \begin{bmatrix} x(\tau) & y(\tau) & z(\tau) & \dot{x}(\tau) & \dot{y}(\tau) & \dot{z}(\tau) \end{bmatrix}^{\mathrm{T}},$$

the trajectory $\mathbf{\Gamma}_1(\tau)$ is also a solution where

$$\mathbf{\Gamma}_1(\tau) = \begin{bmatrix} x(\tau) & y(\tau) & -z(\tau) & \dot{x}(\tau) & \dot{y}(\tau) & -\dot{z}(\tau) \end{bmatrix}^{\mathrm{T}}.$$

This relationship indicates that the CRTBP possesses symmetry across the xy plane. Additionally, if $\tau' = -\tau$, the trajectory

$$\mathbf{\Gamma}_2(\tau) = \begin{bmatrix} x(\tau) & -y(\tau) & z(\tau) & -\dot{x}(\tau) & \dot{y}(\tau) & -\dot{z}(\tau) \end{bmatrix}^{\mathrm{T}}$$

also satisfies the CRTBP equations of motion. This time-invariance symmetry property implies that for every solution to the CRTBP, there exists another solution

reflected across the xz plane in negative time. These forms of symmetry offer opportunities when constructing families of periodic orbits.

Introduction of a pseudopotential function, Ω, allows for a more succinct representation of the CRTBP equations of motion. The pseudopotential is defined as

$$\Omega = \frac{1}{2}n^2\left(x^2+y^2\right) + \frac{1-\mu}{r_{13}} + \frac{\mu}{r_{23}}. \tag{2.28}$$

The pseudopotential, therefore, is a function only of the position. The equations of motion are written in terms of Ω as follows,

$$\ddot{x} - 2n\dot{y} = \Omega_x, \tag{2.29}$$

$$\ddot{x} + 2n\dot{x} = \Omega_y, \tag{2.30}$$

$$\ddot{z} = \Omega_z \tag{2.31}$$

where

$$\Omega_x = \frac{d\Omega}{dx} = x - \frac{(1-\mu)(x+\mu)}{r_{13}^3} - \frac{\mu(x-1+\mu)}{r_{23}^3}, \tag{2.32}$$

$$\Omega_y = \frac{d\Omega}{dy} = y - \frac{(1-\mu)y}{r_{13}^3} - \frac{\mu y}{r_{23}^3}, \tag{2.33}$$

$$\Omega_z = \frac{d\Omega}{dz} = -\frac{(1-\mu)z}{r_{13}^3} - \frac{\mu z}{r_{23}^3}. \tag{2.34}$$

The formulation of the equations of motion in terms of the gradient of pseudopotential in Equations (2.29), (2.30), and (2.31) display similarities with the application the gravitational potential function in the inertial formulation. The equations of motion accommodate the gradient of Ω, but require addition of several terms because of the formulation in the rotating frame. Therefore, total mechanical energy is not conserved in the CRTBP. The lack of energy conservation is due to the assumption that the motion of P_3 does not affect that of P_1 or P_2 because $M_3 << M_1, M_2$; this produces a noncoherent system allowing for total mechanical energy to vary.

2.2.3 Equilibrium Solutions

A fundamental step in the analysis of nonlinear differential equations is the search for equilibrium solutions. The CRTBP possesses five equilibrium points denoted Lagrange or libration points. These points are located by solving the equations of motion for $\mathbf{r}$ when $\dot{\mathbf{r}} = \ddot{\mathbf{r}} = \mathbf{0}$. This substitution yields

$$x_{eq} = \frac{(1-\mu)(x_{eq}+\mu)}{r_{13,eq}^3} + \frac{\mu(x_{eq}-1+\mu)}{r_{23,eq}^3}, \tag{2.35}$$

$$y_{eq} = \frac{(1-\mu)y_{eq}}{r_{13,eq}^3} + \frac{\mu y_{eq}}{r_{23,eq}^3}, \tag{2.36}$$

$$0 = \frac{(1-\mu)z_{eq}}{r_{13,eq}^3} + \frac{\mu z_{eq}}{r_{23,eq}^3}. \tag{2.37}$$

Equations (2.35) - (2.37) are coupled through the $r_{13,eq}$ and $r_{23,eq}$ terms complicating their solution. However, a key observation appears in Equation (2.37), i.e., both terms will have the same sign, thus, all equilibrium solutions will be in the xy plane ($z_{eq} = 0$). If the position of P_3 includes an out-of-plane component, then the net force in the z direction is always directed towards the plane prohibiting any equilibrium fixed state.

By inspection, Equation (2.36) is satisfied if $y_{eq} = 0$. This condition restricts the search to points along the straight line connecting the two primaries and extending in both directions. Thus, the search for Lagrange points on this line simplifies Equation (2.35) to

$$x_{eq} = \frac{(1-\mu)(x_{eq}+\mu)}{|x_{eq}+\mu|^3} + \frac{\mu(x_{eq}-1+\mu)}{|x_{eq}-1+\mu|^3}. \tag{2.38}$$

The existence of the absolute values in the denominator of Equation (2.38) prevents cancellation of terms. To remedy this complexity, the coefficients A_1 and A_2 are introduced such that

$$A_1 = \operatorname{sgn}(x_{eq}+\mu), \tag{2.39}$$

$$A_2 = \operatorname{sgn}(x_{eq}-1+\mu). \tag{2.40}$$

Therefore, Equation (2.38) is rewritten as

$$x_{eq} = \frac{A_1 (1-\mu)}{(x_{eq}+\mu)^2} + \frac{A_2 \mu}{(x_{eq}-1+\mu)^2}. \tag{2.41}$$

Figure 2.2 displays the search space, divided via the signs of A_1 and A_2. Convention-

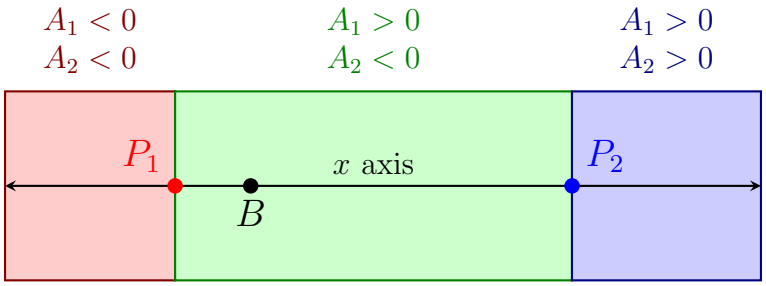

Figure 2.2.: Collinear Lagrange Point Search Regions

ally, the Lagrange point to the left of P_1 is labeled L_3, the Lagrange point between the two primaries is labeled L_1, and the Lagrange point to the right of P_2 is labeled L_2. Polynomial approximations for the location of the Lagrange points are presented by Szebehely [5], in consistent notation, as

$$x_{L1} = 1 - \mu - \nu \left(1 - \frac{1}{3}\nu - \frac{1}{9}\nu^2 - \frac{23}{81}\nu^3 + \frac{151}{243}\nu^4 - \frac{1}{9}v^5\right) + \mathcal{O}(\nu^7), \tag{2.42}$$

$$x_{L2} = 1 - \mu + \nu \left(1 + \frac{1}{3}\nu - \frac{1}{9}\nu^2 - \frac{31}{81}\nu^3 - \frac{119}{243}\nu^4 - \frac{1}{9}\nu^5\right) + \mathcal{O}(\nu^7), \tag{2.43}$$

$$x_{L3} = -\mu - 1 + \tilde{\nu} \left(1 + \frac{23}{84}\tilde{\nu}^2 + \frac{23}{84}\tilde{\nu}^3 + \frac{761}{2352}\tilde{\nu}^4 + \frac{3163}{7056}\tilde{\nu}^5 + \frac{30703}{49392}\tilde{\nu}^6\right) + \mathcal{O}(\tilde{\nu})^8, \tag{2.44}$$

where

$$\nu = \left(\frac{\mu}{3}\right)^{\frac{1}{3}}, \tag{2.45}$$

$$\tilde{\nu} = \frac{7\mu}{12} \tag{2.46}$$

The resulting approximations are then further refined to the desired tolerance using a Newton-Raphson or similar root-finding algorithm.

Beyond the three equilibrium solutions present on the x-axis, two additional equilibrium solutions exist off of the x-axis. Returning to Equation (2.36), if $r_{13,eq}$ is equivalent to $r_{23,eq}$, i.e., the point is equidistant from the primaries, then this equation is satisfied. Let $r_{13,eq} = r_{23,eq} = \tilde{r}$ be the distance to the primaries in this special configuration, then Equations (2.35) and (2.36) become

$$\begin{aligned} x_{eq}\left(\tilde{r}^3 - 1\right) &= 0, \\ y_{eq}\left(\tilde{r}^3 - 1\right) &= 0. \end{aligned}$$

Hence,

$$\tilde{r} = 1.$$

Therefore, the two remaining equilibrium solutions are determined through the intersections of the two unit circles centered at P_1 and P_2. The value of x_{eq} is evaluated by equating the respective equations for a circle as

$$\begin{aligned} \left(x_{eq} + \mu\right)^2 + y^2 &= \left(x_{eq} - 1 + \mu\right)^2 + y^2 \\ \Rightarrow x_{eq} &= \frac{1}{2} - \mu. \end{aligned}$$

Substituting back into the original circle equation yields the corresponding y_{eq} values of $\pm\frac{\sqrt{3}}{2}$. Conventionally, the equilibrium point in the upper half plane is denoted L_4 while the equilibrium point in the lower half plane is denoted L_5, i.e.

$$\begin{aligned} L_4\text{:} \quad & x_{L_4} = \tfrac{1}{2} - \mu \quad y_{L_4} = \tfrac{\sqrt{3}}{2}, \\ L_5\text{:} \quad & x_{L_5} = \tfrac{1}{2} - \mu \quad y_{L_5} = -\tfrac{\sqrt{3}}{2}. \end{aligned}$$

Figure 2.3 displays the location of the Lagrange points in the CRTBP. The two equilibrium solutions off of the x-axis, L_4 and L_5, form two equilateral triangles along with P_1 and P_2 and are, therefore, labelled the triangular or equilateral points. The

triangular points are located on the circular orbit of P_2 but phase shifted 60° in either direction. This behavior is most obvious in observations of the Trojan asteroids near L_4 and L_5 in the Sun-Jupiter system.

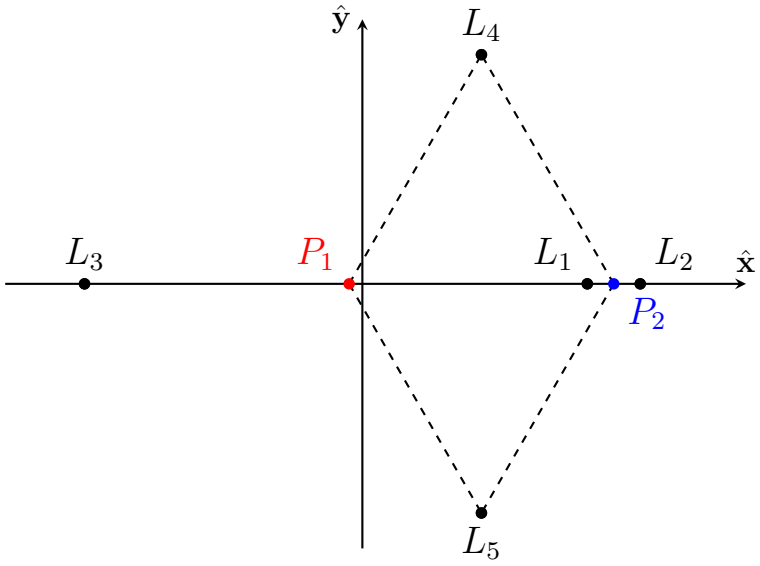

Figure 2.3.: CRTBP Lagrange Points

2.2.4 The Jacobi Integral

No closed-form analytical solution exists for the CRTBP as six first integrals of the motion do not exist. However, one constant of integration is available. This single integral of the motion is an energy-like quantity and is determined, similar to most energy integrals, by first using a dot product between the velocity and acceleration vectors, i.e.

$$\dot{\mathbf{r}} \cdot \ddot{\mathbf{r}} = \dot{x}\ddot{x} + \dot{y}\ddot{y} + \dot{z}\ddot{z}. \tag{2.47}$$

The expression in Equation (2.47) is also written in terms of the pseudopotential function as

$$\dot{x}\ddot{x} + \dot{y}\ddot{y} + \dot{z}\ddot{z} = \dot{x}\Omega_x + \dot{y}\Omega_y + \dot{z}\Omega_z. \tag{2.48}$$

The left side is straightforwardly transformed into the derivative of the square of velocity with respect to τ. The right side is the total derivative of the pseudopotential function with respect to τ. Therefore, both sides of this equation are rewritten in terms of derivatives with respect to τ as

$$\frac{d}{d\tau}\left(\frac{\dot{x}^2}{2}+\frac{\dot{y}^2}{2}+\frac{\dot{z}^2}{2}\right)=\frac{d\Omega}{d\tau}. \tag{2.49}$$

Integrating yields

$$J=2\Omega-v^2 \tag{2.50}$$

where J is the constant of integration, labelled the *Jacobi constant* or *Jacobi integral* and v is the velocity magnitude of P_3 as viewed in the rotating frame. Note that as the velocity of P_3 increases in magnitude, the Jacobi integral decreases. This negative relationship implies that a spacecraft travelling at higher velocities possesses a lower value of J than a spacecraft at the same position with a lower velocity. The negative relationship of Jacobi and speed is contrary to the relationship between speed and the classical definition of mechanical energy.

The Jacobi integral is the only integral available in the CRTBP, but offers significant information, both analytical and numerical. For example, as a constant of integration, the Jacobi integral remains fixed over any ballistic arc, so variations in J observed in a computer-generated numerical solution provide insight into the error present along the integrated path. Additional applications of the Jacobi constant include dimension reduction of the CRTBP and regions of exclusion.

2.2.5 Zero Velocity Surfaces

The existence of the Jacobi integral does offer some insight into the behavior in the CRTBP. Solving Equation (2.50) for velocity yields

$$v=\sqrt{2\Omega-J}. \tag{2.51}$$

Because the velocity of P_3 must be real, the quantity $2\Omega - J$ is necessarily non-negative. Therefore, given P_3 at a particular value of J, regions of space that are not available are identifiable. These regions satisfy the inequality

$$\Omega(\mathbf{r}) < \frac{J}{2} \tag{2.52}$$

where the position dependence of Ω is emphasized. The unavailable, or forbidden, regions are bounded by the loci of positions satisfying $J = 2\Omega$; this equality along with Equation (2.50) also mandate $v = 0$ along these bounding loci, so the loci are denoted Zero Velocity Surfaces (ZVSs).

If analysis is restricted to the xy plane, the points bounding the forbidden regions are labelled the Zero Velocity Curves (ZVCs) and are formed from the cross section of the corresponding ZVSs. The ZVCs, like the ZVSs, are functions of μ, the parameter defining the system, and the value of J. Sample ZVCs in the Earth-Moon system for various values of J are plotted in Figure 2.4. The regions of exclusion are shaded in gray and are bounded by the ZVCs in black. As the Jacobi constant drops, the ZVCs shrink until disappearing from the plane. The fundamental structure of the ZVCs changes as J passes through the values of the Jacobi constant corresponding to each Lagrange point. For example, Figure 2.4(a) illustrates the ZVC when P_3 is at a Jacobi constant value that is higher than the values corresponding to all 5 Lagrange points and at this energy level 3 different regions of motion exist: motion around P_1, motion around P_2, and motion external to the system. It is not possible for P_3 to move between these regions of motion because entering an excluded region is not possible as any change to the boundaries requires a maneuver, i.e., energy change. However, if J is sufficiently reduced, then a gateway opens at L_1 as apparent in Figure 2.4(b). The sufficiently higher energy of P_3 allows movement between the region surrounding the Earth and that near the Moon. Figure 2.5 demonstrates that when $J = J_{L_1}$ the ZVC forms a cusp at L_1. When the Jacobi constant is further reduced the gateway at L_1 expands. Further reducing the Jacobi constant below J_{L_2}, a gateway opens

beyond the Moon. The ZVCs then shrink further until $J = J_{L_3}$ when the gateway at L_3 opens and the ZVCs split forming regions around L_4 and L_5. These regions shrink until disappearing from the plane at $J = J_{L_4} = J_{L_5}$ as observed in Figure 2.4(e).

The relationship between Jacobi constant and regions of exclusion provides information on necessary conditions for certain mission applications. For example, given a spacecraft departing from Low Earth Orbit (LEO) enroute to the Moon, the initial Jacobi constant must be less than J_{L_1} to allow the existence of an open L_1 gateway. At larger values, no feasible transfer exists between the Earth and Lunar regions. Similar logic is applied to mission concepts that exit the system. Alternatively, to remain in the Earth or Lunar region, reducing energy such that $J > J_{L_1}$ ensures remaining in their desired region.

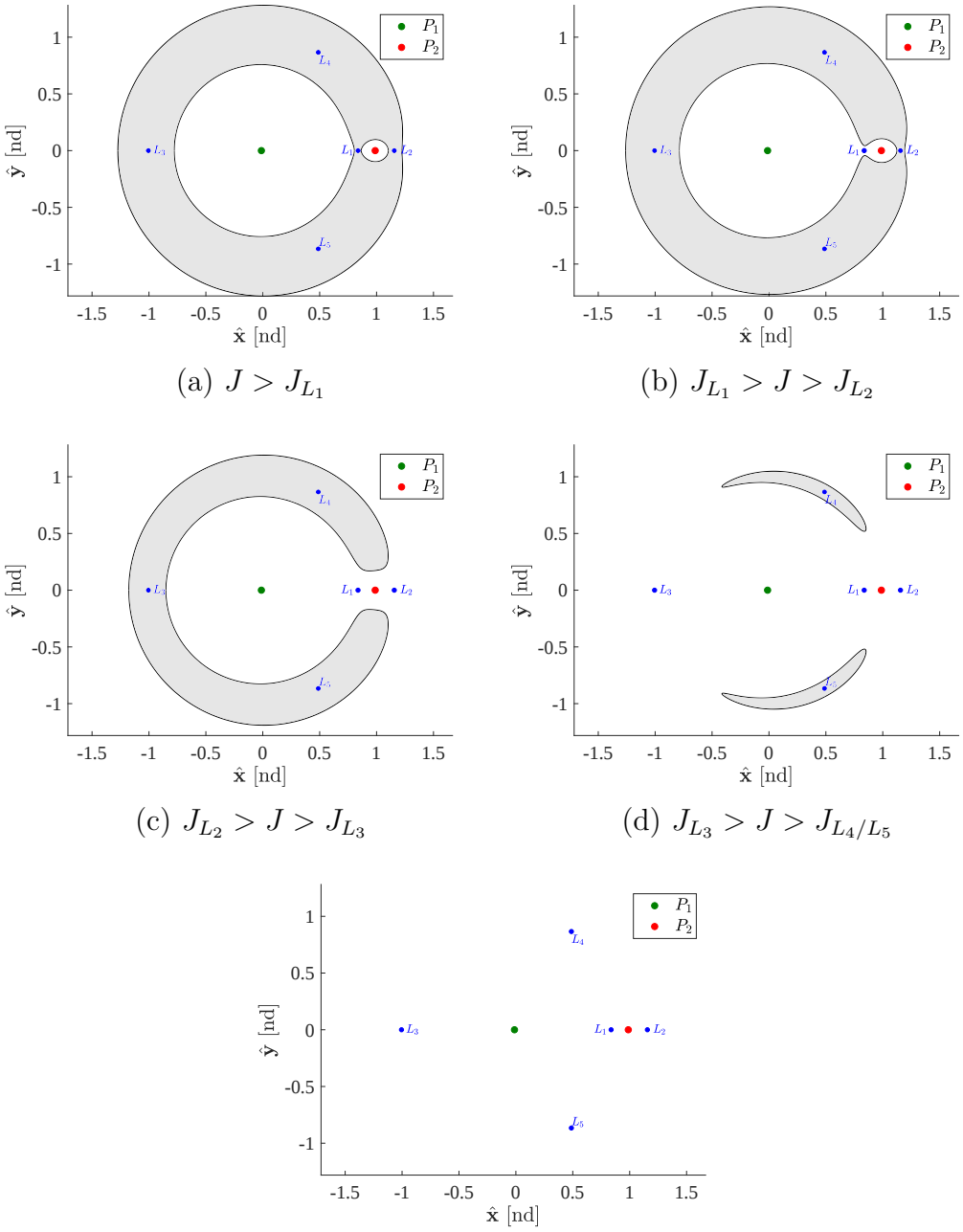

(a) $J > J_{L_1}$

(b) $J_{L_1} > J > J_{L_2}$

(c) $J_{L_2} > J > J_{L_3}$

(d) $J_{L_3} > J > J_{L_{4/5}}$

(e) $J_{L_{4/5}} > J$

Figure 2.4.: Zero Velocity Curves (ZVCs) in the Earth-Moon System at Various Jacobi Constant Values

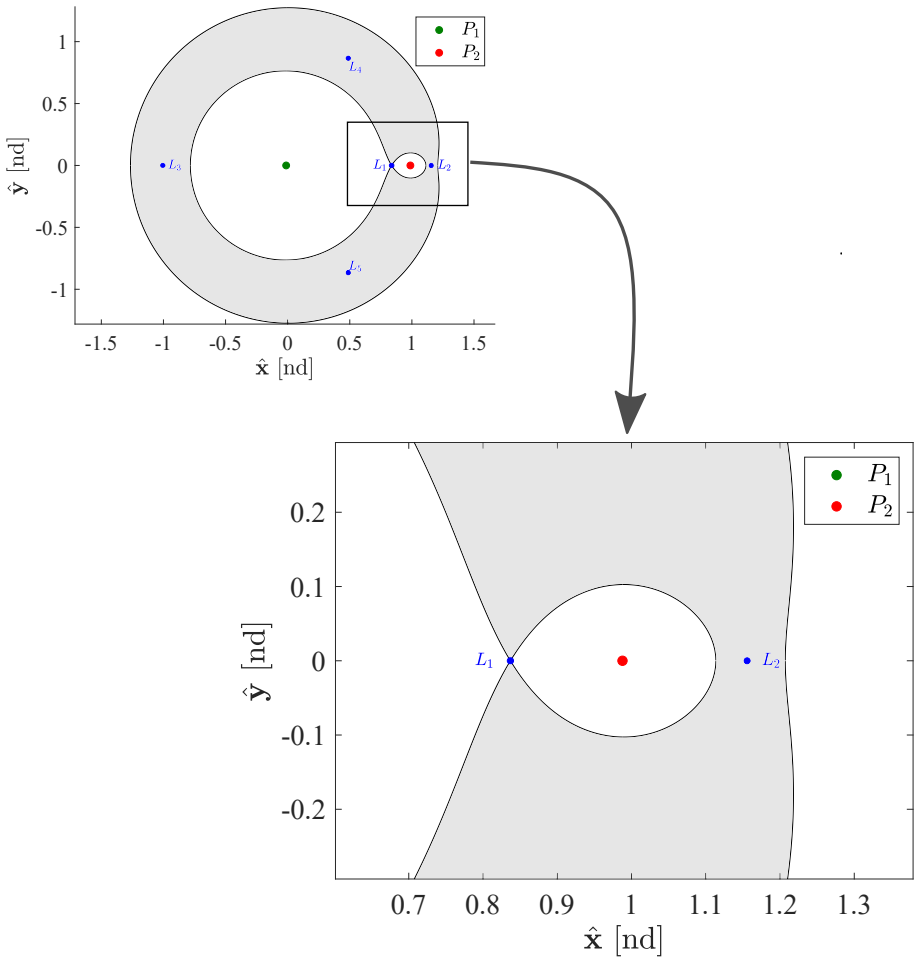

Figure 2.5.: ZVC in the Earth-Moon System When $J = J_{L_1}$

As previously mentioned, the ZVC reflects a cross section of the Zero Velocity Surface (ZVS). The conclusions from inspection of the ZVCs hold for the ZVSs as well. Figure 2.6 displays the ZVS for the same Jacobi constant value as the ZVC in Figure 2.4(a). Two spheres surround the Earth and Moon bounding isolated regions of motion. Additionally, the ZVS prevents objects exterior to the system from entering.

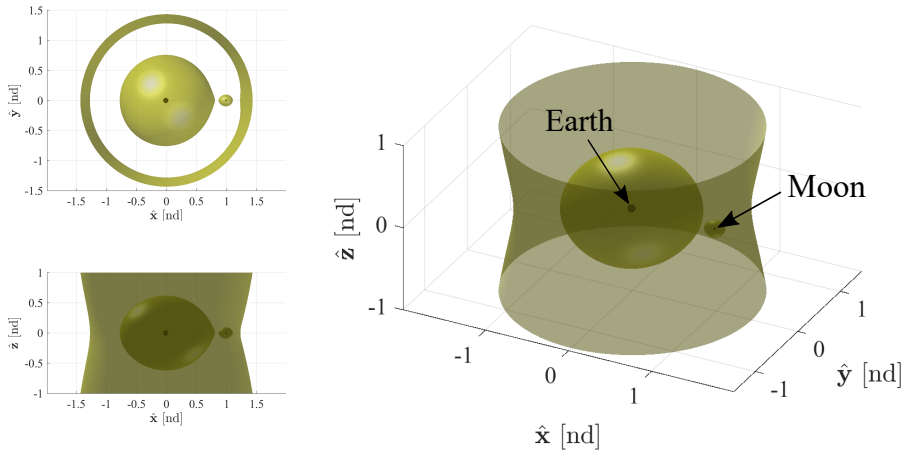

Figure 2.6.: ZVS in the Earth-Moon System when $J > J_{L_1}$

Figure 2.7 displays ZVSs at Jacobi constant values that are less than that of L_4 and L_5 ;the ZVCs disappear in the plane, but the ZVS continue to exist beyond the xy-plane. In this scenario, observe that there is one region of motion, that is P_3 may move between the region relatively closely surrounding P_1 and P_2 or depart the system without any change in energy, however inaccessible regions of space still exist above and below the plane that P_3 can never reach at the current energy. These regions of inaccessibility persist until $J \leq 0$ at which the spacecraft may reach any finite location in three dimensional space.

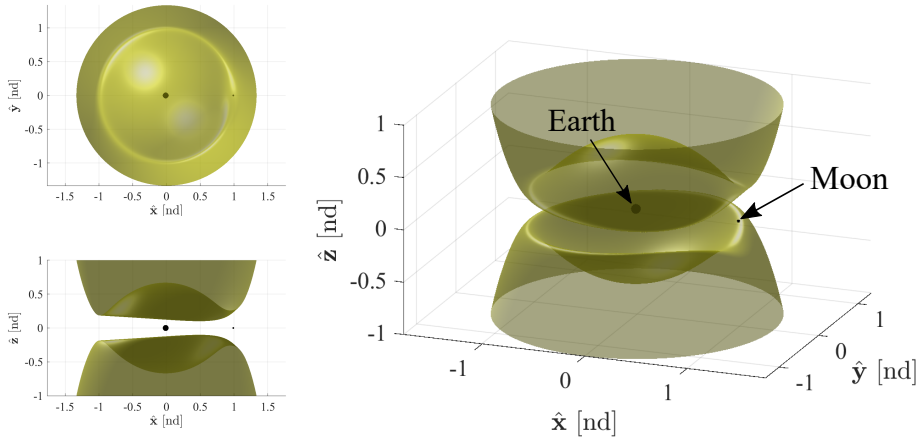

Figure 2.7.: ZVS in the Earth-Moon System when $J < J_{L_{4/5}}$

2.2.6 Linear Variational Equations Relative to the Collinear Lagrange Points

First-order linear variational equations approximating motion near the collinear Lagrange points are analytically solvable and characterize the motion in the near-vicinity surrounding these Lagrange points. The results obtained from the linear system provide a good first approximation for the behavior. The linear variational equations offer critical insight into the stability characteristics of the Lagrange points. In addition to providing stability information, the solutions to the linear variational equation also offer good first guesses for targeting algorithms in the full nonlinear model.

The linear equations are derived by expanding a set of variational equations in the vicinity of the collinear Lagrange points. The first-order form of the equations of motion are written as

$$\mathbf{f}(\mathbf{x}) = \begin{Bmatrix} \dot{x} \\ \dot{y} \\ \dot{z} \\ 2\dot{y} + \Omega_x \\ -2\dot{x} + \Omega_y \\ \Omega_z \end{Bmatrix}. \tag{2.53}$$

Let $\mathbf{x}_{L_i}$ be defined as the six-dimensional state of the Lagrange point and let $\delta\mathbf{x}$ represent a six-dimensional variation from $\mathbf{x}_{L_i}$. Therefore, the state of P_3 is expressed as

$$\mathbf{x} = \mathbf{x}_{L_i} + \delta\mathbf{x}. \tag{2.54}$$

The vector $\delta\mathbf{x}$ is six-dimensional to reflect the displacement in both position and velocity of P_3 from the Lagrange point of interest. A Taylor series expansion relative

to the Lagrange point enables the formulation of the variational equations of motion for $\delta\mathbf{x}$. This Taylor expansion is

$$\dot{\mathbf{x}}_{L_i} + \delta\dot{\mathbf{x}} = \mathbf{f}\left(\mathbf{x}_{L_i}\right) + \left.\frac{d\mathbf{f}}{d\mathbf{x}}\right|_{\mathbf{x}_{L_i}} \delta\mathbf{x} + \mathcal{O}\left(\left|\delta\mathbf{x}\right|^2\right). \tag{2.55}$$

By definition $\dot{\mathbf{x}}_{L_i} = \mathbf{f}\left(\mathbf{x}_{L_i}\right) = \mathbf{0}$, so ignoring terms of order 2 and higher, the linear variational equations are

$$\delta\dot{\mathbf{x}} \approx \left.\frac{d\mathbf{f}}{d\mathbf{x}}\right|_{\mathbf{x}_{L_i}} \delta\mathbf{x}. \tag{2.56}$$

Note that the relationship in Equation (2.56) is approximate due to the removal of the higher order terms. The matrix $\frac{d\mathbf{f}}{d\mathbf{x}}$ is the symmetric Jacobian matrix corresponding to the equations of motion and is constructed as

$$\frac{d\mathbf{f}}{d\mathbf{x}} = \begin{bmatrix} 0 & 0 & 0 & 1 & 0 & 0 \\ 0 & 0 & 0 & 0 & 1 & 0 \\ 0 & 0 & 0 & 0 & 0 & 1 \\ \Omega_{xx} & \Omega_{xy} & \Omega_{xz} & 0 & 2 & 0 \\ \Omega_{yx} & \Omega_{yy} & \Omega_{yz} & -2 & 0 & 0 \\ \Omega_{zx} & \Omega_{zy} & \Omega_{zz} & 0 & 0 & 0 \end{bmatrix} \tag{2.57}$$

where the second order partial derivatives of the pseudopotential function, Ω_{ij}, are

$$\Omega_{xx} = 1 - \frac{1-\mu}{r_{13}^3} - \frac{\mu}{r_{23}^3} + \frac{3\left(1-\mu\right)\left(x+\mu\right)^2}{r_{13}^5} + \frac{3\mu\left(x-1+\mu\right)^2}{r_{23}^5}, \tag{2.58}$$

$$\Omega_{yy} = 1 - \frac{1-\mu}{r_{13}^3} - \frac{\mu}{r_{23}^3} + \frac{3\left(1-\mu\right)y^2}{r_{13}^5} + \frac{3\mu y^2}{r_{23}^5}, \tag{2.59}$$

$$\Omega_{zz} = -\frac{1-\mu}{r_{13}^3} - \frac{\mu}{r_{23}^3} + \frac{3\left(1-\mu\right)z^2}{r_{13}^5} + \frac{3\mu z^2}{r_{23}^5}, \tag{2.60}$$

$$\Omega_{xy} = \frac{3\left(1-\mu\right)\left(x+\mu\right)y}{r_{13}^5} + \frac{3\mu\left(x-1+\mu\right)y}{r_{23}^5} = \Omega yx, \tag{2.61}$$

$$\Omega_{xz} = \frac{3\left(1-\mu\right)\left(x+\mu\right)z}{r_{13}^5} + \frac{3\mu\left(x-1+\mu\right)z}{r_{23}^5} = \Omega zx, \tag{2.62}$$

$$\Omega_{yz} = \frac{3\left(1-\mu\right)yz}{r_{13}^5} + \frac{3\mu yz}{r_{23}^5} = \Omega_{zy}. \tag{2.63}$$

Because $\frac{d\mathbf{f}}{d\mathbf{x}}$ is evaluated at each Lagrange point, each constant equilibrium solution presents a different linear system and potentially different qualitative stability characteristics. However, for each libration point, the variational equations (Equation (2.56)) form a linear homogeneous system with constant coefficients and, therefore, a closed-form analytical solution exists.

The locations of the Lagrange points in the CRTBP offers further simplifications to the variational equations. Specifically, because all Lagrange points are on the xy plane, $\Omega_{xz} = \Omega_{zx} = \Omega_{yz} = \Omega_{zy} = 0$ simplifying the Jacobian to

$$\left.\frac{d\mathbf{f}}{d\mathbf{x}}\right|_{\mathbf{x}_{L_i}} = \begin{bmatrix} 0 & 0 & 0 & 1 & 0 & 0 \\ 0 & 0 & 0 & 0 & 1 & 0 \\ 0 & 0 & 0 & 0 & 0 & 1 \\ \Omega_{xx} & \Omega_{xy} & 0 & 0 & 2 & 0 \\ \Omega_{yx} & \Omega_{yy} & 0 & -2 & 0 & 0 \\ 0 & 0 & \Omega_{zz} & 0 & 0 & 0 \end{bmatrix}_{\mathbf{x}_{L_i}}. \tag{2.64}$$

Clearly, the matrix now decouples the linear in-plane and out-of-plane modes effectively forming two isolated linear systems:

$$\begin{Bmatrix} \delta\dot{z} \\ \delta\ddot{z} \end{Bmatrix} = \begin{bmatrix} 0 & 1 \\ \Omega_{zz} & 0 \end{bmatrix}_{\mathbf{x}_{L_i}} \begin{Bmatrix} \delta z \\ \delta\dot{z} \end{Bmatrix} \tag{2.65}$$

and

$$\begin{Bmatrix} \delta\dot{x} \\ \delta\dot{y} \\ \delta\ddot{x} \\ \delta\ddot{y} \end{Bmatrix} = \begin{bmatrix} 0 & 0 & 1 & 0 \\ 0 & 0 & 0 & 1 \\ \Omega_{xx} & \Omega_{xy} & 0 & 2 \\ \Omega_{yx} & \Omega_{yy} & -2 & 0 \end{bmatrix}_{\mathbf{x}_{L_i}} \begin{Bmatrix} \delta x \\ \delta y \\ \delta\dot{x} \\ \delta\dot{y} \end{Bmatrix}. \tag{2.66}$$

This decoupling allows the two modes of motion to be analyzed separately and their resulting solutions may be superimposed to generate more complex types of motion.

Analyzing the out-of-plane motion, the equation is solved analytically resulting in a description of simple harmonic motion. The scalar out-of-plane variational equation is written simply in second order form as

$$\delta\ddot{z} - \Omega_{zz}\delta z = 0. \tag{2.67}$$

Furthermore, at each Lagrange point, $\Omega_{zz} < 0$, thus, Equation (2.67) is equivalent to a harmonic oscillator with frequency $\omega_z = \sqrt{-\Omega_{zz}}$. (Additionally, at L_4 and L_5, the expression for Ω_{zz} is always unity and therefore the out-of-plane frequency for L_4 and L_5 is always 1.) In general, the scalar solution to the out-of-plane equation is

$$\delta z(\tau) = \delta z_0 \cos\omega_z\tau + \frac{\delta\dot{z}_0}{\omega_z}\sin\omega_z\tau \tag{2.68}$$

where $\delta z_0 = \delta z(0)$ and $\delta\dot{z}_0 = \delta\dot{z}(0)$. The accuracy of this result is consistent with Lyapunov stability analysis.

The in-plane variational equations reduce to a fourth order coupled system of linear differential equations. Following the analysis of Szebehely [5], the matrix determinant,

$$\det\left(\lambda I - \begin{bmatrix} 0 & 0 & 1 & 0 \\ 0 & 0 & 0 & 1 \\ \Omega_{xx} & \Omega_{xy} & 0 & 2 \\ \Omega_{yx} & \Omega_{yy} & -2 & 0 \end{bmatrix}_{\mathbf{x}_{L_i}}\right) = 0 \tag{2.69}$$

yields the characteristic polynomial

$$\lambda^4 + (4 - \Omega_{xx} - \Omega_{yy})\,\lambda^2 + \left(\Omega_{xx}\Omega_{yy} - \Omega_{xy}^2\right) = 0. \tag{2.70}$$

At the collinear points, $y = 0$ and therefore $\Omega_{xy} = 0$; in addition, $\Omega_{xx} > 0$ and $\Omega_{yy} < 0$. Furthermore, defining $\Lambda = \lambda^2$ allows the characteristic polynomial in the following form:

$$\Lambda^2 + 2K_1\Lambda - K_2^2 = 0 \tag{2.71}$$

where

$$K_1 = \frac{1}{2}\left(4 - \Omega_{xx} - \Omega_{yy}\right), \tag{2.72}$$

$$K_2^2 = -\Omega_{xx}\Omega_{yy}. \tag{2.73}$$

Solving this quadratic equations yields the solutions

$$\Lambda_{1,2} = -K_1 \pm \sqrt{K_1^2 + K_2^2}. \tag{2.74}$$

Given the signs on the quantities Ω_{xx} and Ω_{yy}, K_2^2 is always positive. Therefore, $\Lambda_1 > 0$ and $\Lambda_2 < 0$. Subsequently,

$$\lambda_{1,2} = \pm\sqrt{\Lambda_1} \in \mathbb{R}^1, \tag{2.75}$$

$$\lambda_{3,4} = \pm j\sqrt{|\Lambda_2|}. \tag{2.76}$$

$$\tag{2.77}$$

Therefore, λ_1 and λ_2 correspond to the unstable and stable modes of the system, respectively, while λ_3 and λ_4 correspond to a two-dimensional center subspace producing periodic motion.

The solution for in-plane motion is determined through reduction of the general solution to the solutions containing only center mode behavior. The general solution for the in-plane system of equations corresponding to the collinear Lagrange points is

$$\delta x(\tau) = \sum_{i=1}^{4} a_i e^{\lambda_i \tau}, \tag{2.78}$$

$$\delta y(\tau) = \sum_{i=1}^{4} b_i e^{\lambda_i \tau}, \tag{2.79}$$

$$\delta \dot{x}(\tau) = \sum_{i=1}^{4} a_i \lambda_i e^{\lambda_i \tau}, \tag{2.80}$$

$$\delta \dot{y}(\tau) = \sum_{i=1}^{4} b_i \lambda_i e^{\lambda_i \tau}. \tag{2.81}$$

Substituting this general form into Equation (2.66) produces

$$\sum_{i=1}^{4} a_i \lambda_i^2 e^{\lambda_i \tau} = \Omega_{xx} \sum_{i=1}^{4} a_i e^{\lambda_i \tau} + 2 \sum_{i=1}^{4} b_i \lambda_i e^{\lambda_i \tau}. \tag{2.82}$$

Because this relationship must hold for any value of τ, the coefficients of $e^{\lambda_i \tau}$ must be the same on both sides. Therefore, this equation yields the expresion

$$b_i = a_i \gamma_i \tag{2.83}$$

where

$$\gamma_i = \frac{(\lambda_i^2 - \Omega_{xx})}{2\lambda_i}. \tag{2.84}$$

Replacing the b_i coefficients with this functional dependence on a_i allows the expression of the general solution in terms only of a_i, λ_i, γ_i, and τ:

$$\delta x(\tau) = \sum_{i=1}^{4} a_i e^{\lambda_i \tau}, \tag{2.85}$$

$$\delta y(\tau) = \sum_{i=1}^{4} a_i \gamma_i e^{\lambda_i \tau}, \tag{2.86}$$

$$\delta \dot{x}(\tau) = \sum_{i=1}^{4} a_i \lambda_i e^{\lambda_i \tau}, \tag{2.87}$$

$$\delta \dot{y}(\tau) = \sum_{i=1}^{4} a_i \gamma_i \lambda_i e^{\lambda_i \tau}. \tag{2.88}$$

As previously noted, the variations relative to the collinear Lagrange points include both hyperbolic and center modes. Initial conditions may be selected such that only the center mode is excited. To do so, select $a_1 = a_2 = 0$. The solution is then constrained to be

$$\delta x(\tau) = a_3 e^{\lambda_3 \tau} + a_4 e^{-\lambda_3 \tau}, \tag{2.89}$$

$$\delta y(\tau) = a_3 \gamma_3 e^{\lambda_3 \tau} - a_4 \gamma_3 e^{-\lambda_3 \tau}, \tag{2.90}$$

$$\delta \dot{x}(\tau) = a_3 \lambda_3 e^{\lambda_i \tau} - a_4 \lambda_3 e^{-\lambda_3 \tau}, \tag{2.91}$$

$$\delta \dot{y}(\tau) = a_3 \gamma_3 \lambda_3 e^{\lambda_3 \tau} + a_4 \gamma_3 \lambda_3 e^{\lambda_3 \tau}. \tag{2.92}$$

The implementation of this restriction, however, means that only 2 of the 4 initial conditions are variables. Assuming that δx_0 and δy_0 are specified as the variables, expressions for a_3 and a_4 are then

$$a_3 = \frac{\delta y_0 + \gamma_3 \delta x_0}{2\gamma_3}, \tag{2.93}$$

$$a_4 = -\frac{\delta y_0 - \gamma_3 \delta x_0}{2\gamma_3}. \tag{2.94}$$

From these expressions, the initial velocity components are then determined to be

$$\delta \dot{x}_0 = \frac{\lambda_3 \delta y_0}{\gamma_3}, \tag{2.95}$$

$$\delta \dot{y}_0 = \gamma_3 \lambda_3 \delta x_0. \tag{2.96}$$

Let

$$s = \sqrt{K_1 + \sqrt{K_1^2 + K_2^2}}, \tag{2.97}$$

then $\delta \dot{x}_0$ and $\delta \dot{y}_0$ are written

$$\delta \dot{x}_0 = \frac{2s^2}{s^2 + \Omega_{xx}} \delta y_0, \tag{2.98}$$

$$\delta \dot{y}_0 = -\frac{s^2 + \Omega_{xx}}{2} \delta x_0. \tag{2.99}$$

Finally, the solution for in-plane motion near the collinear Lagrange points is evaluated from

$$\delta x(\tau) = \delta x_0 \cdot \cos(s\tau) + \frac{2s \cdot \delta y_0}{s^2 + \Omega_{xx}} \sin(s\tau), \tag{2.100}$$

$$\delta y(\tau) = \delta y_0 \cdot \cos(s\tau) - \frac{(s^2 + \Omega_{xx}) \cdot \delta x_0}{2s} \sin(s\tau). \tag{2.101}$$

Equations (2.100) and (2.101) offer an approximate solution for in-plane motion near the collinear Lagrange points. They represent elliptical motion where the Lagrange point is at the center, not at a focus, with frequency $\omega_{xy} = s$. A similar process

is repeated for the selection of different combinations of initial conditions such as $(\delta x_0, \delta \dot{x}_0)$, $(\delta \dot{x}_0, \delta \dot{y}_0)$, or $(\delta y_0, \delta \dot{y}_0)$.

The in-plane and out-of-plane solutions are superimposed to produce expressions of the general spatial variational behaviors. Combining the in-plane and out-of-plane solutions for the collinear points, and restricting motion to the central mode, supplies the set of solutions

$$\delta x(\tau) = \delta x_0 \cdot \cos(s\tau) + \frac{2s \cdot \delta y_0}{s^2 + \Omega_{xx}} \sin(s\tau) \tag{2.102}$$

$$\delta y(\tau) = \delta y_0 \cdot \cos(s\tau) - \frac{(s^2 + \Omega_{xx}) \cdot \delta x_0}{2s} \sin(s\tau) \tag{2.103}$$

$$\delta z(\tau) = \delta z_0 \cos \omega_z \tau + \frac{\delta \dot{z}_0}{\omega_z} \sin \omega_z \tau. \tag{2.104}$$

for the case where δx_0 and δy_0 are selected as the free variables. These variational expressions produce linear approximations for periodic motion in the vicinity of these equilibrium points to seed nonlinear targeting algorithms for construction of the nonlinear periodic motion.

2.2.7 The State Transition Matrix

The linear variational analysis is also applicable for targeting general reference solutions in the CRTBP. The development of these linear approximations provides information on the region surrounding a particular solution arc via a mapping of initial perturbations from the reference to perturbations at other times, past and future. These mappings are critical in the differential corrections process.

The mapping is constructed through variation from a reference trajectory. Given a solution to the CRTBP, $\mathbf{x}^*(\tau)$, and denoting the variation from this solution as $\delta \mathbf{x}(\tau)$, a nearby perturbed solution is expressed as

$$\mathbf{x}(\tau) = \mathbf{x}^*(\tau) + \delta \mathbf{x}(\tau). \tag{2.105}$$

The relationship between these quantities appears graphically in Figure 2.8. Consis-

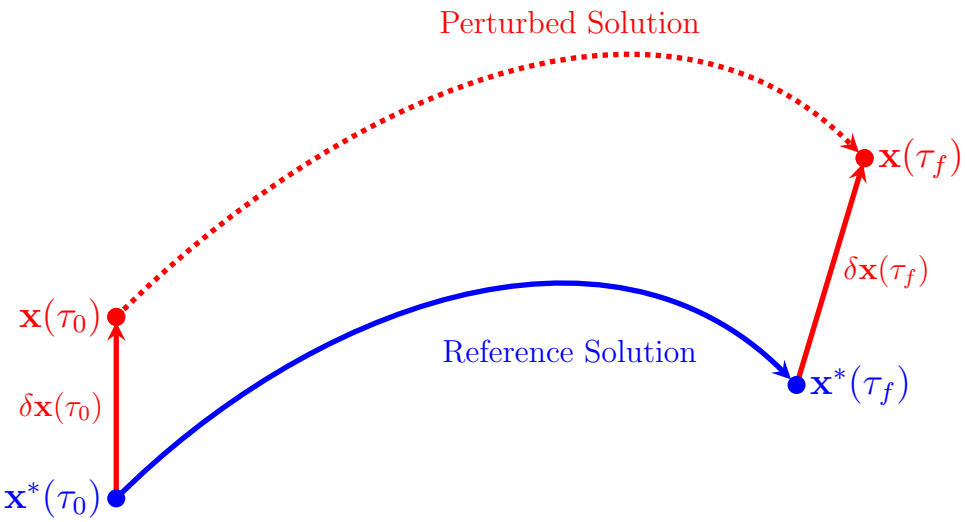

Figure 2.8.: Schematic for a Mapping of the Variations for a General Trajectory in the CRTBP

tent with the process to model variations relative to the equilibrium solutions, the linear variational equations with respect to the general trajectory arc are generated via an application of a first-order Taylor series expansion. The first-order Taylor approximation for the right side of Equation (2.105) is

$$\dot{\mathbf{x}}^*(\tau) + \delta\dot{\mathbf{x}}(\tau) \approx \mathbf{f}(\mathbf{x}^*(\tau)) + \left.\frac{\partial \mathbf{f}}{\partial \mathbf{x}}\right|_{\mathbf{x}(\tau)} \delta\mathbf{x}(\tau). \tag{2.106}$$

Cancelling terms yields the variational equations for the deviation with respect to the reference solution,

$$\delta\dot{\mathbf{x}}(\tau) \approx \left.\frac{\partial \mathbf{f}}{\partial \mathbf{x}}\right|_{\mathbf{x}(\tau)} \delta\mathbf{x}(\tau). \tag{2.107}$$

Equation (2.107) is a linear time-varying homogeneous system of differential equations. Therefore, the general solution to this set of equations is

$$\delta\mathbf{x}(\tau) = \Phi(\tau, \tau_0)\, \delta\mathbf{x}(\tau_0). \tag{2.108}$$

The matrix Φ in Equation (2.108) is denoted the *State Transition Matrix* and contains information on the sensitivity of the perturbation at time τ to the initial perturbation at time τ_0. Let

$$\mathbf{A} = \left.\frac{\partial \mathbf{f}}{\partial \mathbf{x}}\right|_{\mathbf{x}(\tau)} \tag{2.109}$$

then the STM is equally defined as the matrix exponential

$$\Phi\left(\tau, \tau_0\right) = e^{A(\tau)(\tau-\tau_0)}. \tag{2.110}$$

Subsequently, the STM satisfies the linear differential equation

$$\dot{\Phi}\left(\tau, \tau_0\right) = \mathbf{A}\left(\tau\right)\Phi\left(\tau, \tau_0\right). \tag{2.111}$$

Therefore, the STM is computed by integrating (2.111) along with the standard equations of motion in the CRTBP resulting in 42 coupled differential equations. However, the STM may alternatively be numerically approximated through forward, reverse, or central difference methods applied to the standard CRTBP equations of motion. While both are valid methods for constructing a useful STM, the appropriate strategy is determined by computational capabilities and implementation complexity among other factors. The STM is, of course, a first-order linear approximation, thus, only first-order accuracy is delivered in the nonlinear model.

Even as a linear approximation, the structure of the STM offers significant insight for various types of applications. The STM is split into four quadrants, i.e.

$$\Phi = \begin{bmatrix} \Phi_{\mathbf{rr}} & \Phi_{\mathbf{rv}} \\ \Phi_{\mathbf{vr}} & \Phi_{\mathbf{vv}} \end{bmatrix} \tag{2.112}$$

where

$$\Phi_{\mathbf{rr}} = \begin{bmatrix} \frac{\partial x_f}{\partial x_0} & \frac{\partial x_f}{\partial y_0} & \frac{\partial x_f}{\partial z_0} \\ \frac{\partial y_f}{\partial x_0} & \frac{\partial y_f}{\partial y_0} & \frac{\partial y_f}{\partial z_0} \\ \frac{\partial z_f}{\partial x_0} & \frac{\partial z_f}{\partial y_0} & \frac{\partial z_f}{\partial z_0} \end{bmatrix} \quad \Phi_{\mathbf{rv}} = \begin{bmatrix} \frac{\partial x_f}{\partial \dot{x}_0} & \frac{\partial x_f}{\partial \dot{y}_0} & \frac{\partial x_f}{\partial \dot{z}_0} \\ \frac{\partial y_f}{\partial \dot{x}_0} & \frac{\partial y_f}{\partial \dot{y}_0} & \frac{\partial y_f}{\partial \dot{z}_0} \\ \frac{\partial z_f}{\partial \dot{x}_0} & \frac{\partial z_f}{\partial \dot{y}_0} & \frac{\partial z_f}{\partial \dot{z}_0} \end{bmatrix}$$

$$\Phi_{\mathbf{vr}} = \begin{bmatrix} \frac{\partial \dot{x}_f}{\partial x_0} & \frac{\partial \dot{x}_f}{\partial y_0} & \frac{\partial \dot{x}_f}{\partial z_0} \\ \frac{\partial \dot{y}_f}{\partial x_0} & \frac{\partial \dot{y}_f}{\partial y_0} & \frac{\partial \dot{y}_f}{\partial z_0} \\ \frac{\partial \dot{z}_f}{\partial x_0} & \frac{\partial \dot{z}_f}{\partial y_0} & \frac{\partial \dot{z}_f}{\partial z_0} \end{bmatrix} \quad \Phi_{\mathbf{vv}} = \begin{bmatrix} \frac{\partial \dot{x}_f}{\partial \dot{x}_0} & \frac{\partial \dot{x}_f}{\partial \dot{y}_0} & \frac{\partial \dot{x}_f}{\partial \dot{z}_0} \\ \frac{\partial \dot{y}_f}{\partial \dot{x}_0} & \frac{\partial \dot{y}_f}{\partial \dot{y}_0} & \frac{\partial \dot{y}_f}{\partial \dot{z}_0} \\ \frac{\partial \dot{z}_f}{\partial \dot{x}_0} & \frac{\partial \dot{z}_f}{\partial \dot{y}_0} & \frac{\partial \dot{z}_f}{\partial \dot{z}_0} \end{bmatrix}$$

are the submatrices representing different types of sensitivities. The submatrix $\Phi_{\mathbf{rr}}$ reflects the sensitivity to the position components at time τ to the initial position components, $\Phi_{\mathbf{rv}}$ represents the sensitivity of the position components at time τ to the initial velocity components, $\Phi_{\mathbf{vr}}$ depicts the sensitivity of the velocity components at time τ to the initial position components, and $\Phi_{\mathbf{vv}}$ contains sensitivity information of the final velocity components with respect to the initial velocity components. The State Transition Matrix also possesses several important properties that are frequently leveraged, specifically

$$\Phi(\tau_2, \tau_0) = \Phi(\tau_2, \tau_1)\Phi(\tau_1, \tau_0), \tag{2.113}$$

$$\Phi(\tau_0, \tau_1) = \Phi^{-1}(\tau_1, \tau_0), \tag{2.114}$$

$$\det(\Phi) = 1, \tag{2.115}$$

$$\Phi(\tau_0, \tau_0) = \mathbf{I}. \tag{2.116}$$

These properties demonstrating the composability of the STM is vital for the implementation of complex targeting architectures.

The state transition matrix provides a valuable tool for quantifying the sensitivities of state components along a trajectory with respect to the initial conditions. This mapping of initial deviations to final deviations is leveraged extensively during differential corrections processes, orbital stability analysis, and manifold calculation.

2.3 Differential Corrections

During the trajectory design process, a trajectory is sought that satisfies a set of constraints. Due to the lack of an analytical solution, numerical analysis is employed to determine the initial conditions that satisfy the constraints. Fundamentally, this scenario presents a boundary value problem (BVP) and, while various methods exist to solve BVPs, differential corrections provides a particularly powerful method of solving this problem.

Corrections strategies can be implemented using many different numerical schemes. For this investigation, the general corrections problem is abstractly defined by its design variables and constraints. Let $\mathbf{X}$ represent the vector of n design variables and $\mathbf{F}$ serves as the vector of m constraints written algebraically as

$$\mathbf{X} = \begin{Bmatrix} X_1 \\ X_2 \\ \vdots \\ X_n \end{Bmatrix} \tag{2.117}$$

and

$$\mathbf{F}(\mathbf{X}) = \begin{Bmatrix} F_1(\mathbf{X}) \\ F_2(\mathbf{X}) \\ \vdots \\ F_m(\mathbf{X}) \end{Bmatrix}. \tag{2.118}$$

In the design variable vector, $\mathbf{X}$, the variables, X_i, are commonly state components, times of flight, or thrust parameters. The solution is achieved, i.e., $\mathbf{X} = \mathbf{X}^*$, when a set of design variables is found that forces the constraint vector to zero, i.e., $\mathbf{F}(\mathbf{X}^*) = \mathbf{0}$. If $\mathbf{F}$ is an affine function of $\mathbf{X}$ and $n = m$, the root $\mathbf{X}^*$ is computed trivially by

$$\mathbf{X}^* = -\left(\frac{d\mathbf{F}}{d\mathbf{X}}\right)^{-1} \mathbf{F}(\mathbf{0}). \tag{2.119}$$

However, affine constraint vectors rarely arise in trajectory design. Therefore, a corrections algorithm iteratively arrives at the solution, $\mathbf{X}^*$.

The iterative process determining $\mathbf{X}^*$ is based on a Taylor series expansion of $\mathbf{F}(\mathbf{X})$. Given a reference free-variable vector, $\mathbf{X}_k$, the Taylor series expansion of $\mathbf{F}(\mathbf{X})$ relative to $\mathbf{X}_k$, to first-order, is

$$\mathbf{F}(\mathbf{X}) \approx \mathbf{F}(\mathbf{X}_k) + \left.\frac{d\mathbf{F}(\mathbf{X})}{d\mathbf{X}}\right|_{X_k} (\mathbf{X} - \mathbf{X}_k). \tag{2.120}$$

Thus, the constraint function evaluation at $\mathbf{X}^*$ is

$$\mathbf{F}(\mathbf{X}^*) \approx \mathbf{F}(\mathbf{X}_k) + \left.\frac{d\mathbf{F}(\mathbf{X})}{d\mathbf{X}}\right|_{X_k} (\mathbf{X}^* - \mathbf{X}_k). \tag{2.121}$$

By definition $\mathbf{F}(\mathbf{X}^*) = \mathbf{0}$, so, ignoring higher-order terms, Equation (2.121) is simplified to first-order

$$\mathbf{0} = \mathbf{F}(\mathbf{X}_k) + \left.\frac{d\mathbf{F}(\mathbf{X})}{d\mathbf{X}}\right|_{X_k} (\mathbf{X}^* - \mathbf{X}_k). \tag{2.122}$$

The linear approximation in Equation (2.122) is essentially a root-finding problem and generates iterative update equations for determining $\mathbf{X}^*$. Solving Equation (2.122) depends on the shape and rank of the Jacobian of the constraint vector, $\frac{d\mathbf{F}(\mathbf{X})}{d\mathbf{X}}$. Assuming a full rank Jacobian, i.e.,

$$\operatorname{rank}\left(\frac{d\mathbf{F}(\mathbf{X})}{d\mathbf{X}}\right) = \min(n, m) \tag{2.123}$$

where $\frac{d\mathbf{F}(\mathbf{X})}{d\mathbf{X}}$ is an $m \times n$ matrix, three cases exist for the shape of the Jacobian: $m > n$ (tall), $m = n$ (square), and $n > m$ (wide). The solution of each case is different and, thus, they are examined separately.

As one possibility, if the Jacobian matrix is tall, i.e., $m > n$, then there are more constraints than free variables. The result of this configuration is the existence of either 1 or 0 solutions. The general procedure for solving these types of systems is

the least-squares approach. However, trajectory design problems often incorporate time, position, and velocity continuity in the constraint equations. Consequently, least-squares solutions are rarely applicable to these problems as tolerances must be met absolutely for results to be dynamically coherent.

If the Jacobian matrix is square ($m = n$) and nonsingular, then Equation (2.122) is solved via a typical Newton update. Therefore, the equation is rearranged to solve for the zero as

$$\mathbf{X}^* = \mathbf{X}_k - \left[\frac{d\mathbf{F}(\mathbf{X})}{d\mathbf{X}}\right]^{-1}_{X_k} \mathbf{F}(\mathbf{X}_k). \tag{2.124}$$

The linear approximation in Equation (2.124) ignores the nonlinear dynamics of the problem due to the truncation of higher-order terms and, therefore, requires the implementation of an iterative procedure. The iteration equation is determined from Equation (2.124) as

$$\mathbf{X}_{k+1} = \mathbf{X}_k - \left[\frac{d\mathbf{F}(\mathbf{X})}{d\mathbf{X}}\right]^{-1}_{X_k} \mathbf{F}(\mathbf{X}_k). \tag{2.125}$$

Equation (2.125) is seeded with an initial guess, $\mathbf{X}_0$, and iterated until a stopping condition is met. The iteration stopping condition varies based on the application but often requires the Euclidean norm of $\mathbf{F}(\mathbf{X}_k)$ to be below a predetermined absolute or relative tolerance.

In the wide case where the Jacobian matrix contains more columns than rows, i.e., $n > m$, then there are more free variables than constraints and the problem is under-determined. Under-determined problems possess either zero or an infinite number of solutions to Equation (2.122). Assuming the Jacobian matrix has full rank, the zero-solution case is ignored. Various options exist for selecting the "best" solution from among the infinite possibilities, but one of particular interest is the minimum-norm solution. The minimum-norm solution allows the solution of Equation (2.122) while minimizing the deviation from the initial guess. This solution is especially useful for preserving some desired properties of the initial guess, e.g., geometry. To determine the form of the minimum norm solution, the problem is reformulated and the method

of Lagrange multipliers is applied. The minimum-norm solution is the solution to the optimization problem

$$\begin{aligned} \min_{\mathbf{X}^*} \quad & ||\mathbf{X}^* - \mathbf{X}_k||_2^2 \\ \text{s.t.} \quad & \left.\frac{d\mathbf{F}(\mathbf{X})}{d\mathbf{X}}\right|_{X_k} (\mathbf{X}^* - \mathbf{X}_k) + \mathbf{F}(\mathbf{X}_k) = \mathbf{0}. \end{aligned} \tag{2.126}$$

Therefore, the Lagrangian of the optimization problem is written

$$\mathcal{L}(\mathbf{X}^*, \lambda) = \frac{1}{2}(\mathbf{X}^* - \mathbf{X}_k)^{\mathrm{T}}(\mathbf{X}^* - \mathbf{X}_k) + \lambda^{\mathrm{T}}\left(\left.\frac{d\mathbf{F}(\mathbf{X})}{d\mathbf{X}}\right|_{X_k} (\mathbf{X}^* - \mathbf{X}_k) + \mathbf{F}(\mathbf{X}_k)\right). \tag{2.127}$$

Differentiating with respect to $\mathbf{X}^*$ and λ_k and setting the expression to zero yields

$$\frac{\partial \mathcal{L}(\mathbf{X}^*, \lambda)}{\partial \mathbf{X}^*} = (\mathbf{X}^* - \mathbf{X}_k) + \left(\frac{d\mathbf{F}(\mathbf{X})}{d\mathbf{X}}\right)^{\mathrm{T}}_{X_k} \lambda = \mathbf{0}, \tag{2.128}$$

$$\frac{\partial \mathcal{L}(\mathbf{X}^*, \lambda)}{\partial \lambda} = \left.\frac{d\mathbf{F}(\mathbf{X})}{d\mathbf{X}}\right|_{X_k} (\mathbf{X}^* - \mathbf{X}_k) + \mathbf{F}(\mathbf{X}_k) = \mathbf{0}. \tag{2.129}$$

Equations (2.128) and (2.129) reflect the conditions for the minimum-norm solution to the root finding problem in Equation (2.122). Solving for $\mathbf{X}_*$ in Equation (2.128) produces

$$\mathbf{X}^* = \mathbf{X}_k - \left(\frac{d\mathbf{F}(\mathbf{X})}{d\mathbf{X}}\right)^{\mathrm{T}}_{X_k} \lambda \tag{2.130}$$

that is substituted into Equation (2.129) to render the expression for λ

$$\lambda = \left[\frac{d\mathbf{F}(\mathbf{X})}{d\mathbf{X}}\left(\frac{d\mathbf{F}(\mathbf{X})}{d\mathbf{X}}\right)^{\mathrm{T}}\right]^{-1}_{X_k} \mathbf{F}(\mathbf{X}_k). \tag{2.131}$$

Combining Equations (2.131) and (2.130) results in the final result for $\mathbf{X}^*$,

$$\mathbf{X}^* = \mathbf{X}_k - \left(\frac{d\mathbf{F}(\mathbf{X})}{d\mathbf{X}}\right)^{\mathrm{T}}_{X_k} \left[\frac{d\mathbf{F}(\mathbf{X})}{d\mathbf{X}}\left(\frac{d\mathbf{F}(\mathbf{X})}{d\mathbf{X}}\right)^{\mathrm{T}}\right]^{-1}_{X_k} \mathbf{F}(\mathbf{X}_k). \tag{2.132}$$

Similar to the case involving a square Jacobian matrix, Equation (2.132) ignores the nonlinear dynamics of the problem and requires iterations to deliver a solution to the desired accuracy. Thus, the iterate form of the minimum-norm solution is

$$\mathbf{X}_{k+1} = \mathbf{X}_k - \left(\frac{d\mathbf{F}\left(\mathbf{X}\right)}{d\mathbf{X}}\right)^{\mathrm{T}}_{X_k} \left[\frac{d\mathbf{F}\left(\mathbf{X}\right)}{d\mathbf{X}} \left(\frac{d\mathbf{F}\left(\mathbf{X}\right)}{d\mathbf{X}}\right)^{\mathrm{T}}\right]^{-1}_{X_k} \mathbf{F}\left(\mathbf{X}_k\right). \tag{2.133}$$

The result from iterating Equation (2.133) is a root of the differential corrections problem that remains close to the initial guess. An alternative method of solution may be necessary to deliver other characteristics of a solution.

Equations (2.125) and (2.133) detail iterative differential corrections methods. However, neither approach guarantees convergence. Therefore, generally, initial guesses must be sufficiently close to the solution for such procedures to converge. Additionally, because both approaches rely upon the Jacobian matrix information in the constraint vector, these algorithms may require substantial analytical partial differentiation or computational power to numerically determine the partial derivatives. Despite these challenges, the techniques in Equations (2.125) and (2.133) offer effective methods of converging nonlinear trajectories in the CRTBP, given reasonable initial guesses.

2.3.1 Single Shooting

Leveraging the multi-dimensional Newton-Raphson algorithm to solve for initial states over a single propagated segment is denoted here as *Single Shooting*. Single shooting schemes are some of the simplest forms of differential corrections used in trajectory design. The surface-level simplicity of a single shooting method should not be mistaken for inferiority, however. Single shooting algorithms are frequently effective in quickly solving boundary value problems, particularly in the absence of highly nonlinear dynamics.

A demonstrative example of a single shooting strategy applied to trajectory design is a simple planar position targeter. The design problem is stated as the following: given a initial state

$$\mathbf{x}_0 = \begin{Bmatrix} x_0 \\ y_0 \\ \dot{x}_0 \\ \dot{y}_0 \end{Bmatrix}, \tag{2.134}$$

an initial velocity adjustment is sought such that the final position is

$$\mathbf{r}_d = \begin{Bmatrix} x_d \\ y_d \end{Bmatrix}. \tag{2.135}$$

This problem is envisioned graphically in Figure 2.9 with the initial nondimensional states

$$\mathbf{x}_0 = \begin{Bmatrix} 0.6 & 0 & -0.1 & 0.3 \end{Bmatrix}^{\mathrm{T}} \tag{2.136}$$

and the position target location is

$$\mathbf{r}_d = \begin{Bmatrix} 0.15 & 0 \end{Bmatrix}^{\mathrm{T}}. \tag{2.137}$$

Furthermore, the integration time, τ_f, for the problem is fixed at 10.25 days. The trajectory propagated using these initial states and integration time serves as a reference trajectory, $\mathbf{x}^*$, and the basis for the variations evaluated by the STM. Because no analytical solution to the CRTBP exists, it is not possible to write the initial conditions as a closed form function of the desired final states. Therefore, the shooting algorithm is leveraged. Transforming the problem definition into the free-variable constraint notation yields

$$\mathbf{X} = \begin{Bmatrix} \dot{x}_0 \\ \dot{y}_0 \end{Bmatrix} \quad \text{and} \quad \mathbf{F}(\mathbf{X}) = \begin{Bmatrix} x_f - x_d \\ y_f - y_d \end{Bmatrix}.$$

The problem as formulated is described by two variables and two constraints yielding a square Jacobian matrix. Consequently, it is solved via the standard Newton-Raphson update algorithm. The constraints are not explicit functions of the free-variables so the Jacobian is written abstractly as

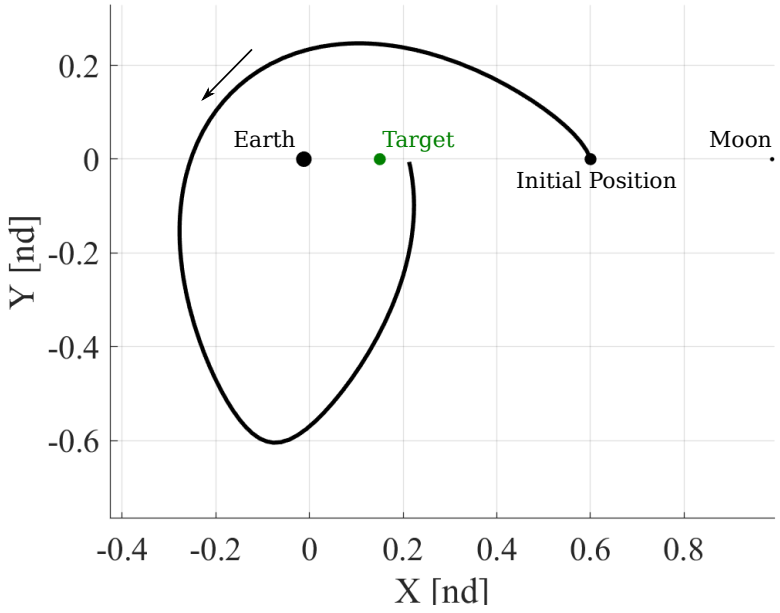

Figure 2.9.: Initial guess for planar single shooting problem

$$\frac{d\mathbf{F}\left(\mathbf{X}\right)}{d\mathbf{X}} = \begin{bmatrix} \frac{\partial x_f}{\partial \dot{x}_0} & \frac{\partial x_f}{\partial \dot{y}_0} \\ \frac{\partial y_f}{\partial \dot{x}_0} & \frac{\partial y_f}{\partial \dot{y}_0} \end{bmatrix}. \tag{2.138}$$

The elements of Equation (2.138) are sensitivities of the final position components along the trajectory to the initial velocity components. This relationship is encapsulated in the state transition matrix, STM. In fact, the elements of Equation (2.138) are the planar components of Φ_{rv}. Therefore, using the propagated STM, evaluated

along the reference path, the sensitivities along the trajectory are assessed, and the update equation for the single shooting algorithm is implemented as

$$\begin{Bmatrix} \dot{x}_0 \\ \dot{y}_0 \end{Bmatrix}_{k+1} = \begin{Bmatrix} \dot{x}_0 \\ \dot{y}_0 \end{Bmatrix}_{k} - \begin{bmatrix} \frac{\partial x_f}{\partial \dot{x}_0} & \frac{\partial x_f}{\partial \dot{y}_0} \\ \frac{\partial y_f}{\partial \dot{x}_0} & \frac{\partial y_f}{\partial \dot{y}_0} \end{bmatrix}^{-1} \begin{Bmatrix} x_f - x_d \\ y_f - y_d \end{Bmatrix}. \tag{2.139}$$

Iterating Equation (2.139) until $|\mathbf{F}| <$ 1e-12 yields the corrected trajectory plotted in Figure 2.10. The geometry of the updated trajectory arc remains qualitatively similar to that of the initial guess (or reference) but the initial velocity is noticeably different.

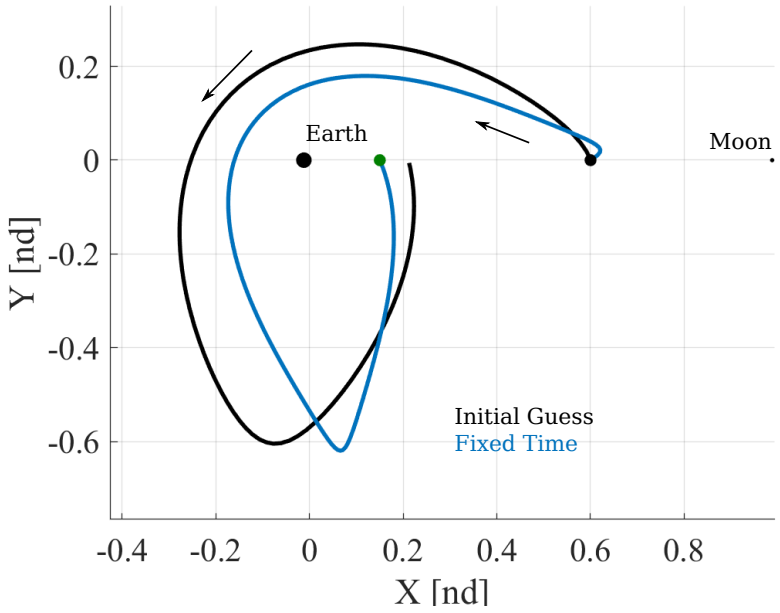

Figure 2.10.: Updated trajectory for fixed-time single shooting algorithm

To reduce the initial velocity deviation between the initial guess and the converged fixed time transfer, time-of-flight is allowed to vary. Incorporating time-of-flight as a design variable provides a greater solution search space and, in some cases, reduces

the initial variation with respect to the initial condition. Adding time of flight, T, as a free variable produces the free-variable and constraint vectors

$$\mathbf{X} = \begin{Bmatrix} \dot{x}_0 \\ \dot{y}_0 \\ \tau_f \end{Bmatrix} \quad \text{and} \quad \mathbf{F}(\mathbf{X}) = \begin{Bmatrix} x_f - x_d \\ y_f - y_d \end{Bmatrix}$$

resulting in the Jacobian matrix

$$\frac{d\mathbf{F}(\mathbf{X})}{d\mathbf{X}} = \begin{bmatrix} \frac{\partial x_f}{\partial \dot{x}_0} & \frac{\partial x_f}{\partial \dot{y}_0} & \frac{\partial x_f}{\partial \tau_f} \\ \frac{\partial y_f}{\partial \dot{x}_0} & \frac{\partial y_f}{\partial \dot{y}_0} & \frac{\partial y_f}{\partial \tau_f} \end{bmatrix}. \tag{2.140}$$

Note that the matrix is not square. Intuitively, the scalar partials $\frac{\partial x_f}{\partial \tau_f}$ and $\frac{\partial y_f}{\partial \tau_f}$ representing the sensitivity of the final position to the integration time are the $\dot{x}_f$ and $\dot{y}_f$ evaluated at the end of the trajectory arc, respectively. Therefore, the Jacobian matrix simplifies to

$$\frac{d\mathbf{F}(\mathbf{X})}{d\mathbf{X}} = \begin{bmatrix} \frac{\partial x_f}{\partial \dot{x}_0} & \frac{\partial x_f}{\partial \dot{y}_0} & \dot{x}_f \\ \frac{\partial y_f}{\partial \dot{x}_0} & \frac{\partial y_f}{\partial \dot{y}_0} & \dot{y}_f \end{bmatrix}. \tag{2.141}$$

Using the minimum-norm solution, the adjusted variable-time shooting trajectory that reaches the target position is plotted in Figure 2.11. Similar to the result in the fixed time case, the overall structure of the transfer is similar in shape to the initial guess. However, the variable time solution displays a reduction in the initial velocity variation relative to the reference solution. This reduction does not hold generally, but demonstrates the greater freedom available to the corrector if time is allowed to vary.

The addition of time as a free variable also enables the implementation of another constraint without producing an overdetermined system. A frequent constraint in the CRTBP is a perpendicular x-axis crossing that is used extensively in the correc-

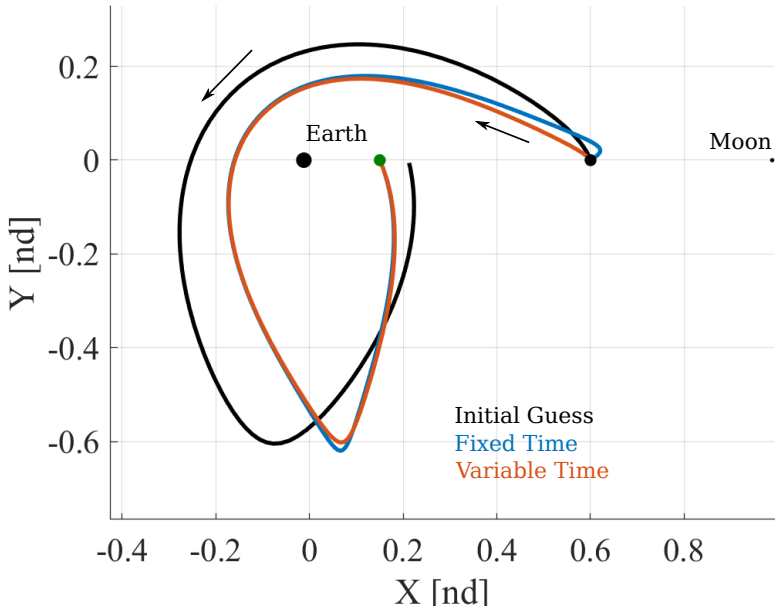

Figure 2.11.: Corrected trajectory for fixed-time and variable-time single shooting algorithms

tions process to produce periodic orbits. In the planar problem, this constraint is implemented by simply requiring $\dot{x}_f = 0$ and expanding the constraint vector to

$$\mathbf{F}(\mathbf{X}) = \begin{Bmatrix} x_f - x_d \\ y_f - y_d \\ \dot{x}_f \end{Bmatrix}. \tag{2.142}$$

Consequently, the constraint Jacobian matrix is updated to

$$\frac{d\mathbf{F}(\mathbf{X})}{d\mathbf{X}} = \begin{bmatrix} \frac{\partial x_f}{\partial \dot{x}_0} & \frac{\partial x_f}{\partial \dot{y}_0} & \dot{x}_f \\ \frac{\partial y_f}{\partial \dot{x}_0} & \frac{\partial y_f}{\partial \dot{y}_0} & \dot{y}_f \\ \frac{\partial \dot{x}_f}{\partial \dot{x}_0} & \frac{\partial \dot{x}_f}{\partial \dot{y}_0} & \ddot{x}_f \end{bmatrix}, \tag{2.143}$$

facilitating the new constraint. The existence of a second-order derivative, $\ddot{x}_f$, in the Jacobian matrix demands that the equations of motion are evaluated at the final time as the acceleration information is not available directly in the final state vector.

Given that the number of constraints and free-variables is three in both cases, the new formulation returns the Jacobian to a square matrix and the Newton-Raphson update equation again returns a single solution. Figure 2.12 displays the resultant transfer that delivers a perpendicular x-axis crossing at the final time.

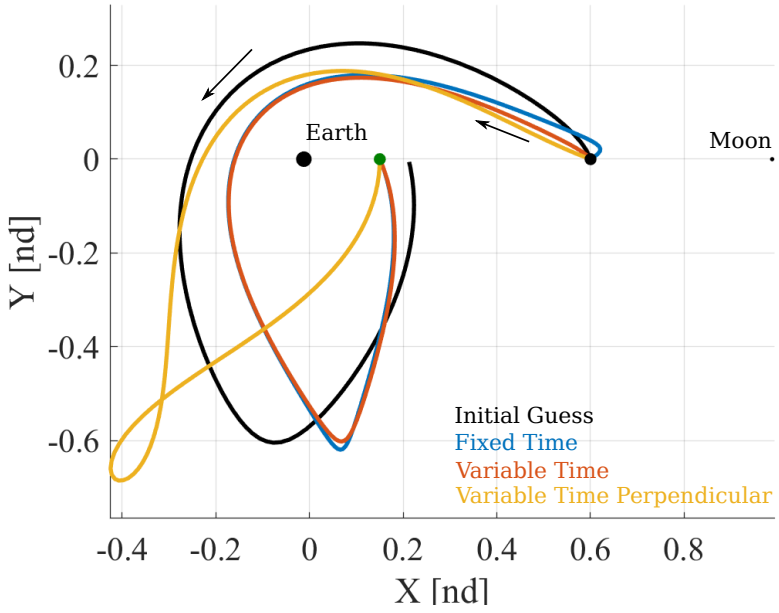

Figure 2.12.: Corrected trajectory for fixed-time and variable-time single shooting algorithms

Single shooting methods provide fast numerical solutions to the nonlinear trajectory design processes in the CRTBP. By leveraging the linear approximations for motion near a reference solution and the state transition matrix, initial conditions are updated to meet the nonlinear constraints. However, attempts to implement single shooting methods in regions of space where highly nonlinear dynamics dominate can be challenging. Convergence in these regions usually requires alternative corrections strategies. One such numerical option is a multiple shooting scheme.

2.3.2 Multiple Shooting

Trajectories passing through highly sensitive regions often exhibit unpredictable changes in final states in response to small variations in the initial states. Alternative corrections, beyond single shooting, are frequently necessary for successful design processes. By segmenting a reference trajectory and correcting these segments in parallel, the corrections process is less sensitive to chaotic dynamics. This method, denoted *multiple shooting*, reduces the time interval over which a linear approximation is applied allowing for more accurate predictions of the design variable sensitivities in the nonlinear model.

Figure 2.13 displays a simplified depiction of a multiple shooting problem prior to corrections. The initial guess is formed by a possibly discontinuous set of arcs. The multiple shooting iteration adjusts the free variables to achieve the desired continuity between segments and satisfy additional constraints on the trajectory. The free variables are typically a subset of the initial conditions along each segment ($\mathbf{x}_{1,0}$, $\mathbf{x}_{2,0}$, $\mathbf{x}_{3,0}$, ..., $\mathbf{x}_{N,0}$) and the integration times τ_1, τ_2, τ_3, ..., τ_N. The multiple shooting problem also requires the addition of continuity constraints to enforce state and time continuity between the segments represented by the red arrows in Figure 2.13. For a ballistic trajectory, full state and time continuity is required; if the spacecraft possesses impulsive capabilities, the constraints on velocity continuity between segments is removed to simulate an impulsive maneuver.

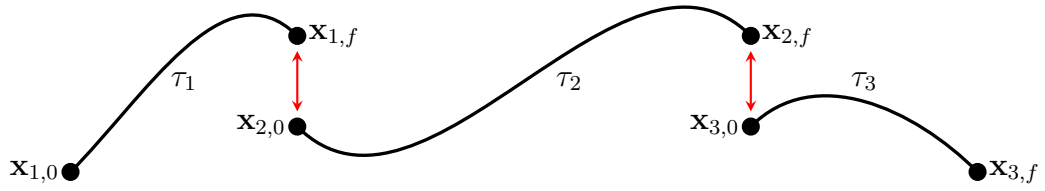

Figure 2.13.: Multiple Shooting Schematic

Consider a trajectory comprised of N segments with an initial state, $\mathbf{x}_{i,0}$, and duration τ_i. The general free variable vector for this trajectory would, therefore, be written

$$\mathbf{X} = \begin{Bmatrix} \mathbf{x}_{1,0} \\ \mathbf{x}_{2,0} \\ \vdots \\ \mathbf{x}_{N,0} \\ \tau_1 \\ \tau_2 \\ \vdots \\ \tau_N \end{Bmatrix} \tag{2.144}$$

and would include $7N$ free variables. Furthermore, enforcing full state continuity along the trajectory yields a continuity constraint vector written as

$$\mathbf{F}_{\text{cont.}}(\mathbf{X}) = \begin{Bmatrix} \mathbf{x}_{2,0} - \mathbf{x}_{1,f} \\ \mathbf{x}_{3,0} - \mathbf{x}_{2,f} \\ \vdots \\ \mathbf{x}_{N,0} - \mathbf{x}_{N-1,f} \end{Bmatrix} \tag{2.145}$$

containing $6(N-1)$ scalar constraint equations. Consequently, the Jacobian matrix for the continuity constraints is the $6(N-1) \times 7N$ matrix

$$\frac{d\mathbf{F}_{\text{cont.}}}{d\mathbf{X}} = \begin{bmatrix} -\Phi_1 & I_{6\times6} & 0 & 0 & 0 & -\dot{\mathbf{x}}_{1,f} & 0 & 0 & \cdots & 0 \\ 0 & -\Phi_2 & I_{6\times6} & 0 & 0 & 0 & -\dot{\mathbf{x}}_{2,f} & 0 & \cdots & 0 \\ \vdots & \vdots & \ddots & \ddots & 0 & 0 & 0 & \ddots & \cdots & \vdots \\ 0 & 0 & 0 & -\Phi_{N-1} & I_{6\times6} & 0 & 0 & 0 & -\dot{\mathbf{x}}_{N-1,f} & 0 \end{bmatrix}. \tag{2.146}$$

The Jacobian matrix given in Equation (2.146) is not square and has a $(N+6)$-dimensional null-space. Therefore, the update is performed using a minimum-norm solution. However, it is often advantageous to reduce this null-space dimension prior

to construction of a solution. A significant amount of the flexibility present is due to the fact that the times of flight of each segment are allowed to vary, thus, a given solution geometry is recreated through any combination of the times, τ_i, that yields a constant total time, $\sum \tau_i$. Therefore, a common method of reducing the dimension of the null-space is restricting the segment times of flight such that $\tau_1 = \tau_2 = \ldots = \tau$ removing $N - 1$ degrees of freedom. This restriction reduces the free-variable vector to

$$\mathbf{X} = \begin{Bmatrix} \mathbf{x}_{1,0} \\ \mathbf{x}_{2,0} \\ \vdots \\ \mathbf{x}_{N,0} \\ \tau \end{Bmatrix}. \tag{2.147}$$

The corresponding Jacobian matrix is, therefore, a $6\,(N-1) \times (6N+1)$ matrix that is formed by collapsing the time partial components of Equation (2.146) into a single column, i.e.

$$\frac{d\mathbf{F}_{\text{cont.}}}{d\mathbf{X}} = \begin{bmatrix} -\Phi_1 & I_{6\times6} & 0 & 0 & 0 & -\dot{\mathbf{x}}_{1,f} \\ 0 & -\Phi_2 & I_{6\times6} & 0 & 0 & -\dot{\mathbf{x}}_{2,f} \\ \vdots & \vdots & \ddots & \ddots & 0 & \vdots \\ 0 & 0 & 0 & -\Phi_{N-1} & I_{6\times6} & -\dot{\mathbf{x}}_{N-1,f} \end{bmatrix}. \tag{2.148}$$

The resulting system delivers a 7-dimensional null-space consistent with an unconstrained single shooting problem. The fundamental continuity constraints are then be augmented or modified according to the corrections problem requirements. Specific components of velocity continuity constraints may be removed from the problem by deleting the corresponding rows in Equation (2.145) and (2.148). Additional constraints are incorporated into the multiple shooting algorithm similarly to the single shooting algorithm, i.e., by appending the constraints to the $\mathbf{F}$ vector and their corresponding partials to the Jacobian matrix. Common additional constraints include state components, periapses/apoapses, two-body elements, and perpendic-

ularity constraints. However, any equality constraint can be incorporated into the current formulation given that an analytical expression in terms of the state variables is available.

2.4 Continuation Methods

Any trajectory resulting from a shooting algorithm or procedure offers a single solutions to the targeting problem; but it is often desired to produce a *family* of solutions. Families of solutions share a common qualitative or quantitative characteristic and offer a larger design space. The continuation of a single solution into a family is accomplished in various ways, each offering advantages in different scenarios. Two common approaches are *Natural Parameter Continuation* and *Pseudo-Arclength Continuation*. Both are flexible and successful in this investigation; numerous other strategies are available as necessary.

2.4.1 Natural Parameter Continuation

Natural parameter continuation builds a family of solutions by evolving a physical parameter such as a state component, energy, or time-of-flight. By evolving through a physical parameter, it is often possible to leverage *a priori* knowledge about the shape and characteristics of a family in the continuation process.

The natural parameter continuation process begins with an initial guess for a solution. Following a successful convergence process, the natural parameter is incremented and the corrections process is repeated using the previously converged family member as an initial guess for the new shooting iteration. This iterative process continues until the family of solutions ends, a predetermined condition is met, or the convergence process fails.

While often effective, natural parameter continuation can face difficulties arising from the parameter not evolving in a monotonic fashion and the necessity for intuition on the characteristics of a family. If the parameter varies monotonically across

a family, then each step in the parameter yields a new family member. Therefore, a solution in the family is identified by the evolution parameter. Families with this characteristic are labelled *single parameter families*. In general, however, this property does not hold and multiple members of a family possess the same parameter value. The algorithm must then be adapted by adding a second continuation parameter, using a nonlinear update function for the continuation parameter, or risk "jumping over" family members possibly failing to converge.

2.4.2 Pseudo-Arclength Continuation

Pseudo-arclength continuation allows solutions to evolve using a non-physical parameter; solutions are then continued without knowledge or intuition concerning the shape of the family. Given a differential corrections problem with

$$\mathbf{X} = \begin{Bmatrix} x_1 \\ x_2 \\ \vdots \\ x_n \end{Bmatrix}, \quad \text{and} \quad \mathbf{F}(\mathbf{X}) = \begin{Bmatrix} F_1(\mathbf{X}) \\ F_2(\mathbf{X}) \\ \vdots \\ F_m(\mathbf{X}) \end{Bmatrix} \tag{2.149}$$

and assuming $n - m = 1$, the dimension of the kernel for the Jacobian matrix $\frac{d\mathbf{F}(\mathbf{X})}{d\mathbf{X}}$ is 1. Therefore, there is 1 degree of freedom in the linear update equation along the line defined by the kernel. Let $\mathbf{X}_i$ be the previously converged member of the family and, thus, $\mathbf{F}(\mathbf{X}_i) = \mathbf{0}$. Furthermore, let

$$\xi = \ker\left(\frac{d\mathbf{F}(\mathbf{X}_i)}{d\mathbf{X}}\right) \in \mathbb{R}^n \tag{2.150}$$

then $\mathbf{X}_i + s\xi$ is a solution to the linear constraint equations around $\mathbf{X}_i$ for any $s \in \mathbb{R}$. This property is leveraged in the nonlinear corrections process by forcing the step

from the previous to next converged family member, $\mathbf{X}_{i+1}$, to be in the direction of ξ. This constraint is written

$$G\left(\mathbf{X}\right) = \left\langle \mathbf{X}_{i+1} - \mathbf{X}_i, \xi \right\rangle - s = 0 \tag{2.151}$$

where s is the scalar continuation parameter. The differential corrections constraints are then augmented as

$$\mathbf{H}\left(\mathbf{X}\right) = \begin{Bmatrix} F_1\left(\mathbf{X}\right) \\ F_2\left(\mathbf{X}\right) \\ \vdots \\ F_m\left(\mathbf{X}\right) \\ G\left(\mathbf{X}\right) \end{Bmatrix} \tag{2.152}$$

with

$$\frac{d\mathbf{H}\left(\mathbf{X}\right)}{d\mathbf{X}} = \begin{Bmatrix} \frac{d\mathbf{F}(\mathbf{X})}{d\mathbf{X}} \\ \xi^T \end{Bmatrix}. \tag{2.153}$$

The augmented corrections process defined in Equation (2.152) and (2.153) incorporates a square Jacobian matrix and allows for converging the next family member without any intuition concerning the shape of the family. While often very robust, the application of the pseudo-arclength continuation process requires the construction of an initial corrections scheme with a one-dimensional null-space limiting the space of applications for which it can be employed. Furthermore, the generation of families of solutions using a pseudo-arclength continuation process does not permit families to be grown in a specific fashion, e.g., with increasing period or initial x value. However, in contrast to natural parameter continuation, pseudo-arclength continuation does not suffer if the parameter does not vary strictly monotonically along a family.

2.5 Periodic Solutions in the CRTBP

Perfectly periodic motion provides many additional particular solutions beyond the Lagrange points. Linearization about the collinear Lagrange points demonstrates

the existence of a four-dimensional center subspace in the linear model. The resultant linear approximations can be corrected in the full nonlinear model and produce nonlinear periodic trajectories.

The validity of the linear approximation is dependent on the initial perturbation from the central Lagrange point. Figure 2.14 displays three linear approximations and their corresponding nonlinear propagations for three initial conditions defined on the x-axis and derived from the linear model centered at Earth-Moon L_1. The linear approximation holds moderately well for a single revolution for an initial position perturbation of one half kilometer from the Lagrange point, but the trajectory at 10 kilometer perturbation in position already demonstrates a substantial inaccuracy in the linear approximation. The proximity to P_2 greatly influences the small bound on which the linear approximation is accurate.

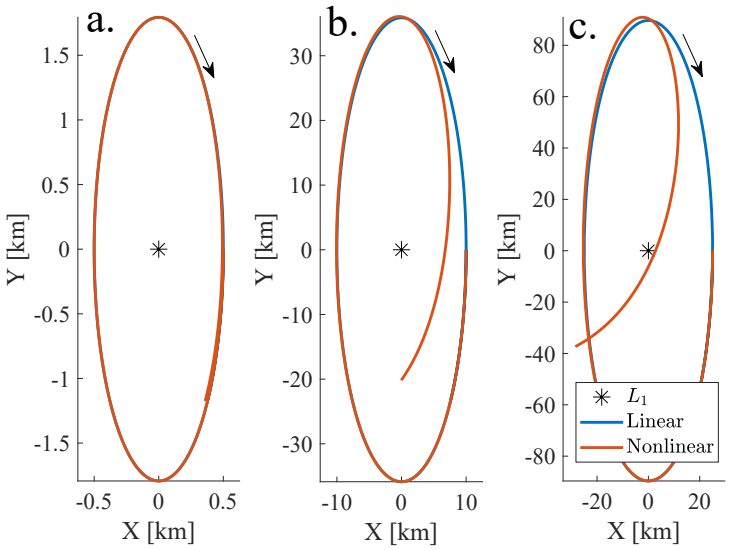

Figure 2.14.: Linear Approximation Versus Nonlinear Propagation for Planar Periodic Orbits Around Earth-Moon L_1 for a) 0.5 km, b) 10 km, and c) 25 km

A single shooting algorithm is used to converge the nonlinear orbit at a 10 kilometer deviation from L_1. While targeting directly for periodicity directly is feasible, the

targeting is successfully accomplished by leveraging the *Mirror Theorem* as presented by Roy and Ovenden [7].

Theorem 2.5.1 (Mirror Theorem) *If n point-masses are moving under their mutual gravitational forces only, their orbits are periodic if, at two separate epochs, a mirror configuration occurs [7].*

For the CRTBP, mirror conditions occur at perpendicular crossings of the xz-plane. Therefore, with an initial condition that is perpendicular to the xz-plane, a corrections scheme targets another perpendicular crossing to determine a periodic orbit. Essentially targeting a half-period, reducing the required propagation time and, therefore, therefore inaccuracy of the linear STM approximation. The corrections process is, therefore, defined by the free-variable formulation as

$$\mathbf{X} = \begin{Bmatrix} \dot{y}_0 \\ \tau \end{Bmatrix}, \quad \mathbf{F} = \begin{Bmatrix} y_f \\ \dot{x}_f \end{Bmatrix}, \quad \text{and} \quad \frac{d\mathbf{F}}{d\mathbf{X}} = \begin{bmatrix} \frac{dy_f}{d\dot{y}_0} & \dot{y}_f \\ \frac{d\dot{x}_f}{d\dot{y}_0} & \ddot{x}_f \end{bmatrix}. \tag{2.154}$$

The straightforward application of the single shooting formulation yields the corrected nonlinear periodic orbit plotted in Figure 2.15. Due to the proximity to the Lagrange point, the linear initial guess is sufficient to achieve convergence using the Newton-Raphson model in two iterations. The availability of initial conditions, as well as the low iteration count, is a demonstration of the advantage afforded by leveraging the linear approximation.

Correcting the linear approximation is a strategy applied to the generation of planar periodic orbits about L_1, L_2, and L_3 at larger initial displacements from the Lagrange points. However, eventually, the initial condition from the linear approximation fails to yield a sufficiently accurate guess to the nonlinear periodic orbit initial state due to the dominance of higher-order terms. Therefore, an approach is required to continue the nonlinear orbit(s) and produce a family. The periodic orbit families generated from the linear approximations at L_1, L_2, and L_3 are continued with a natural parameter scheme. Figure 2.16 displays this continuation of the nonlinear pe-

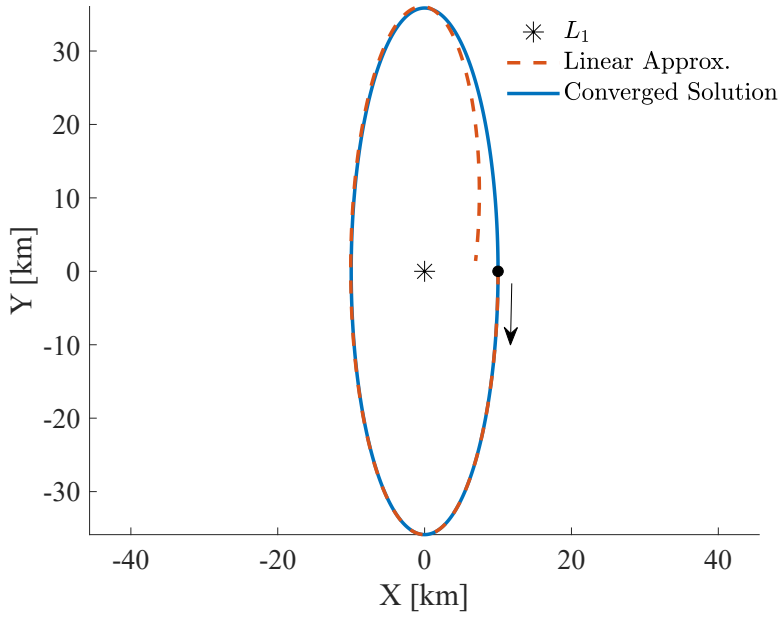

Figure 2.15.: Converged Periodic Orbit Around Earth-Moon L_1 Compared to the Initial Guess from Linear Variational Equations

riodic orbits. These periodic orbits around L_1, L_2, and L_3 are denoted the *Lyapunov* orbits. The members of the L_1, L_2, and L_3 Lyapunov families in Figure 2.16 do not constitute the entirety of each family but are indicative of the general form. Similarly, the out-of-plane motion is isolated to generate the Vertical orbits at L_1, L_2, and L_3 in the Earth-Moon system in Figure 2.17. The Lyapunov and Vertical orbit families represent the nonlinear extensions of the in-plane and out-of plane approximations developed in Section 2.2.6.

2.6 Invariant Manifold Theory

Periodic orbits and equilibrium solutions represent two types of motion in the CRTBP. Lagrange points and periodic orbits exhibit some instability and are distinguished by their stability characteristics. Any unstable solutions imply flow toward

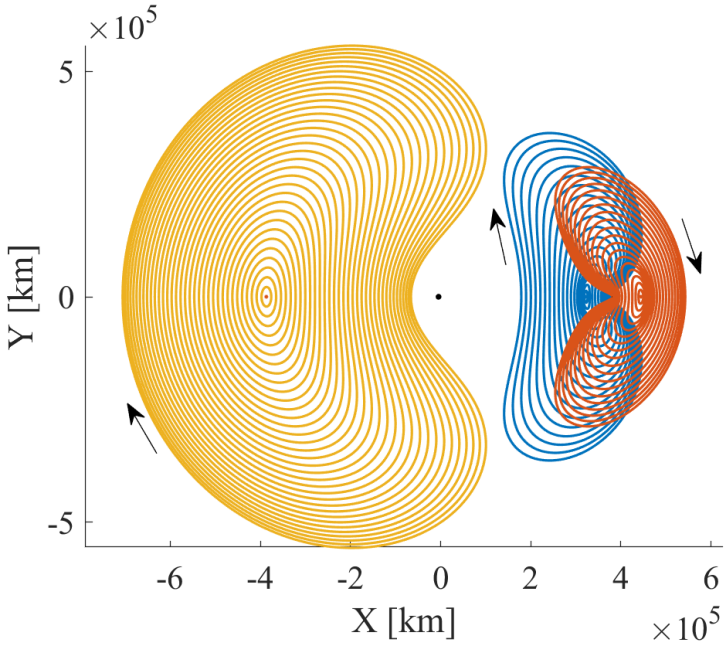

Figure 2.16.: Lyapunov Orbit Families for Earth-Moon L_1, L_2, and L_3

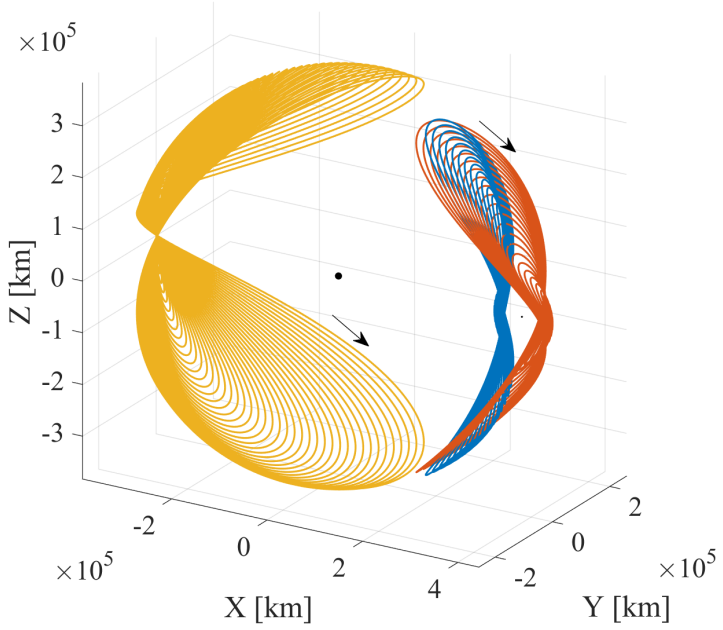

Figure 2.17.: Vertical Orbit Families for Earth-Moon L_1, L_2, and L_3

or away from the reference solution. These flows can be understood in the context of dynamical systems theory.

2.6.1 Hyperbolic Manifolds Associated with the Collinear Lagrange Points

Linearization of the nonlinear differential equations of motion for the CRTBP relative to the collinear libration points yields four purely imaginary eigenvalues and two real non-zero eigenvalues of opposite sign. These Real eigenvalues also represent flow to and from the Lagrange point. Therefore, the linear system possesses both a one-dimensional stable subspace, E^S, and a one-dimensional unstable subspace, E^U. The relationship between the linear system subspaces and the invariant manifolds in the nonlinear system is characterized by the *Stable Manifold Theorem* [8]:

Theorem 2.6.1 (Stable Manifold Theorem) *Let E be an open subset of $\mathbb{R}^n$ containing the origin, let $\boldsymbol{f} \in C^1(E)$, and let ϕ_t be the flow of the nonlinear system. Suppose the $\boldsymbol{f}(\boldsymbol{0}) = \boldsymbol{0}$ and that $\frac{d\boldsymbol{f}(\boldsymbol{0})}{dt}$ has k eigenvalues with negative real part and $n-k$ eigenvalues with positive real part. Then there exists a k-dimensional differentiable manifold S tangent to the stable subspace E^s of the linear system at $\boldsymbol{0}$ such that for all $t \geq 0$, $\phi_t(S) \subset S$ and for all $\boldsymbol{x}_0 \in S$,*

$$\lim_{t\to\infty} \phi_t(\boldsymbol{x}_0) = \boldsymbol{0};$$

and there exists an $n-k$ dimensional differentiable manifold U tangent to the unstable subspace E^U of the linear system at $\boldsymbol{0}$ such that for all $t \leq 0$, $\phi_t(U) \subset U$ and for all $\boldsymbol{x}_0 \in S$,

$$\lim_{t\to-\infty} \phi_t(\boldsymbol{x}_0) = \boldsymbol{0}.$$

Due to the tangency condition in the *Stable Manifold Theorem*, the invariant manifolds associated with the nonlinear system are approximated by small perturbations from the equilibrium point in the direction of the linear stable and unstable subspaces, E^U and E^S. The perturbed state is numerically integrated to generate a representa-

tion of the global stable or unstable subspace to some acceptable level of accuracy. The accuracy to which the representation approximates the invariant manifold depends on the length of the step in the linear subspace directions. However, due to the growth of error in numerical integration of the equations of motion, small steps result in large integration times yielding greater error. Figure 2.18 demonstrates a numerically integrated approximation to the global stable and unstable manifolds for Earth-Moon L_1. Note that the true dynamical manifolds exist at the same value of Jacobi constant as L_1 as the true manifolds asymptotically approach or depart L_1.

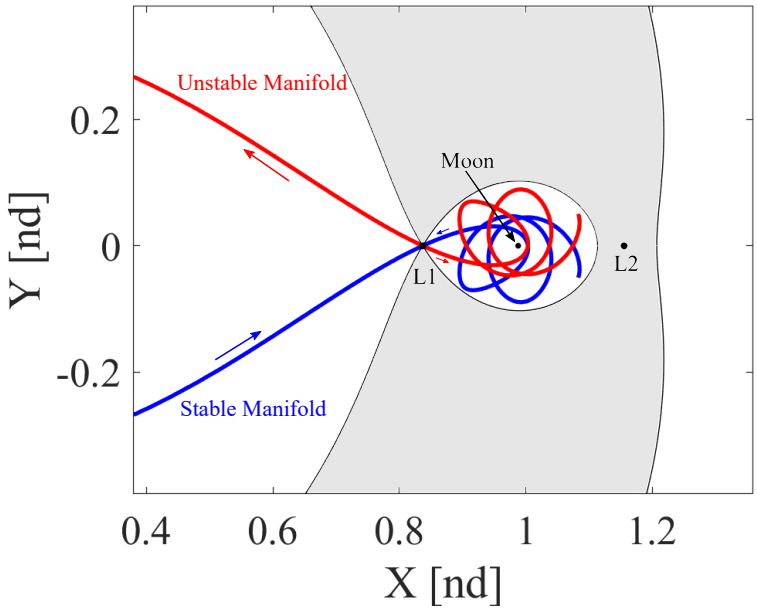

Figure 2.18.: Global Invariant Manifolds for Earth-Moon L_1

2.6.2 Poincaré Maps for Dynamical Systems Analysis

The Poincaré map serves as a tool to reduce the dimensionality of the nonlinear flow by sampling trajectories as they cross through a surface of section. Lowering the dimension of the problem allows the visualization of the flow for both chaotic and structured motion over long intervals in a single map and, as a consequence, adds

clarity. The Poincaré section is defined by a surface of section, Σ. The surface of section, Σ, can be geometrical in phase space, e.g., $x = 0$, or reflect other functions of the state such as periapse locations. Given a state, $\mathbf{x}^*$ on Σ, the state is evolved through the flow and the next return to the map is identified and plotted on the map. The characterization of the motion, therefore, is moved from the continuous-time dynamical system evolving over the full phase-space to a discrete-time system evolving on the map.

The general structure of a Poincaré map is illustrated in Figure 2.19. Given a point $\mathbf{x}$ and a surface of section Σ transverse to the flow at $\mathbf{x}$, $\mathbf{x}$ is evolved through the flow until it returns to the map at $P(\mathbf{x})$. Furthermore, if an orbit is periodic, then it returns to the map at the same location, i.e., $\mathbf{x}^* = P(\mathbf{x}^*)$. Therefore, periodic orbits appear as fixed points on the surface of section while chaotic orbits appear as a "dusting" of the surface after many returns.

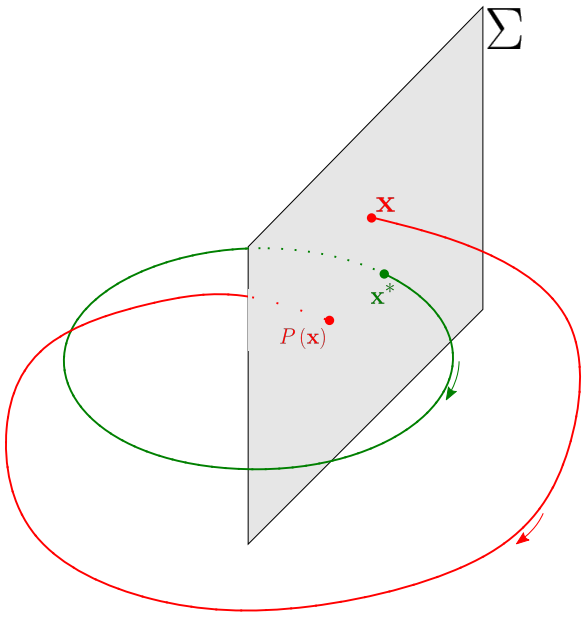

Figure 2.19.: Schematic of Poincaré Map Adapted from Palis et. al [9] and Perko [8]

The surface of section, Σ, is a hyperplane and thus possesses codimension 1 to the ambient space leading to a 3-dimensional hyperplane in the planar problem and a 5-dimensional hyperplane in the general spatial CRTBP. The dimension of the map

is further reduced by intersecting the map with a system constant; in the CRTBP, it is reduced to states evolving all with a fixed Jacobi constant value. Therefore, given an initial set of points on the hyperplane at the same Jacobi constant value, the dimension of the resulting map is reduced by two. For the planar problem this dimension reduction yields a two-dimensional map that is typically visualized in a standard planar plot. One such plot is plotted in Figure 2.20; each point in Figure 2.20 is fully characterized in a two-dimensional plot due to the reduction of dimension. One caveat to the full representation is an ambiguity in the sign of the velocity component due to the v^2 term in the Jacobi constant equation. This ambiguity is removed by displaying a *one-sided map* that limits the points on the map to those where $\dot{y} > 0$. Chain-of-islands structures are observed demonstrating multi-revolution periodic orbits as well as the quasi-periodic orbit structure surrounding them. Several fixed points are observed on the x-axis corresponding to planar periodic orbits. In

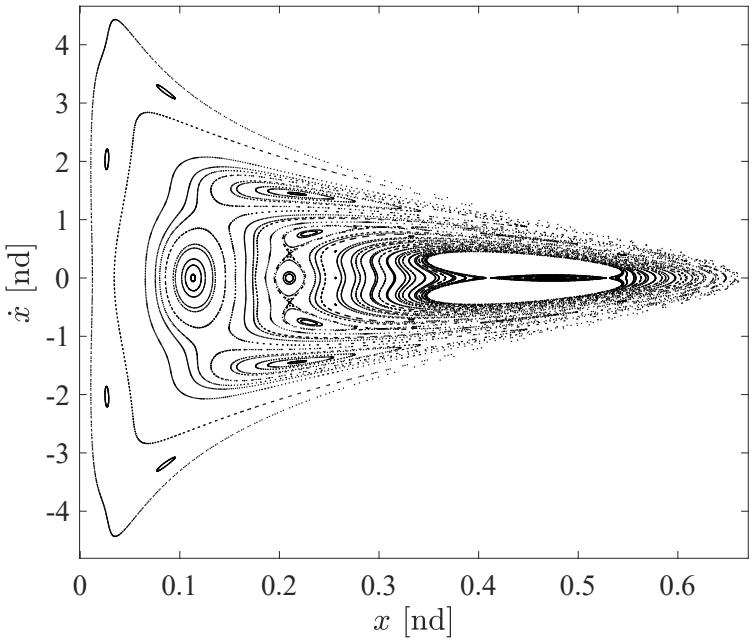

Figure 2.20.: One-Sided ($\dot{y} > 0$) Planar CRTBP Poincaré Map at $J = 3.44$ in the Earth-Moon System

the 6-dimensional spatial CRTBP, a fixed Jacobi constant Poincaré map reduces the

dimensionality to 4. Therefore, alternative visualization aspects such as color or glyphs are often included to compensate for the inability to successfully visualize 4 spatial dimensions [10].

2.6.3 Stability and Invariant Manifolds for Periodic Orbits

The idea of a Poincaré map is fundamental to the determination of stability properties and, therefore, invariant manifolds associated with periodic orbits. The stability of a periodic orbit requires a generalization of the techniques employed to assess the flow to and from the equilibrium solutions. The stability of the equilibrium solutions is evaluated in terms of the eigenvalues of the linear motion with respect to the Lagrange point. Similarly, the stability of a periodic orbit is evaluated in terms of it's characteristic multipliers [11].

Following the method of Parker and Chua, the dynamics are linearized about the fixed point, x^*, on the Poincaré map. This linearization provides the discrete time dynamical system

$$\delta \mathbf{x}_{k+1} = DP\left(\mathbf{x}^*\right) \delta \mathbf{x}_k \tag{2.155}$$

where $DP\left(\mathbf{x}^*\right)$ is the sensitivity of the return state on the map with respect the departure state and is analogous to the constant coefficient matrix resulting from the linearization around the equilibrium solution. The eigenvalues of the matrix $DP\left(\mathbf{x}^*\right)$ are called the characteristic multipliers, m_i [11]. The stability of the system described in Equation (2.155) depends on the magnitude of the characteristic multipliers, i.e. for any particular multiplier m_i the corresponding stability follows

$$\begin{aligned} |m_i| > 1 \quad & \text{Unstable} \\ |m_i| < 1 \quad & \text{Stable} \\ |m_i| = 1 \quad & \text{Center.} \end{aligned} \tag{2.156}$$

Any periodic orbit with an unstable periodic orbit is itself called unstable. Additionally, if a periodic orbit possesses no multiplier on the unit circle it is called *hyperbolic*.

The characteristic multipliers are independent of the position of Σ intuitively making them a property of the periodic orbit.

The matrix $DP(\mathbf{x}^*)$ defines the stability properties of the orbit. Parker and Chua demonstrate that for a periodic orbit in an autonomous system the eigenvalues of $DP(\mathbf{x}^*)$, the characteristic multipliers, are a subset of the eigenvalues of the state transition matrix evaluated over the period of the orbit, $\Phi(T, 0)$, called the *monodromy* matrix. Furthermore, the only eigenvalue of $\Phi(T, 0)$ not present in $DP(\mathbf{x}^*)$ is the unity eigenvalue in the direction of $\mathbf{f}(\mathbf{x}^*)$.

The stability characteristics determined from the monodromy matrix are leveraged to build the stable and unstable manifolds of periodic orbits. States around the orbit are perturbed in the stable and unstable manifold directions to generate trajectories on the stable and unstable manifold surfaces, respectively. Figure 2.21 demonstrates manifold generation for an L_2 Lyapunov orbit in the Earth-Moon system. The trajectories shown are example paths along the two-dimensional manifolds associated with the stable and unstable subspaces of the periodic orbit.

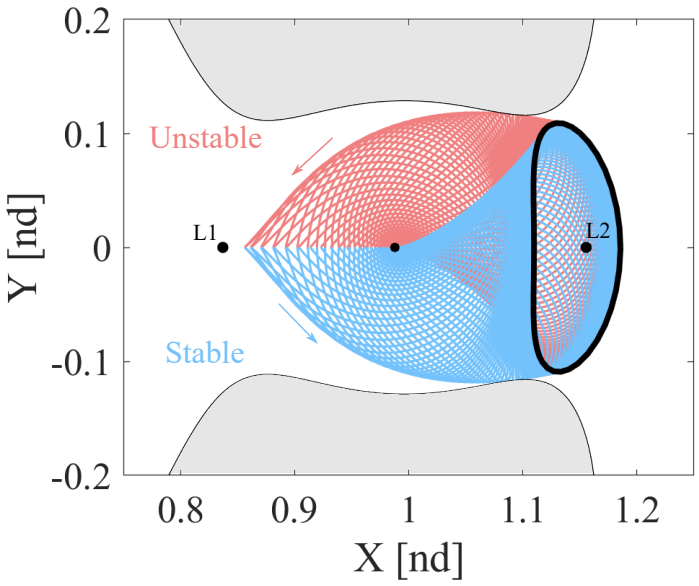

Figure 2.21.: Stable (blue) and Unstable (red) Manifolds for L_2 Lyapunov Orbit (black) in the Earth-Moon System

3. MOTIVATING APPLICATION: LUNAR IMPACT CHARACTERISTICS OF 9:2 LSR NRHO

NASA's Gateway will operate as a staging location for missions beyond Earth orbit as well as missions destined for Low Lunar Orbit (LLO) and the Lunar surface [12]. Consequently, various objects will be departing Gateway such as modules, cubesats, and debris. Within this general departure trajectory space, lunar impact trajectories are one group of particular interest and understanding of the characteristics associated with these impacting trajectories is important for disposal applications, science missions, ejecta study, and heritage site avoidance. However, the behavior of the trajectories departing Gateway vary greatly with the location, magnitude, and direction of the departure maneuver. Furthermore, the chaotic nature of the Lunar region makes general prediction of the impact conditions difficult. The 9:2 Lunar Synodic Resonant (LSR) Near Rectilinear Halo Orbit (NRHO) that the Gateway will orbit in is a nearly stable orbit without well defined manifolds The investigation by Davis et al. of departure and recontact behavior from the 9:2 Lunar Synodic Resonant (LSR) Near Rectilinear Halo Orbit (NRHO) demonstrates general increase in impacts with corresponding maneuver magnitudes and significant variations in behavior as departure location changes along the NRHO [12]. The current investigation expands on this analysis to include the Lunar locations, velocities, and angles of these impacts to characterize available trajectories for mission applications. The resulting information is then applied to finding impact trajectories from the 9:2 LSR NRHO impacting at the Shackleton Crater on the Lunar surface.

3.1 Background and Definitions

Prior to investigation, the 9:2 LSR NRHO and various parameters are defined to enable further analysis. The L_2 9:2 LSR NRHO, pictured in Figure 3.1, completes 9 revolutions for every two Earth-Moon-Sun synodic periods (each approximately 29.5 days). Consequently, the period of the 9:2 LSR NRHO is $\mathbb{P} \approx 6.5$ days with a Jacobi

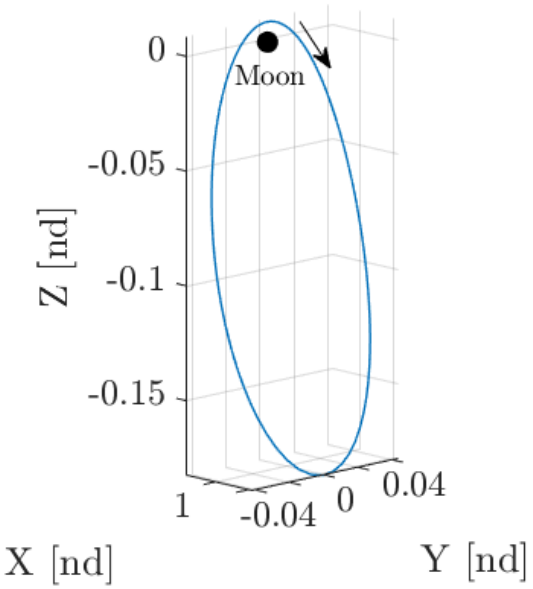

Figure 3.1.: 9:2 LSR NRHO in the Earth-Moon System

constant around 3.05. The periapse and apoapse radius of the 9:2 LSR NRHO are approximately $3,200$ km and $70,000$ km, respectively.

Because useful manifold arcs do not exist for the 9:2 LSR NRHO [13], departure directions are parameterized by the location around the orbit, magnitude of the departure maneuver, and the direction of departure. Consistent with the methodology of Davis et al., the NRHO is discretized by osculating true anomaly, θ^*, and the ma-

neuver directions are defined in terms of the Velocity-Normal-Binormal (VNB) frame. The frame is constructed as

$$\hat{\mathbf{V}} = \frac{\mathbf{v}}{|\mathbf{v}|}, \tag{3.1}$$

$$\hat{\mathbf{N}} = \frac{\mathbf{r}}{|\mathbf{r}|} \times \hat{\mathbf{V}}, \tag{3.2}$$

$$\hat{\mathbf{B}} = \hat{\mathbf{V}} \times \hat{\mathbf{N}}. \tag{3.3}$$

Yaw and pitch with respect to this frame are used to orient the maneuver direction. Note, because the VNB frame is dependent on the base point along the orbit, it varies continuously and periodically repeating every period. Figure 3.2 provides the definition of the yaw and pitch with respect to the VNB frame where $\Delta\mathbf{v}$ is the maneuver vector. Figure 3.3 presents the locations of the VNB unit vectors in the

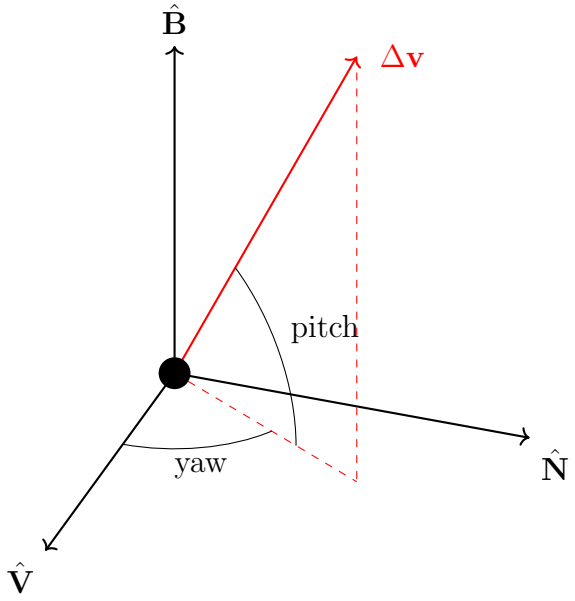

Figure 3.2.: Latitude, Longitude, and Range Definition with Respect to P_2 in CRTBP Rotating Frame

yaw-pitch plane. This plane is used to color departure directions based on impact criteria and is defined consistent with the yaw and pitch definitions given by Davis et al..

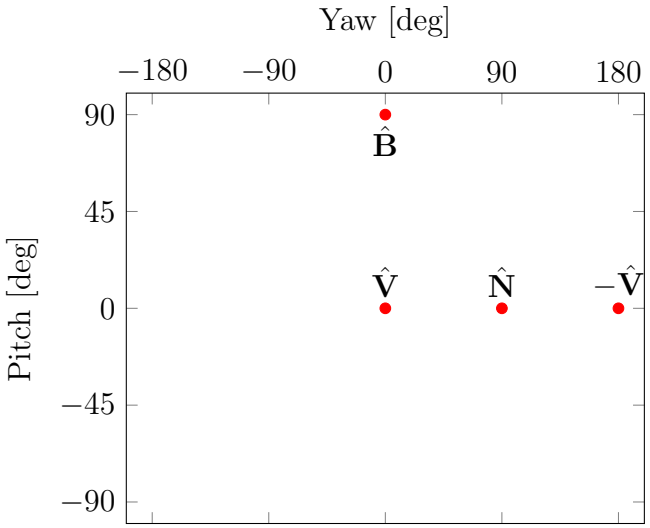

Figure 3.3.: Location of VNB Unit Vectors in Yaw-Pitch Grid

3.1.1 Definition of Lunar Impact Characteristics

To investigate Lunar impact capabilities, trajectories are integrated until a Lunar impact condition or a maximum integration time is reached. Several important characteristics regarding the impacting trajectory are then recorded; these characteristics are the Jacobi constant value, impact longitude (φ), impact latitude (λ), speed at impact, angle of impact, and time of flight after departing the periodic orbit. Knowledge of the longitude and latitude of impact offers the capability for selecting candidate trajectories that impact desired Lunar surface locations or that avoid certain locations due to mission constraints, e.g., heritage sites. Impact speed and angle are used in lunar ejecta study as well as determining valid trajectories for kinetic impactors [14, 15]. The TOF of the impacting trajectories provides information on whether a particular arc is congruent with mission time of flight requirements. Given the set of impact characteristics identified, candidate trajectories can be filtered and incorporated into a mission design process.

The latitude, longitude, and range definitions used in this investigation are defined with respect to the rotating inertial axes shown in Figure 3.4 and are denoted λ, φ, and ϱ, respectively. The definition used is fixed within the CRTBP rotating frame;

therefore, values obtained are independent of epoch. For a given point in space, q, the longitude is defined as the angle between the position vector relative to P_2 and the positive x-axis with the $\hat{\mathbf{z}}$ direction defining the positive rotation. Longitudes are defined to take on values between $-180°$ and $180°$. Furthermore, the latitude is defined as the angle between the position vector with respect to P_2 and the xy-plane, thus, taking on values between $-90°$ and $90°$. The range is simply defined as the distance from the center of the Moon ($x = 1 - \mu$), but, for Lunar impacts, the range will be always equal to the mean Lunar radius, $R_{Moon} \approx 1737.4$ km. In the xy-plane,

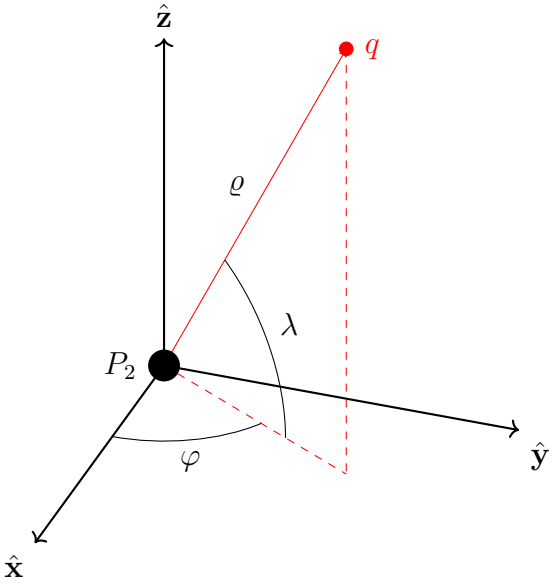

Figure 3.4.: Latitude, Longitude, and Range Definition with Respect to P_2 in CRTBP Rotating Frame

the definition of longitude in Figure 3.4 allows for the definition of four quadrants around P_2 shown in Figure 3.5. These definitions are congruent with those presented by Davis [16]. Locations on P_2 opposite P_1 are, therefore, in quadrants I and IV while locations on the near side of P_2 with respect to P_1 are in quadrants II and III.

In addition to the latitude, longitude, and range definitions, the Lunar impact speed and angle are defined to avoid ambiguity. The velocity important for impact

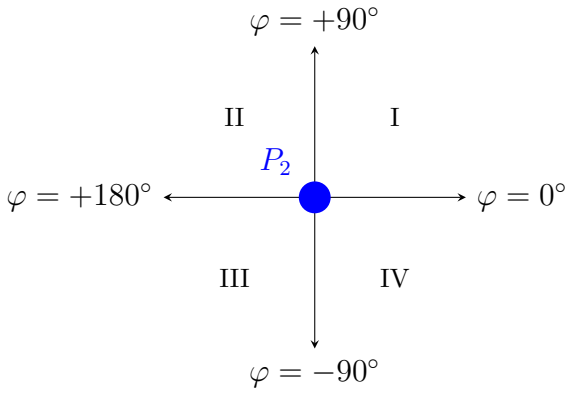

Figure 3.5.: Quadrant Definitions Around P_2 in xy-Plane

analysis is the velocity of the impacting spacecraft viewed by an observer on the Lunar surface. This velocity is equivalent to the velocity in the CRTBP rotating frame, i.e. $\left[\dot{x}\ \dot{y}\ \dot{z}\right]^{\mathrm{T}}$. Therefore, the impact speed value desired is v. The impact speed is bound by the Jacobi of the impacting trajectory as described by Davis et al. [12]. The velocity at impact is written in terms of the Jacobi constant, J, and position as

$$\mathrm{v}_{impact} = \sqrt{2\left(\frac{1-\mu}{r_{13}} + \frac{\mu}{r_{23}} + \frac{1}{2}\left(x^2+y^2\right)\right) - J}. \tag{3.4}$$

At impact with the Moon, the position variables are bounded by corresponding extrema on the Lunar surface, i.e,

$$\begin{gathered} 1 - \tfrac{R_{Moon}}{l^*} \leq r_{13} \leq 1 + \tfrac{R_{Moon}}{l^*}, \\ r_{23} = \tfrac{R_{Moon}}{l^*}, \\ \left(1 - \mu - \tfrac{R_{Moon}}{l^*}\right)^2 \leq \left(x^2+y^2\right) \leq \left(1 - \mu + \tfrac{R_{Moon}}{l^*}\right)^2. \end{gathered} \tag{3.5}$$

Therefore, the minimal and maximal impact speeds for a given Jacobi constant are

$$\mathrm{v}_{min} = \sqrt{2\left(\frac{1-\mu}{1+\frac{R_{Moon}}{l^*}} + \frac{\mu}{\frac{R_{Moon}}{l^*}} + \frac{1}{2}\left(1-\mu-\frac{R_{Moon}}{l^*}\right)\right) - J}, \tag{3.6}$$

$$\mathrm{v}_{max} = \sqrt{2\left(\frac{1-\mu}{1-\frac{R_{Moon}}{l^*}} + \frac{\mu}{\frac{R_{Moon}}{l^*}} + \frac{1}{2}\left(1-\mu+\frac{R_{Moon}}{l^*}\right)\right) - J}, \tag{3.7}$$

respectively. The minimum and maximum values across a range of Jacobi constants are shown in Figure 3.6(a). The curves representing the minimum and maximum are difficult to distinguish and, thus, the differences between the two curves are shown in Figure 3.6(b). The extrema curves monotonically decrease until $\mathrm{v}_{min/max} = 0$ at $J \approx 8.35$ where the ZVC passes through the Lunar surface and no valid impacting trajectories exist. Over the entire range of Jacobi constants shown, the difference between the two curves is small, as a result, a small range of impact velocities will be observed for a given Jacobi constant. Therefore, given a trajectory with a particular Jacobi constant, the impacting speed is known to 100 m/s (in the worst case) without integration assuming an impact occurs. For the majority of Jacobi constants observed in current analysis, the impact velocities are expected to be between 2 and 3 km/s.

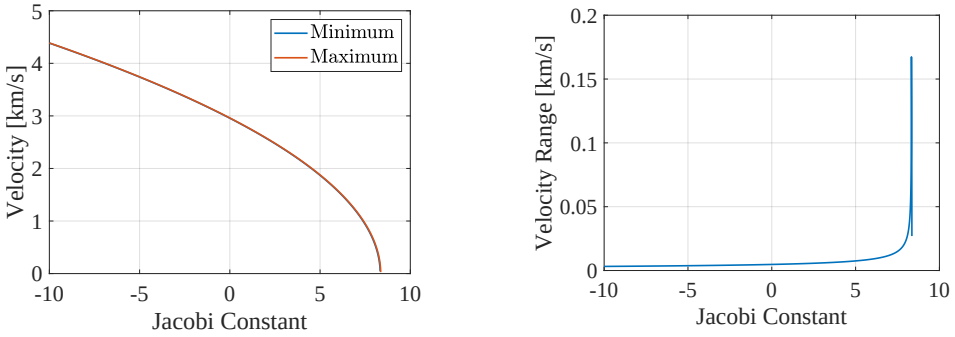

(a) (b)

Figure 3.6.: (a) Minimum and Maximum Theoretical Impact Speeds and, (b) the Difference Between The Maximum and Minimum Values

The impact angle, ϑ, is defined as the angle between the local surface normal and standard CRTBP rotating frame velocity vector at impact as depicted in Figure 3.7. Therefore, the impact angle is defined between 0° and 90° representing an impact normal to the surface and an impact "skimming" the surface, respectively.

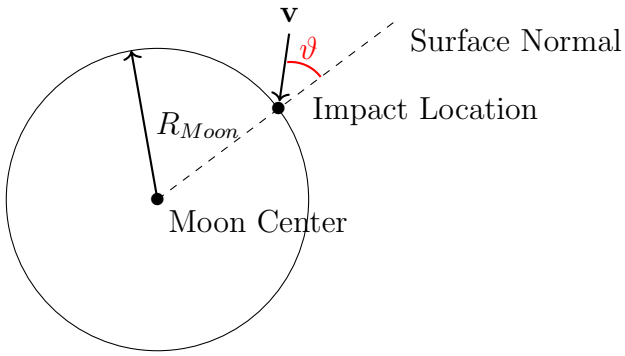

Figure 3.7.: Impact Angle Definition Diagram

3.2 Lunar Impact Trajectories

Lunar impact trajectories are found through propagation of initial conditions generated by applying $\Delta\mathbf{v}$ maneuvers at points along the 9:2 LSR NRHO. Two maneuver magnitudes are selected: 1 and 15 m/s. These magnitudes are congruent with those investigated by Davis et al. and demonstrate characteristic geometries originating from the 9:2 LSR NRHO. The NRHO is discretized into 180 true anomaly values, i.e. steps are taken in increments of 2°, and a sphere of initial conditions around each point is formed by applying the maneuver at various yaw and pitch values. These initial conditions are propagated for 130 days, until Lunar impact, or until the trajectory departs the Lunar region. The Lunar region departure is specified as the x coordinate along the trajectory moving outside the range $x_{L_1} \leq x \leq x_{L_2}$ where x_{L_1} and x_{L_2} are the x-coordinates of the L_1 and L_2 Lagrange points, respectively. The impact velocity, angle, location, and time-of-flight are recorded for the trajectories yielding Lunar surface impacts.

Impact Conditions for 15 m/s Maneuver Magnitudes

A 15 m/s magnitude maneuver is applied at 180 points around the 9:2 LSR NRHO. At each point, the pitch is varied between $-90°$ and $90°$ and the yaw is varied between $-180°$ and $180°$. Figure 3.8 displays the time-of-flight to impact for these initial conditions for those conditions that yield Lunar impacts colored. As the yaw angle is

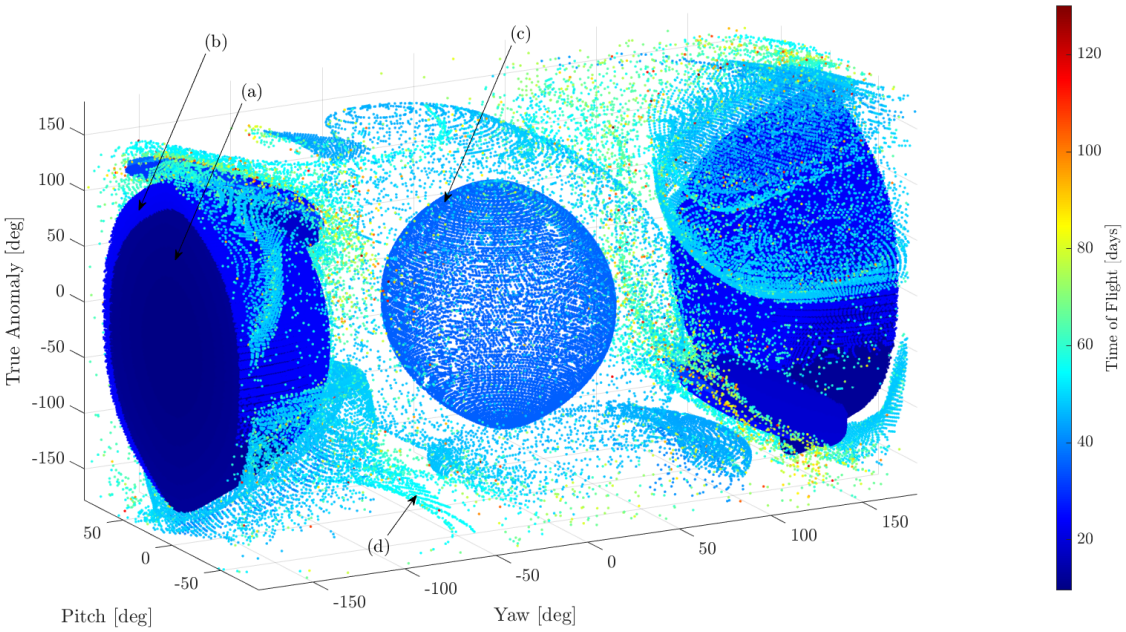

Figure 3.8.: Impacting Departure Conditions for Δv = 15 m/s Colored by Time of Flight

cyclic, the conditions at a yaw of $-180°$ are identical to those at $180°$; similar logic applies for the true anomaly. Two major spheres of impacting initial conditions are observed centered around yaw angles of $0°$ and $\pm 180°$. These maneuver directions correspond to maneuvers in the velocity and anti-velocity directions, thus, equate to larger increases and decreases in Jacobi constant, respectively. Importantly, the sphere in the anti-velocity direction (yaw of $\pm 180°$) is filled, i.e. solid, while the sphere in the velocity direction is a spherical shell. Consequently, variations in departure location or maneuver direction in the anti-velocity sphere will still yield an impacting trajectory while similar variations applied in the velocity direction may fail to result

in a Lunar impact. Thus, the anti-velocity direction maneuvers possess a decreased sensitivity to maneuver direction perturbations. Outside of these two main lobes of impact conditions, conditions are found at many location and maneuver direction. A majority of the impact conditions occur at times-of-flight below 60 days as most trajectories depart the Lunar region at times beyond this. A large portion of the impacting initial conditions outside of the main lobes occur at times-of-flight around 60 days. While the time-of-flight in the velocity-direction sphere is relatively constant in the 40 day range, a gradient is observed in the anti-velocity sphere. Figures 3.9(a) and 3.9(b) display trajectories from the interior and exterior of the anti-velocity direction sphere, respectively. The outer, higher time-of-flight conditions yield impact trajectories with four revolutions around the Moon prior to impact while the inner, lower time-of-flight conditions yield two revolution impact trajectories. This geometry holds for all the initial conditions in the anti-velocity sphere. Figure 3.9(c) demonstrates a trajectory from the spherical shell of initial conditions in the velocity direction and is representative of the geometry across the entire shell. Clearly, this impacting trajectory is larger than those presented in Figures 3.9(a) and 3.9(b), an observation consistent with the lower Jacobi constant. The final trajectory given in Figure 3.9(d) presents a common impact geometry found outside of the two main initial condition spheres. The trajectories depicted in Figure 3.9 represent the most common forms of impact geometries found across all maneuver magnitudes.

In addition to the times-of-flight, the impacting speeds are also investigated. Figure 3.10 plots the same impact conditions as those found in Figure 3.8 but colored corresponding to the speed at impact. A significant relationship is observed between the departure maneuver direction and the impact speed. This relationship is a direct result of the bounds established for the impact speed as a function of the Jacobi constant of the trajectory in Equations (3.6) and (3.7). Because the departure directions nearer zero pitch and zero yaw represent maneuvers in the velocity direction, they correspond to the greatest increase in Jacobi constant. Therefore, these trajectories will yield the highest impact velocities and the opposite holds true for the maneu-

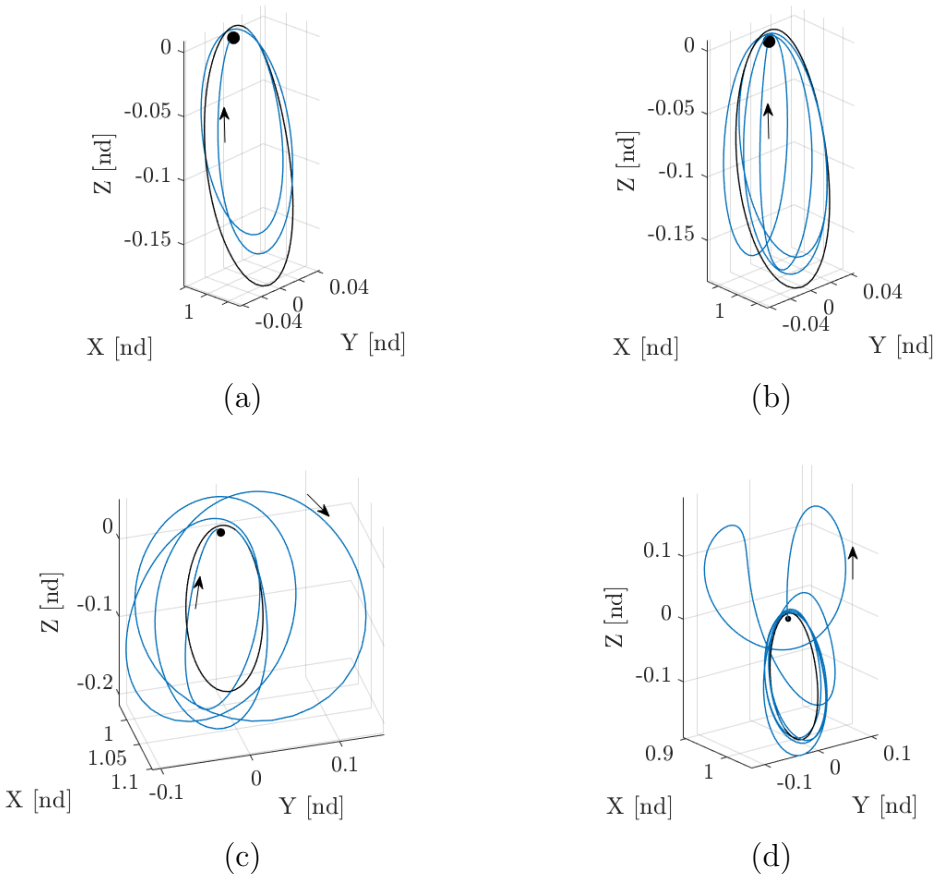

Figure 3.9.: Sample Impact Trajectories for 15 m/s Magnitude Departures Corresponding to Marked Locations in Figure 3.8

vers closest to zero pitch and a yaw of $\pm 180°$. However, impact speed varies by less than 20 m/s across all the impacting initial conditions. Note, the theoretical bounds predict minimal and maximal impact speeds of 2.34 and 2.37 km/s, respectively.

The impact angles associated with the impacting initial conditions are given in Figure 3.11. In general, very little predictable structure is observed for the impact angles. However, in the anti-velocity sphere, a smooth gradient of impact angles is observed. This gradient starts with angles around 25° at conditions near the center of the sphere and progresses to higher impact angles before dropping back down to 0° and again progressing higher until the sphere boundary. This progression occurs as the impact location moves from nearly equatorial latitudes to northern latitudes

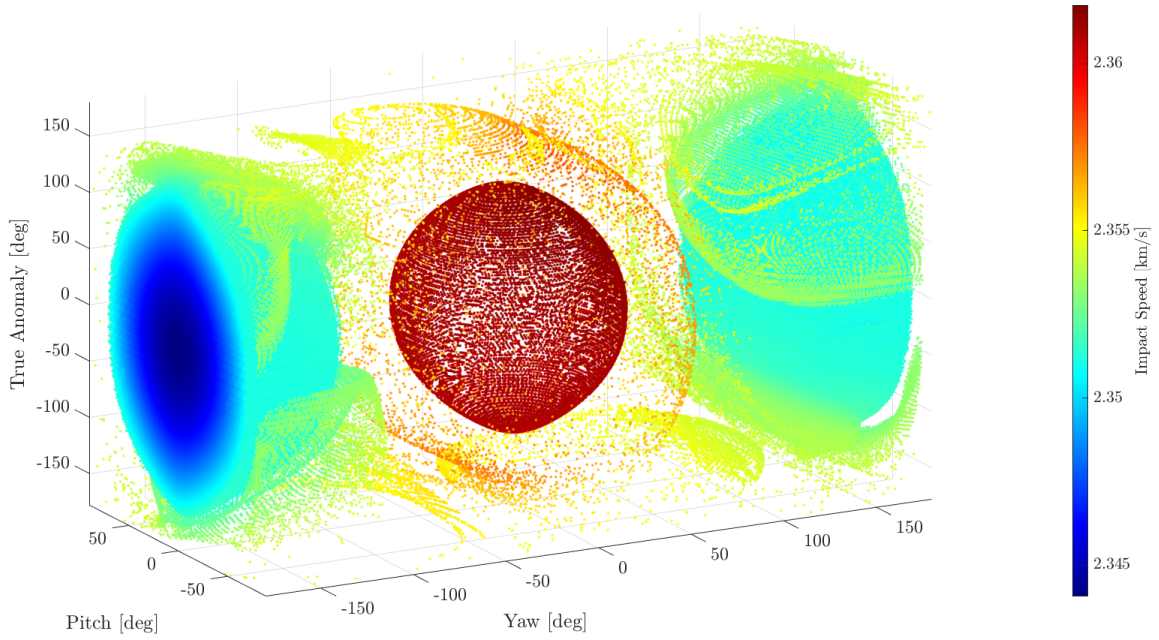

Figure 3.10.: Impacting Departure Conditions for Δv = 15 m/s Colored by Impact Speed

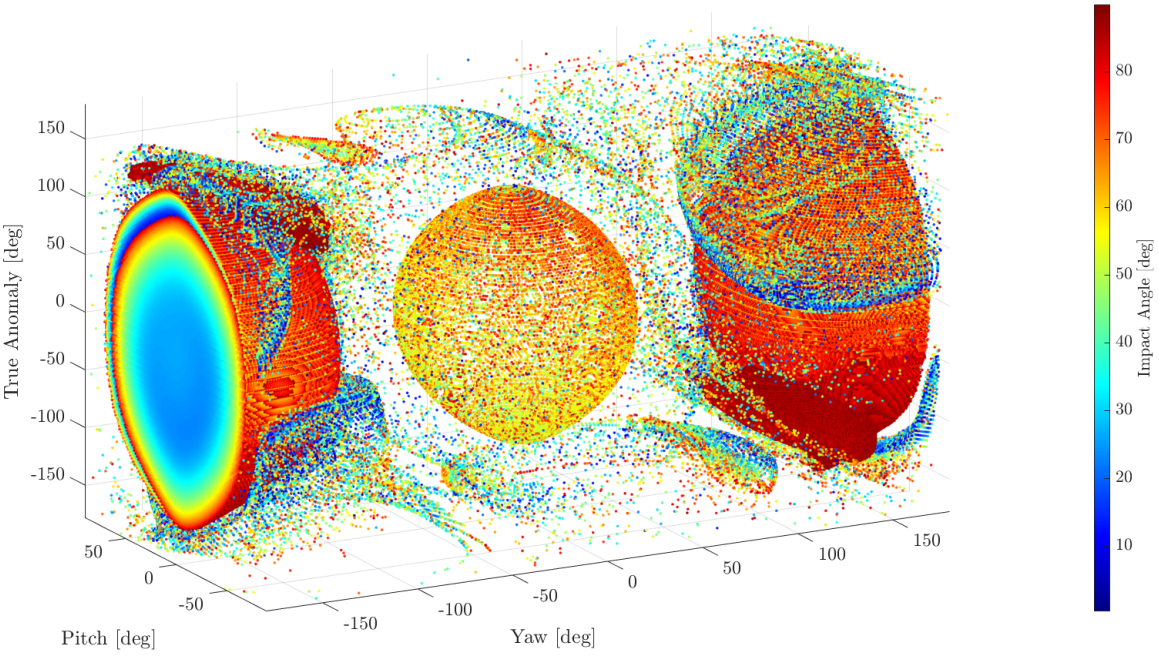

Figure 3.11.: Impacting Departure Conditions for Δv = 15 m/s Colored by Impact Angle

and the sudden drop occurs when the additional revs are added as the impact location moves beyond the Lunar surface. This connection with latitude is observed in Figure 3.12. Similar to the impact angle, impact latitude displays little predictable

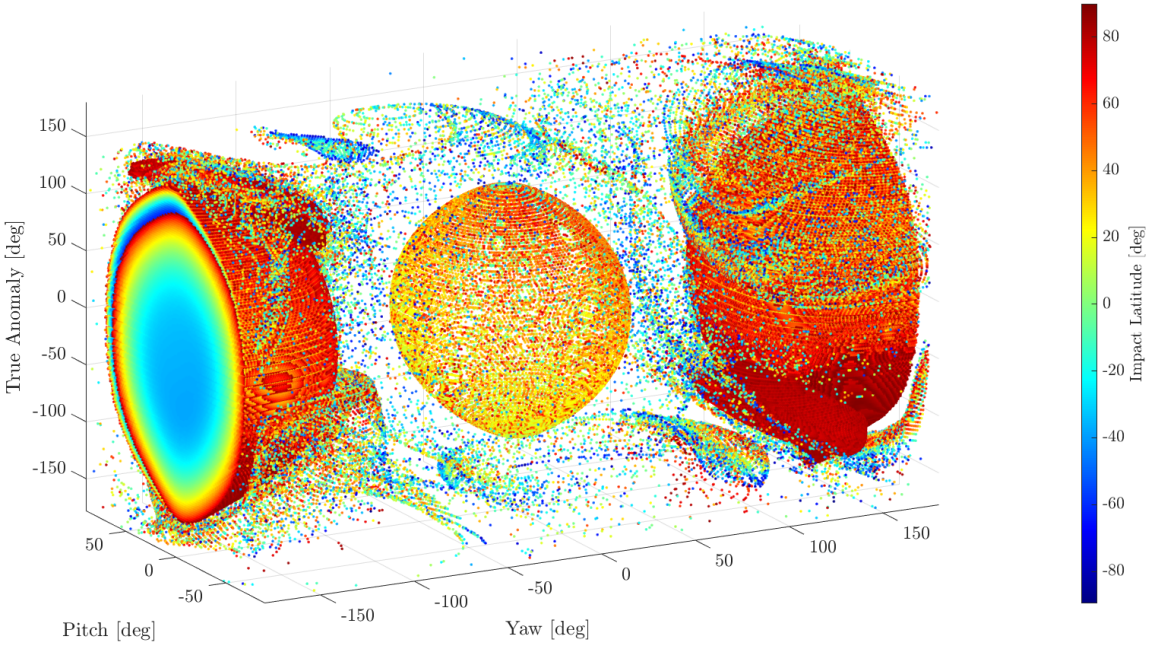

Figure 3.12.: Impacting Departure Conditions for $\Delta v = 15$ m/s Colored by Latitude At Impact

structure for initial conditions outside of the anti-velocity sphere. However, in both cases, the sphere centered around the velocity direction demonstrates higher overall impact angles and latitudes. In fact, for all impact conditions, lower latitudes are less common indicating potential difficulty in reaching southern locations on the Moon. The impact longitudes corresponding to the initial conditions are given in Figure 3.13. Both the velocity and anti-velocity spheres present a majority of the impacts in the fourth quadrant. This is consistent with the impact geometries observed as well as the geometry of the 9:2 LSR NRHO itself. Outside of the main spheres of initial conditions, other impact longitudes are available but present substantially more sensitivity to departure location as well as maneuver direction.

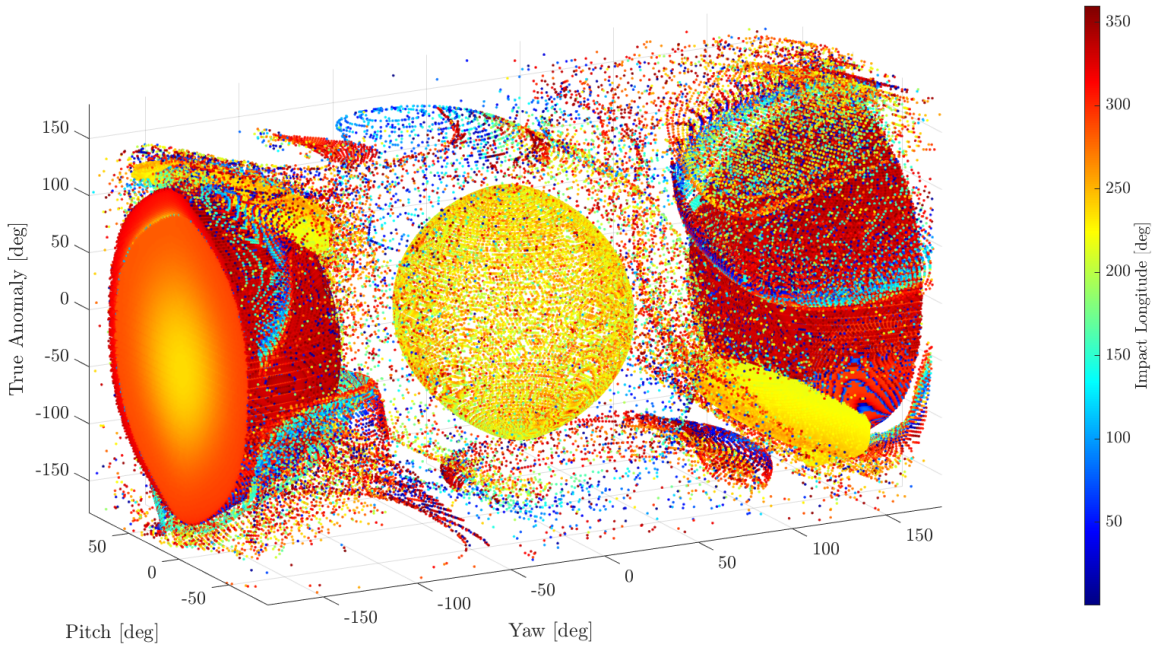

Figure 3.13.: Impacting Departure Conditions for $\Delta v = 15$ m/s Colored by Longitude At Impact

Impact Conditions for 1 m/s Maneuver Magnitudes

An identical analysis as that performed for the 15 m/s maneuver magnitude is performed for a maneuver magnitude of 1 m/s. The impacting initial conditions are plotted in Figure 3.14 colored by the time-of-flight to impact. Clearly, the 1 m/s maneuver magnitude yields fewer and less well structured impacting initial conditions. Spherical groups of initial conditions yielding impacting trajectories still exist surrounding the velocity and anti-velocity maneuver directions. However, these groups are smaller than their 15 m/s counterparts and demonstrate greater variability in the time of flight across the group. Furthermore, the anti-velocity direction sphere is not solid meaning maneuvers in directions very close to the anti-velocity direction fail to yield impacts. For yaw values between $-50°$ and $-180°$ a group of impacts occur at true anomalies near apoapsis appearing as a outgrowth of the normal spherical shell; this geometry is demonstrated in Figure 3.15(b). The geometry of the velocity-direction departure maneuver trajectories is similar to those of the 15 m/s case; the

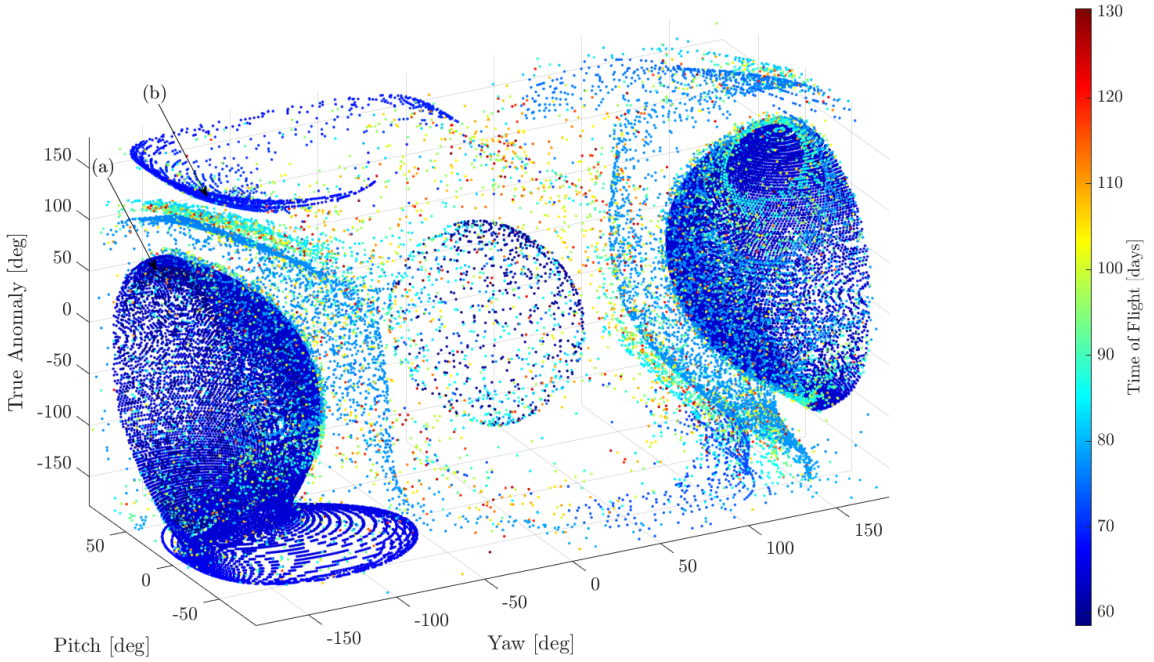

Figure 3.14.: Impacting Departure Conditions for Δv = 1 m/s Colored by Time of Flight

anti-velocity direction maneuvers, however, display the geometry shown in Figure 3.15(a), different than what is observed in the 15 m/s departure case. Overall, the

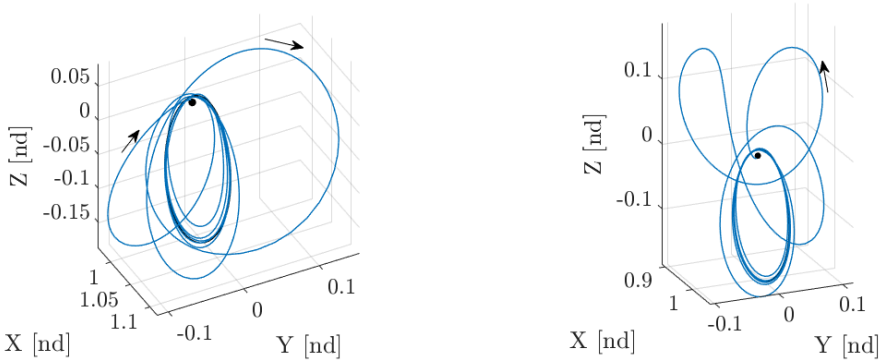

Figure 3.15.: Sample Impact Trajectories for 1 m/s Magnitude Departures Corresponding to Marked Locations in Figure 3.14

impacting initial conditions and geometries observed are similar to those found in the 15 m/s case but with greater variations between nearby conditions.

The impact speeds of the initial conditions yielding impacting trajectories for the 1 m/s magnitude departure maneuver case are shown in Figure 3.16. Consistent

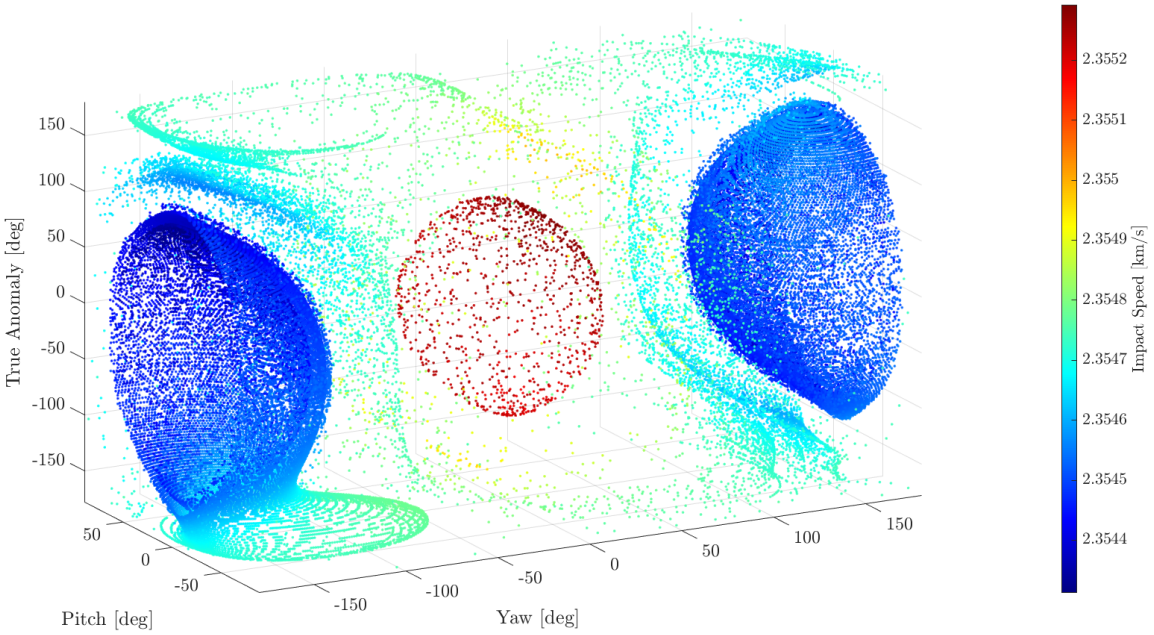

Figure 3.16.: Impacting Departure Conditions for Δv = 1 m/s Colored by Impact Speed

with the 15 m/s Δv case and the theoretical extrema derivation, the impact speed varies directly with the departure maneuver direction. The higher impact speeds occur when the maneuver direction is oriented towards the velocity direction and the converse holds for the lower impact speeds. However, due to the small departure magnitude, the total variation in impact velocity over the 1 m/s impact conditions is less than 2 m/s despite the theoretical impact speed bounds allowing for impact speeds from 2.35 to 2.36 km/s.

The impact angles for the 1 m/s case are shown in Figure 3.17. The impact angles are predominantly higher resulting in warmer colors appearing more often in the figure. Despite the dominance of higher impact angles, little consistency is observed

between neighboring points in general. Consequently, it is difficult to predict the impact angle of a trajectory as a function of the departure angle direction.

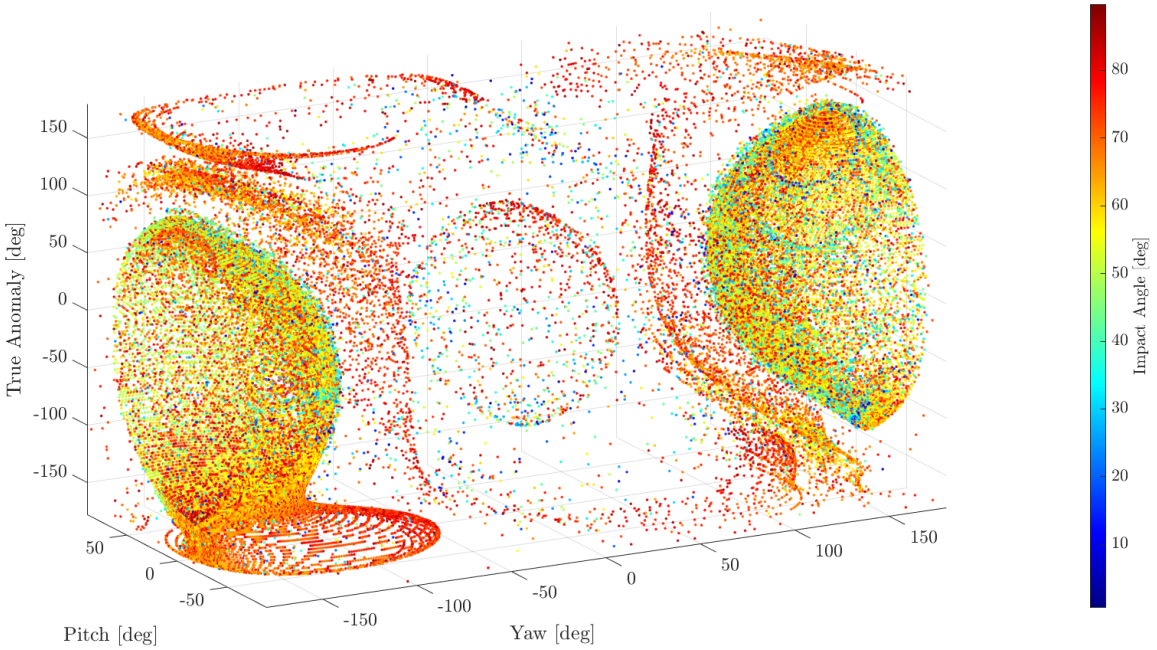

Figure 3.17.: Impacting Departure Conditions for Δv = 1 m/s Colored by Impact Angle

The impact latitudes and longitudes given in Figures 3.18 and 3.19, respectively, demonstrate similar unpredictability to that observed in the impact angle. However, the 1 m/s departure magnitude presents a significantly higher percentage of southern hemisphere impact locations that that observed in the 15 m/s case evident by the cooler overall color of Figure 3.18. Despite the consistent general color, large variations in impact latitude are observed between nearby points. A similar feature is observed for the longitudes in Figure 3.19. Overall, the majority of impacts occur in the fourth quadrant (similar to the 15 m/s case), but large variations are observed between neighboring points.

In general, the lower maneuver magnitude amplifies the variations observed in impact angle and location compared to the higher magnitude departure maneuver. Furthermore, the decrease in maneuver magnitude provides a smaller range of achievable

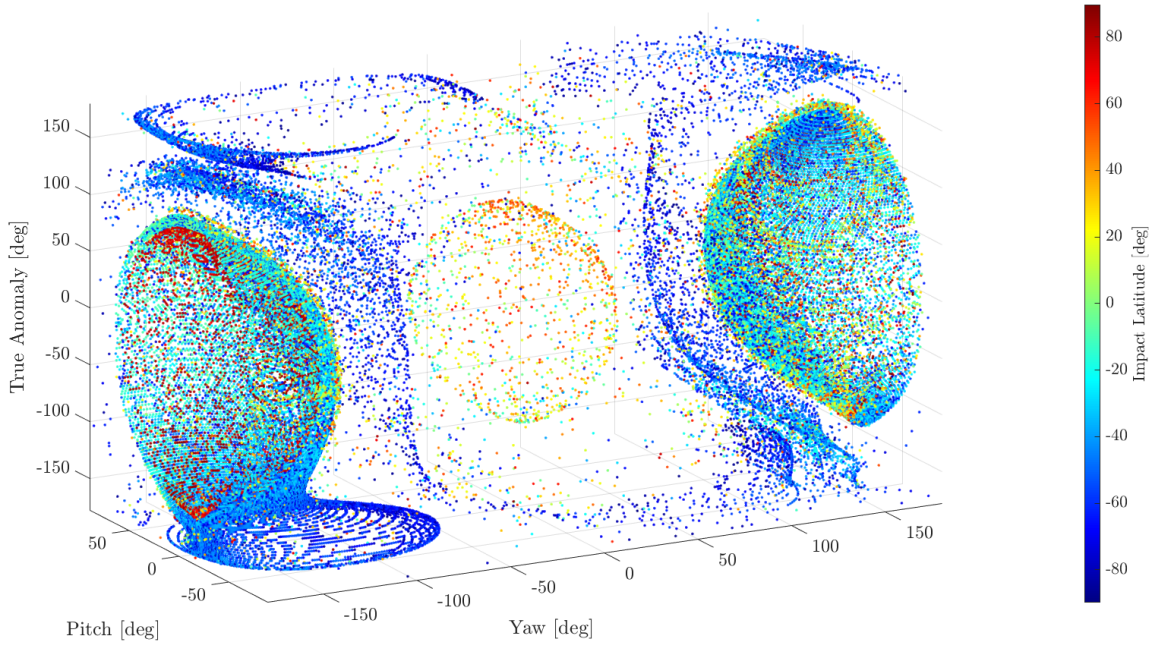

Figure 3.18.: Impacting Departure Conditions for Δv = 1 m/s Colored by Latitude At Impact

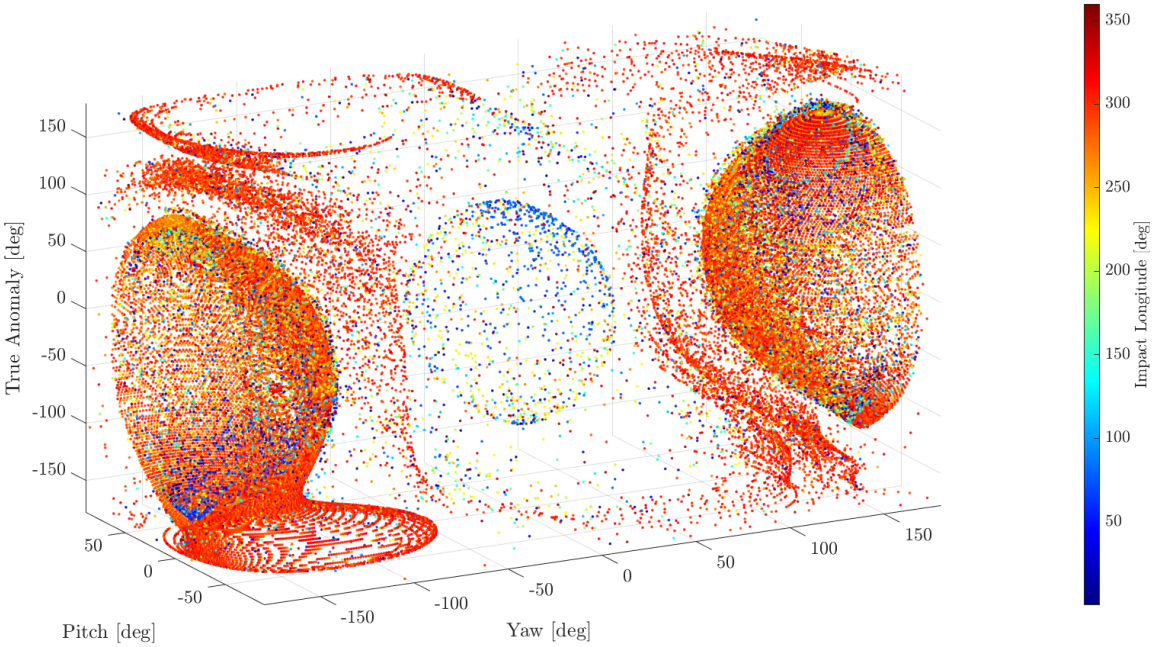

Figure 3.19.: Impacting Departure Conditions for Δv = 1 m/s Colored by Longitude At Impact

impact velocities and limits the number of maneuver directions yielding impacting trajectories. However, the lower maneuver magnitude presents a greater amount of southern hemisphere access and, obviously, a reduced maneuver cost.

3.2.1 Application: Impact Trajectories at the Shackleton Crater

While no specific Lunar landing locations have been selected for NASA's Lunar surface activities, areas in and around Shackleton crater are potential candidates for these missions [17,18]. Therefore, trajectories impacting in Shackleton crater from the 9:2 LSR NRHO present mission candidates for future operations from Gateway to the Lunar surface. Locations of Shackleton crater over the year 2023 are determined in the CRTBP rotating frame and nearby impacting orbits are identified and corrected.

The Shackleton crater sits at a latitude and longitude of $-89.66°$ and $129.17°$, respectively [19]. However, the coordinates describing the location of the crater are fixed in Lunar fixed frames, not in the Earth-Moon rotating frame used for the CRTBP. While the Moon is "tidally locked", small angular deviations are observed between the Moon-fixed and Earth-Moon rotating frames. Consequently, the position in the Earth-Moon rotating frame of Shackleton crater is dependent on the epoch selected. Epochs are spaced across 2023, selected because it is the year following Gateway's planned launch [20], at 16 regularly spaced intervals. Figure 3.20 presents the latitudes and longitudes as defined in Figure 3.4 of Shackleton crater over 2023 determined via the SPICE toolkit provided by NAIF [21]. Additionally, Figures 3.21(a) and 3.21(b) show the longitudes and latitudes at each of the selected epochs. From all three figures, it is clear that greater variations are observed in longitude than latitude as latitudes range from $-89°$ to $-76°$ while longitudes span values from $132°$ to $278°$. Furthermore, as expected, the motion demonstrates periodicity with a dominant period of 27 days consistent with the Lunar period.

Using data from the 15 m/s impact analysis performed, impacts from the NRHO departure are found that are close in position space to the identified Shackleton

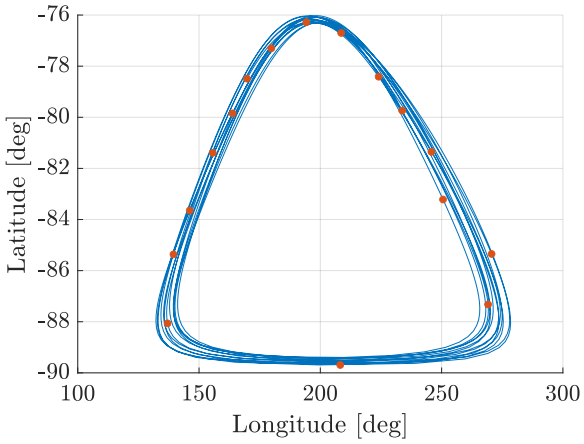

Figure 3.20.: Latitudes and Longitudes of Shackleton Crater at Selected Epochs in 2023

crater locations over the year 2023. The 15 m/s Δv magnitude is used due to the increased number of impact conditions and reduced time of flight of the impacting trajectories. Figure 3.22 displays the identified locations of Shackleton crater in 2023 overlaid on the impact conditions for the 15 m/s departure magnitude case. Clearly, many impact conditions occur near the Shackleton crater locations demonstrating the existence of potential transfers from the NRHO to the crater. However, little variation is observed in the times-of-flight yielding potential transfers; most impact conditions near the crater locations impact at around 50 days. Figures 3.23(a) and 3.23(b) display the speeds and impact angles of the surface impact conditions shown in Figure 3.22. While the impact speeds display little variation in the times-of-flight, the impact angles demonstrate greater variety as both low ($\vartheta < 10°$) and high ($\vartheta > 80°$) impact angles are observed. Figure 3.24 demonstrates examples of the representative low and high impact angle geometries impacting nearby the crater locations. The low impact angle trajectory maintains the general southern behavior of the NRHO while high impact angle flips into a northern type motion before impacting the Lunar surface. The times-of-flight of the two trajectories are similar with the low impact angle trajectory taking 47 days and the high impact angle trajectory taking 61

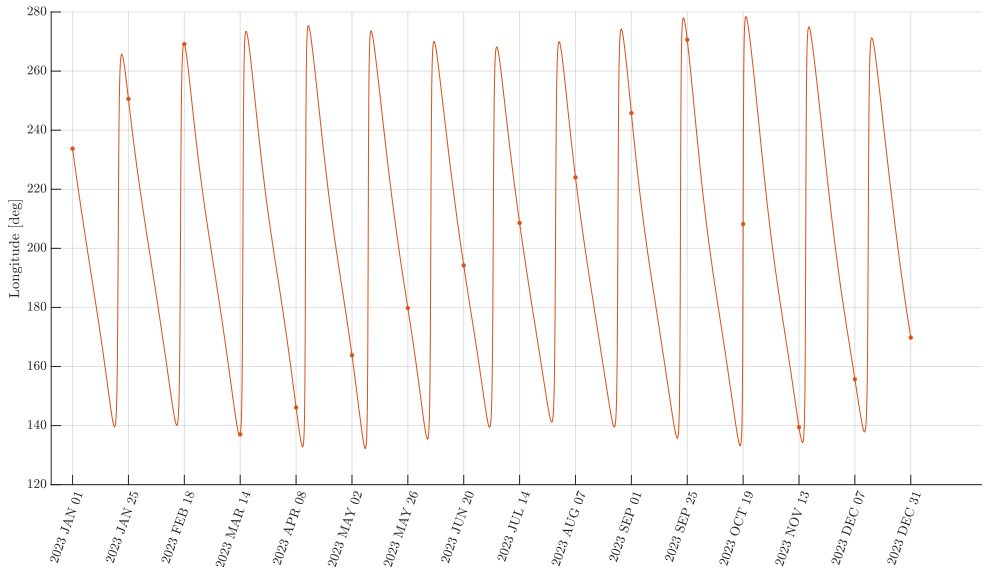

(a)

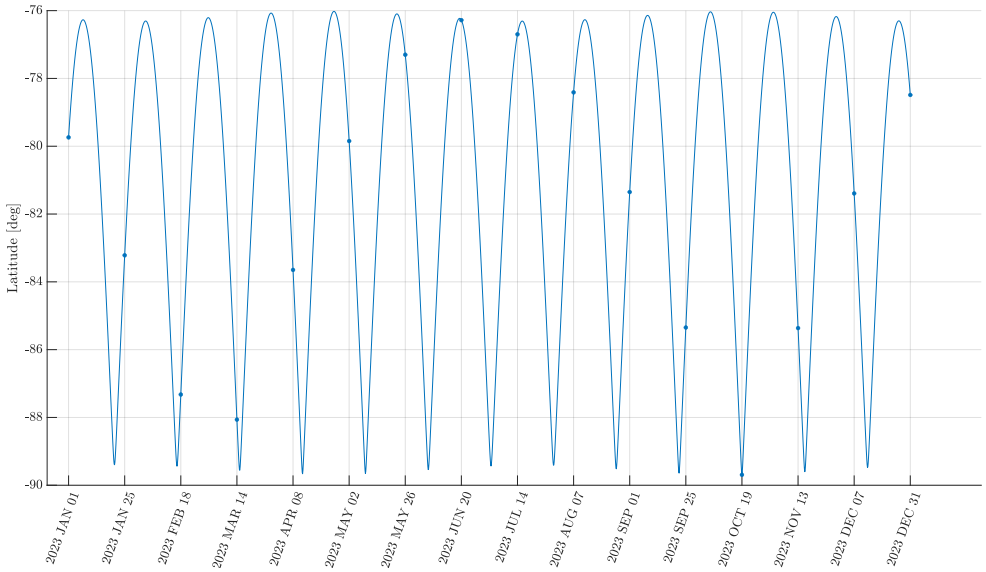

(b)

Figure 3.21.: Longitudes and Latitudes of the Shackleton in 2023 with Selected Epochs Marked

days to impact the surface. These two geometries are representative of all impacting trajectories with times-of-flight below 100 days in the crater region.

The two impacting trajectories presented in Figure 3.24 do not impact exactly at any of the positions. Therefore, the initial maneuver direction and magnitudes

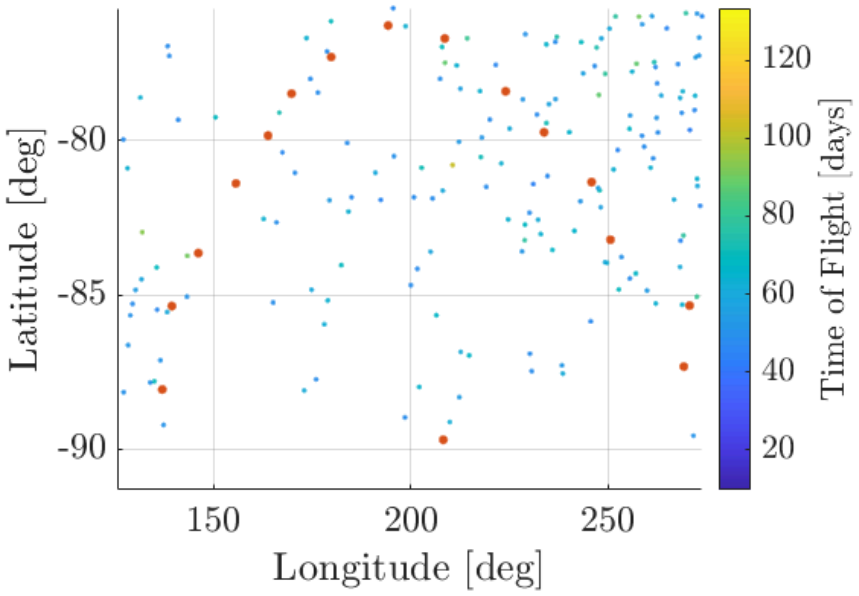

Figure 3.22.: Locations of Shackleton Crater in 2023 (in Red) Overlaid on Latitude and Longitude of Impact Conditions Originating from the 9:2 LSR NRHO with a 15 m/s Departure Maneuver

must be corrected for each of the impact locations to converge trajectories impacting exactly at the Shackleton crater locations. The free variable constraint multiple shooting formulation is used to determine the initial departure locations, maneuver magnitudes, and maneuver directions required to impact the Shackleton crater. Thus, the free variables are defined as

$$\mathbf{X} = \begin{bmatrix} \tau_N & \Delta \mathrm{v} & \mathbf{x}_1^0 & \mathbf{x}_2^0 & \cdots & \mathbf{x}_M^0 & \tau_1 & \tau_2 & \cdots & \tau_M \end{bmatrix}^{\mathrm{T}}, \tag{3.8}$$

where τ_N is the time-of-flight along the NRHO before the maneuver is performed, $\Delta \mathbf{v}$ is the maneuver vector, and $\mathbf{x}_i^0$ and τ_i are the initial state and time of flight

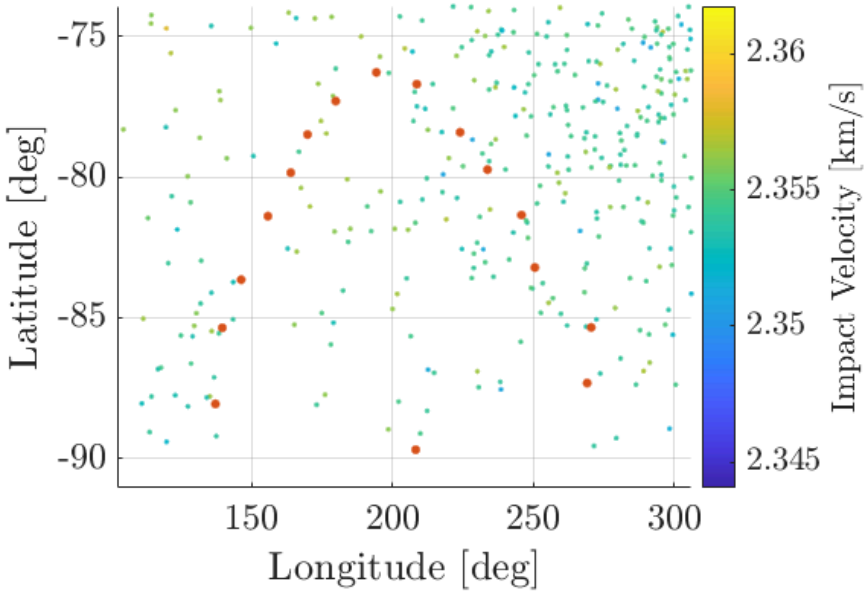

(a)

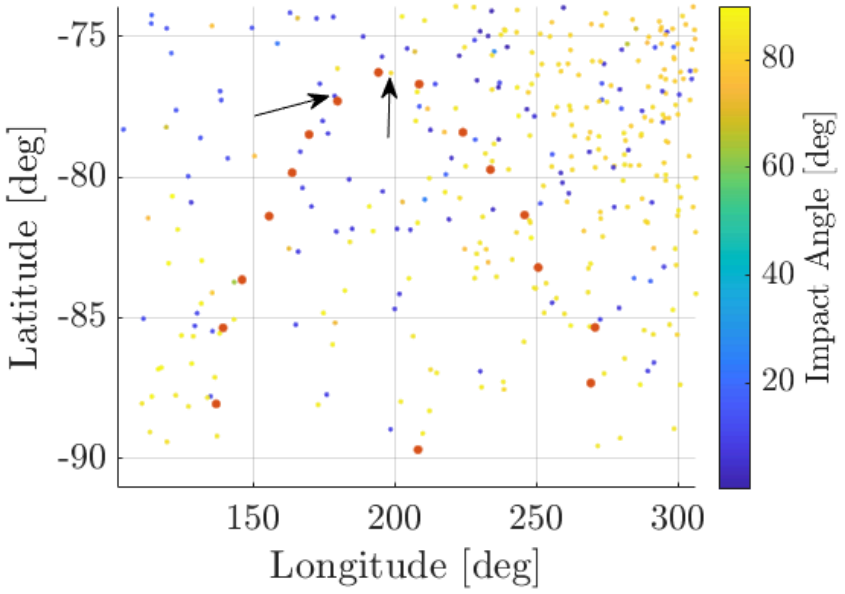

(b)

Figure 3.23.: Locations of Shackleton Crater in 2023 (in Red) Overlaid on Latitude and Longitude of Impact Conditions Originating from the 9:2 LSR NRHO with a 15 m/s Departure Maneuver

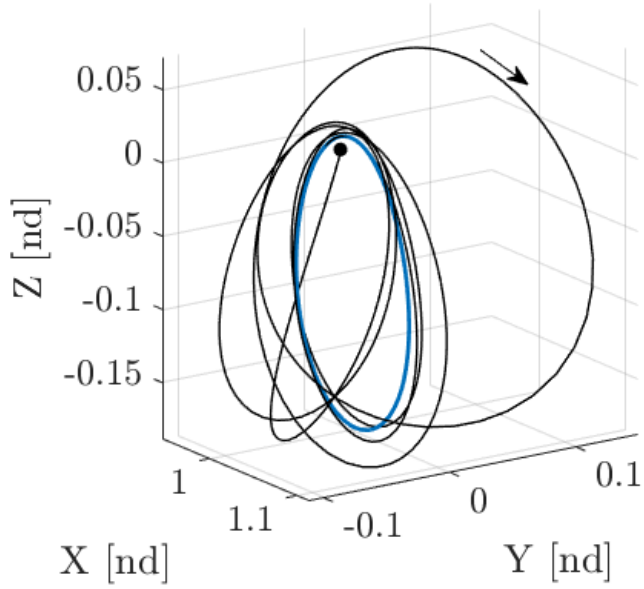

(a) Low Impact Angle

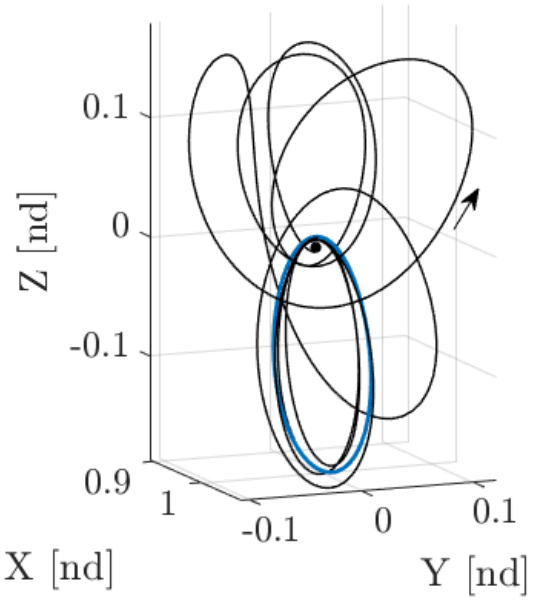

(b) High Impact Angle

Figure 3.24.: Example Low and High Impact Angle Trajectories from 9:2 LSR NRHO to Shackleton Crater Area

along the ith trajectory segment for $i = 1, \ldots, M$, respectively. The constraints are straightforwardly

$$\mathbf{F}(\mathbf{X}) = \begin{bmatrix} \mathbf{r}_0^{\tau_N} - \mathbf{r}_1^0 \\ \mathbf{v}_0^{\tau_N} + \Delta\mathbf{v} - \mathbf{v}_1^0 \\ \mathbf{x}_2^0 - \mathbf{x}_1^{\tau_1} \\ \mathbf{x}_3^0 - \mathbf{x}_2^{\tau_2} \\ \vdots \\ \mathbf{x}_M^0 - \mathbf{x}_{M-1}^{\tau_{M-1}} \\ \mathbf{r}_M^{\tau_M} - \mathbf{r}_S \end{bmatrix}, \tag{3.9}$$

where $\mathbf{r}_S$ is the position of the Shackleton crater obtained from the latitude and longitude at the specified epoch. More specifically, when an epoch is selected and the latitude, λ, and longitude, φ, of Shackleton crater in the CRTBP rotating frame are determined, the corresponding position components are calculated as

$$x = R_{Moon} \cos(\lambda) \cos(\varphi), \tag{3.10}$$

$$y = R_{Moon} \cos(\lambda) \sin(\varphi), \tag{3.11}$$

$$z = R_{Moon} \sin(\lambda). \tag{3.12}$$

Using the free variables and constraints specified, the two geometries are converged to all 16 of the locations determined for Shackleton crater in 2023.

Using the impacting initial conditions from the locations in Figure 3.23, the corrected trajectories are generated and displayed in Figure 3.25. Converged solutions are obtainable for both types of transfer geometries to all Shackleton crater locations included in the analysis. Evident in both families of transfers, the underlying geometry of the converged trajectories varies little from the initial guess. This lack of departure from initial geometry indicates that the geometries selected provide sufficiently flexible initial guesses for crater transfers. Therefore, in the current context, the 9:2 LSR NRHO provides Lunar access to the Shackleton crater for all epochs analyzed given freedom of phasing in the NRHO. The times-of-flight for the NRHO

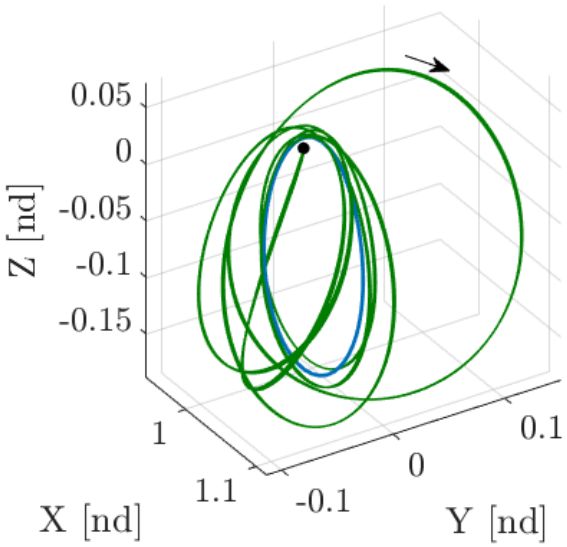

(a) Low Impact Angle

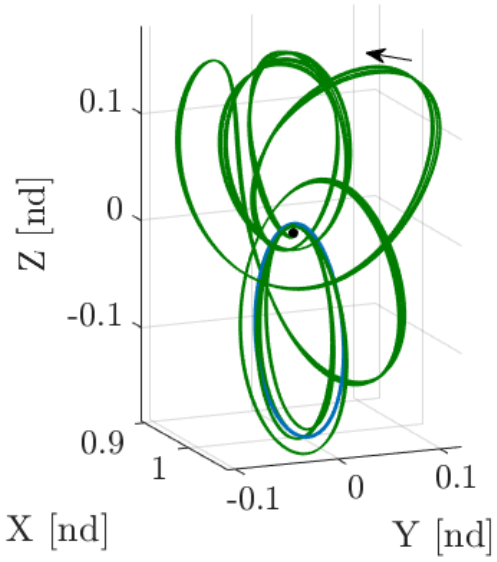

(b) High Impact Angle

Figure 3.25.: Corrected Trajectories from NRHO to Shackleton Crater for All Selected Epochs

to crater transfers at each arrival date are given in Figure 3.26. Clearly, very little variation in the TOFs is observed across all dates. This result is congruent with the

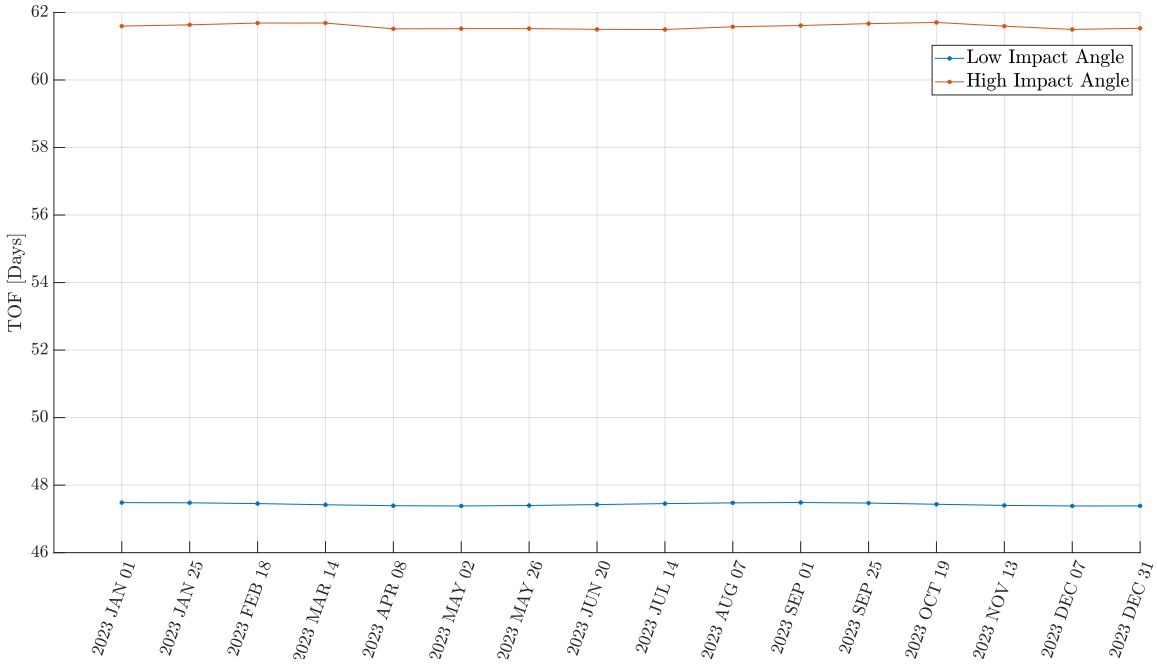

Figure 3.26.: TOF Values for Corrected Transfers from NRHO to Shackleton Crater

lack of major variation in the transfer geometries seen in Figure 3.25 as the transfer geometry and TOF are tightly coupled in general. The low impact angle trajectory remains around 47 days while the high impact angle trajectory hovers around 62 days over 2023. The maneuver magnitudes for the corresponding epochs are shown in Figure 3.27. The required Δv for the NRHO to crater transfers displays slightly greater variation that that observed for the time-of-flight. The low impact angle geometry oscillates with a 6 m/s amplitude while the high impact angle geometry has a range of around 3 m/s. While the variations observed are large in relative terms, the absolute variations are small.

The use of step of maneuvers to determine candidate geometries to correct into desired impact trajectories offers a valid way to design missions from the NRHO to the Lunar surface in the CRTBP. However, due to a large number of impacts not reaching the Lunar surface and the chaotic flow surrounding the NRHO, the number of available geometries and transfer types is limited. As a result, a large number of candidate maneuver directions and magnitudes must be integrated to generate enough

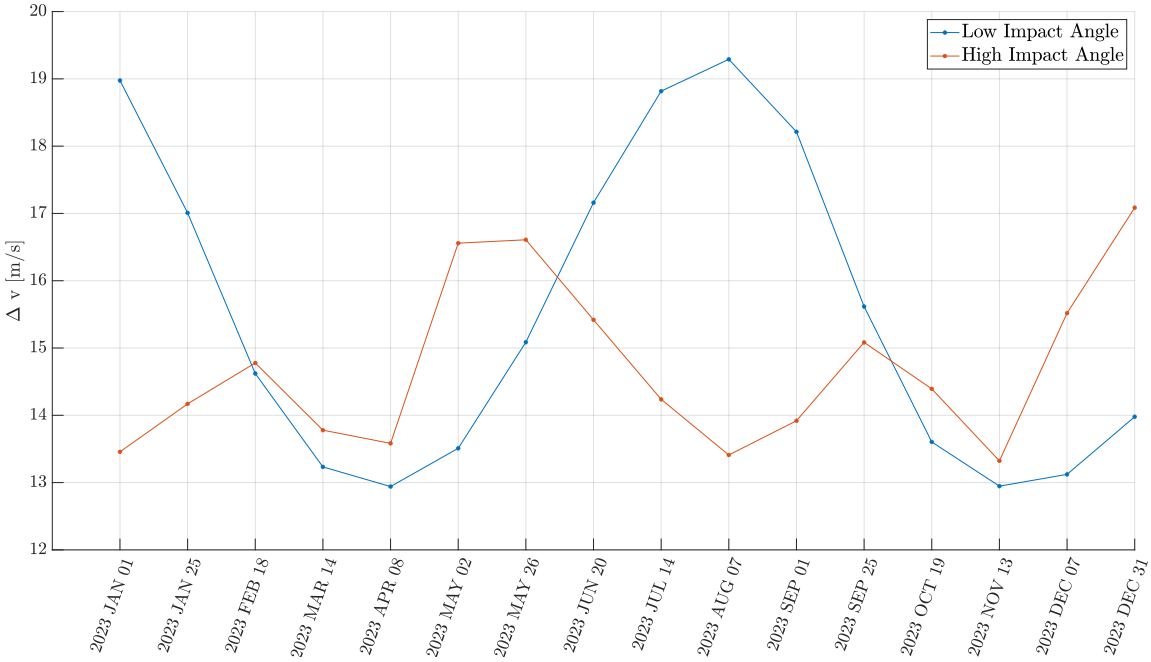

Figure 3.27.: **Δv** Magnitudes for Corrected Transfers from NRHO to Shackleton Crater

data points for the design process (over 72,000,000 in this analysis) to overcome the low number of impacts. This limitation reduces the ability to determine trajectories with desired impact locations **and** impact conditions with desired or predictable geometry. This is observed in the limited number of speeds and angles available for the Shackleton crater transfers. Consequently, alternative methods for determining desirable geometry and impact conditions is sought for mission design from periodic orbits to the Lunar surface and Low Lunar Orbit (LLO).

4. LUNAR ACCESS CHARACTERISTICS OF PERIODIC ORBITS IN THE LUNAR REGION

Invariant manifolds associated with periodic orbits in the Lunar region provide structures that are beneficial to Lunar access trajectory design. Manifold structures leading to desirable Lunar altitudes or likely impacts offer predictable and structured pathways for mission design applications. Therefore, an understanding of the available manifold structures is a key element for efficiency and flexibility in design procedures. The stability index for associated periodic orbit family members is defined and leveraged to determine orbits possessing stable and unstable manifolds providing theoretically zero-cost arrivals and departures. Finally, the Lunar access characteristics of the unstable manifolds of these periodic orbits are evaluated.

4.1 The Stability Index

The stability of periodic orbits is assessed via the characteristic multipliers derived from the monodromy matrix, $\Phi(T, 0)$. The monodromy matrix possesses 6 eigenvalues and a periodic orbit possesses stable and unstable manifolds if and only if the modulus of one or more of these eigenvalues is greater than 1. It is beneficial to define a stability index for every periodic orbit that supplies a scalar valued that indicates the existence of unstable and stable manifolds for a periodic orbit.

Grebow and Zimovan each offer a definition of a stability index leveraging the complex conjugate nature of the eigenvalue pairs from the monodromy matrix [22,23]. These definitions allow for the isolation of unstable orbits with purely real eigenvalues.

However, a modification of the definition allows for the detection of orbits possessing unstable spiral manifolds. The stability index, ς, is thus defined as

$$\varsigma := \left|\left|\bar{\lambda}_T\right|\right|_\infty \tag{4.1}$$

where $\bar{\lambda}_T$ is the vector of eigenvalues of $\Phi\left(T,0\right)$ and $\bar{\lambda}_T \in \mathbb{C}^6$. A stability index greater than 1 indicates that a periodic orbit is unstable. Furthermore, because $\det \Phi\left(T,0\right) = 1$, the minimum possible stability index is 1. The definition of the stability index, therefore, allows determination of the periodic orbit stability characteristics via the inspection of a single scalar-valued quantity.

Associating periodic orbits with their corresponding stability indices identifies members of periodic orbit families that possess unstable and stable manifolds. A periodic orbit family may have no unstable members, all unstable members, or a bands of unstable members separated by periodic orbits with no stable or unstable subspaces. As an example, Figure 4.1 displays the stability indices for a large region across the Earth-Moon L_2 northern halo family of periodic orbits. Four distinct regions are observed: two bands of unstable family members with stability indices greater than 1 and two bands of family members possessing no stable or unstable subspaces with unit stability indices. This figure further demonstrates that leveraging the stability index enables the visual inspection of stability properties within a family of periodic orbits without requiring numerical inspection of all the characteristic multipliers of individual orbits. The L_2 northern halo family corresponding to the hodograph in Figure 4.1 is displayed in Figure 4.2 and colored based on the stability properties predicted by the stability index, ς. Congruent with Figure 4.1, four distinct bands of motion are observed. The region of this family highlighted in the figure is unstable at its planar bifurcation with the L_2 Lyapunov orbits and remains unstable until near its maximum z-amplitude where the orbits become stable. Two more stability changes occur as the periapse radius continues below the Lunar radius.

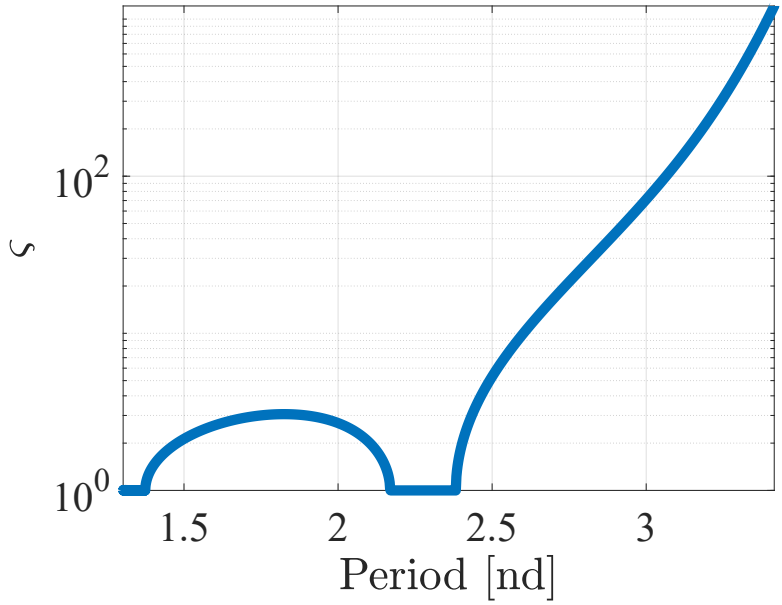

Figure 4.1.: Stability Indices for Earth-Moon L_2 Northern Halo Family

The application of Lyapunov stability methods to periodic orbits result in binary notions of stability, i.e., periodic orbits possessing characteristic multipliers of modulus greater than one are unstable and are otherwise stable with no mixed option. However, in application, periodic orbits with stability indices "slightly" greater than one possess unstable manifold structures that diverge slowly from the underlying periodic orbit. Furthermore, the stability index is coupled with the period of the underlying periodic orbit; a higher stability index does not indicate that a manifold departs faster if the period of the orbit is also longer. Therefore, a time constant, κ_τ, quantifies the slow divergence of unstable behavior, that is,

$$\kappa_\tau = \frac{T}{\ln(\varsigma)}, \tag{4.2}$$

where T is the period of the orbit, thus, the time required for the divergence to grow by a factor of e [23]. As the stability index approaches 1, therefore, the time constant tends towards infinity indicating no divergence of the initial perturbations

from the periodic orbit. Additionally, because the stability index is never less than 1, the time constant is always non-negative. The time constants computed for the

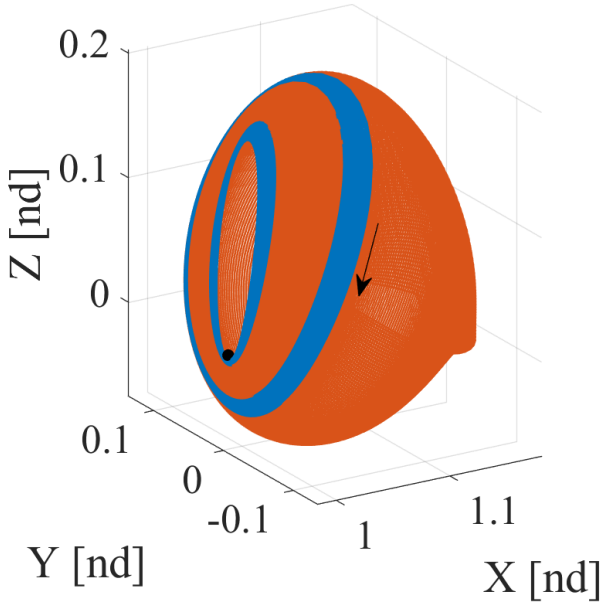

Figure 4.2.: Earth-Moon L_2 Northern Halo Family where Red Orbits Possess Unstable Manifolds and Blue Orbits Possess a Four-Dimensional Center Manifold

L_2 northern halo family are displayed in Figure 4.3 in a manner similar to that by Zimovan [23]. The time constants for the higher-period band of unstable orbits (those closer to the L_2 Lyapunov bifurcation orbit) possess much lower time constants than the shorter-period group of unstable orbits. Physically, a lower time constant corresponds to manifold structure that grows away from the underlying periodic orbit at a faster rate. Periodic orbits with large time constants (stability indices close to unity) possess unstable manifold structures that require many revolutions before significant deviation is observed. Figures 4.5 and 4.4 demonstrate the difference between high and low time constants associated with an unstable periodic orbit. The trajectory arc on the unstable manifold of the low-time-constant orbit departs the periodic orbit after a single revolution while the trajectory on the unstable manifold of the high-time-constant orbit remains close to the originating orbit after 13 revolutions.

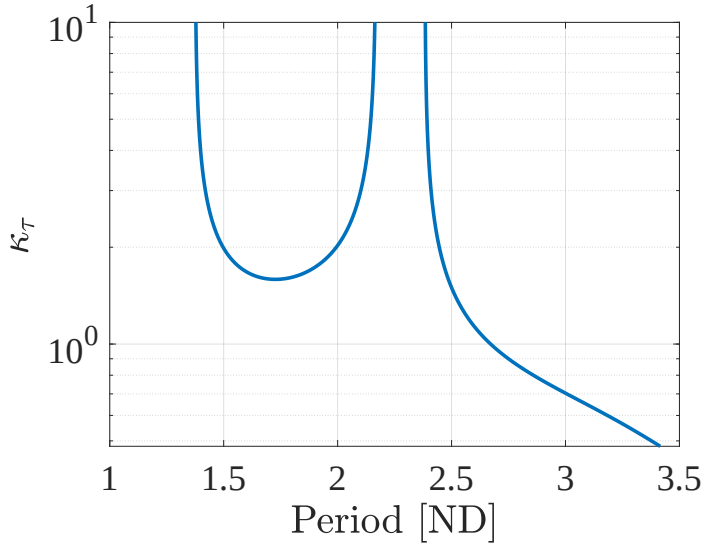

Figure 4.3.: Time Constants of Earth-Moon L_2 Northern Halo Family

Therefore, while both orbits are *unstable* from a Lyapunov stability theory perspective, the time constant provides information on whether the manifold structures offer practical departure (or arrival) characteristics.

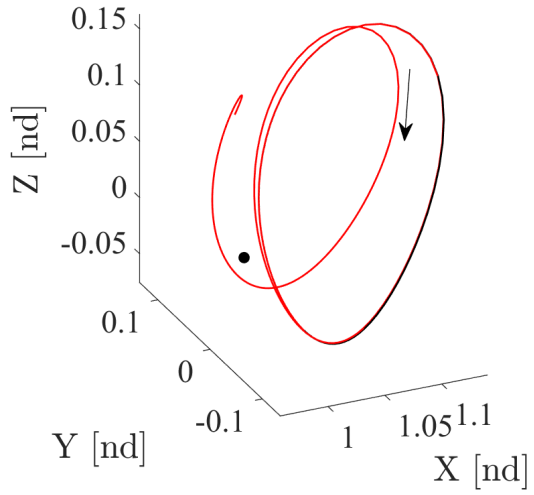

Figure 4.4.: Trajectory Arc on Unstable Manifold Originating from Periodic Orbit with Low Time Constant ($\kappa_\tau = 0.8$) Propagated for 2 Revolutions

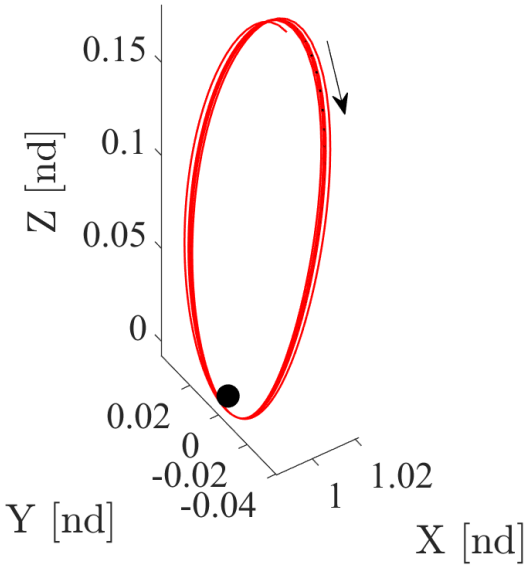

Figure 4.5.: Trajectory Arc on Unstable Manifold Originating from Periodic Orbit with High Time ($\kappa_\tau = 1.8$) Constant Propagated for 13 Revolutions

No analytical prediction exists for a value of κ_τ that constitutes a "fast" departure; therefore, the application of the time constant is evaluated within the context of a heuristic. The current investigation limits "fast" departure characteristics to a value such that $\kappa_\tau \leq 1.5$. This critical time constant corresponds to growth that is consistent with two orders-of-magnitude at around 30 days in the linear model and anecdotally demonstrates desirable characteristics in the full nonlinear model.

4.2 Stability of Periodic Orbit Families in the Lunar Region

Invariant manifold structures associated with unstable periodic orbits provide low-cost transfer opportunities to and from the underlying periodic orbit. However, not all families of periodic orbits possess unstable members. Therefore, the availability of unstable periodic orbits in a subset of Lunar region periodic orbits is explored. This subset of Lunar-Region periodic orbits is described and the stability characteristics associated with each family are investigated.

4.2.1 Definition of Lunar Region Periodic Families of Interest

Within the Circular Restricted Three Body Problem (CRTBP) model, a significant variety of periodic orbit families exist in the Lunar Region. Diversity in orbital geometry, range of Jacobi constant values, period, and stability characteristics is observed between families. The subset of the Lunar-Region periodic orbits in Table 4.1 is selected that reflects a significant span across the variation observed in these quantities. While not included, alternative families to those specified in Table 4.1 may offer additional transfer structures. The table is divided into the planar and spatial families. While offering a smaller phase space and, thus, easing analysis, the unstable and stable manifold structures associated with the planar orbits are also planar limiting the available LLOs and Lunar impact sites to those intersecting the Earth-Moon orbital plane.

Table 4.1.: Investigated Subset of Lunar Region Periodic Orbits

Planar Orbit Families	**Spatial Orbit Families**
Distant Retrograde Orbits (DROs)	L_1 and L_2 Halo Orbits
Low Prograde Orbits (LPOs)	L_1 and L_2 Axial Orbits
L_1 and L_2 Lyapunov Orbits	L_1 and L_2 Vertical Orbits
	Butterfly Orbits
	Period 4 Halo Orbits

4.2.2 Earth-Moon Distant Retrograde Orbits

The Distant Retrograde Orbits (DROs) are essentially retrograde Lunar circular orbits viewed and computed in the CRTBP. A large subset of the Distant Retrograde Orbits is displayed in Figure 4.6, and includes the corresponding stability indices. The stability index for every distant retrograde orbit is unity; therefore, there exists no period-1 planar DRO with an unstable (and therefore stable) subspace. The DROs possess four-dimensional center subspaces, i.e., the non-trivial eigenvalues all lie on the

unit circle. The stability of the DRO family of orbits has led to the incorporation of DROs into mission concepts such as the Asteroid Redirect Mission [24], but provides no unstable manifolds for low-cost lunar access.

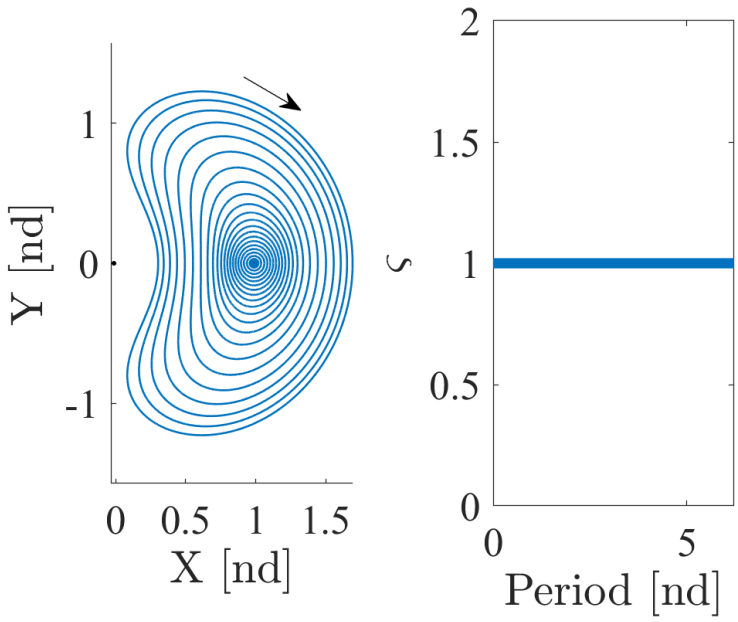

Figure 4.6.: Simply Symmetric Planar Distant Retrograde Orbits (DROs) and Corresponding Stability Indices

4.2.3 Earth-Moon Low Prograde Orbits

Low Prograde Orbits (LPOs) are similar to the DROs but with velocities such that the periodic motion is in the prograde direction, i.e., counter-clockwise as viewed in the CRTBP rotating frame. Representative orbits from across the LPO family appear in Figure 4.7.

The LPO family contains members with Lunar periapse radii well within the Moon radius and extending to approximately 22,000 km. In Figure 4.8, the Jacobi constant is plotted as a function of Lunar periapse radius across the LPO family. The Jacobi constant varies significantly ranging from around 3.172 to 9.016. Therefore, at the lowest Jacobi value, the L_1 gateway is open, allowing transportation between the Lu-

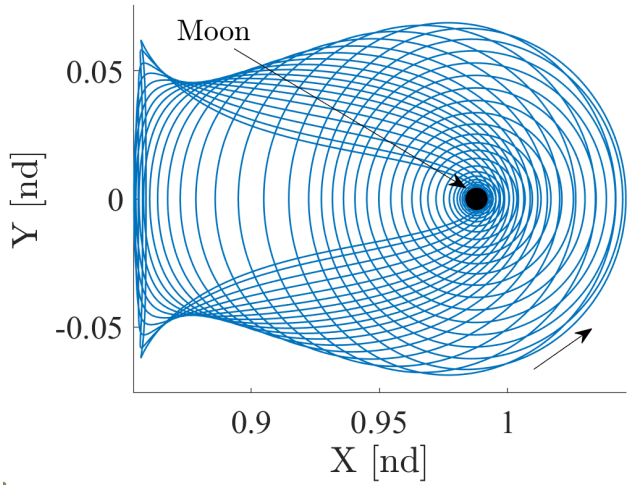

Figure 4.7.: Low Prograde Orbits (LPOs)

nar and Earth regions. The stability index across the LPO family is plotted in Figure

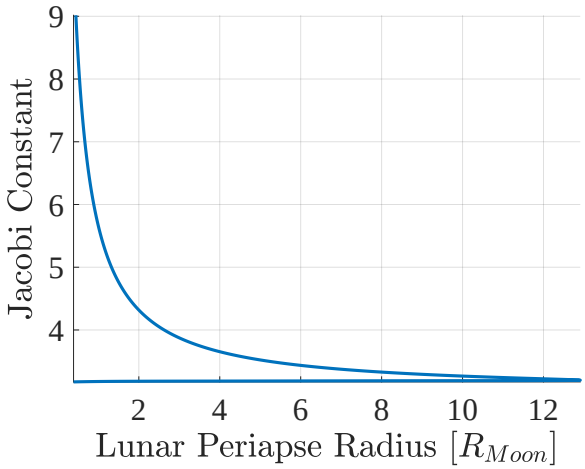

Figure 4.8.: Jacobi Constant as a Function of Lunar Periapse Radius for Earth-Moon Low Prograde Orbits

4.9(a) and is characterized by initially high values at low periapse radii and Jacobi constants followed by a nearly-instantaneous drop to unity for the remainder of the family except for a small section around $r_p = 0.6R_{Moon}$. The unstable members of the LPO family are located at a r_p near and below 5,200 km (approximately 3,500 km altitude); the corresponding Jacobi constant values all fall below 3.184. In Fig-

ure 4.10, the LPOs are colored by stability index. The unstable periodic orbits are observed as extending to relatively high lunar altitudes, thus, the possibility exists for Lunar orbit insertion at altitudes commonly required for Lunar missions. The existence of unstable family members in the LPO family differs from observations in the DRO family. This instability indicates possible utility of the invariant manifolds associated with the family members. However, as discussed in Section 4.1, the rate at which trajectories on the stable and unstable manifolds approach and depart the periodic orbit, respectively, must be sufficiently high such that the departure mechanics are aligned with mission criteria. Therefore, the time constants associated with the unstable LPOs are explored. The time constant values across the LPO family are plotted in Figure 4.9(b). Periodic orbits with time constants near and below 1.5 exist indicating the existence of unstable orbits with manifold structures departing at sufficiently fast rates. Furthermore, as apparent in Figure 4.9(b), many of these advantageous periodic orbits exist with periapse radii between 1 and 2.5 Lunar Radii offering ideal altitudes for Low Lunar Orbit mission applications.

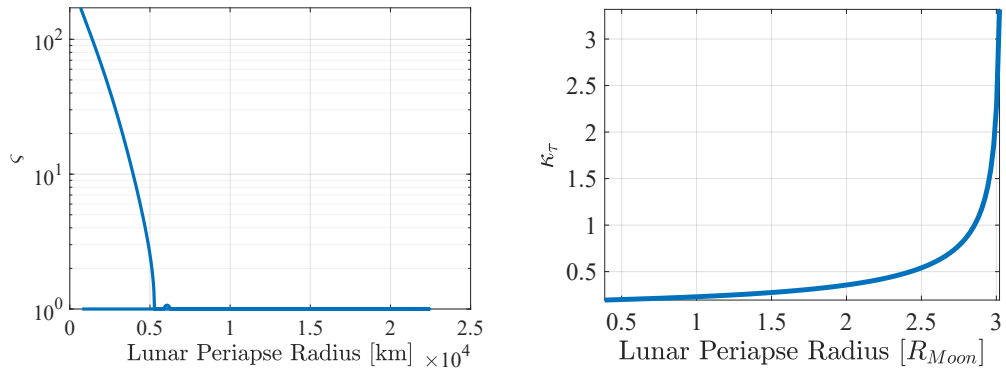

(a) Stability Index (b) Time Constant

Figure 4.9.: Stability Characteristics of Earth-Moon Lunar Prograde Orbit Family

The Low Prograde Orbit (LPO) family possesses unstable orbits with desirable time constants at altitudes beneficial for Low-Lunar operations. The manifold structures associated with these orbits provide opportunities for low-cost transfers to the

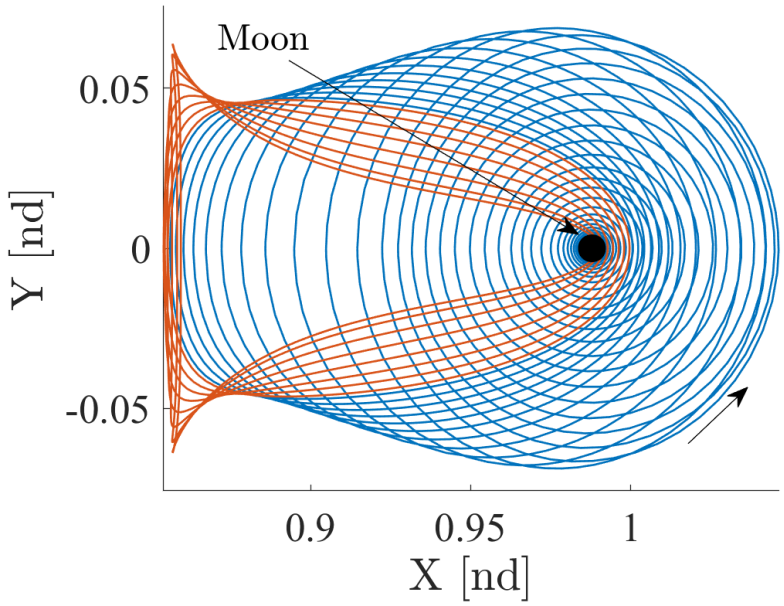

Figure 4.10.: Low Prograde Orbits (LPOs) Where Red Indicates Unstable Orbits and Blue Indicates Stable Orbits

Lunar surface, Low-Lunar Orbit, and other orbits in the Lunar vicinity. Furthermore, due to the relatively low Jacobi constant values, given the proximity to the second primary, the LPO family presents a promising intermediate step for spacecraft at higher energies to enter the Low-Lunar space.

4.2.4 Earth-Moon Lyapunov Orbits

The final planar orbit families included in the investigation are the Lyapunov orbit families. In Figure 4.11, both the L_1 and L_2 families appear; while an additional Lyapunov family exists around L_3, none of the family members extend into the Lunar region and, therefore, it is not included in the current study.

Both the L_1 and L_2 Lyapunov families grow to large y amplitudes, approaching the Moon at arbitrarily low periapse radii. Intuitively, as the size of the Lyapunov orbit expands and the periapse radius drops, the Jacobi constant value drops as well. The relationship between the Jacobi constant and the Lunar periapse radius is plotted

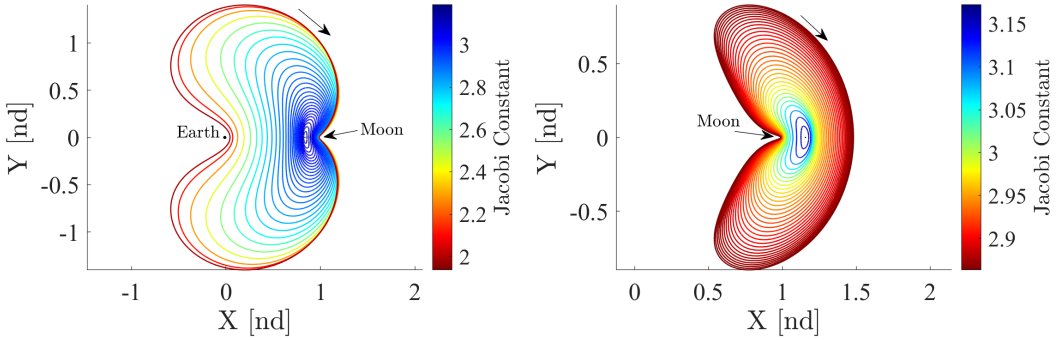

(a) L_1 Lyapunov Orbits (b) L_2 Lyapunov Orbits

Figure 4.11.: Earth-Moon Lyapunov Orbit Families

in Figure 4.12. At low lunar periapse radii, the Jacobi constant is also low indicating high periapse velocities. These orbits defined by low Jacobi constant values reflect high-energy members that, in conjunction with their sub-surface Lunar radii, present challenges to incorporation for cislunar mission designs. However, both the L_1 and L_2 families possess members with higher Jacobi constant values and Lunar altitudes ideal for Low-Lunar operations.

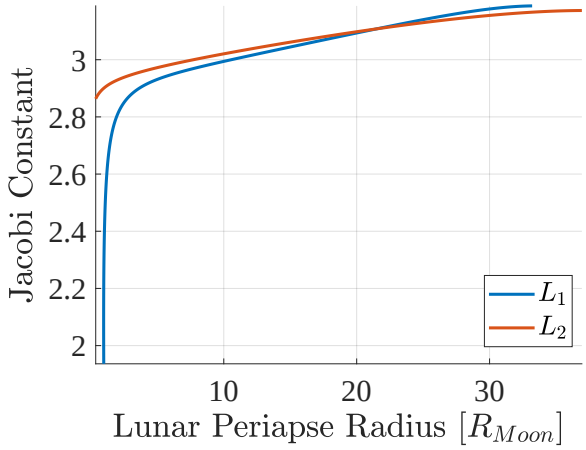

Figure 4.12.: Jacobi Constant Value Versus Lunar Periapse Radii for Earth-Moon L_1 and L_2 Lyapunov Orbit Families

The stability properties of the Lunar-Region Lyapunov families are characterized in Figure 4.13. Every member of both the L_1 and L_2 Lyapunov orbit families possesses unstable and stable subspaces with a minimum observed stability index of $\varsigma = 107$ for L_1 and $\varsigma = 99$ for L_2. Furthermore, the time constants, plotted in Figures 4.13(c) and 4.13(d), are on the order of 1.0 indicating "fast" departure and arrival mechanics. The L_2 family does posses orbits with time constant values $\kappa_\tau = 1.6$, i.e., above the pre-defined critical time constant value; but for a significant portion of the family, κ_τ lies below the 1.5 value. Therefore, the Lyapunov families in the Lunar region

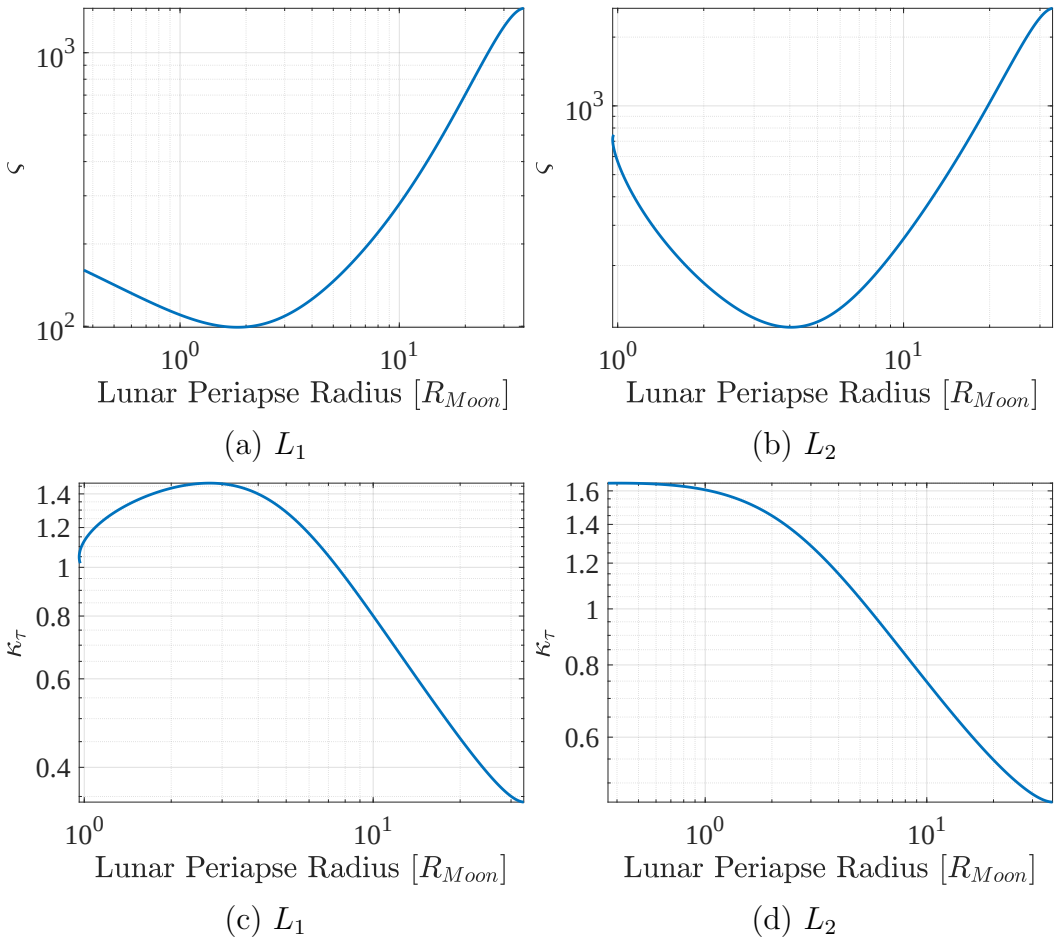

Figure 4.13.: Stability Characteristics of Earth-Moon Lyapunov Orbit Families

include unstable periodic orbits across a large span of Lunar radii and values of Jacobi constant with sufficiently low time constants and, consequently, a significant

opportunity for incorporation into mission designs leveraging the Lyapunov manifold structures.

4.2.5 Earth-Moon Halo Orbits

The L_1 and L_2 halo orbit families are three-dimensional periodic orbit families that bifurcate from the L_1 and L_2 Lyapunov families, respectively. Sections of the northern halves of the L_1 and L_2 halo orbit families are displayed in Figure 4.14. Due to the symmetry across the xy-plane in the CRTBP, the southern L_1 and L_2 northern halo orbit families also exist with opposite signs on z and $\dot{z}$, effectively appearing as mirror images of the orbits as observed in Figure 4.14 across the xy-plane. Furthermore, due to this symmetry, the stability characteristics of the northern half-families are equivalent to those of the southern half-families.

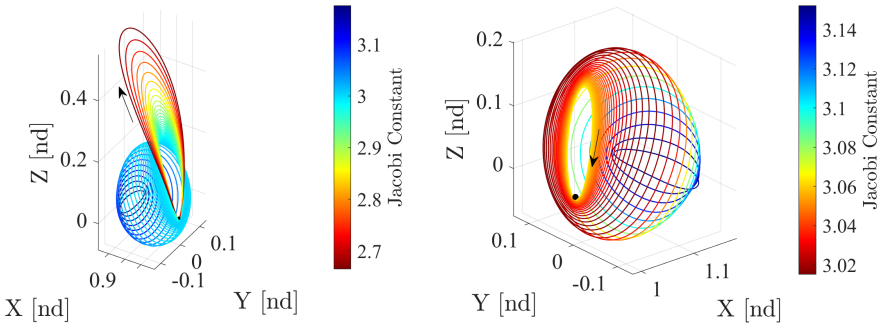

(a) L_1 (b) L_2

Figure 4.14.: Northern Halo Orbit Families in the Earth-Moon System

The stability characteristics of the northern halo families are summarized in Figure 4.15. Both the L_1 and L_2 families possess four bands of unstable and stable periodic orbits with regions of stable orbits at $r_p \approx 10R_{Moon}$ (17,400 km). At periapse radii beyond this 10 R_{Moon} distance, both families possess unstable orbits with increasing value of the stability index as the families evolve towards the planar bifurcation point in their corresponding Lyapunov families. The time constants for the unstable

periodic orbits with $r_p > 10R_{Moon}$ shrink consistent with the growth of ς and the family then enters regions of desirable values, i.e., near and below 1.5. However, at periapse radii less than $r_p \approx 10R_{Moon}$, more notable stability structure is observed. Both the L_1 and L_2 families include regions of instability below the stable region at $10R_{Moon}$ and then returns to $\varsigma = 1$ as the periapse radius is decreased further. For the L_1 halo orbit family, the central unstable region contains a subset of periodic orbits with desirable time constants however, for the L_2 halo orbit family this central region displays time constants at and above 1.6 indicating slow manifold departure.

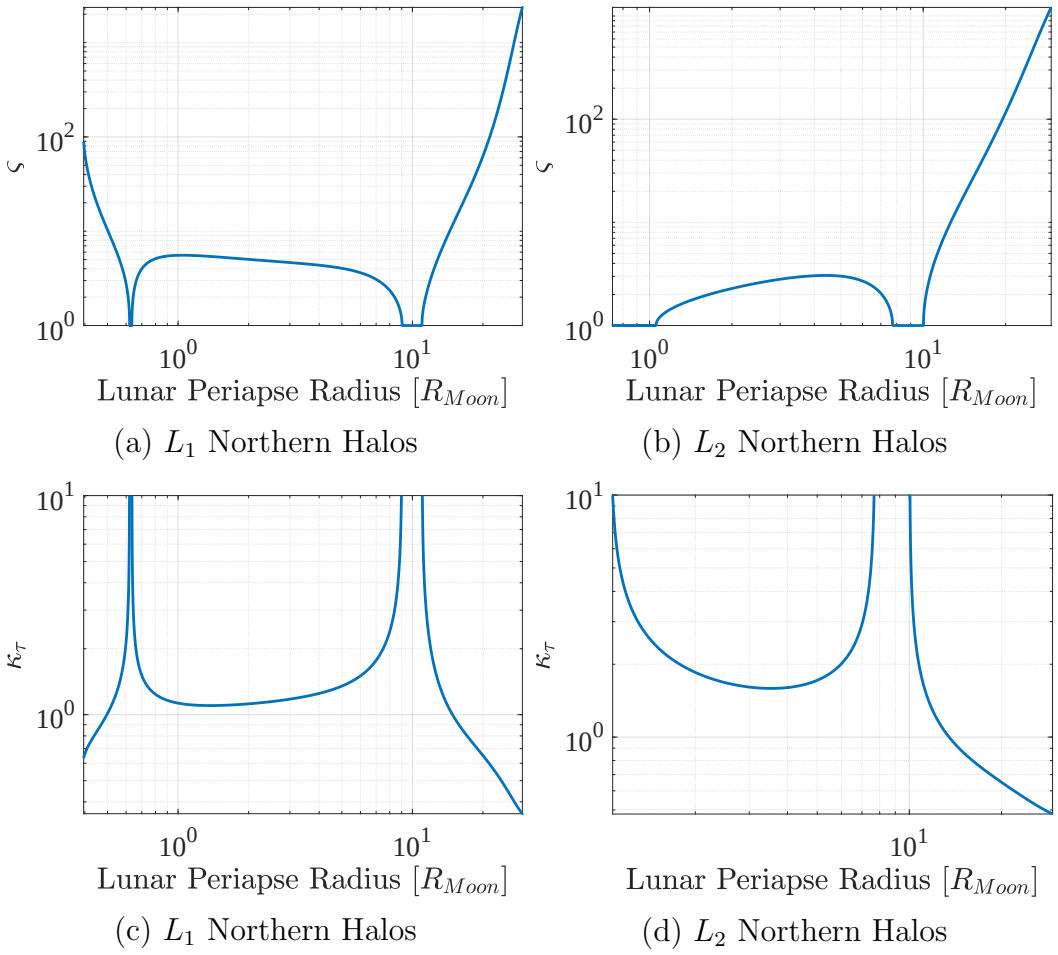

(a) L_1 Northern Halos (b) L_2 Northern Halos

(c) L_1 Northern Halos (d) L_2 Northern Halos

Figure 4.15.: Stability Characteristics of Earth-Moon Northern Halo Orbit Families

The unstable bands near the planar bifurcation orbit in both the L_1 and L_2 halo orbit families along with the central unstable band in the L_1 Halo family suggest

manifold structures with low time constants that may be leveraged for Lunar access. In Figures 4.16 and 4.17 the L_1 and L_2 families are colored by stability. In both families, the bands of unstable orbits near the Lyapunov bifurcation orbits extend significantly out of plane and represents a "large" portion of the family geometry. These structures offer candidate orbits for cost-free departures and arrivals from LLOs or the Lunar surface.

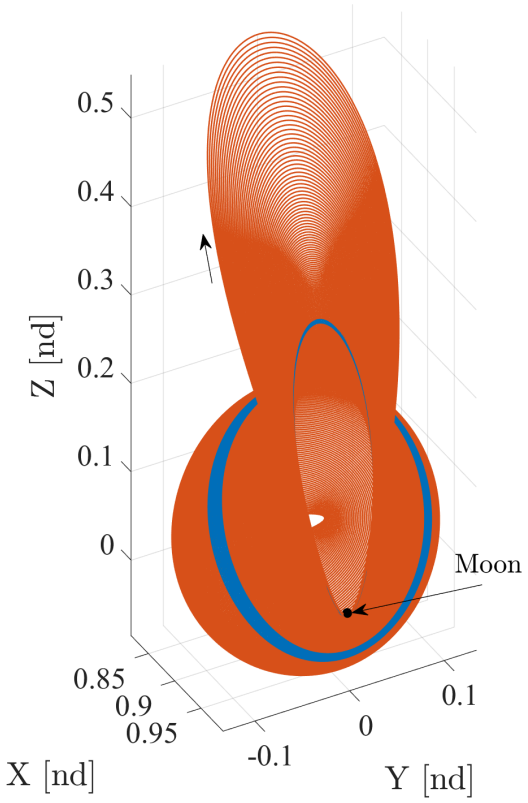

Figure 4.16.: L_1 Halo Orbit Family Colored by Stability where Red Indicates Unstable and Blue Indicates Stable

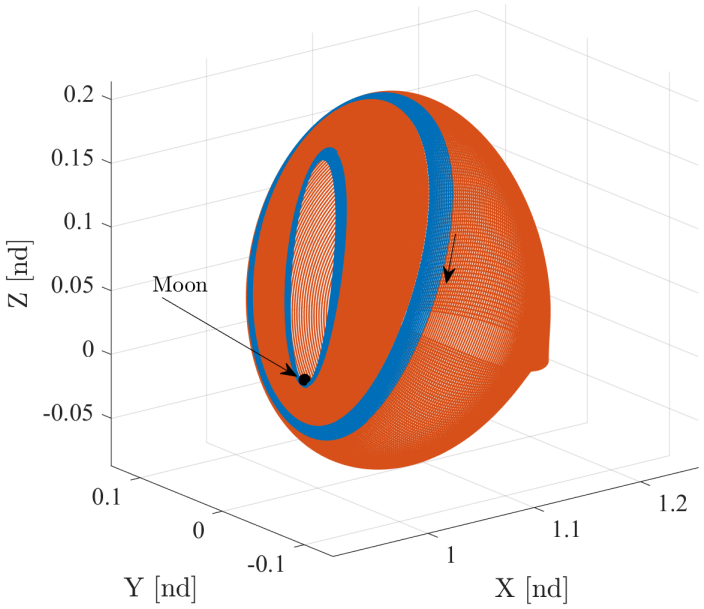

Figure 4.17.: L_2 Halo Orbit Family Colored by Stability where Red Indicates Unstable and Blue Indicates Stable

4.2.6 Earth-Moon Vertical Orbits

The Earth-Moon Vertical Orbits are generated from the out-of-plane center mode present in the linear variational analyses relative to the collinear libration points. These orbits are, thus, denoted vertical orbits because, in the neighborhood of the Lagrange points, they approach the harmonic oscillation described in Equation (2.68). Orbits across both the L_1 and L_2 vertical families are plotted in Figure 4.18. Characteristic of the vertical orbit families is a large out-of-plane component and figure-eight motion centered above and below the xy-plane. Because of the large out-of-plane component of certain members along the family, the Jacobi constant values are negative values near -1 for both the L_1 and L_2 families as observed in Figure 4.19. The members with low Jacobi constant values may be intractable for mission applications, however, the vertical orbits with smaller out-of-plane components evolve to higher Jacobi values, i.e., near 3, and, therefore, may present opportunities at energies closer to those of other orbits in the Lunar region.

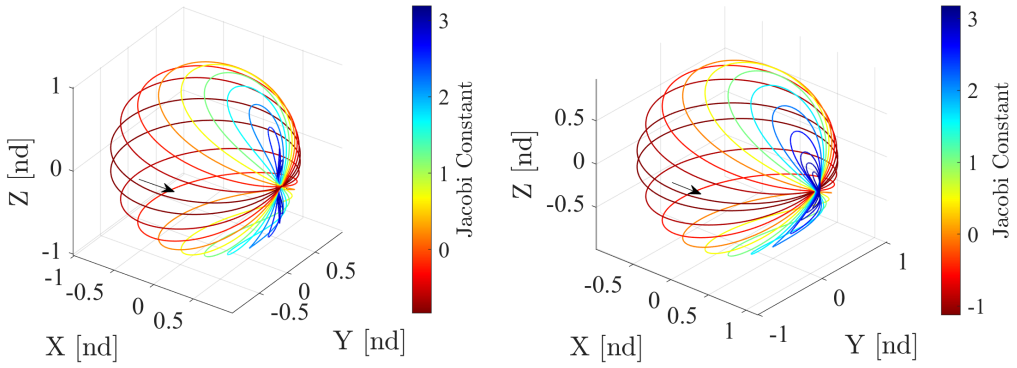

(a) L_1 (b) L_2

Figure 4.18.: Vertical Orbit Families in the Earth-Moon System

The stability characteristics of the L_1 and L_2 vertical orbit families appear in Figure 4.20. Obviously, every orbit across both families is unstable. Furthermore, at Lunar periapse radii beyond $r_p \approx 16R_{Moon}$ the vertical orbits demonstrate low time constants congruent with fast departure mechanisms. Because fast departures

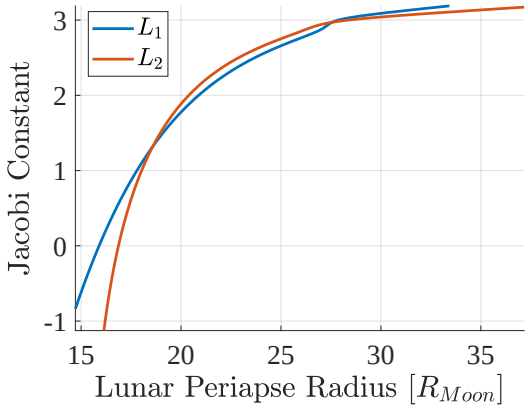

Figure 4.19.: Jacobi Constant Versus Lunar Periapse Radius for Earth-Moon Vertical Orbit Families

correspond to the high Jacobi constant values, they offer manifold structures possibly accessible from other Lunar region orbits. The Earth-Moon L_1 and L_2 vertical orbits include unstable periodic orbits with low time constants across a wide range of Jacobi constant values and geometries. Noticeably, significantly unstable orbits are observed at Jacobi constant values near 3, a Jacobi constant value repeated in every family investigated. These instability characteristics indicate that the Vertical families' invariant manifold structures associated with the vertical family likely provide desirable pathways for moving through Lunar space.

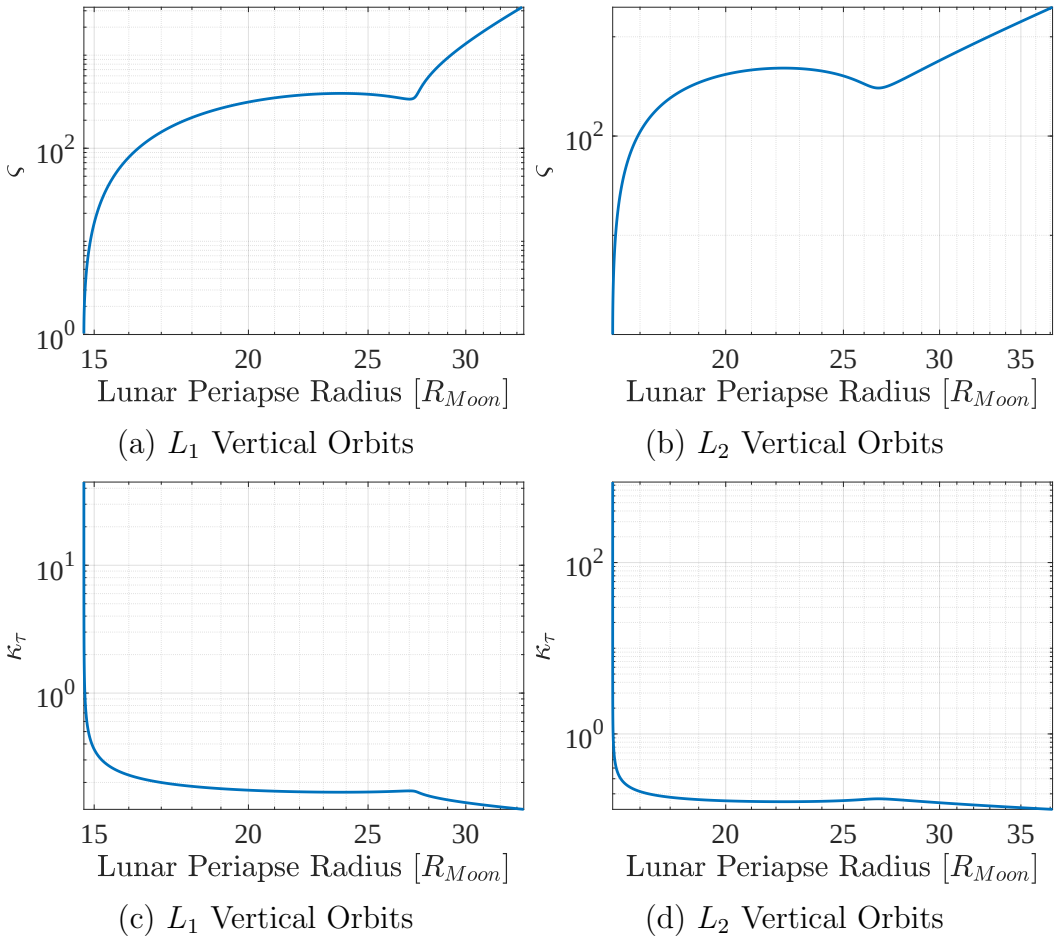

(a) L_1 Vertical Orbits

(b) L_2 Vertical Orbits

(c) L_1 Vertical Orbits

(d) L_2 Vertical Orbits

Figure 4.20.: Stability Characteristics of Earth-Moon Vertical Orbits

4.2.7 Earth-Moon Axial Orbits

The Earth-Moon L_1 and L_2 axial orbit families are, like the halo orbits, evolve from bifurcations with the L_1 and L_2 Lyapunov orbit families, respectively. Each axial orbit possesses two perpendicular crossings with the x-axis but not necessarily at perpendicular crossings of the xy and/or xz-planes. Both axial families are plotted in Figure 4.21. The perpendicular crossings with the x-axis are observed leading to the appearance of an axle passing through the center of both families. In Figure 4.22, the

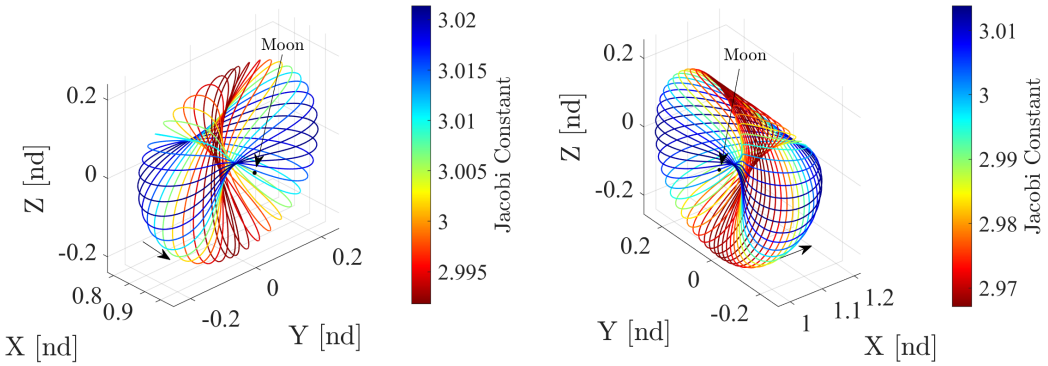

(a) L_1 (b) L_2

Figure 4.21.: Axial Orbit Families in the Earth-Moon System

Jacobi constant values versus Lunar periapse radius are plotted across both the L_1 and L_2 axial families. Very little variation in the Jacobi constant value is observed through the axial families as compared to variations observed in other periodic orbit families. This small variation is congruent with the geometry in the axial orbit families; the periodic orbits in both families possess similar geometry but are rotated around the x-axis leading to the largest contribution to the Jacobi constant variation across a family from changes in the z amplitude. Note, the axial families evolve down then back up curves present in Figure 4.22 as both families close on themselves forming closed hodographs.

The axial orbit families, like the vertical families, possess all unstable members as observed in Figure 4.23. Similar to Jacobi constant, little variation is observed

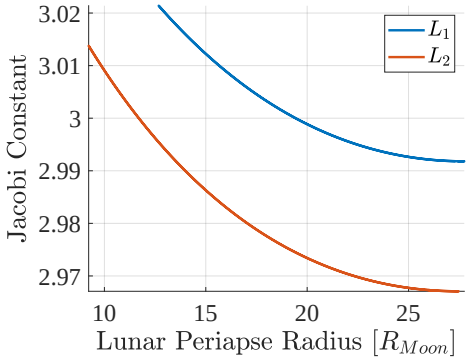

Figure 4.22.: Jacobi Versus Lunar Periapse Radius for Earth-Moon Axial Families

in the values of ς across each axial family. The L_1 axial orbits are slightly more unstable on average than the L_2 Axial orbits but the stability indices are on the same order of magnitude. In Figures 4.23(c) and 4.23(d), the L_1 axial orbits possess time constants near 0.656 and the time constants evaluated for the L_2 axial orbits possess values near 0.770 predicting fast departure mechanisms for both families. The stability characteristics along the axial families indicate that both the L_1 and L_2 families exhibit valid unstable structures to explore access for the Lunar region.

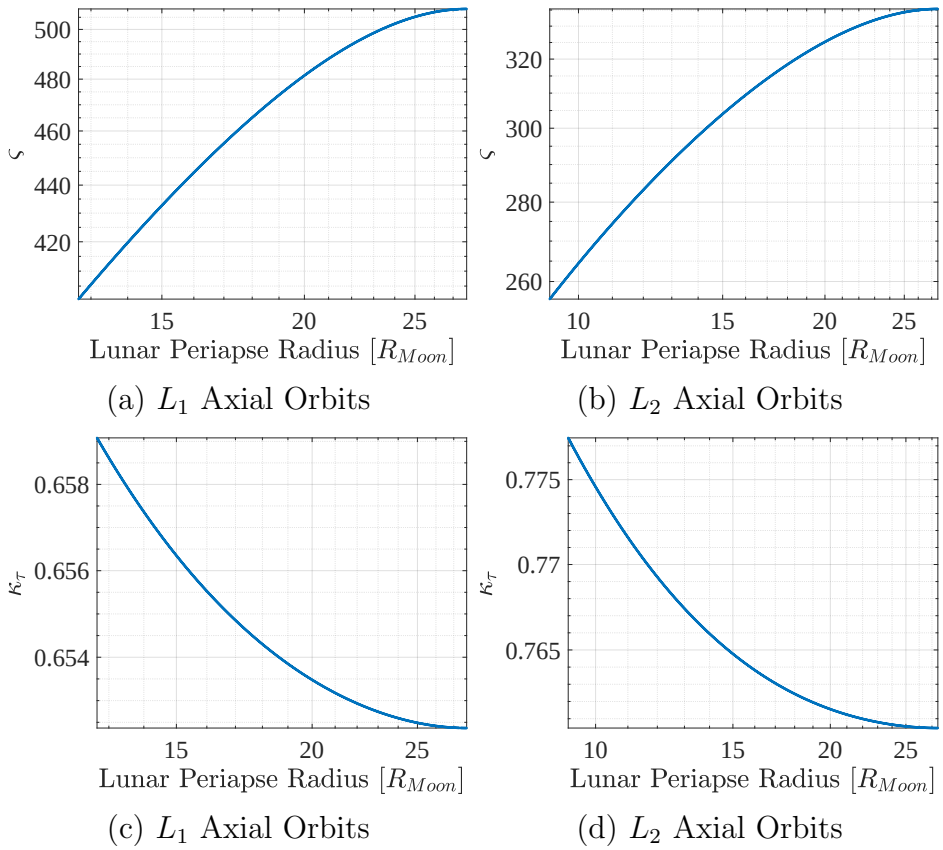

(a) L_1 Axial Orbits (b) L_2 Axial Orbits

(c) L_1 Axial Orbits (d) L_2 Axial Orbits

Figure 4.23.: Stability Characteristics of Earth-Moon Axial Orbit Families

4.2.8 Earth-Moon Butterfly Orbits

The Earth-Moon butterfly orbits emerge from a period-doubling bifurcation along the L_2 halo orbit families. The general geometry in a section of the northern butterfly orbit family in the Lunar region is plotted in Figure 4.24. Similar to the halo orbit families, the Butterfly orbits possess northern (shown in Figure 4.24) and southern families. Likewise, the stability characteristics are the same for both. The Jacobi

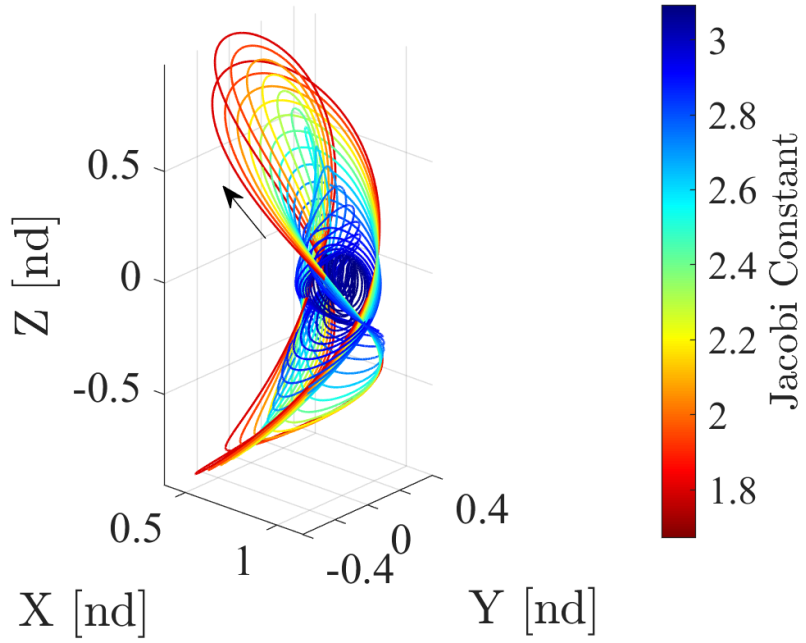

Figure 4.24.: Northern Butterfly Orbit Family in the Earth-Moon System

constant values appear as a function of the Lunar periapse radius in Figure 4.25. The butterflies in Figure 4.24 span Jacobi constants from $J \approx 1.5$ to $J \approx 3.0$. These Jacobi constant values are similar to those commonly observed in the other periodic orbit families indicating connection opportunities. Also apparent in Figure 4.25, the butterfly orbits span a wide range of Lunar periapse radii. This proximity to the Moon at higher Jacobi constant values suggests that manifold structures may be leveraged for transfers to low-Lunar regimes.

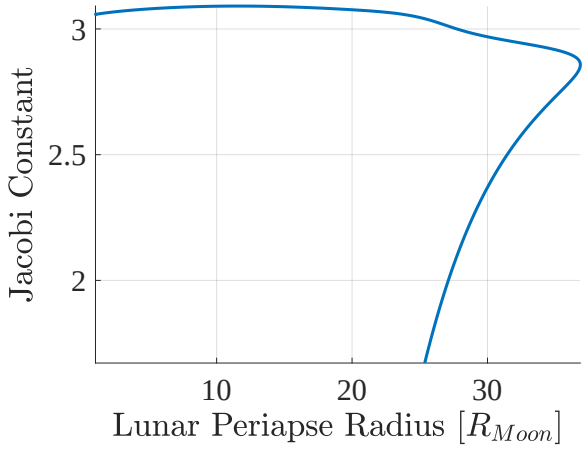

Figure 4.25.: Jacobi Versus Lunar Periapse Radius for Earth-Moon Northern Butterfly Orbits

The butterfly orbit family stability characteristics are plotted in Figure 4.26. Similar to the axial and vertical orbits, all members of the butterfly orbit family are unstable. However, the butterfly orbits exhibit linear instability at lower periapse altitudes than observed for both the axial and vertical families. The time constants associated with the butterfly orbits are below 1.5 for several sections across the family members presented. One section of sufficiently low time constants occur below $10R_{Moon}$ and another section occur above this cut-off. Therefore, similar to the L_1 Lyapunov family, while all orbits are unstable, sections appear to decay too slowly. However, the low-altitude instability in the Butterfly orbit offers the opportunity for transfer into regions with Low-Lunar altitudes.

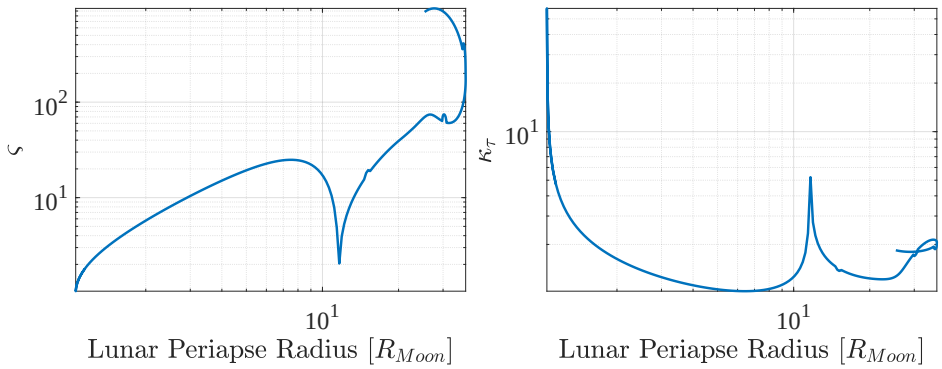

(a) Stability Index (b) Time Constant

Figure 4.26.: Stability Characteristics of Earth-Moon Butterfly Orbit Families

4.2.9 Earth-Moon Period-4 Halo Orbits

The final set of spatial periodic orbit families that are included in this analysis are the orbit families formed from the period-quadrupling bifurcations with the L_2 Halos presented by Zimovan-Spreen and Howell [25]. These period-four halo orbits are denoted the P4HO1 and P4HO2 families observed in Figures 4.27 and 4.28, respectively. Note, the geometry apparent in the P4HO2 represents a subset of the complete family formed by removing the significantly out-of-plane and high energy members. Both families display complex geometry quite different as compared to the halo orbits from which they originated via the bifurcation. The Jacobi constants as a

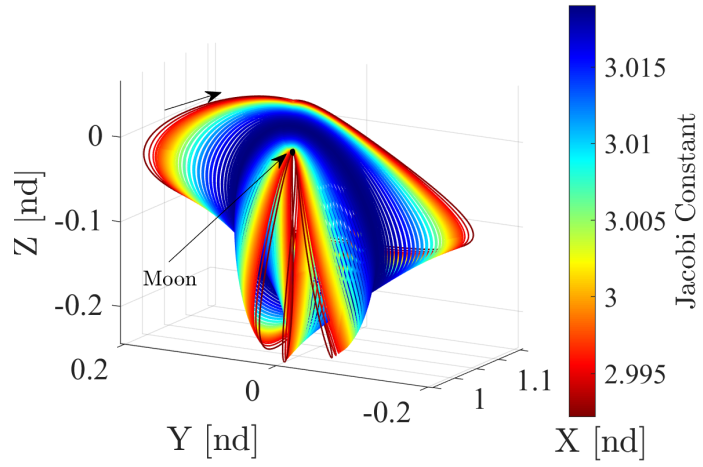

Figure 4.27.: P4HO1 Family in the Earth-Moon System

function of Lunar periapse radius for both period-four halo orbit families are plotted in Figures 4.29 and 4.30. Both families display only slight variations in Jacobi constant values centered around $J = 3.0$ indicating compatibility with Jacobi constant values observed for the other families in this analysis. The P4HO1 family includes members with extremely low periapse radii extending well below the lunar surface; but the family does not include members whose periapse radii extend beyond $7R_{Moon}$. This range of periapse radii offers significant advantage to low Lunar operations. The P4HO2 family does not reach the low periapse radii observed in the P4HO1 family

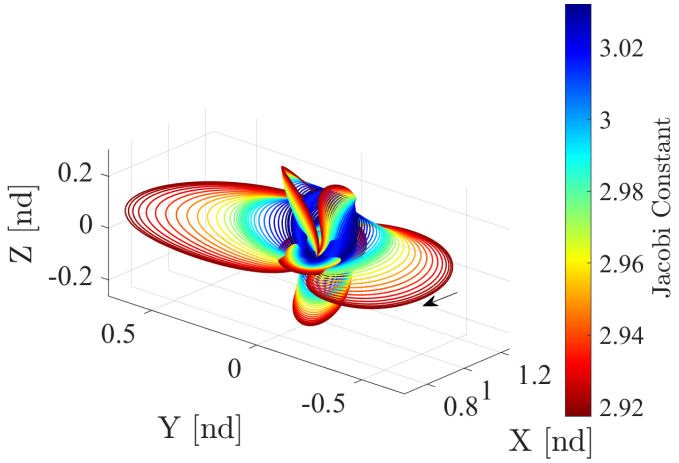

Figure 4.28.: P4HO2 Family in the Earth-Moon System

but does not extend beyond approximately $10R_{Moon}$, again in the range of low Lunar operations.

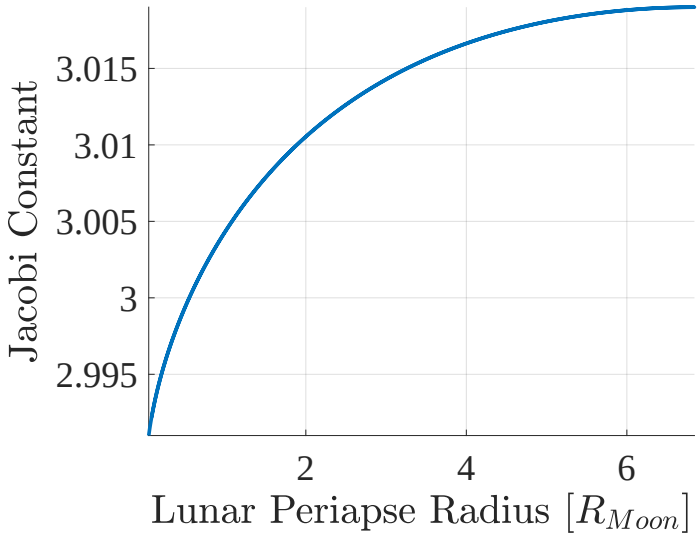

Figure 4.29.: Jacobi Constant Versus Periapse Radius for the P4HO1 Family in the Earth-Moon System

The stability characteristics in the P4HO1 and P4HO2 families are apparent in Figure 4.31. Evident from the figure, most orbits belonging to the P4HO1 or P4HO2 families are unstable with the exception of small groups of stable orbits.

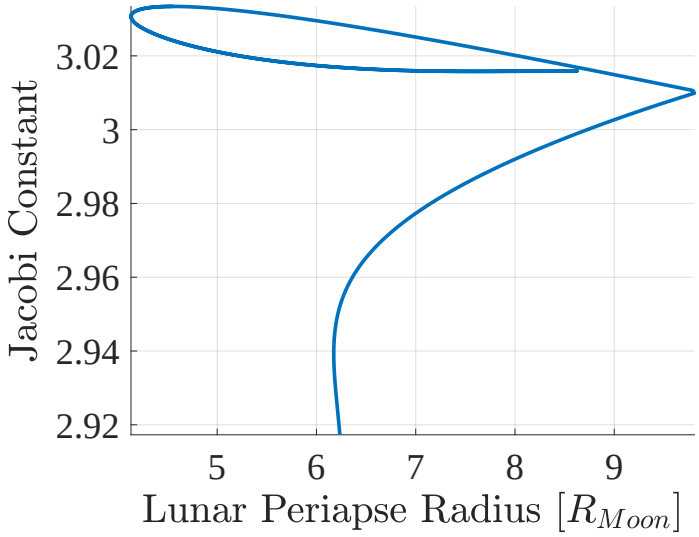

Figure 4.30.: Jacobi Constant Versus Periapse Radius for the P4HO2 Family in the Earth-Moon System

The P4HO1 family possesses a very brief section of stable orbits with periapse radii around $r_p \approx 3R_{Moon}$ and the P4HO2 Family possesses two small bands of unstable orbits between the periapse radii of $7R_{Moon}$ and $9R_{Moon}$. However, apart from these stable members, all other orbits in both families present unstable and stable subspaces. The P4HO2 family demonstrates a greater overall instability when compared to the P4HO1 family. This distinction is consistent with the time constants observed. Nearly all of the time constants are below 1 for the P4HO2 family while only a small section at low Lunar periapse radius in the P4HO1 orbits display desirable time constants. The low time constants in the P4HO1 family are reconciled with the apparently high stability indices by recalling that the P4HO1 family forms as a period-four bifurcation, thus, its period is four times greater than the originating bifurcating Halo orbit. Therefore, while the stability index is high, the deviation it predicts (in the linear sense) is distributed over the long period. Consequently, the stability index must be much greater than that of a lower period orbit to observe the same contemporaneous deviations from the reference. Because the P4HO2 family incorporates much greater stability indices, the extended period is overcome by

the instability in the orbit yielding fast departure characteristics. While the P4HO1 family fails to yield time constants below 1.5 for a majority of the family, members with desirable time constants do exist at and below $r_p \approx 0.2R_{Moon}$.

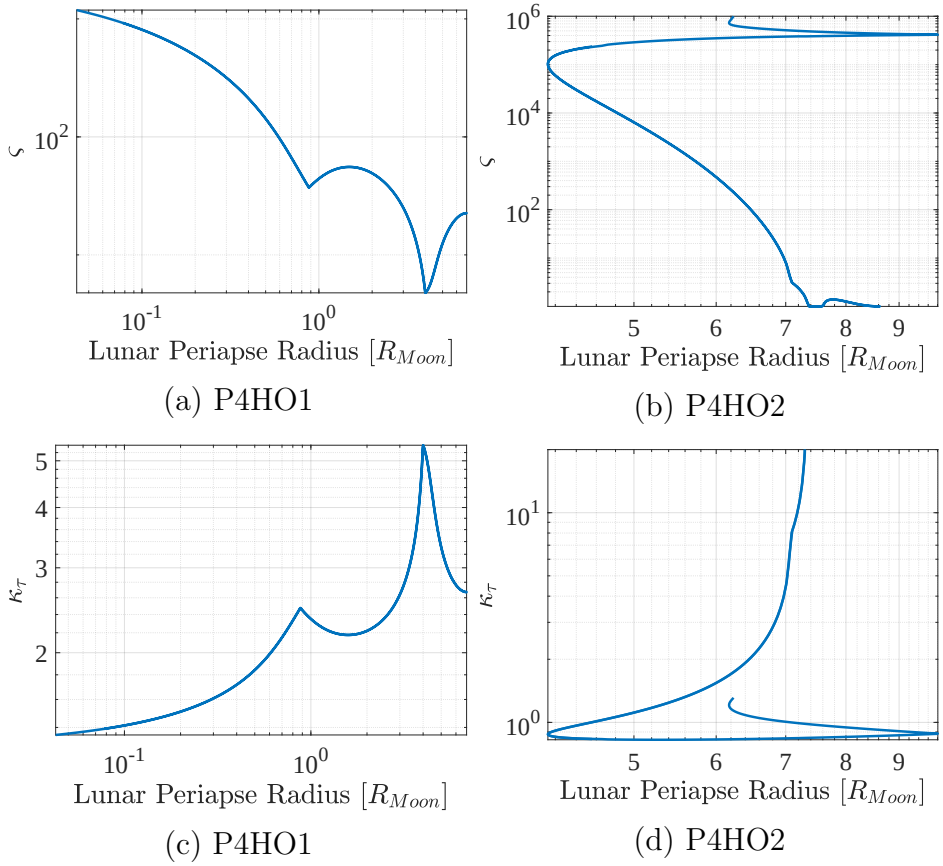

(a) P4HO1 (b) P4HO2

(c) P4HO1 (d) P4HO2

Figure 4.31.: Stability Characteristics of Earth-Moon Period-Four Halo Orbit Families

In summary, the P4HO1 and P4HO2 families of periodic orbits each offer candidate members yielding unstable invariant manifold structures with sufficiently low time constants. The P4HO1 family yields fewer of these members, but contains them at altitudes potentially beneficial for low-Lunar operations. The P4HO2 family, alternatively, is comprised of many unstable members, but at higher altitudes with respect to the Lunar surface.

4.2.10 Summary of Earth-Moon Periodic Orbit Stability Characteristics

Every Lunar-region orbit family in Table 4.1 offers unstable manifold structures except the Distant Retrograde Orbits (DROs). The Jacobi constant values observed for the unstable orbits among these families varies, but all include values around 3.0 for each family. The LPO, halo, P4HO1, and P4HO2 families include regions of stable orbits while the Lyapunov, axial, vertical and butterfly orbit families are comprised completely by unstable members for the sections included in this analysis. Time constant analysis demonstrates that not all unstable orbits yield desirable manifold departure rates. The $L1$ halo, L_2 halo, and P4HO1 orbit families include orbits with time constants greater than the 1.5 critical value. The families in Table 4.1 include substantial manifold structure for Lunar trajectory design. The manifold paths originating from the periodic orbits demonstrating fast manifold departure rates are now explored to determine available Lunar access geometry.

4.3 Lunar Access Characteristics

The invariant manifolds associated with the unstable periodic orbits yielding low time constants are investigated to determine their Lunar access characteristics. For the purpose of investigation, Lunar access is divided into two classes: (1) Lunar impact, and (2) insertion into Low Lunar Orbit (LLO).

4.3.1 Definition of Lunar Orbit Insertion Characteristics

Alongside the Lunar surface access capabilities, characteristics of the trajectories on the invariant manifolds regarding the insertion into Low Lunar Orbits (LLOs) are also desired. The surface of the Moon served as the surface of section for the Lunar impact analysis, but, for the LLO insertion investigation, a periapse surface of section

will be defined [16]. A periapse with respect to the Moon is defined as a state, $\mathbf{x}_p$, with position, $\mathbf{r}_p$, and velocity, $\mathbf{v}_p$, satisfying

$$(\mathbf{r}_p - \mathbf{r}_{Moon}) \cdot \mathbf{v}_p = 0, \tag{4.3}$$

$$\mathrm{v}_p^2 + (\mathbf{r}_p - \mathbf{r}_{Moon}) \cdot \ddot{\mathbf{r}}_p > 0. \tag{4.4}$$

Given the set of periapses corresponding to a trajectory on the invariant manifold associated with the unstable periodic orbit, the apse radii with respect to the Moon, inclination (i), and Jacobi constant values are determined. The radii and inclinations of the periapse points provide information on the possible two-body Lunar orbits a velocity-direction burn at that particular apse the spacecraft can insert into. Therefore, given the set of apse conditions available from a given periodic orbit family for a given integration time, the achievable two-body orbit altitudes and inclinations are known.

4.3.2 Lunar Impact Characteristics of Planar Orbit Families

Given the existence of unstable members in the Lyapunov and LPO families of periodic orbits, Lunar impact characteristics are sought for both families. As these families are planar, the impact latitude is fixed at 0°. Therefore, the remaining non-zero quantities are determined for the unstable members of the LPO and Lyapunov families. The unstable members of the planar orbit families with $\kappa_\tau \leq 1.5$ are depicted in red in Figure 4.32. The time constant restriction removes candidate orbits from the LPO and L_2 Lyapunov orbit families. The large amplitude L_2 Lyapunov orbits, while unstable, have prohibitively low time constants removing the L_2 Lyapunov orbits with sub-surface Lunar periapse radii. Conversely, the L_1 Lyapunov orbits retain sufficiently low time constants throughout. However, for the current analysis, trajectories are ignored that contain Lunar periapse radii less than the radius of the Moon. Trajectories on the unstable manifolds from the low time constant periodic

orbits are propagated forward in time for 10 nondimensional time units equivalent to approximately 43 days. The impact conditions of the trajectories are recorded.

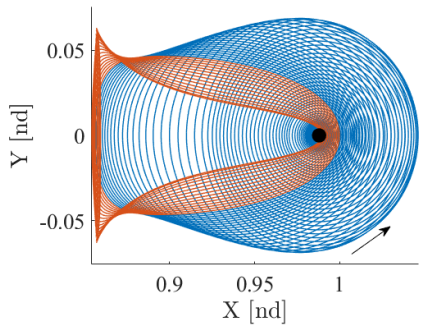

(a) Low Prograde Orbits

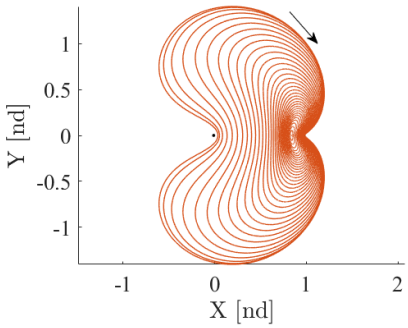

(b) L_1 Lyapunov Orbits

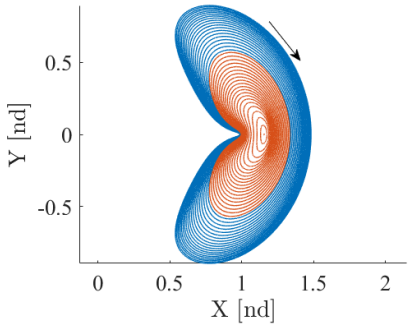

(c) L_2 Lyapunov Orbits

Figure 4.32.: Planar Orbit Families where Red Indicates Unstable Orbits with $\kappa_\tau \leq 1.5$ and Blue Indicates $\kappa_\tau > 1.5$

The Lunar impact characteristics of interest for the planar families are the longitude of impact, impact angle, impact speed, TOF, and Jacobi of the impacting trajectory as the impact latitude, λ, will always be 0° for planar trajectories. Recall, Lunar impact is defined as $r_{13} = R_{Moon}$ where $R_{Moon} = 1737.4$ km.

Low Prograde Orbits

Beginning with the LPO family of periodic orbits, the time-of-flight to impact for the LPOs as a function of φ is shown in Figure 4.33. The data points are further colored by the Jacobi constant of the corresponding trajectory. From the plot, it is

clear that the LPO orbits do not present impact locations at all possible longitude values within the time frame investigated. Figure 4.34 presents trajectories appearing to reach the Lunar surface at 0 days. These points correspond to the LPO family mem-

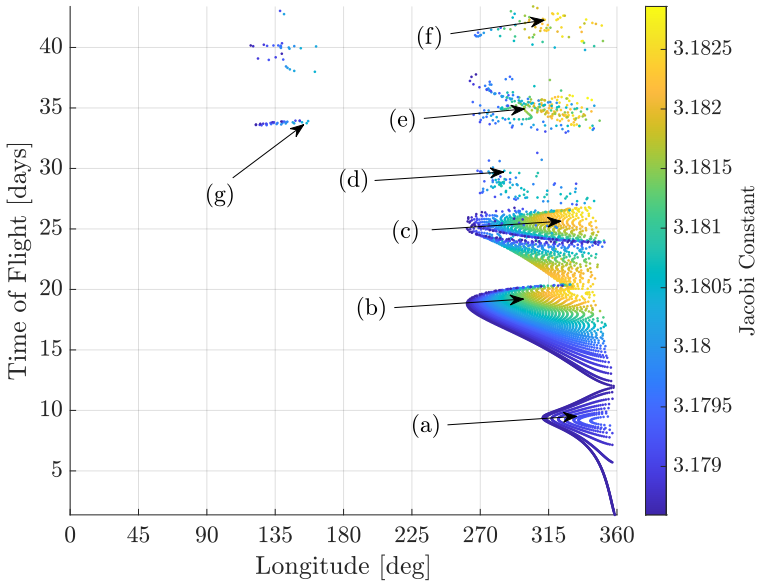

Figure 4.33.: Time of Flight Versus Impact Longitude for Unstable Manifolds Associated with Earth-Moon Low Prograde Orbits Colored by Jacobi Constant Value with Selected Points

bers that have periapse radii approximately equal to the Lunar radius and, therefore, have manifolds that nearly instantaneously impact the Moon after departure. At low times-of-flight, i.e., within 30 days, LPO manifold impact are restricted to longitudes in quadrant IV ($270° \leq \varphi \leq 360°$). This fourth quadrant behavior is consistent with the orbit geometry observed in Figure 4.32(a); the LPO family members are descending in quadrant IV before reaching a perilune at $\varphi = 0°$, thus, perturbations along the trajectory lowering periapse radius will lead to quadrant IV impacts. At higher TOFs, impacts are observed at around 135° longitude. However, no impacts are found in the large sections on the ranges $\varphi \in [0°, 125°]$ or $\varphi \in [145°, 270°]$ at any time investigated. These ranges correspond roughly to the first and third quadrants. For impact in the first and third quadrants, apoapses mainly occur in the fourth and second quadrants, respectively, but, as discussed by Davis, apoapses in

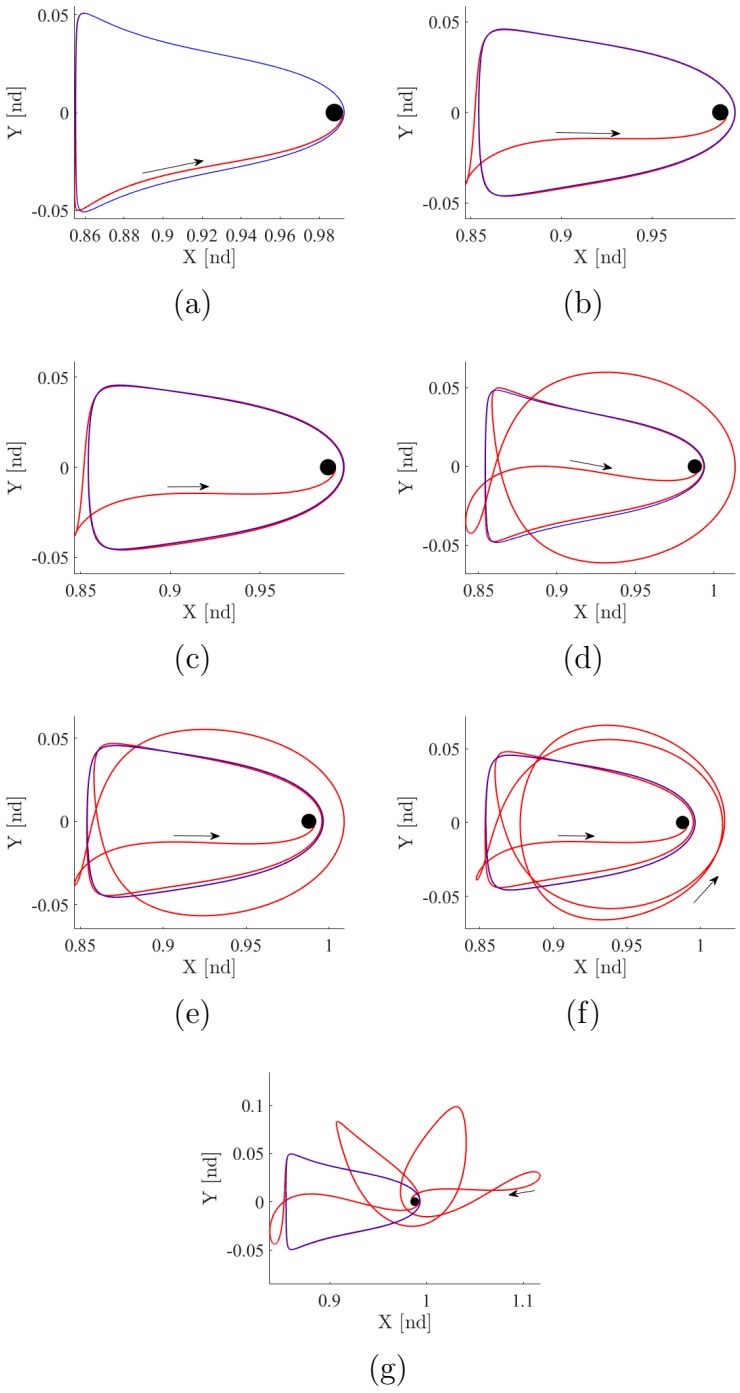

Figure 4.34.: Selected Trajectories from Figure 4.33 where the Blue Trajectories are the Periodic Orbits and the Red Trajectories are on the Manifolds

the even-numbered quadrants lead to an increase in periapse radius, in general, due to tidal effects [16]. Therefore, fewer impacts at low times-of-flight in the first and third quadrants are expected. Several points representing different geometry types are selected in Figure 4.33 and the corresponding trajectories are plotted in Figure 4.34. The trajectories in Figures 4.34(a), 4.34(b), and 4.34(c) perform 0, 1, and 2 revolutions about the Moon before impact, respectively. These revolution counts correspond to the lobes observed at 10, 20, and 25 days in Figure 4.33, respectively. At TOFs beyond 25 days, more complex geometry is observed as evident in Figure 4.34(d) where an additional high periapse-radius revolution emerges. Again, revolutions are added in the geometries seen in Figures 4.34(e) and 4.34(f). The unstable manifold trajectories in Figures 4.34(a) to 4.34(f) all impact in the fourth quadrant congruent with the baseline geometry of the LPO family; however, the trajectory observed in Figure 4.34(g) presents a departure from this trend and impacts in the second quadrant around $\varphi = 150°$. The trajectory in Figure 4.34(g) performs several revolutions about the Moon, reaches a final apoapse in quadrant one before impacting in quadrant two. The multi-revolution characteristic of this geometry indicates why it is only observed at higher TOF values, as the trajectory requires time to evolve to reach the quadrant one apoapse. Furthermore, this hints that more quadrant two impacts may exist at even higher times of flight. While only a small range of Jacobi constants are observed in the unstable LPO family members, stratification in impact locations is observed. Lower Jacobi constant values present a greater number of impacts as well as a greater range in available impact longitudes particularly at lower times-of-flight.

In addition to the Jacobi constant coloration observed in Figure 4.33, plots colored by impact speed and impact angle are presented in Figures 4.35(a) and 4.35(b), respectively. As predicted by the impact speed bounds, the impact speeds show little variation and lie between 2.324 and 2.325 km/s. Additionally, the lower Jacobi constant trajectories yield higher impact velocities, as expected. No impacts are observed with impact angles below 50° indicating most trajectories are impacting

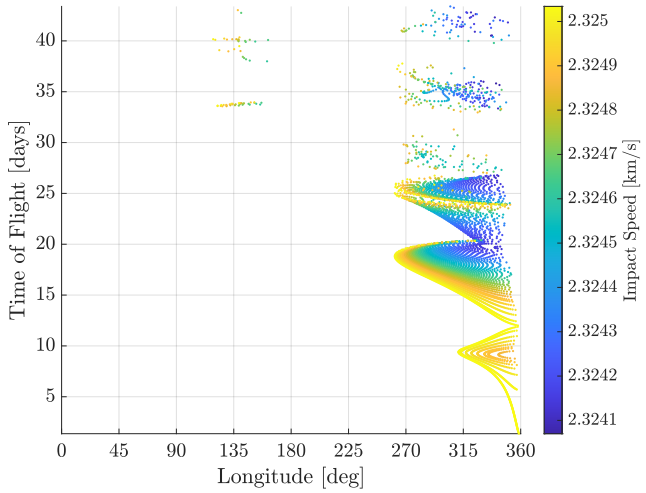

(a) Impact Speed

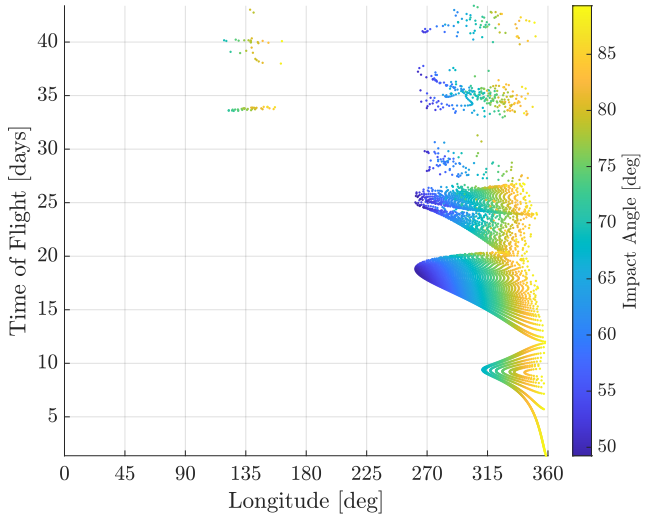

(b) Impact Angle

Figure 4.35.: Impact Speed and Angle for Unstable Manifolds Associated with Earth-Moon LPO Family

with large velocity components nearly tangent to the Moon's surface. This behavior is congruent with the fact that most impacts occur in quadrant IV resulting from periapse lowering maneuvers; as periapse is lowered, a tangency condition is reached with the lunar surface and many of the LPO impact trajectories do not drop much further than this condition. Figure 4.36 demonstrates this evolution from near tangent impacts at high longitudes evolving into more vertical impacts at the higher-energy

lower-latitude impacts. The trajectory impacting at a high impact angle (yellow) is

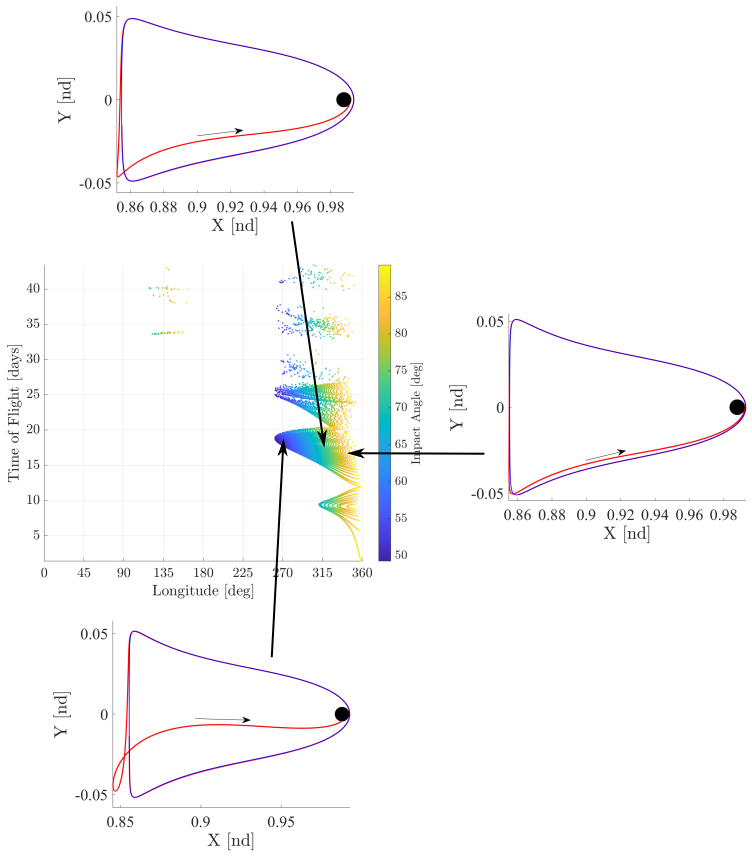

Figure 4.36.: Impact Evolution for LPO Unstable Orbit Manifolds Example

close to the tangency at periapse and this angle increases as the periapse drops farther below the surface and the point moves toward the darker blue color.

The Low Prograde Orbits (LPOs) present low time of flight impact trajectories for impacts in quadrant IV and several higher TOF impacts for quadrant II impacts. However, the LPOs do not offer impacts in quadrants I or III for the time interval investigated. Furthermore, the LPO manifold structures only present impact angles greater than 50° and speeds around 2.32 km/s. However, the low time-of-flight transfers may offer ideal conditions for a staging orbit with fast access to the lunar surface.

Lyapunov Orbit Families

A similar process to that of the LPO family is followed in the analysis of the L_1 and L_2 Lyapunov orbit families in the Earth-Moon system. Inspecting the L_1 family first, Figure 4.37 presents the impact condition TOFs versus longitudes colored by Jacobi constant for unstable manifolds associated with the L_1 Lyapunov orbit family. The impact conditions presented in Figure 4.37 represent a departure from the

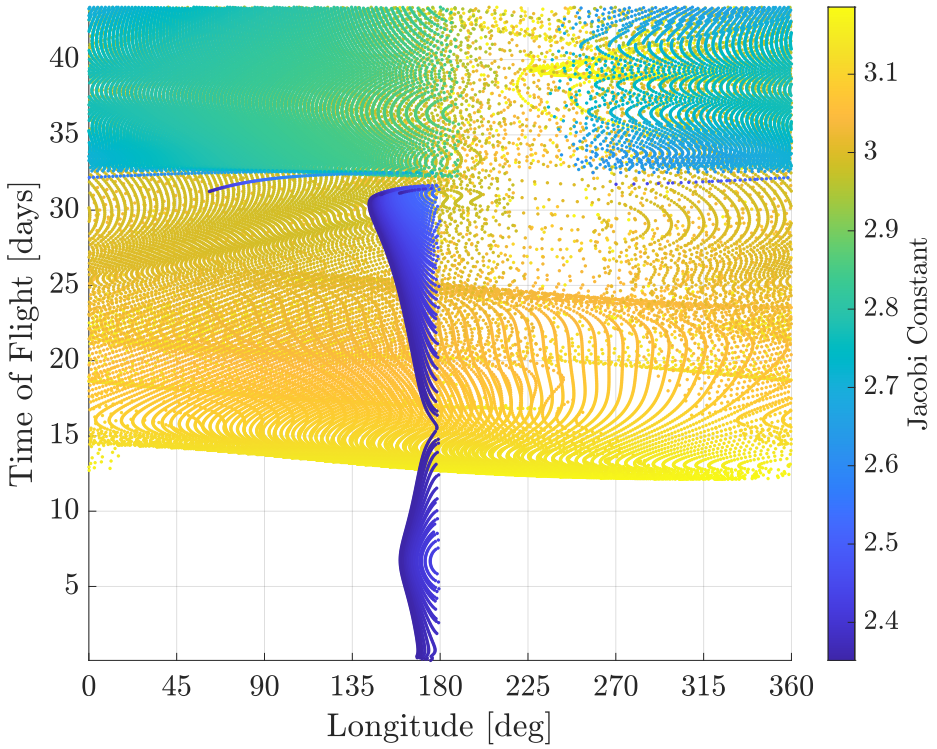

Figure 4.37.: Time of Flight Versus Impact Longitude for Unstable Manifolds Associated with Earth-Moon L_1 Lyapunov Orbits Colored by Jacobi Constant Value

behavior observed in the LPO family. The dark streak around 180° longitude and extending from $TOF \approx 0$ days to $TOF \approx 33$ days originates from the large amplitude, high energy L_1 Lyapunov orbits with periapse radii approximately equal to the Lunar radius. The low TOF impacts on this streak represent the trajectories departing very near periapsis and the high TOF impacts represent those that depart farther back along the orbit. Impacts are observed starting around 13 days at Jacobi constant

values exceeding 3.1 covering all longitudes. Therefore, unlike the LPO family, the L_1 Lyapunovs present candidate trajectories impacting in all four quadrants at all longitudes. Furthermore, the spanning of longitudes occurs at nearly all Jacobi constants greater than 3. A gap is observed in the Jacobi constant values around 2.8 spanning quadrant III from approximately 33 days and higher. This gap shows up for the low Jacobi constant orbits as the geometry leads to impacts in the second and fourth quadrants as shown in Figure 4.38. The two trajectories plotted in Figure

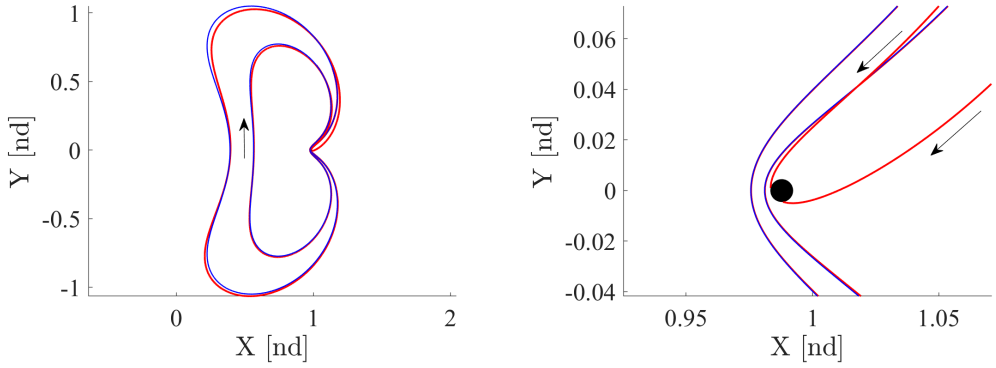

(a) Impacting Trajectories with Orbits (b) Close-Up on Impact

Figure 4.38.: Example Demonstrating Quadrant III Avoidance of Large Lyapunov Impacting Manifolds

4.38 represent points around 35 day TOF on either side of the gap observed in Figure 4.37. While the gap exists for low Jacobi constant orbits, Figure 4.37 demonstrates that the orbits with Jacobi constants greater than 3 span all TOF values and Longitudes of impact. This span of available impact longitudes for orbits with high Jacobi constant values stems from these orbit being farther away from the Moon and high TOF tolerances. Trajectories originating from these orbits are allowed to evolve and develop complex geometry allowing for impacts at a large number of longitudes. Figure 4.39 demonstrates an example of this complex geometry; the trajectory impacts in quadrant III at a similar TOF to the trajectories shown in Figure 4.38.

The impact speeds and angles for the L_1 Lyapunov family are additionally investigated. Figures 4.40(a) and 4.40(b) display the impact data colored by impact

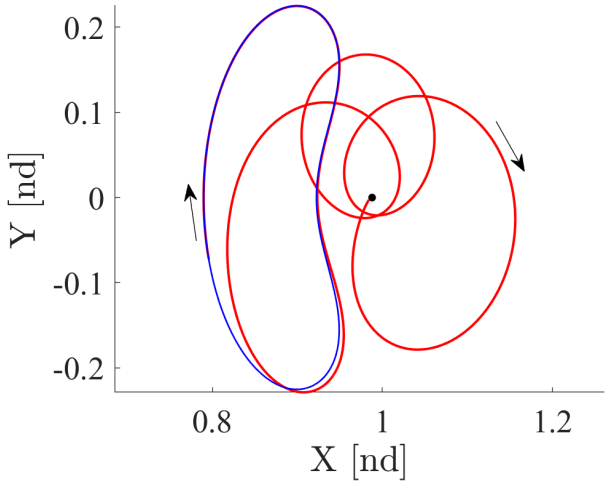

Figure 4.39.: Example of Complex Geometry from L_1 Earth-Moon Lyapunov Orbit Unstable Manifold Impacting at $\varphi = 225°$ After 37 Days

speed and angle, respectively. Similar to the LPO investigation and predicted by the

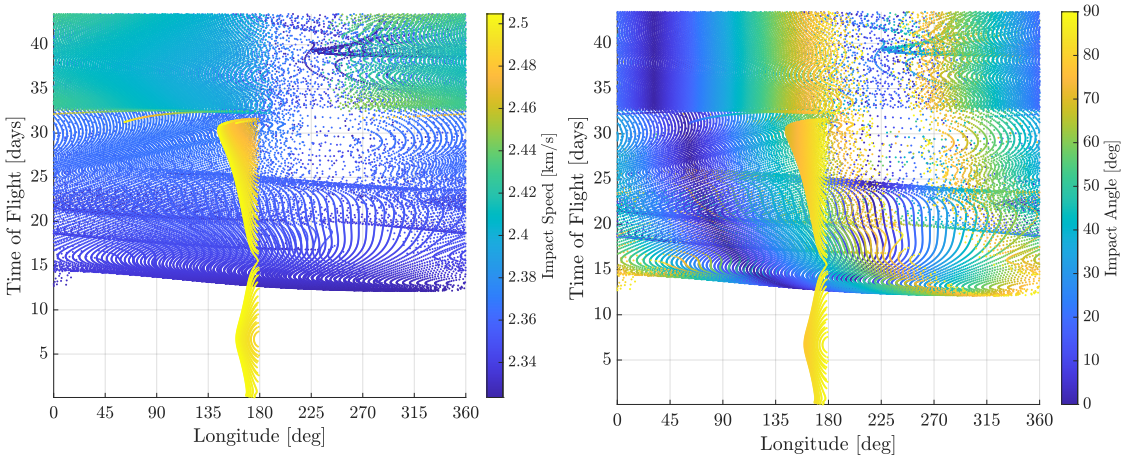

(a) Impact Speed

(b) Impact Angle

Figure 4.40.: Impact Speed and Angle for Unstable Manifolds Associated with Earth-Moon L_1 Lyapunov Family

theoretical bounds, the impact speeds are directly correlated to the Jacobi constant of the impacting trajectories. The L_1 Lyapunov impacts possess impact speeds from approximately 2.33 km/s to 2.5 km/s, slightly higher than those of the LPO orbits.

Unlike the LPO family, the L_1 Lyapunov impacts span impact angles from 0° to 90°. Clear bands are observed in the impact angle plot demonstrating smooth evolution across impact longitudes in impact angle. At low TOFs, minimal impact angles are observed near 135° impact longitude while maximal impact angles are observed near 360°. Example trajectories from these two impact longitudes are shown in Figure 4.41.

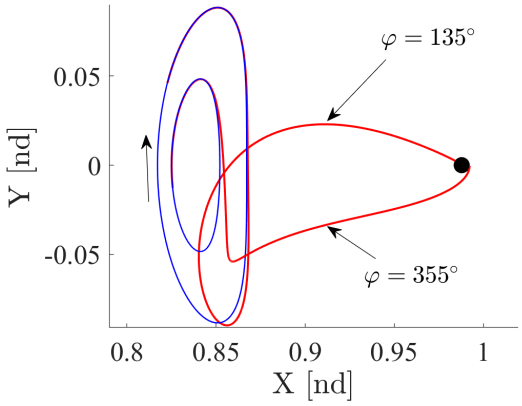

Figure 4.41.: Impacting Trajectory Examples for 15 Day TOF from Earth-Moon L_1 Lyapunov Orbits

The L_1 Lyapunov orbit family presents a large number of impacting trajectories spanning all impact longitudes for all times of flight investigates. Furthermore, while orbits at a lower Jacobi constant do not possess impacting trajectories at all longitudes for the TOFs investigated, orbits at and above a Jacobi constant of 3.0 do span the longitudes at all TOFs greater than 15 days. Therefore, the L_1 Lyapunov family presents a large amount of opportunities for impacting trajectories at Jacobi constants common in Lunar region orbits.

The impact conditions of the Earth-Moon L_2 Lyapunov orbits are shown in Figure 4.42. Similar to the L_1 Lyapunov family, the L_2 Lyapunovs display stratification in the Jacobi constant as trajectories with higher Jacobi constants constitute a larger percentage of the the low TOF impacts. Because the large amplitude L_2 Lyapunovs possess low time constants and are excluded from the analysis, the streak of low TOF,

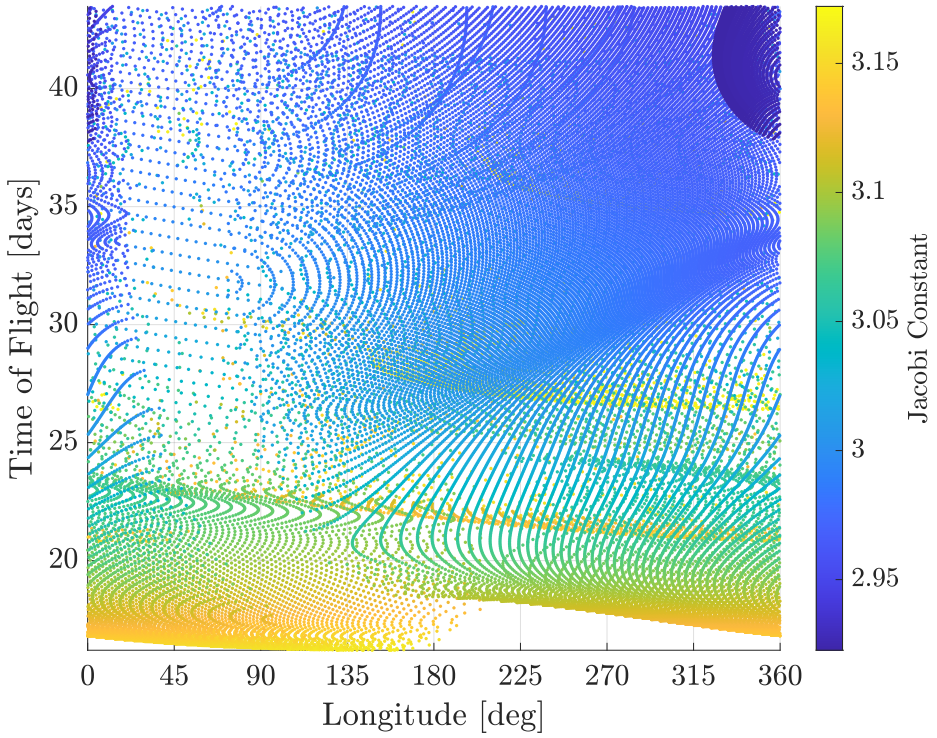

Figure 4.42.: Time of Flight Versus Impact Longitude for Unstable Manifolds Associated with Earth-Moon L_2 Lyapunov Orbits Colored by Jacobi Constant Value

high Jacobi constant impact points is absent from the L_2 Lyapunov plot, unlike the L_1 Lyapunov graph in Figure 4.37. Gaps appearing at lower Jacobi constant values in quadrant 1 for the L_2 Lyapunov orbits are similar in nature to the gaps observed in quadrant 3 for the L_1 Lyapunovs. Figure 4.43 demonstrates two example orbits from either side of the gap. The larger amplitude L_2 Lyapunov orbits impact in quadrants II and IV generating the sparsity pattern observed in Figure 4.42. This sparsity, however, declines as the TOF is increased. Overall, the L_2 Lyapunov orbits present impacts with similar TOFs to the L_1 family at all longitudes.

The impact speed and impact angle plots for the L_2 Lyapunov orbits are shown in Figures 4.44(a) and 4.44(b), respectively. The impact speed of the unstable manifolds associated with the L_2 Lyapunov orbits center around 2.36 km/s, lower than those of the L_1 Lyapunov family congruent with the relative Jacobi constant values. Furthermore, the impact speeds vary less than the L_1 Lyapunov family. The impact angles in

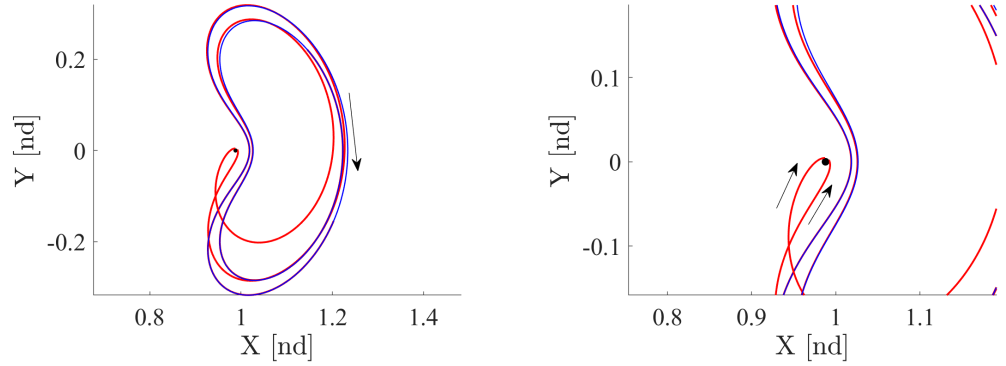

(a) Impacting Trajectories with Orbits (b) Close-Up on Impact

Figure 4.43.: Example Demonstrating Quadrant I Avoidance of L_2 Lyapunov Impacting Manifolds

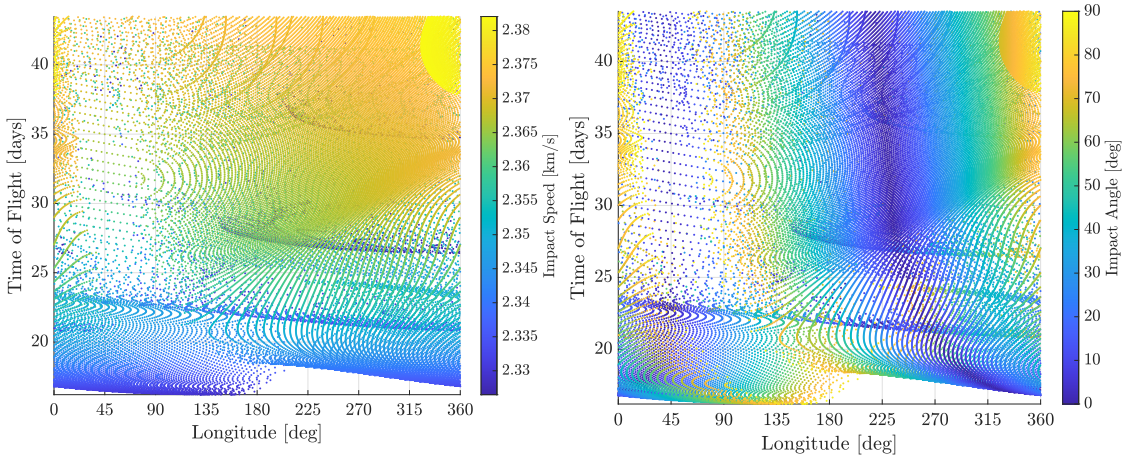

(a) Impact Speed (b) Impact Angle

Figure 4.44.: Impact Speed and Angle for Unstable Manifolds Associated with Earth-Moon L_2 Lyapunov Family

Figure 4.44(b) demonstrate vertical stratification with minimal impact angles occurring around 50° and 250°. Due to the vertical stratification of the impact speeds and the horizontal stratification of the impact angle, combinations of any nearly observed impact angle and speed exist.

The impact characteristics of the L_2 Lyapunov orbits are similar to those of the L_1 Lyapunov orbits in most respects. At TOFs larger than $\approx$ 15 days, all longitudes

are covered at nearly all Jacobi constants. The impact speeds are tightly coupled to the Jacobi constants and therefore both quantities present similar plots. The L_2 Lyapunov orbits, like the L_1 family, present impacts at all impact angles at any time of flight. However, impact angle and longitude are not independent and therefore cannot be constrained independently. Ultimately, the L_2 Lyapunov orbits offer an abundance of impact opportunities to be leveraged in Lunar access mission design.

4.3.3 Low Lunar Orbit Access Characteristics of Planar Orbit Families

The low Lunar orbit access characteristics of the planar orbit families are investigated via the periapse locations (as defined in Equations (4.3) and (4.4)) of the unstable manifolds associated with the unstable members of the LPO, L_1 Lyapunov, and L_2 Lyapunov orbit families. The unstable manifolds of the unstable orbits shown in Figure 4.32 are propagated for approximately 43 days and locations of periapses with respect to the Moon are recorded and, similarly to the impact analysis, orbits with sub-surface periapse radii are ignored. Because the LPO, L_1 Lyapunov, and L_2 Lyapunov families are planar, all periapses will occur with $\lambda = 0$ and, thus, latitude is not presented.

Low Prograde Orbits

The locations of periapses on the unstable manifolds associated with the LPO family near to the Moon are shown in Figure 4.45. By inspection, it is evident that the LPO family presents periapse locations at all altitudes extending to around 50,000 km. Furthermore, the Jacobi constant coloring indicates the existence of periapses at nearly all available altitudes for all Jacobi constant values. The various "arms" of the periapse locations shown in Figure 4.45 represent different trajectory geometries; several of these geometries are highlighted in Figure 4.46. Figures 4.46(a), 4.46(b), and 4.46(c) are the 3, 2, and 1 revolution members of a similar trajectory evolution, respectively, while Figure 4.46(d) presents a departure from this geometry

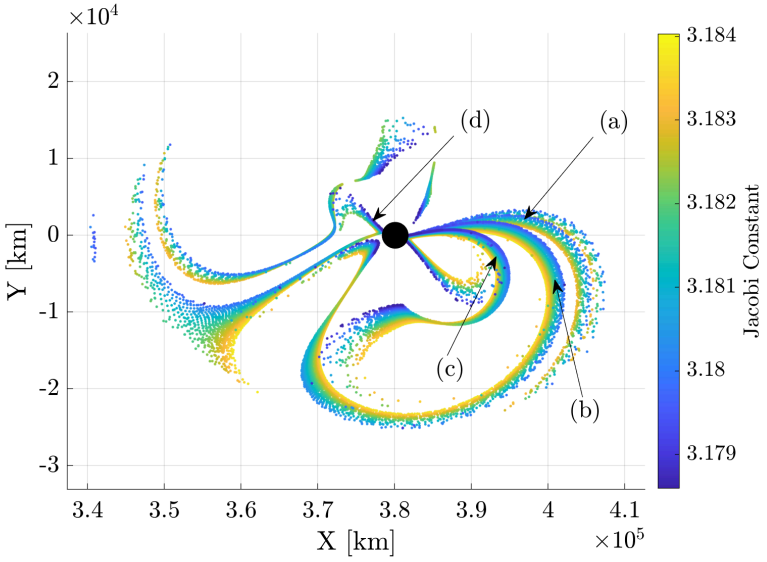

Figure 4.45.: Lunar Periapse Locations for Unstable Manifolds Associated with the LPO Family in the Earth-Moon System

and resembles the impact trajectory observed in Figure 4.34(g). The existence of groups of geometry indicates that the flow is less sensitive to the initial condition for these apse trajectories, i.e, the existence of nearby orbits demonstrating similar behavior provides possible slack for initial conditions to yield similar geometry.

The time of flight is visualized as a function of the altitude with respect to the Moon at the periapse locations in Figure 4.47(a) with a closer inspection of lower altitudes in Figure 4.47(b). The nearly vertical sections of low TOF apse locations near altitudes of 0 km and 50,000 km correspond to the left and right apses of the periodic orbit family members. As time of flight increases, a greater amount of variation and unpredictability is observed in the periapse altitudes. Periapses are observed at all times of flight for altitudes less than 3000 km, but, at altitudes above 3000 km, times of flight must exceed around 17 days for the orbits investigated. As time of flight is increased further, higher periapse altitudes are possible with values of approximately 25,000 km becoming available after 43 days. The higher Jacobi constants dominate lower altitudes at higher times of flight due to the tendency of

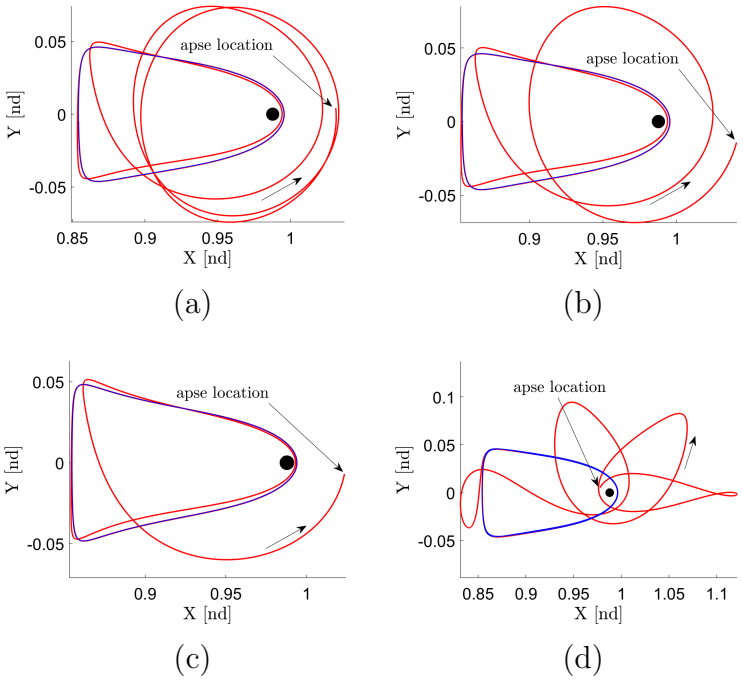

Figure 4.46.: Sample Geometries of LPO Unstable Manifold Periapses from Figure 4.45

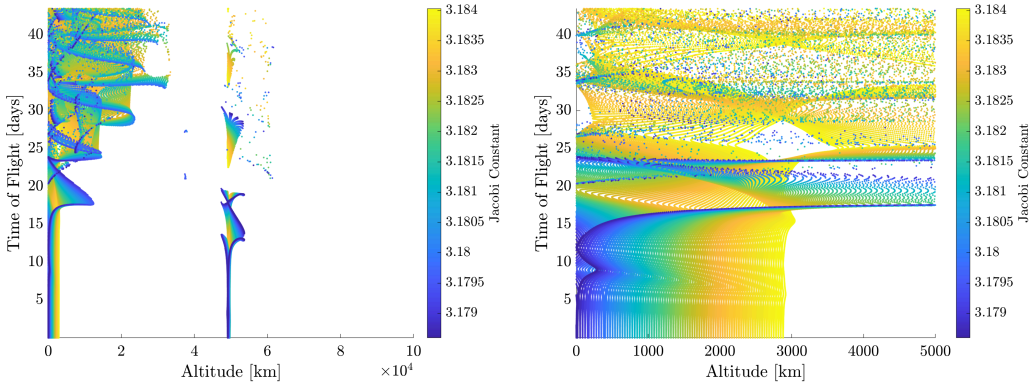

Figure 4.47.: Lunar Periapse Locations for Unstable Manifolds Associated with the LPO Family in the Earth-Moon System

lower Jacobi constant orbits to depart the Lunar region as the propagation time is increased. However, as the variation in Jacobi constant across the LPO family is

small, candidate trajectories at all available altitudes exist for the range of Jacobi constants spanned by the family.

The LPO apse analysis demonstrates extensive altitude range across all Jacobi constants for the orbits analyzed. This range indicates that the LPO family may provide desirable LLO insertion characteristics to a mission design profile. For insertion altitudes less than 3000 km altitude, low TOF transfers are available for all Jacobi constant values represented in the LPO family. At higher altitudes, longer TOF transfers are available, again, at all Jacobi constants in the family.

Lyapunov Orbit Families

Similar to the LPO investigation, the locations of apses originating from the unstable manifolds of the L_1 Lyapunov orbits are shown in Figure 4.48. The apses near

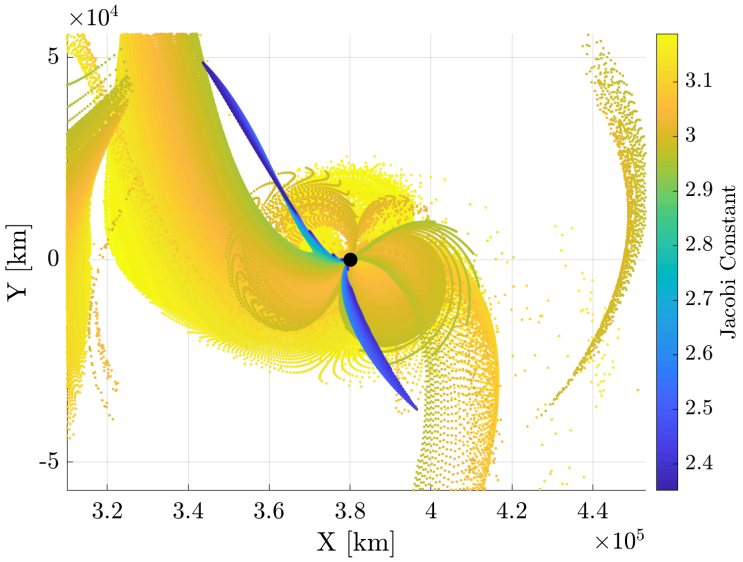

Figure 4.48.: Lunar Periapse Locations for Unstable Manifolds Associated with the L_1 Lyapunov Family in the Earth-Moon System

the Moon are dominated by higher Jacobi constant values as evident by the larger number of yellow points. The trajectories with Jacobi constants less than 3.0 tend to

depart the Lunar region as observed in the LPO investigation. However, periapses at all low altitudes are observed for the Jacobi constants represented in the L_1 Lyapunov family. Figure 4.49 presents the TOF versus periapse altitude for the L_1 Lyapunov manifold trajectories. Noticeably, L_1 Lyapunov orbits present a denser covering of

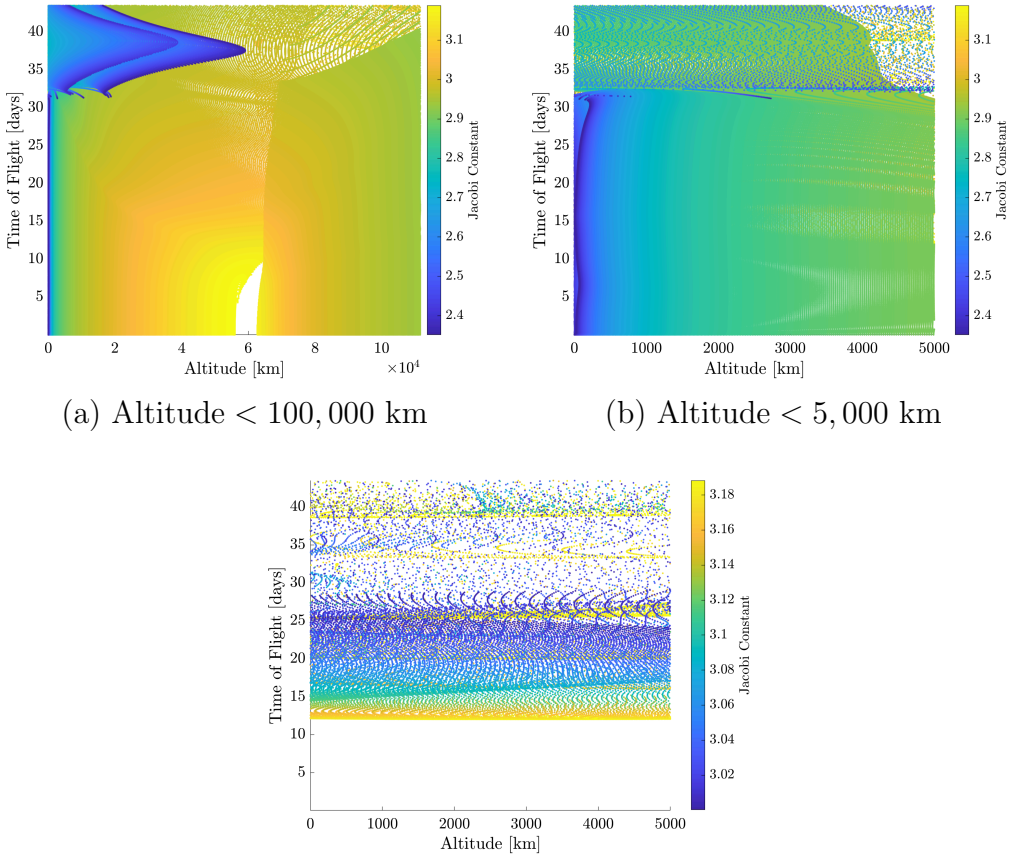

(a) Altitude $< 100,000$ km

(b) Altitude $< 5,000$ km

(c) Altitude $< 5,000$ km, $J > 3.0$

Figure 4.49.: Lunar Periapse TOF Versus Altitude for the Unstable Manifolds Associated with the Earth-Moon L_1 Lyapunov Family

TOFs and altitudes compared to the LPO family. Nearly all TOF and altitude combinations are represented except for a gap at $60,000$ km altitude for TOF < 10 days. In the sub-5000 km altitude plot in Figure 4.49(b), low Jacobi constant trajectories provide periapses at all altitudes and TOF values. Figure 4.49(c) removes the trajectories with $J < 3.0$ from Figure 4.49(b) to allow inspection of the high Jacobi

constant periapses. This filtering demonstrates that, while apses at all the Jacobi constant values greater than 3.0 exist for all altitudes investigated, transfer times of greater than approximately 12 days are required. These large TOF values are primarily a result of the high Jacobi constant orbits being farther in position space from the Moon than the lower Jacobi constant orbits as observed in Figure 4.12.

The apse locations presented by the L_1 Lyapunov family offer substantial LLO insertion opportunities. At all Jacobi constant values included in the analysis, these opportunities exist at all low altitudes and indicate usefulness for a wide variety of low Lunar operations.

The L_2 Lyapunov orbit periapse locations are shown in Figure 4.50. Similar to

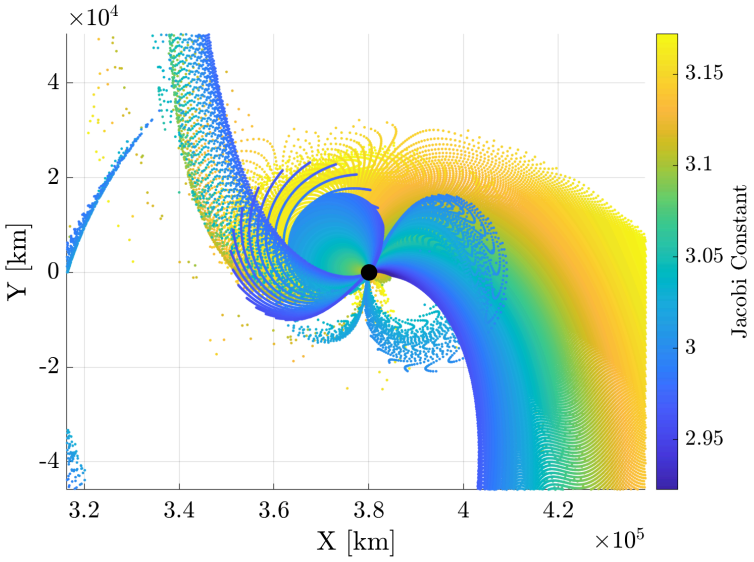

Figure 4.50.: Lunar Periapse Locations for Unstable Manifolds Associated with the L_2 Lyapunov Family in the Earth-Moon System

the L_1 Lyapunov family figure, periapses are observed spanning a large range of Lunar radii and Jacobi constant values. Furthermore, a larger amount of low Jacobi constant apses are observed in the low Lunar vicinity compared to the apses of the invariant manifolds associated with the L_1 Lyapunov family. The time-of-flight to periapse versus the periapse altitude plots for the L_2 Lyapunov manifold apse states

are shown in Figure 4.51. Periapse conditions are observed at nearly all altitudes for

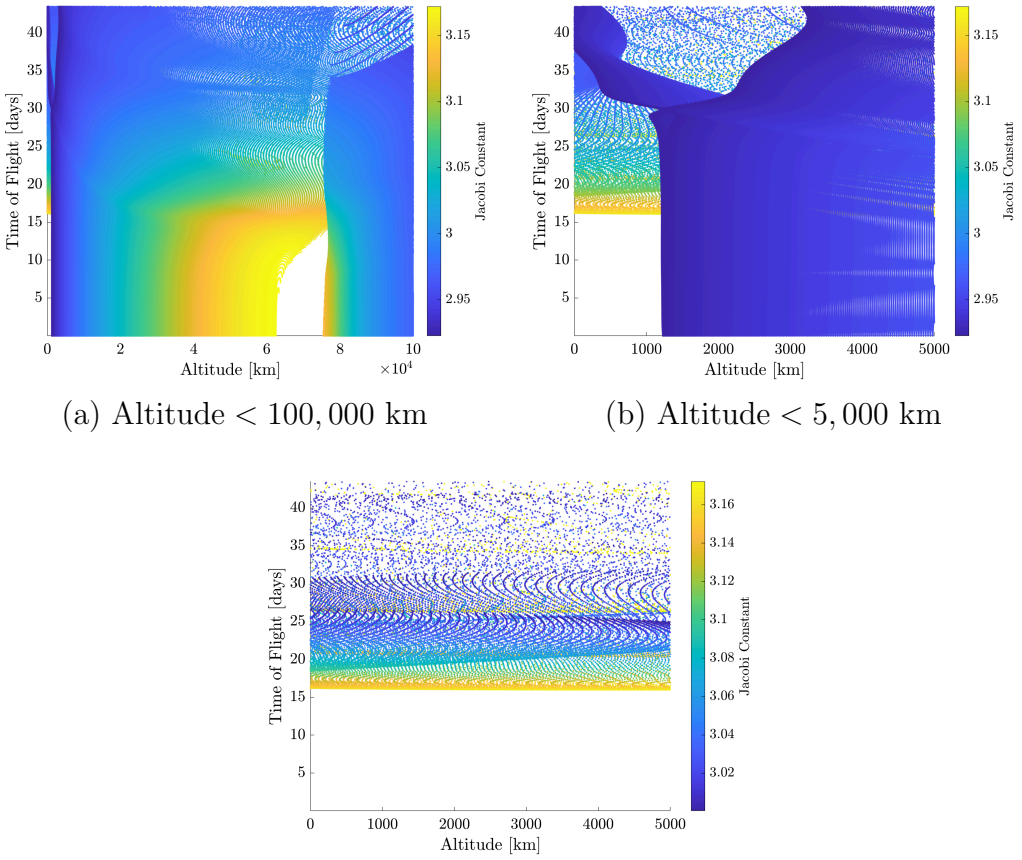

(a) Altitude $< 100,000$ km

(b) Altitude $< 5,000$ km

(c) Altitude $< 5,000$ km, $J > 3.0$

Figure 4.51.: Lunar Periapse TOF Versus Altitude for the Unstable Manifolds Associated with the Earth-Moon L_2 Lyapunov Family

all times-of-flight, similar to the characteristics observed in the L_1 Lyapunov family. Because of the low time constants of the large amplitude L_2 Lyapunov orbits, low time-of-flight periapses with low altitudes are not found, contrary to what is observed in the L_1 Lyapunov family. Therefore, for insertions into LLOs with Altitude < 1200 km required TOFs greater than 15 days. Beyond this 15 day mark, apse conditions are observed at all Jacobi constant values, but lower Jacobi constant trajectories demonstrate higher TOFs to reach the same altitude of the lower Jacobi constant conditions.

Ultimately, the periapse portrait provided by the unstable manifolds associated with the L_2 Lyapunov orbits is similar qualitatively to that of the L_1 Lyapunov family. A large number of periapse conditions are available spanning Lunar altitudes exceeding $100,000$ km. These conditions, furthermore, occur at Jacobi constants ranging from 2.8 to 3.16.

4.3.4 Lunar Impact Characteristics of Spatial Orbit Families

The Lunar impact characteristics of the spatial orbit families are investigated similarly to the planar families. However, while the planar nature of the Lyapunov and LPO families allows for the removal of impact latitude as a quantity of interest, the spatial parameters permit no such simplification. Therefore, trajectories on the unstable manifolds associated with each periodic orbit in the spatial families presenting a sufficiently small time constant are propagated through 10 nondimensional time units ($\approx$ 43 days) or until an impact condition is reached, similar to the planar investigation, but unlike the planar investigation, the latitude of impact is recorded in addition to the longitude, impact angle, and impact speed.

Halo Orbit Families

The L_1 and L_2 halo orbit families each contain unstable members with sufficiently low time constants, i.e. $\kappa_\tau < 1.5$. These periodic orbits are pictured in Figure 4.52 colored corresponding to the stability characteristics. In both families, the sections of orbits with $\kappa_\tau > 1.5$ arise as the sections of unstable orbits, as seen in Figures 4.16 and 4.17, surrounded by a band of unstable orbits with high time constants. However, as evident in Figure 4.52, both families present a substantial number of unstable periodic members with time constants indicating potentially useful unstable manifold structures. Trajectories on these manifolds associated with the unstable L_1 and L_2 halo orbits are propagated for approximately 43 days and the impact conditions are determined.

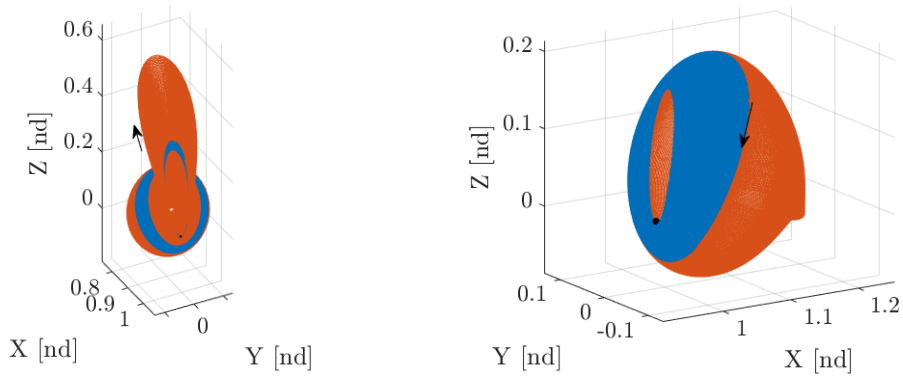

(a) L_1 (b) L_2

Figure 4.52.: L_1 and L_2 Halo Orbit Families where Red Indicates Unstable Orbits with $\kappa_\tau < 1.5$ and Blue Indicates $\kappa_\tau > 1.5$

Not all sufficiently unstable L_1 halo orbits yield Lunar impacting manifold structures. Figure 4.53 presents the L_1 halos colored by the presence of unstable manifolds that impact the Moon. Noticeably, many of the orbits near the Moon fail to yield

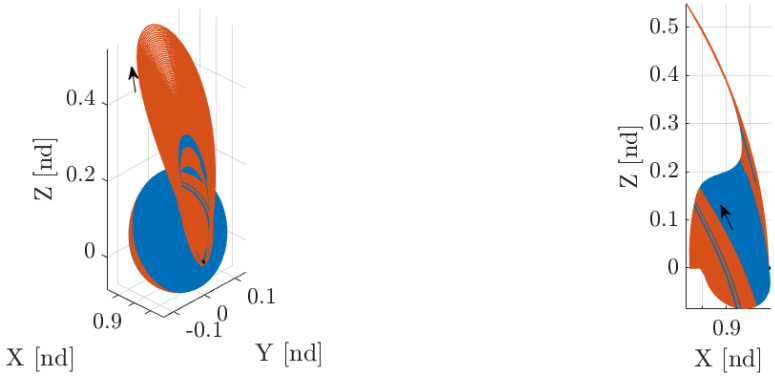

(a) (b)

Figure 4.53.: Unstable L_1 Halo Orbits with Manifold Structures Impacting the Moon Within 43 Days

impacting manifolds. However, a large portion of the halo orbits near the planar bifurcation with the L_1 Lyapunov orbits present impacting manifolds. The times-of-flight and longitudes, φ, of the impact conditions associated with these impacting

manifolds are presented in Figure 4.54. The impacts span Jacobi constant values

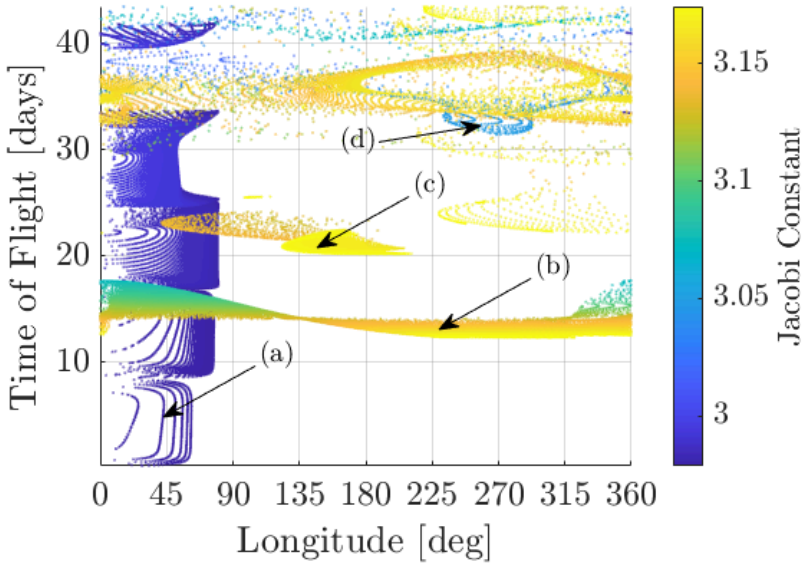

Figure 4.54.: Time of Flight and Longitude of Impact Conditions for Unstable Manifolds Associated with L_1 Halo Orbits

from $J \approx 2.97$ to $J \approx 3.16$ presenting a limited range, but this range spans the Jacobi constants most commonly observed in the Lunar region periodic orbits of interest. A column of low Jacobi impacts is observed at longitudes from $\varphi = 0°$ to $\varphi = 80°$; this column represents impacts originating from the large z-amplitude orbits observed in Figure 4.53(a). These impacts occur in the first quadrant congruent with the geometry of the orbits observed and, thus, require little deviation from the reference periodic orbit. Near the 15 day time-of-flight mark, a band exists covering all impact longitudes and includes impacts at Jacobi constants ranging from $J = 3.08$ to $J = 3.16$ Smaller groups occur at higher TOF values, but, beyond 35 days, scattering is observed indicating less structured motion. Figure 4.55 presents several example geometries corresponding to those marked in Figure 4.54. Clearly, due to the large variation in geometry across the halo family, many different transfer geometries are observed. Interestingly, the simple geometry present in Figure 4.55(b) corresponds to the band observed near 15 days in Figure 4.54 providing simple access to all Lu-

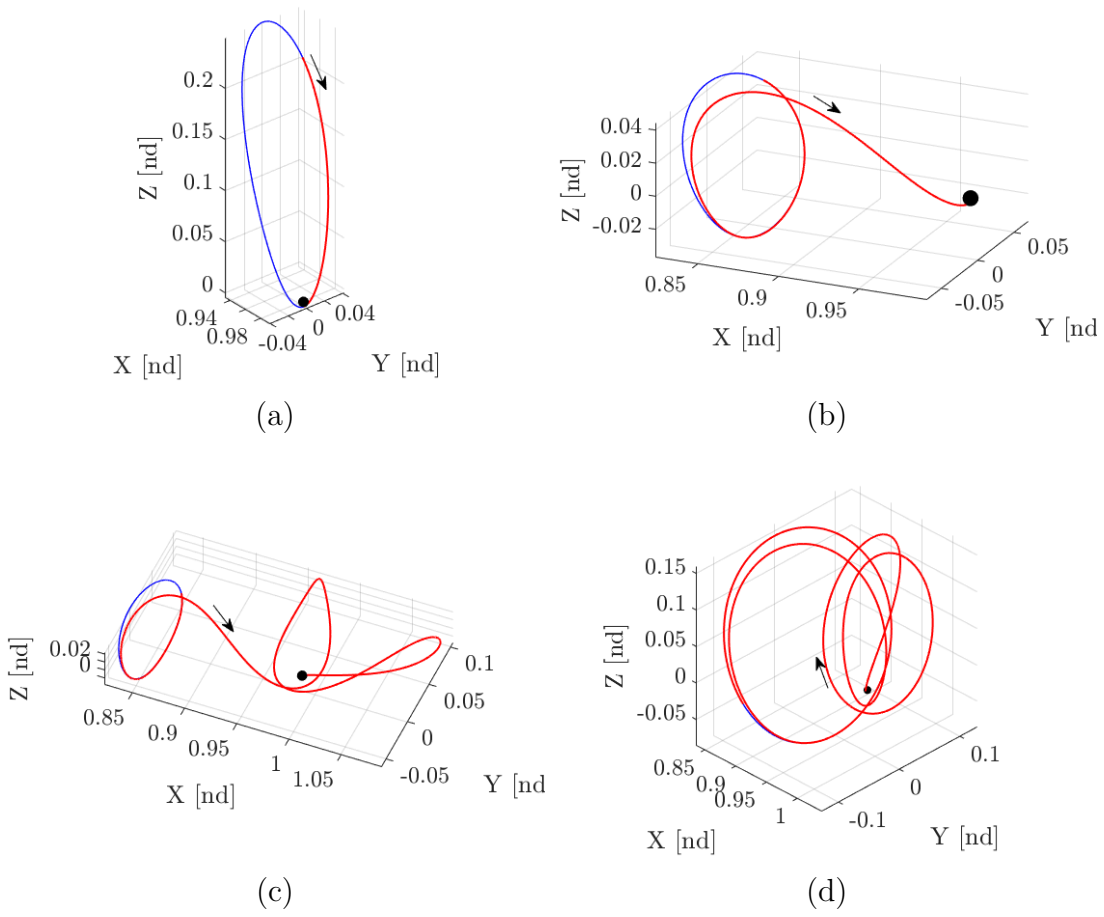

Figure 4.55.: Example Impacting Trajectories from L_1 Halo Orbits Corresponding to Marked Points in Figure 4.54

nar longitudes at a large range of Jacobi constants. As time-of-flight is increased beyond that of this simple geometry, the complexity of the observed impact geometry increases as well with Figures 4.55(c) and 4.55(d) presenting examples of the multi-revolution geometry present at higher integration times. Figure 4.56 presents the latitudes of the impact conditions displayed in Figure 4.54. Similar stratification by TOF is observed with the largest group forming again at 15 days. Furthermore, this group spans longitudes spanning all values between the poles. The group of low Jacobi constant impacts cluster at values in the southern hemisphere with available latitudes increasing with TOF and reaching a maximum at $\lambda = 0°$. At higher times

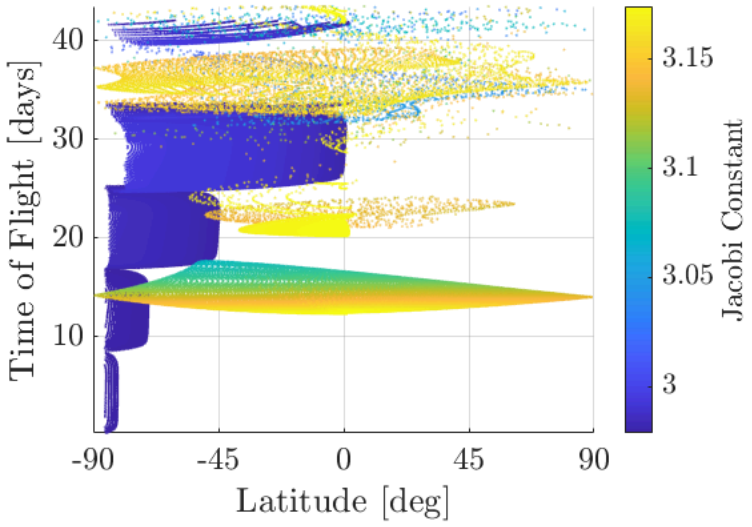

Figure 4.56.: Time of Flight as a Function of Latitude of Lunar Impact Conditions of Unstable Manifolds Associated with L_1 Halo Orbits

of flight, latitudes are spanned by higher Jacobi constant impacts. The latitude and longitude data for the impact is combined in Figure 4.57 to display accessible Lunar impact locations. Overall, a significant portion of the Lunar surface is covered. Low

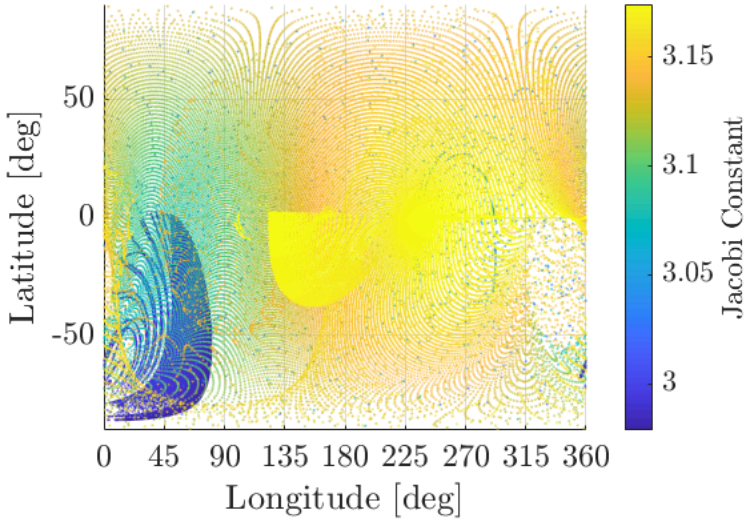

Figure 4.57.: Latitude Versus Longitude of Impact Conditions of Unstable Manifolds Associated with the L_1 Halo Orbit Family

Jacobi constant impacts are primarily restricted to the bottom southern latitudes in the first quadrant while higher Jacobi constant impacts span a greater range of the Lunar surface concentrating at $\lambda = 0°$, $\varphi = 0°$. Recall, because the impacts shown represent the northern halo family, a reflection across $\lambda = 0°$ presents the southern halo data. In this case the lower Jacobi constant impacts would occupy the first longitude quadrant of the northern hemisphere. This data is alternatively colored in terms of the impact angle and speed in Figures 4.58(a) and 4.58(b), respectively. Outside of the low Jacobi constant cluster in the bottom left and the high Jacobi constant cluster in the center of Figure 4.58(a), little general prediction is available for the impact angle. Impact angles are lower in the northern hemisphere, especially at central longitudes. Both the low and high Jacobi constant clusters present near tangential impacts The impact speed is directly correlated to the Jacobi constant of the impacting orbit. As a result, Figure 4.58(b) presents very similar structure to Figure 4.57 with low speed impacts occurring in the center of the plot and high speed impacts existing in the bottom left section corresponding to the low Jacobi constant manifolds. The range of impact speeds is only approximately 40 m/s across all the L_1 halo impacts consistent with the low variation predicted by the theoretical extremes.

A similar analysis is conducted for the northern L_2 halo orbits. Figure 4.59 presents the L_2 northern halos colored by the possession of impacting unstable manifolds. Similar to the L_1 halo orbits, the orbits possessing impacting manifolds are those closer to the planar bifurcation with the L_2 Lyapunov orbits. However, unlike the L_1 halo orbits, none of the orbits closer to the Moon yield impacting manifolds. Inspecting the impact conditions of the L_2 halos, the TOFs and longitudes are shown in Figure 4.60. The first impact is observed at 16 days, similar to the 15 day grouping observed for the L_1 halo orbits with the time of flight for impacts in the third and fourth quadrants slightly higher than those for the first and second. Figure 4.61(a) demonstrates and example trajectory from this group and is similar to that observed for the L_1 halos in Figure 4.55(b). Furthermore, the first and second quadrants are populated by the higher Jacobi constant impacts for the 15 day TOF grouping, while

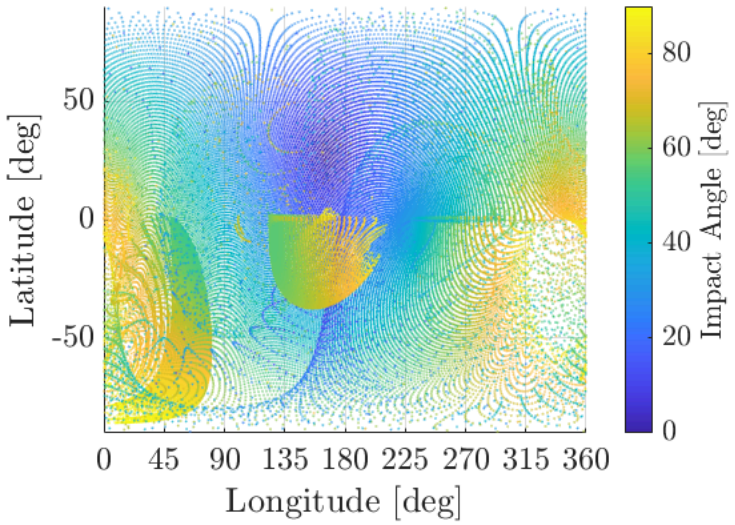

(a) Impact Angle

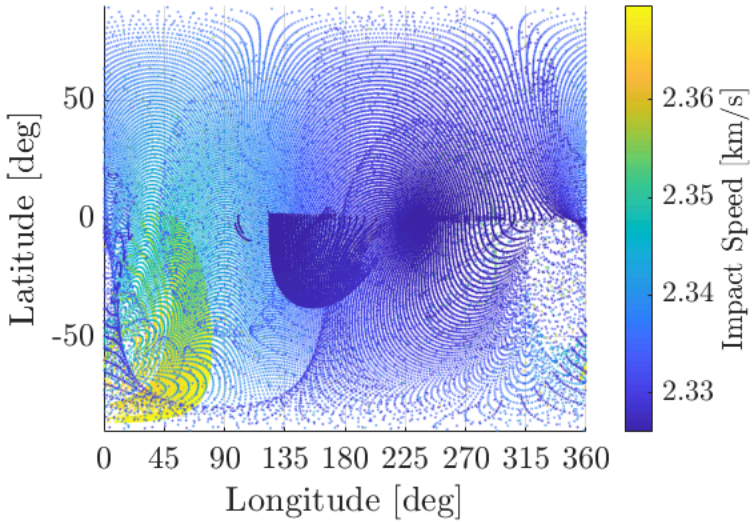

(b) Impact Speed

Figure 4.58.: Latitude Versus Longitude for Impacts of Unstable Manifolds Associated with the L_1 Halo Orbits

the third and fourth quadrants contain mainly lower Jacobi constant impacts. Figure 4.61(b) presents an example impact stemming from the higher time-of-flight impact demonstrating the increased complexity in the geometry. The latitudes of the impact locations are presented in Figure 4.62. Very similar structure is observed in

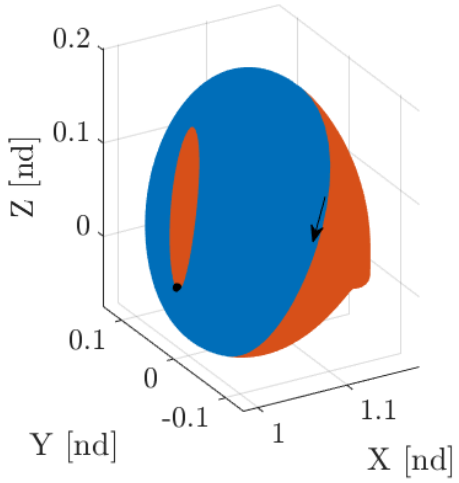

Figure 4.59.: Unstable L_2 Halo Orbits with Manifold Structures Impacting the Moon Within 43 Days

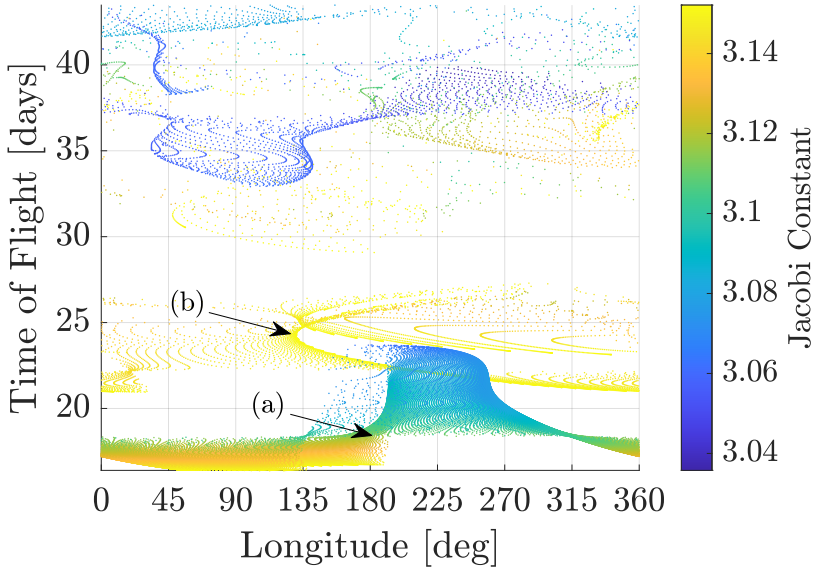

Figure 4.60.: Time of Flight and Longitude of Impact Conditions for Unstable Manifolds Associated with L_2 Halo Orbits

the L_2 halo TOF versus latitude plot as is observed in the L_1 halo case except the lower Jacobi constant impacts present in the southern hemisphere of the L_1 halo impacts diagram. Impacts at all latitudes are observed with higher Jacobi constants concentrating in the center while Jacobi constants near $J = 3.1$ present the great-

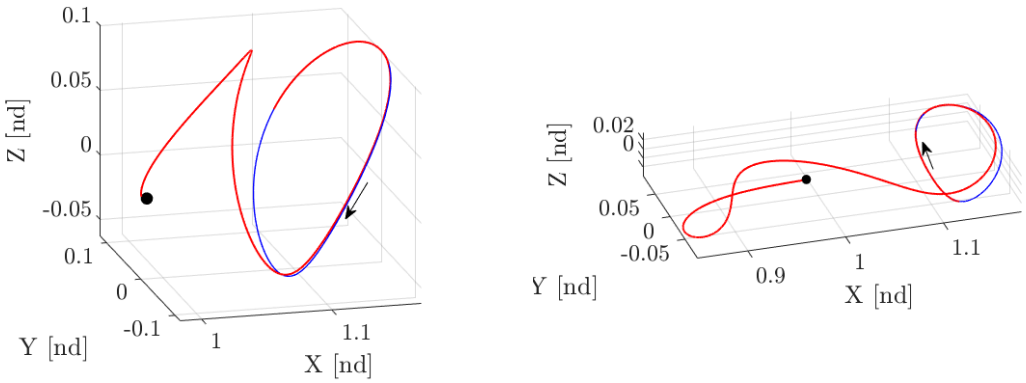

Figure 4.61.: Example Impacting Trajectories from L_2 Halo Orbits Corresponding to Marked Points in Figure 4.60

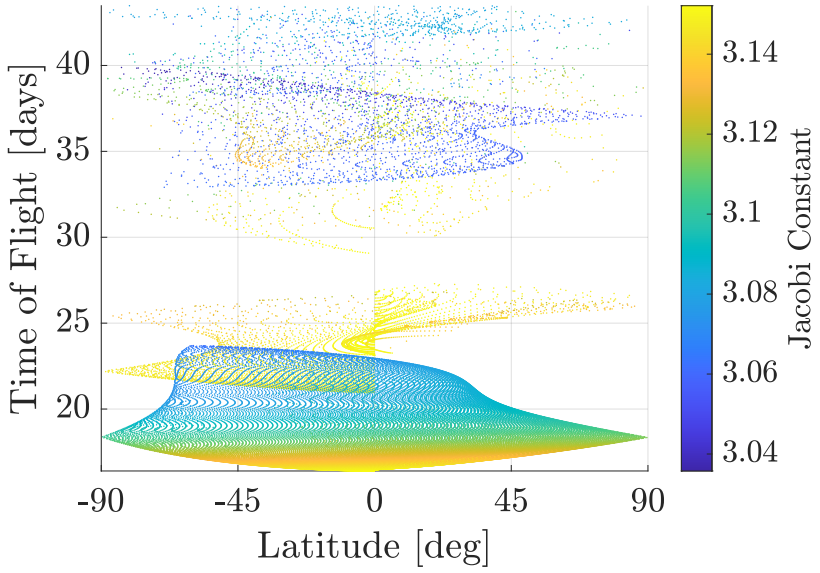

Figure 4.62.: Time of Flight as a Function of Latitude of Lunar Impact Conditions of Unstable Manifolds Associated with L_2 Halo Orbits

est range in impact latitude. At large times-of-flight lower Jacobi constants present spread out impacts appearing as a "dusting". Figure 4.63 presents the combination of latitude and longitude information for the L_2 halo impact conditions. Opposite the L_1 case, higher Jacobi constant impacts dominate the first and second quadrants while lower Jacobi constant impacts dominate the third and fourth. In both cases,

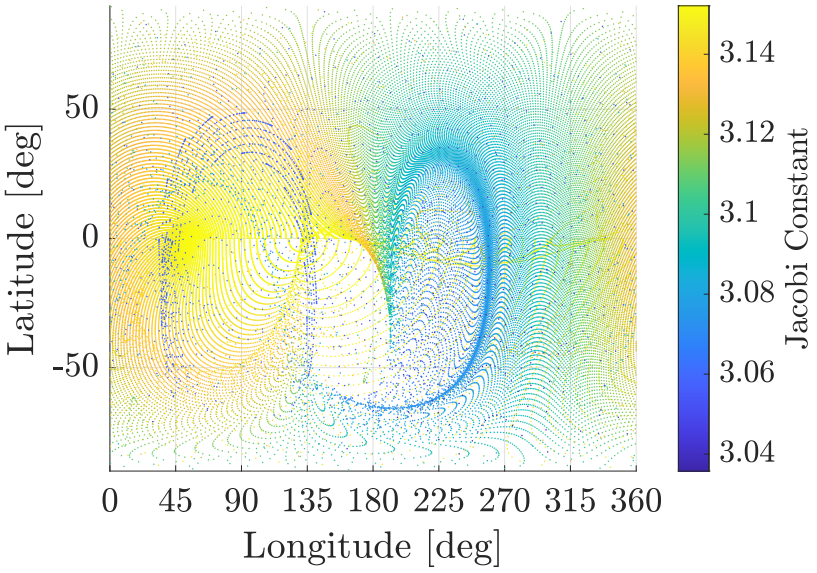

Figure 4.63.: Latitude Versus Longitude of Impact Conditions of Unstable Manifolds Associated with the L_2 Halo Orbit Family

the extreme Jacobi constant impacts tend toward the equator. Overall, the L_2 halos provide a significant Lunar coverage with impacts extending to a significant portion of longitudes and latitudes across the Lunar surface. These impact conditions are additionally colored corresponding to the angle and speed of impact in Figures 4.64(a) and 4.64(b), respectively. As is observed in the L_1 halo impact conditions, the impact angles in Figure 4.64(a) present high amounts of variation between consecutive impacts. However, in general, impacts in the southern hemisphere tend toward higher impact angles compared to those in the northern hemisphere. The impact speeds, again, vary only by around 20 m/s with lower impact speeds occurring in the first and second quadrants consistent with the Jacobi constants of the observed impacts presented in Figure 4.63,

Overall, the L_1 and L_2 halo families present many lunar impact conditions covering the Lunar surface at Jacobi constants between $J \approx 3.04$ and $J \approx 3.15$. Furthermore, due to the symmetry with their respective southern families, the data presented additionally possesses a reflected set over $\lambda = 0^\circ$ presenting additional candidate impact

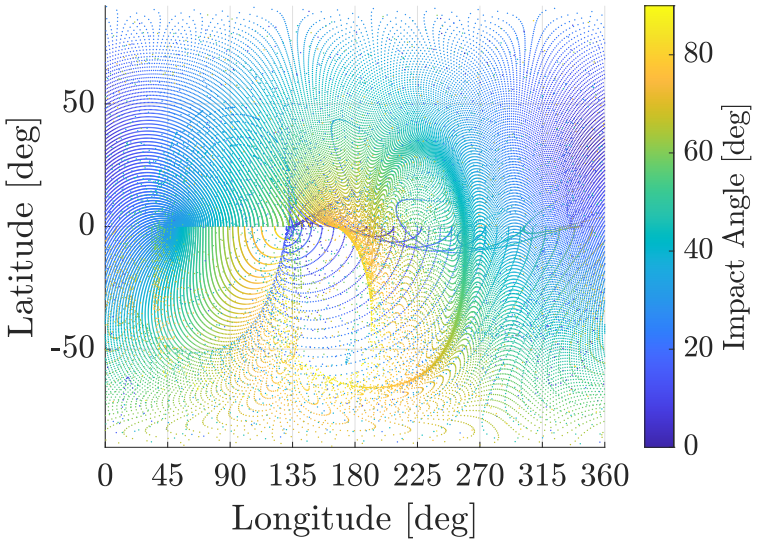

(a) Impact Angle

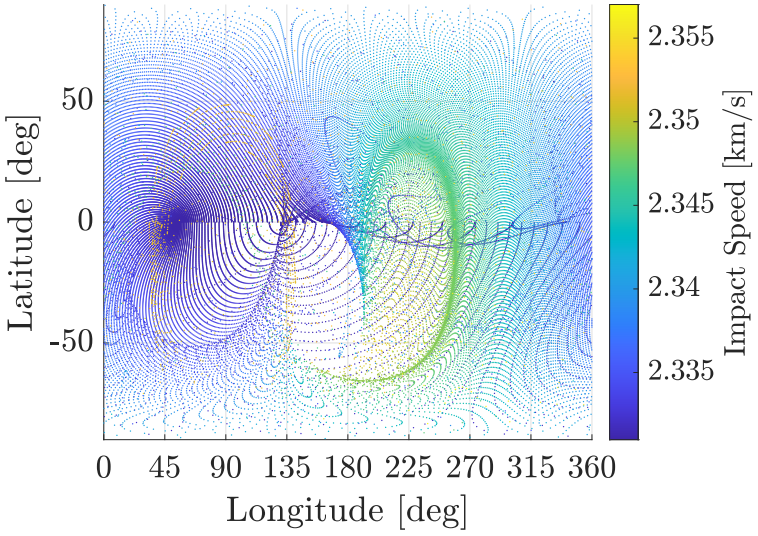

(b) Impact Speed

Figure 4.64.: Latitude Versus Longitude for Impacts of Unstable Manifolds Associated with the L_2 Halo Orbits

trajectories. This reflection as well as the large number of impact points presented yield considerable opportunity for Lunar impact.

Vertical Orbit Families

Both the L_1 and L_2 vertical orbit families present unstable members with sufficiently low time constants. Figure 4.65 displays the members of the L_1 and L_2 vertical orbit families with coloring indicating whether a fast departure manifold exists for the specific orbit. Evident from the figure, both families possess a large amount of orbits

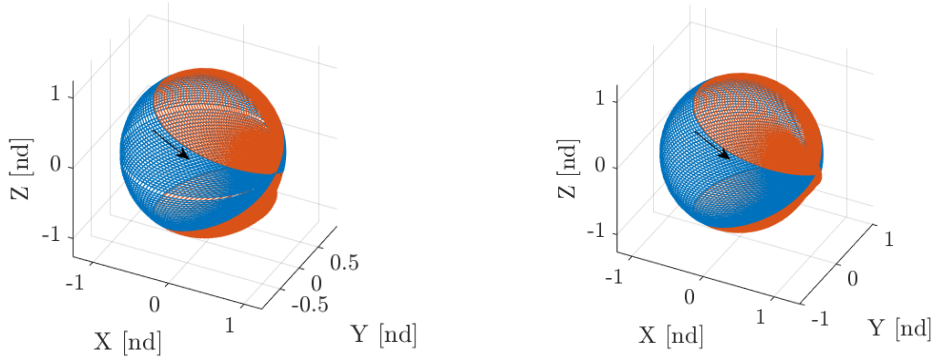

(a) L_1 (b) L_2

Figure 4.65.: L_1 and L_2 Vertical Orbit Families where Red Indicates Unstable Orbits with $\kappa_\tau < 1.5$ and Blue Indicates $\kappa_\tau > 1.5$

with fast departure characteristics extending to large z amplitudes. The unstable manifolds associated with these orbits are propagated for $\approx$ 43 days to determine Lunar impact conditions.

Beginning with the analysis of the L_1 vertical orbit family, the members of the family with unstable manifolds impacting the Moon are shown in Figure 4.66. Of the 1003 vertical orbits investigated, only 37 were found possessing manifolds impacting the the Lunar surface. This sparsity in impact conditions severely limits the Jacobi constants available; the Jacobi constants of the impacting orbits only span the range from $J = 3.051$ to $J = 3.105$ (the fast departure orbits spanned Jacobi constants from $J = -0.057$ to $J = 3.188$). Therefore, while the vertical orbits demonstrate high levels of instability, the manifold structures of these orbits do not venture close to the Lunar surface. However, the L_1 vertical orbits that do impact the surface span

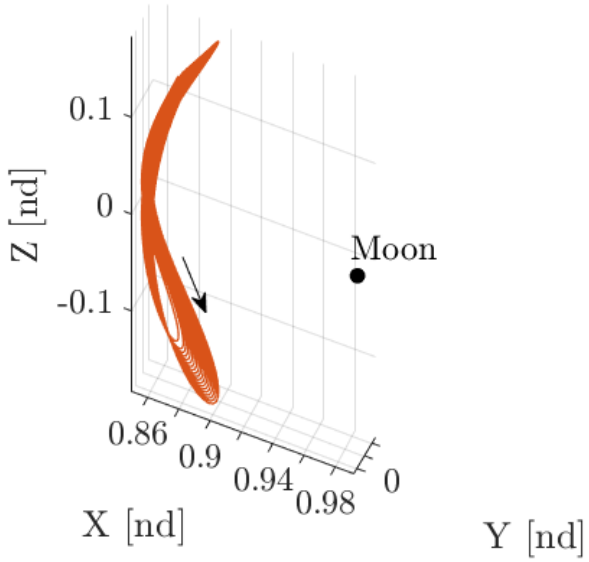

Figure 4.66.: Unstable L_1 Vertical Orbits with Manifold Structures Impacting the Moon Within 43 Days

a range of Jacobi constants common in the Lunar region families indicating possible utility.

The longitudes of the impact conditions are explored in Figure 4.67. The first impact appears at approximately 21 days; therefore, low TOF transfers are not available from the L_1 vertical orbits resulting from the distance of the identified vertical orbits from the Moon. Inspecting Figure 4.67, the impact conditions span all longitudes (from 0° to 360°) and occur in groups corresponding to their times-of-flight. The impact occurring in the first and second quadrants possess a higher average Jacobi constant value than those impacting in the third and fourth quadrants with a relatively smooth gradient apparent for the lower TOF impacts. The lower two TOF groups at approximately 22 days and 31 days contain relatively consistent geometry across the group shown in Figures 4.68(a) and 4.68(b), respectively. At higher TOF values, the geometry for a given TOF ceases to remain consistent. Figure 4.68(c) presents an example trajectory corresponding to the designated point in Figure 4.67. The trajectories in Figures 4.68(b) and 4.68(c) display southern-dominant motion,

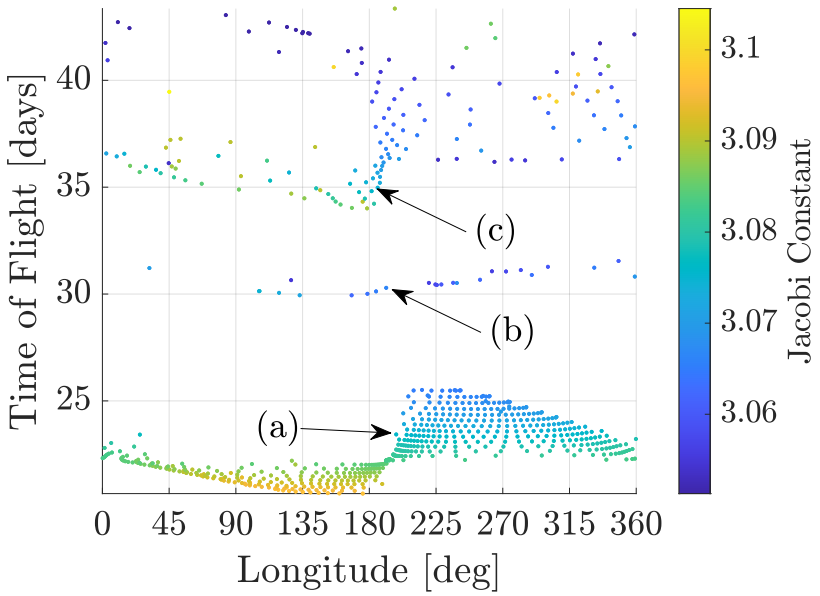

Figure 4.67.: Time of Flight and Longitude of Impact Conditions for Unstable Manifolds Associated with L_1 Vertical Orbits

i.e. the trajectories spend a larger amount of time below the xy-plane, while the trajectory in Figure 4.68(a) displays northern-dominant motion. However, each impact point on Figure 4.67 is two points on top of each other. This doubling of points is due to the symmetry of the vertical orbits with respect to the xy-plane and the $\pm z$ symmetry in the CRTBP equations of motion. Because this symmetry is across the xy-plane, it is not visible on the longitude plot. To display this difference, Figure 4.69(a) presents the TOF versus latitude plot for the L_1 vertical orbits. Mirror symmetry of the impact points is observed over the $\lambda = 0$ axis. Figure 4.69(b) presents two orbits impacting at the same longitude but at $\lambda = \pm 83°$, i.e. at opposite latitudes. This mirror condition, obviously, exists at all times of flight and latitudes. Consequently, the vertical manifolds demonstrate a large range of available of latitudes; latitudes extending to $\pm 87°$ are observed indicating the vertical orbits present polar impact conditions. Furthermore, the maximal latitudes are observed for Jacobi constants around 3.07 with higher Jacobi constants presenting a significantly smaller range. Lower Jacobi constants, however, present a similar range of available lati-

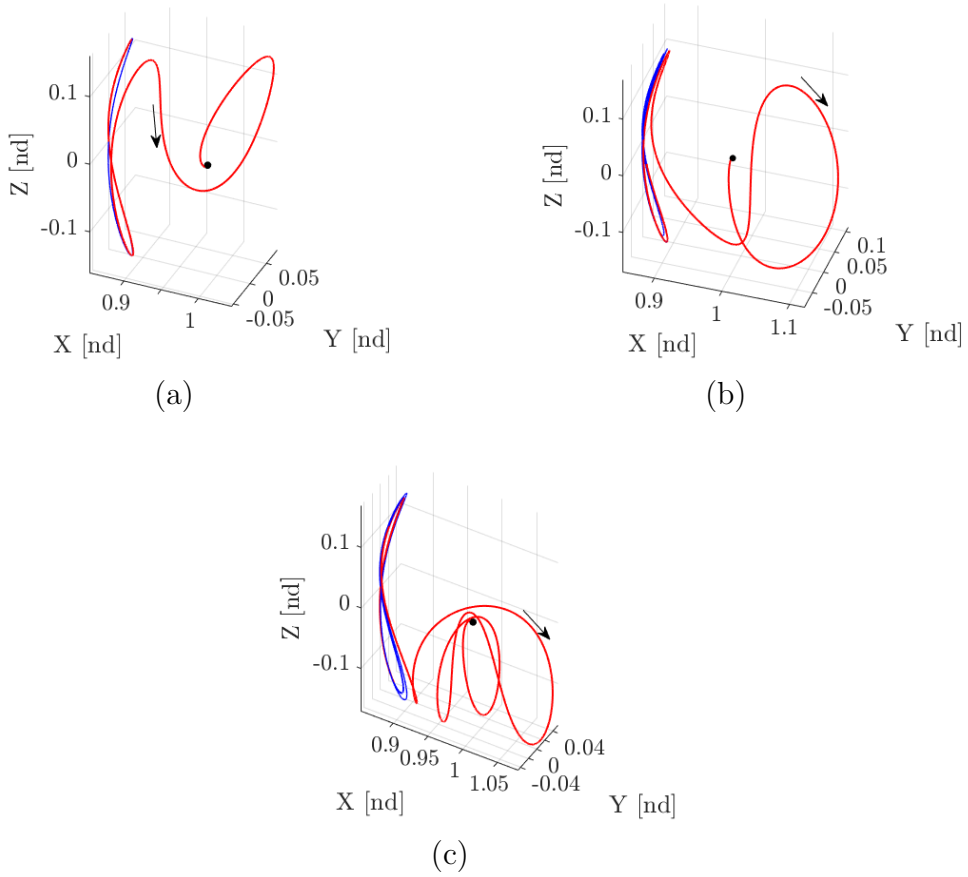

Figure 4.68.: Example Impacting Trajectories from L_1 Vertical Orbits Corresponding to Marked Points in Figure 4.67

tudes. Figure 4.70 presents the latitude as a function of the longitude of the impact conditions. Again, the symmetry over the $\lambda = 0°$ line is observed. Furthermore, the gradient of Jacobi constant over the longitude is observed with higher Jacobi constants near $\varphi = 90°$ evolving to lower Jacobi constants around $\varphi = 270°$. Overall, the vertical manifolds present a large range of longitudes despite the low number of orbits with impacting manifolds.

Figure 4.70 is also colored corresponding to impact angle and impact speed in Figure 4.71. The impact angles range from 1° to 87° with the lower and higher impact angles occurring at more extreme latitudes and higher impact angles and the moderate impact angles occurring near the Lunar equator. This result hints that vertical orbits

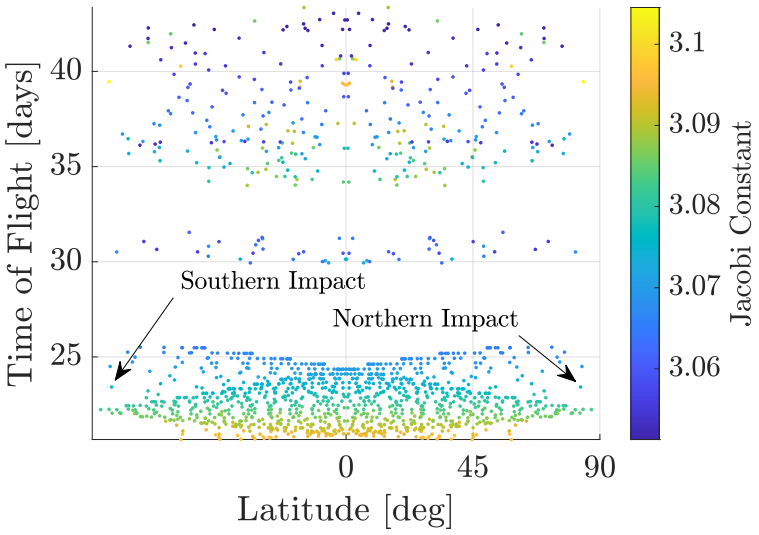

(a)

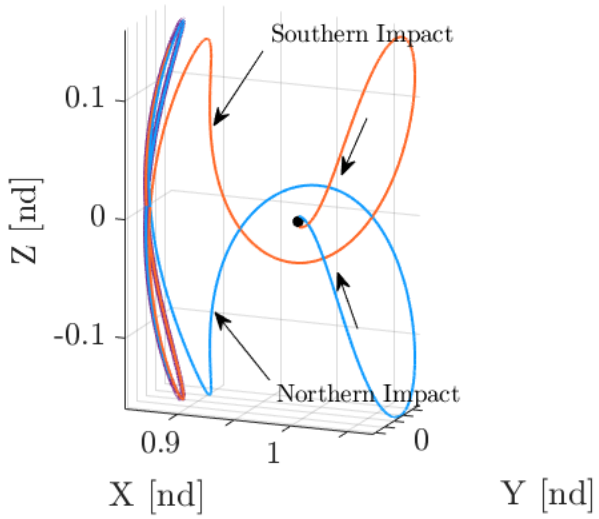

(b)

Figure 4.69.: Latitude of Impact for L_1 Vertical Impacting Manifolds

will rarely deliver impacts normal or tangent to the surface near the equator. The impact speeds, as previously observed, are closely tied to the Jacobi constant of the impacting trajectory. Consequently, due to the limited range in Jacobi constant of the L_1 vertical orbits possessing manifolds that impact the Moon, the observed impact

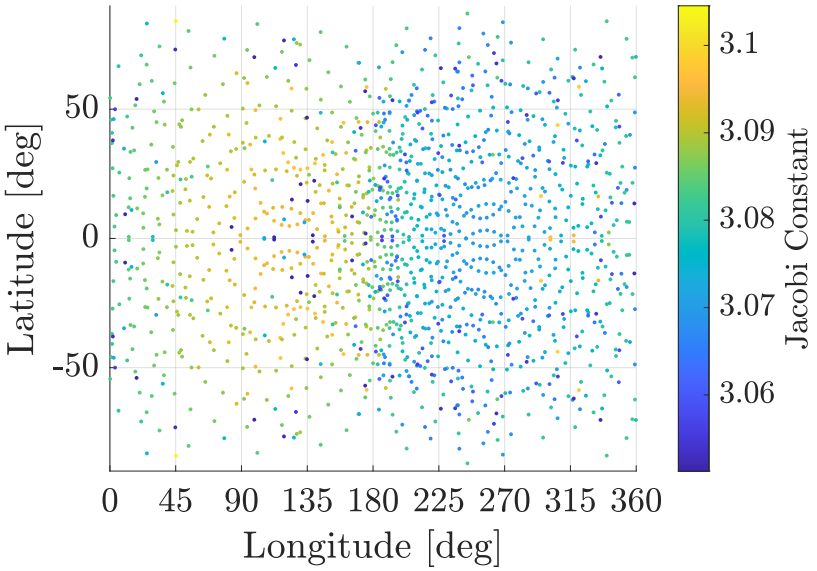

Figure 4.70.: Latitude Versus Longitude of Impact Conditions of Unstable Manifolds Associated with the L_1 Vertical Orbit Family

speeds are correspondingly limited. Higher impact speeds are observed in the first and third quadrants consistent with the tidal acceleration presented by Davis [16].

The symmetry and variation of the unstable manifolds associated with the L_1 vertical orbits present equal access to northern and southern latitudes and enable a large range of available impact locations despite the low percentage of orbits with impacting manifolds. However, due to this sparsity, little variation is observed in impact velocity, all impacts require long times-of-flight, and selection of an impact location greatly restricts the TOF values available.

Similarly to the L_1 vertical orbits, the L_2 vertical orbits present only a small percentage of members with manifolds structures impacting the Moon within the 43 day propagation horizon. These members are displayed in Figure 4.72. Starting with 921 L_2 vertical orbits, 29 are found with impacting manifold structures giving a similar impacting percentage as the L_1 vertical orbit family. Also similar to the L_1 family, the restricted Jacobi constant range, therefore, spans values from $J = 3.039$ to $J = 3.140$.

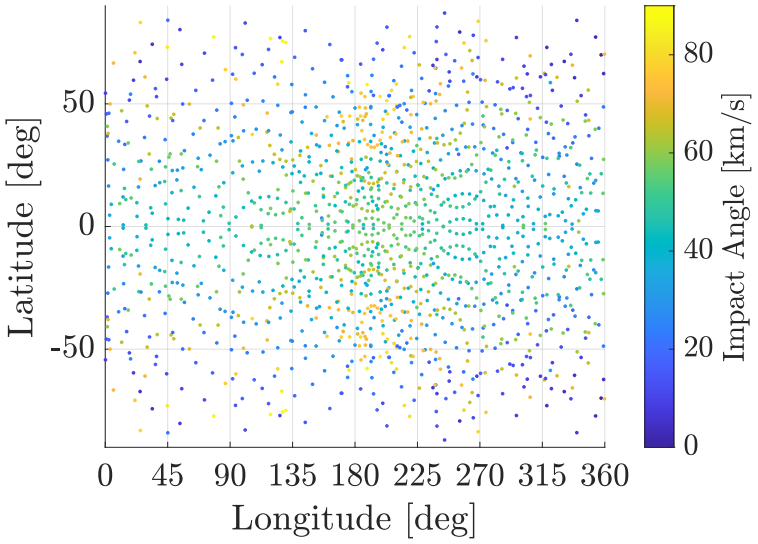

(a) Impact Angle

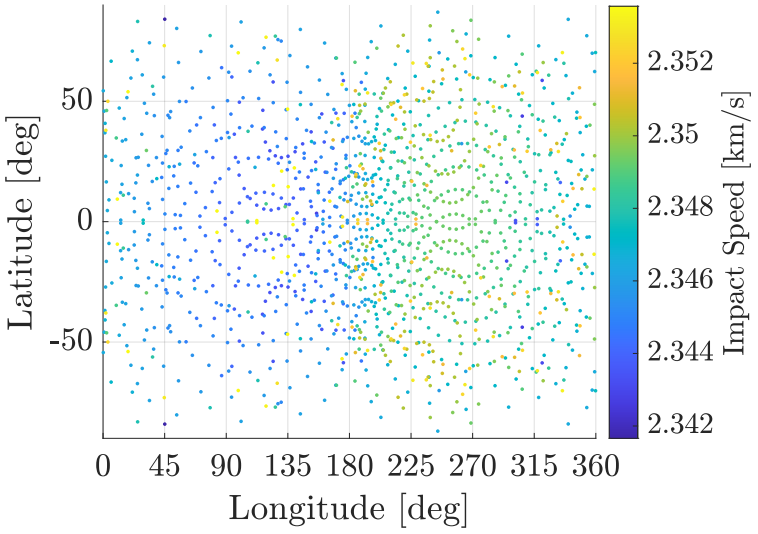

(b) Impact Speed

Figure 4.71.: Latitude Versus Longitude for Impacts of Unstable Manifolds Associated with the L_1 Vertical Orbits

The TOFs and longitudes of the unstable manifold impact conditions for the L_2 vertical orbits are shown in Figure 4.73. Like the L_1 conditions, grouping by TOF is observed with groups forming near 26, 35, 40, and 45 days. While impacts are observed at all longitudes, a larger proportion of the impacts are seen in the first and second quadrants ($0° \leq \varphi \leq 180°$). The first observed impact takes place at 24.5 days

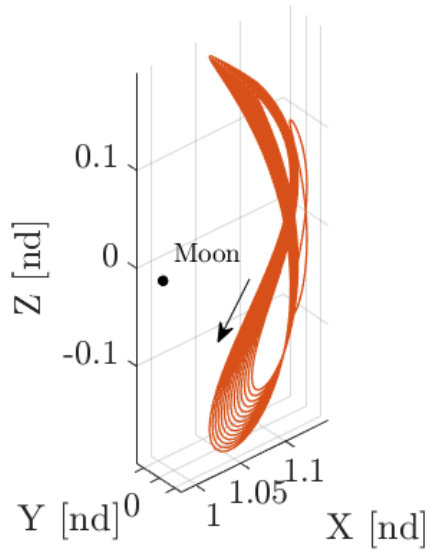

Figure 4.72.: Unstable L_2 Vertical Orbits with Manifold Structures Impacting the Moon Within 43 Days

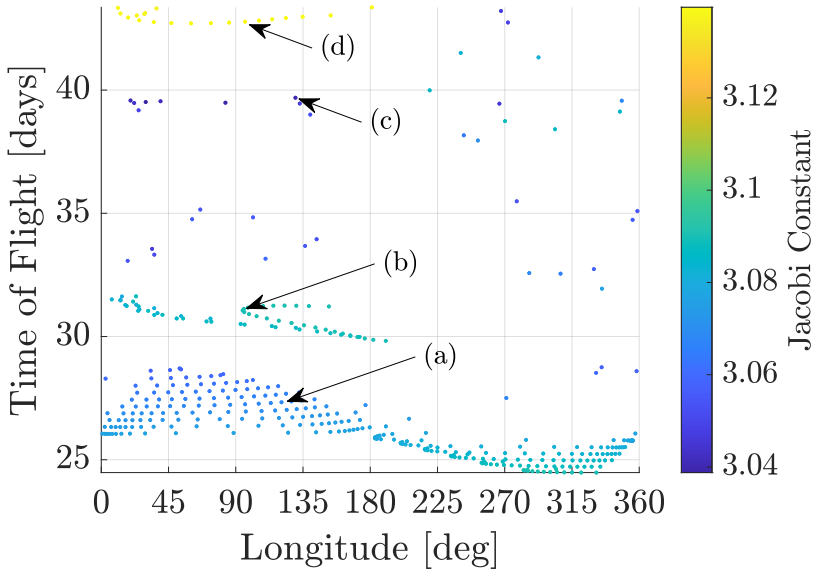

Figure 4.73.: Time of Flight and Longitude of Impact Conditions for Unstable Manifolds Associated with L_2 Vertical Orbits

and impacts are observed extending to the 43 day integration limit. The low time-of-flight impacts are dominated by mid-to-low Jacobi constant values with no high ($J > 3.12$) Jacobi constant impacts occurring before 41 days, a trend not observed

in the $L1$ vertical orbits. Sample trajectories corresponding to the indicated points in Figure 4.73 are provided in Figure 4.74. Similar to the L_1 verticals, northern

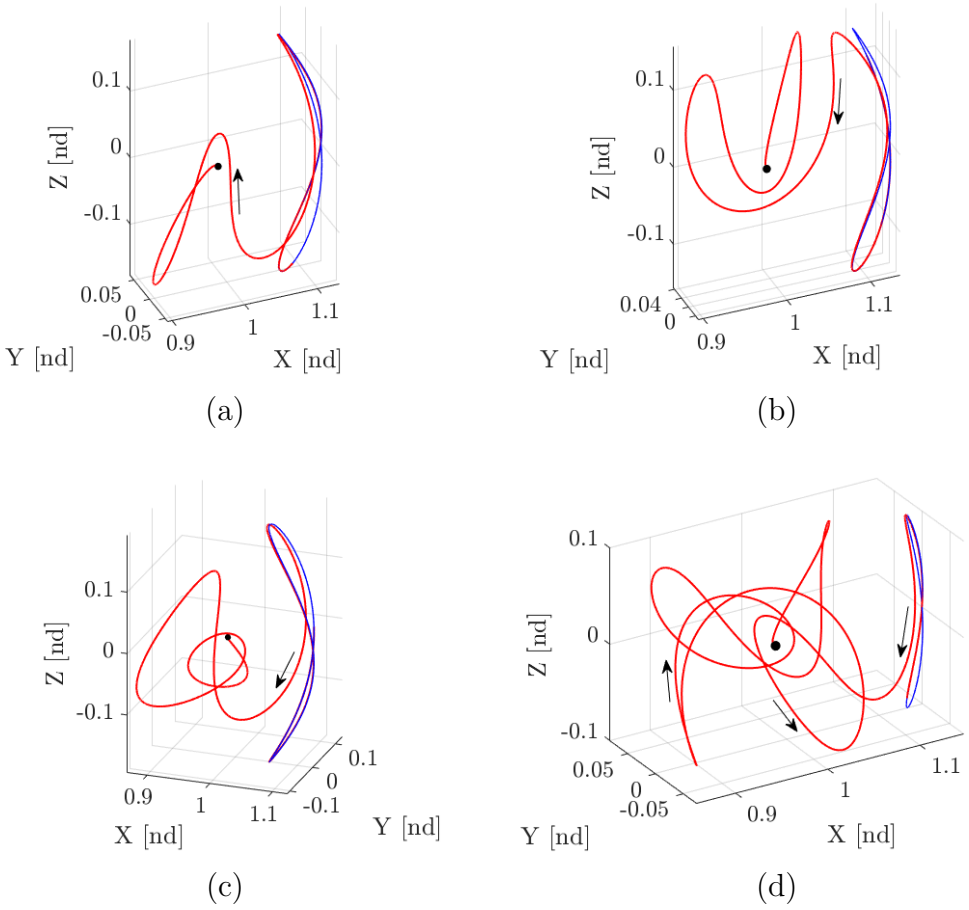

Figure 4.74.: Example Impacting Trajectories from L_2 Vertical Orbits Corresponding to Marked Points in Figure 4.73

and southern motion is apparent with more complex motion occurring at higher TOFs. The symmetry between the northern and southern motion is observed in the latitude versus longitude plot in Figure 4.75. Again, a symmetry across the $\lambda = 0°$ axis is apparent showing identical access properties for the northern and southern hemispheres of the Moon. The high Jacobi constant impact are restricted to the $0° \leq \varphi \leq 180°$, evident as well in Figure 4.75. Furthermore, lower Jacobi impacts are also observed in the first and second quadrants with the moderate Jacobi constant

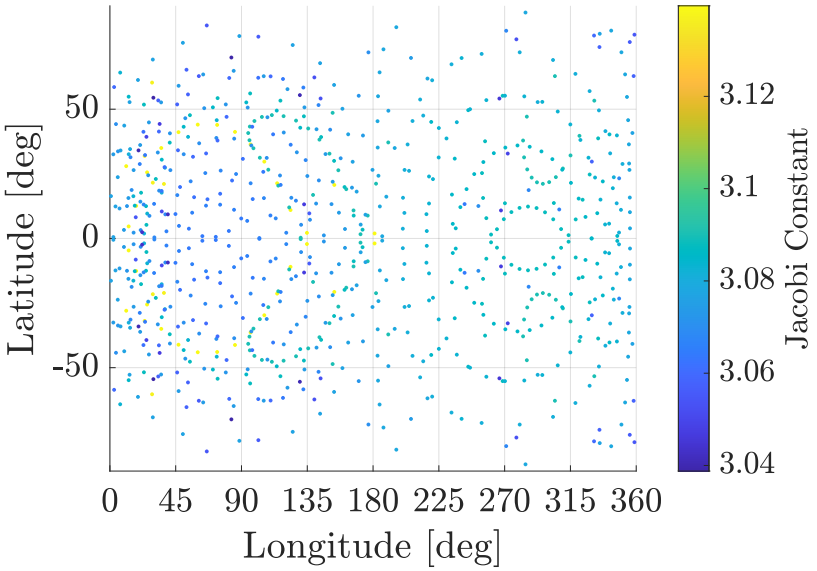

Figure 4.75.: Latitude Versus Longitude of Impact Conditions of Unstable Manifolds Associated with the L_2 Vertical Orbit Family

values populating the third and fourth. Overall, the L_2 vertical orbits demonstrate considerable Lunar surface coverage given the low number of impacting orbits. The extreme latitudes reached are $\lambda = \pm 87.4°$ at $J = 3.08$ and the longitudes span the entire range with extreme longitudes occurring for Jacobi constant values around $J = 3.08$.

The latitude and longitudes of the impact locations are presented colored corresponding to impact angle and impact speed in Figure 4.76. Nearly all impact angles are observed with mid-range angles occurring closer to $\lambda = 0°$ and more extreme impact angles occurring at latitudes farther from the equator. However, impact angle behavior presents greater unpredictability than impact location or speed as is observed in the L_1 vertical case as well. The impact speed plot shown in Figure 4.76(b) reflects the Jacobi constant of the impact condition and therefore presents the extreme speeds in the first and second quadrants and the moderate speeds in the third and fourth. However, overall variation in impact speed is minimal due to the low variation in Jacobi constants across the impacting L_2 vertical manifolds.

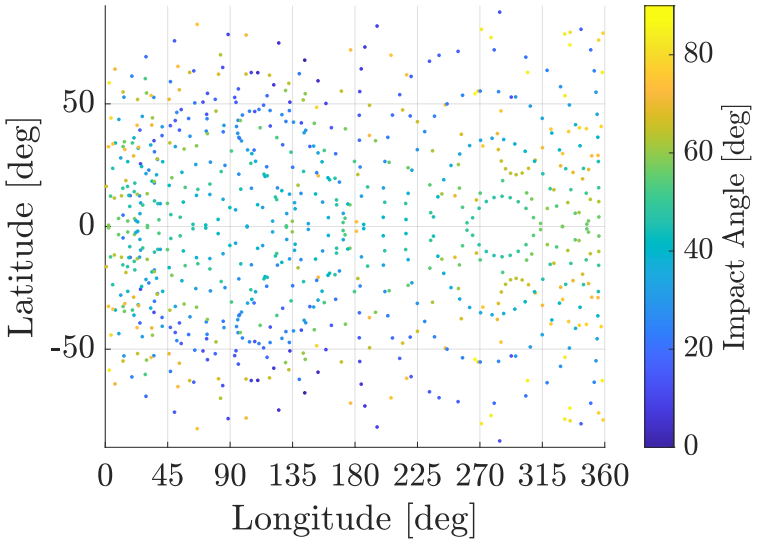

(a) Impact Angle

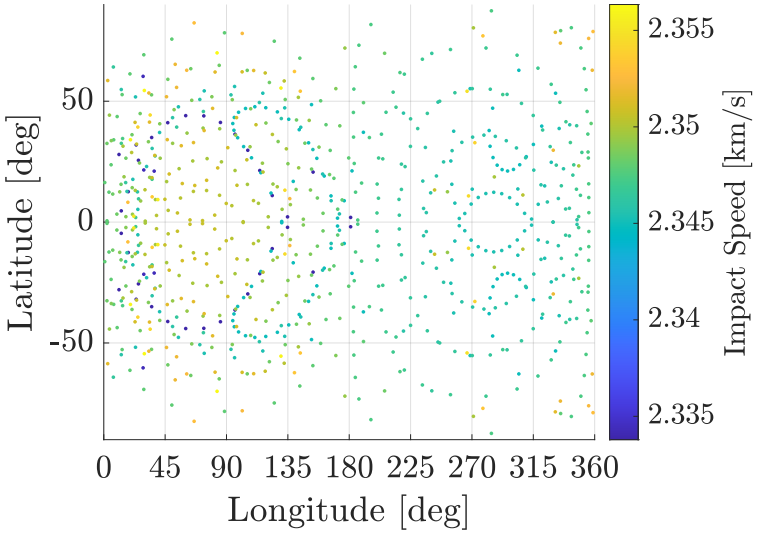

(b) Impact Speed

Figure 4.76.: Latitude Versus Longitude for Impacts of Unstable Manifolds Associated with the L_2 Vertical Orbits

The L_1 and L_2 vertical orbit families each present very few members whose unstable invariant manifolds yield Lunar impact conditions. Despite this sparsity, however, a large range of impact locations is observed for each family; impacts are found at all longitudes spanning latitudes between $\lambda \approx -87°$ to $\lambda \approx 87°$ in each case. However, due to the few impacting manifolds and the tight coupling of impact speed

and Jacobi constant, impact speeds for both the L_1 and L_2 families sit around 2.34 km/s with variations less than 15 m/s. As previously noted, impact speed and angle are relatively difficult to predict across the vertical orbit impact conditions based on characteristics of the initial condition, but knowledge of similar nearby geometry yields decent estimates for the impact angle. Overall, the vertical orbit families in the Earth-Moon system present a substantial amount of impact possibilities across the Lunar surface in a small range of Jacobi constant values with relatively consistent impact angles.

Axial Orbit Families

As explored in Section 4.2.7, all members of both the L_1 and L_2 axial orbit families present unstable manifolds with sufficiently low time constants. Therefore, the unstable manifolds associated with every L_1 and L_2 axial orbit are propagated for approximately 43 days to determine Lunar impact conditions.

The L_1 axial orbits are shown in Figure 4.77 colored according to the presence of impacting unstable manifolds. The majority of the impacting orbits are those near to the xy-plane. Only several small bands of orbits with impacting manifolds are observed outside of the large group surrounding the planar bifurcation from the L_1 Lyapunov orbits. Of the 818 axial orbits in Figure 4.77, 376 present impacting manifold structures; thus, the axial orbits present a greater percentage of impacting orbits than the vertical families but still yield a large number of orbits without impacting manifolds. However, because the Jacobi constant range across the axial family is small, the restriction to impacting orbits yields a significantly reduced range of Jacobi constants for impacts. The impacting orbits span Jacobi constants from $J = 3.001$ to $J = 3.021$. The TOFs versus impact longitudes of the integrated trajectories on the unstable manifolds associated with the L_1 axial orbits are shown in Figure 4.78. The minimal TOF observed is 22.5 days, the TOFs extend to the 43 day limit, and all impact longitudes are achieved. The higher Jacobi constants, i.e. the near planar

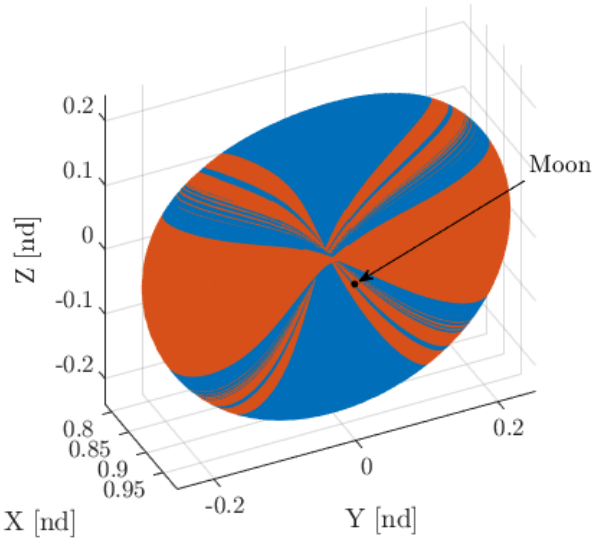

Figure 4.77.: L_1 Axial Orbits Where Red Indicates Axial Orbits with Impacting Manifolds and Blue Indicates Axial Orbits without Impacting Manifolds

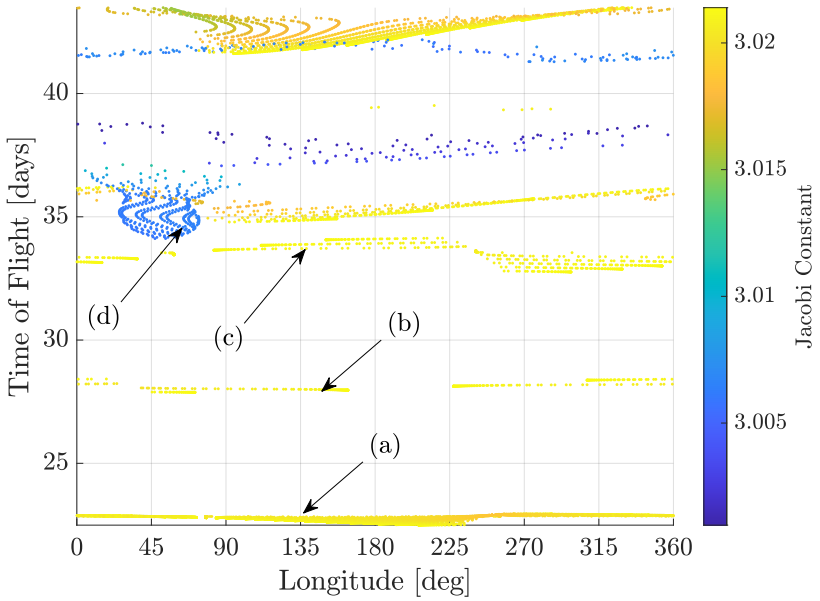

Figure 4.78.: Time of Flight as a Function of Longitude of Lunar Impact Conditions of Unstable Manifolds Associated with L_1 Axial Orbits

orbits, dominate the impact points across all times-of-flight. Higher Jacobi impact conditions are not observed until 34 days of propagation and are restricted to lon-

gitudes around 45° until 37 days. Thus, the axial orbits with a larger out-of-plane component fail to yield short TOF transfers to the Lunar surface and present limited impact locations. Groups of transfers stratified by TOF are observed in Figure 4.78 similar to those observed in the vertical orbit families. Several example impact trajectories are marked in Figure 4.78 and displayed in Figure 4.79. The depicted tra-

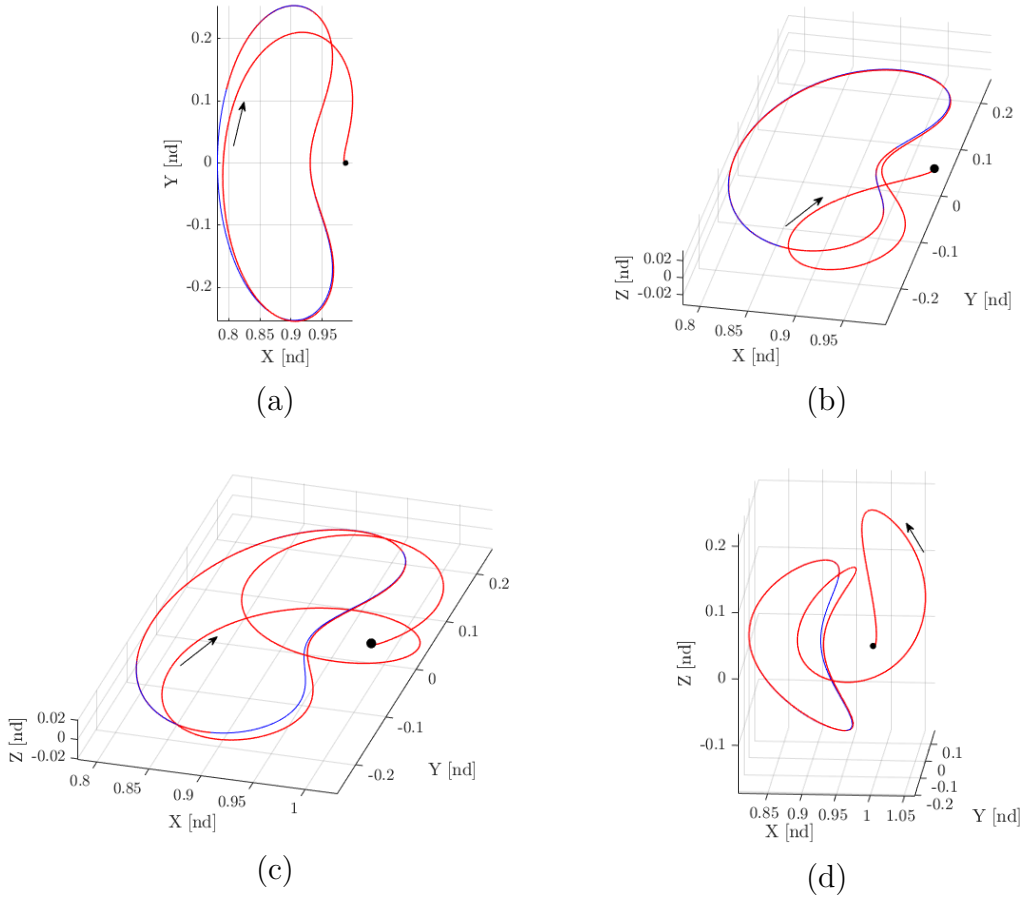

Figure 4.79.: Example Impacting Trajectories from L_1 Axial Orbits Corresponding to Marked Points in Figure 4.78

jectories demonstrate that the TOF groups associated with Figure 4.79(a), 4.79(b), and 4.79(c) represent trajectories with three different geometries originating from the nearly-planar axial orbits. Conversely, Figure 4.79(d) presents an impact trajectory not originating from a nearly-planar axial orbit impacting around $\varphi = 45°$. At higher

TOFs than those shown in Figure 4.79, trajectories exist across all the represented Jacobi constants spanning all longitudes. Therefore, while the axial orbits present a restricted range of Jacobi constants at low times-of-flight, higher times-of-flight yield greater flexibility. Similar to the vertical orbit families, the axial impact conditions display a large amount of symmetry; to explore this symmetry, the TOF versus latitude plot is displayed in Figure 4.80. A line of symmetry is observed across $\lambda = 0°$.

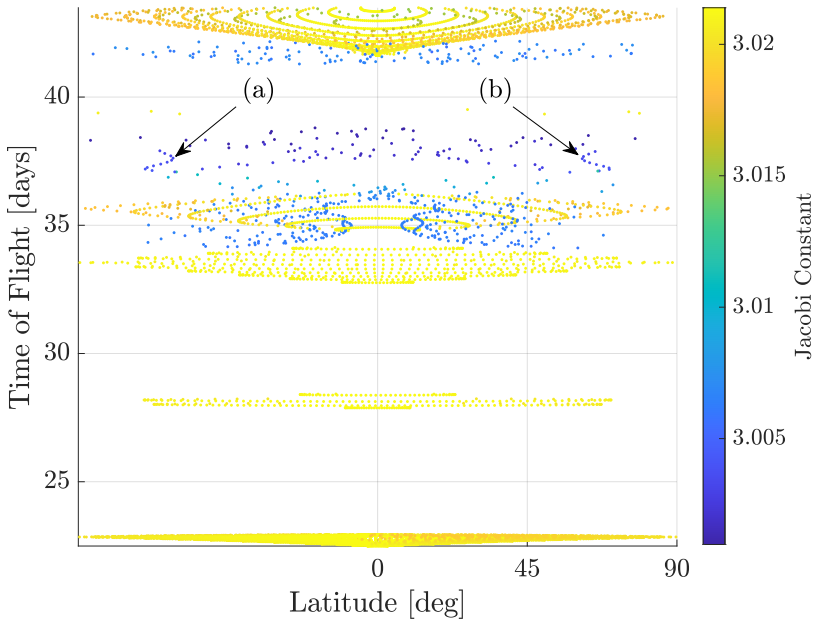

Figure 4.80.: Time of Flight as a Function of Latitude of Lunar Impact Conditions of Unstable Manifolds Associated with L_1 Axial Orbits

However, unlike the vertical orbits, the symmetry is not perfect as depicted in Figure 4.80. This imperfection is a result of the symmetry occurring between two orbits in the family rather than a single orbit. Figure 4.81 demonstrates two trajectories yielding symmetric impact conditions and geometry with respect to the xy-plane. Where the vertical displayed symmetry between two trajectories on the same manifold, the axial orbits possess symmetry between two trajectories on the manifolds of the two axial family members with xy-symmetry. Because the symmetry exists between two family members, if the members calculated are not exactly the correct pair, then the resulting conditions will be slightly off true symmetry. This effect is the cause of

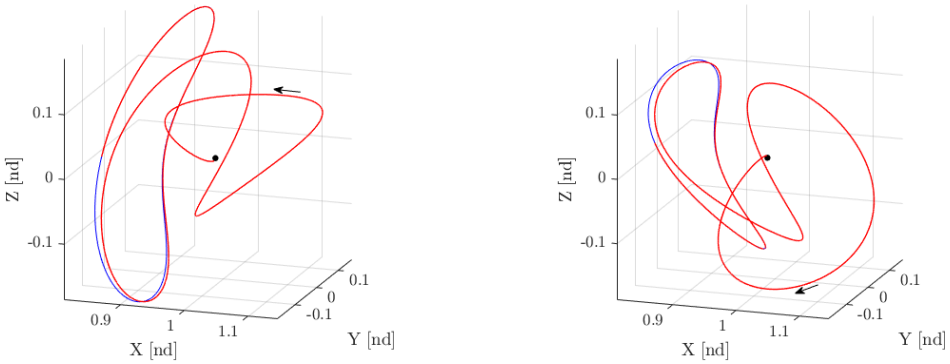

Figure 4.81.: Example Impacting Trajectories from L_1 Axial Orbits Corresponding to Marked Points in Figure 4.80

the approximate symmetry observed in Figure 4.80. However, if the infinite number of members were plotted, then perfect symmetry would be observed. Beyond the symmetry, Figure 4.80 demonstrates a large span of available latitudes with extreme latitude reaching $\lambda = \pm 89.9°$ at several different TOFs.

The latitudes and longitudes for the impact conditions associated with the L_1 axial orbits are shown in Figure 4.82. Congruent with the observations of Figures 4.78 and 4.80, a large range of available impact locations is observed and the impact conditions are dominated by the high Jacobi constant orbits. Furthermore, the symmetry across $\lambda = 0°$ is clearly apparent in Figure 4.82. The low Jacobi constant orbits are concentrated at $\varphi = 45°$ with sporadic impacts elsewhere. Impacts occur over the entirety of the Lunar surface extending from the northern to southern poles; continuous line structures are observed corresponding to the impacting manifolds. The latitude versus longitude diagram is repeated in Figures 4.83(a) and 4.83(b) colored corresponding to impact angle and impact speed, respectively. The maximal and minimal impact angles are observed occurring near the equator in the first and third quadrants. Impacts in the second and fourth quadrants present moderate impact angles centered around $\vartheta = 45°$, thus, impacts normal to the surface are not found near the Lunar poles, a condition desirable for Lunar ice investigations. As

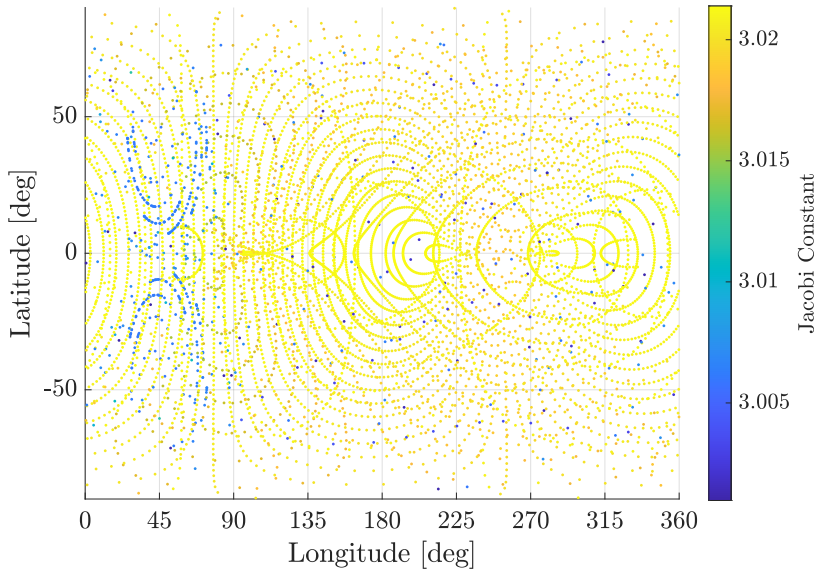

Figure 4.82.: Latitude Versus Longitude of Impact Conditions of Unstable Manifolds Associated with the L_1 Axial Orbit Family

expected, the Lunar impact velocities are dominated by lower values corresponding to the prevalence of impact conditions with higher Jacobi constants. However, due to the low Jacobi constant variation, the absolute difference between the "low-speed" and "high-speed" impact amounts to less than 5 m/s.

The L_2 axial orbit family is presented in Figure 4.84 colored according to the existence of impacting manifolds, similar to the L_1 axial orbit diagram in Figure 4.77. Congruent with behavior observed for the L_1 family, the bulk of L_2 axial orbits with impacting unstable manifolds surround the xy-plane. Several smaller groups are observed farther out of plane, but the majority exist near the bifurcation from the L_2 Lyapunov family. Of the 1080 orbits presented in Figure 4.84, 308 possessed manifolds with impacting conditions. Therefore, the L_2 axial orbits present a smaller percentage of impacting orbits when compared to the L_1 family. Additionally, the Jacobi constants of the L_2 axial impact conditions are lower than those of the L_1 family ranging from $J = 2.979$ to $J = 3.014$, but are similarly restricted in the length of values spanned. The times-of-flight and impact longitudes, φ, for the manifolds associated withe the L_2 axial orbits are given in Figure 4.85. Similar TOF stratifi-

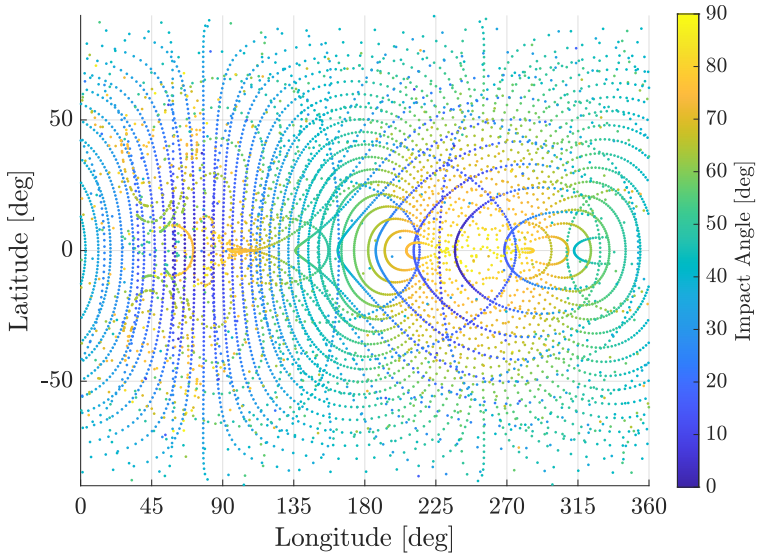

(a) Impact Angle

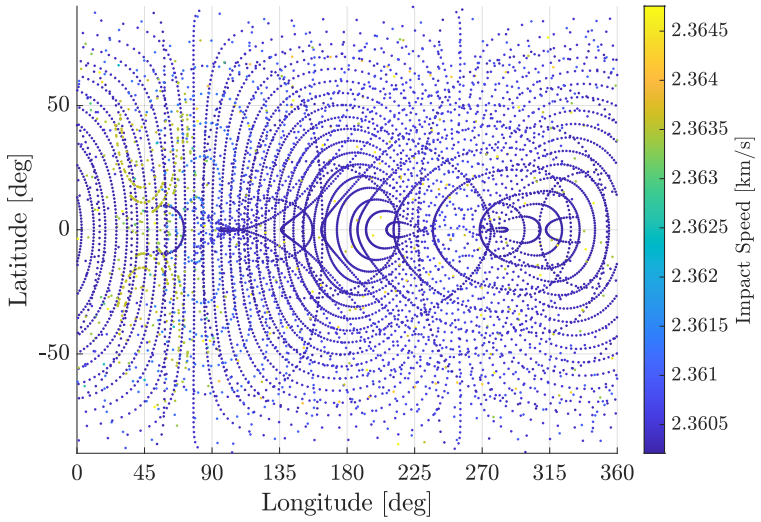

(b) Impact Speed

Figure 4.83.: Latitude Versus Longitude for Impacts of Unstable Manifolds Associated with the L_1 Axial Orbits

cation to that observed in the L_1 family is shown. However, the minimum TOF is 25.7 days, several days longer that that of the L_1 axial orbit family. Furthermore, no low Jacobi constant impacts are observed until nearly 40 days of propagation. This increased TOF provides reasoning for the reduced number of impacting orbits discovered. The sample trajectories from Figure 4.85 are displayed in Figure 4.86. Similar

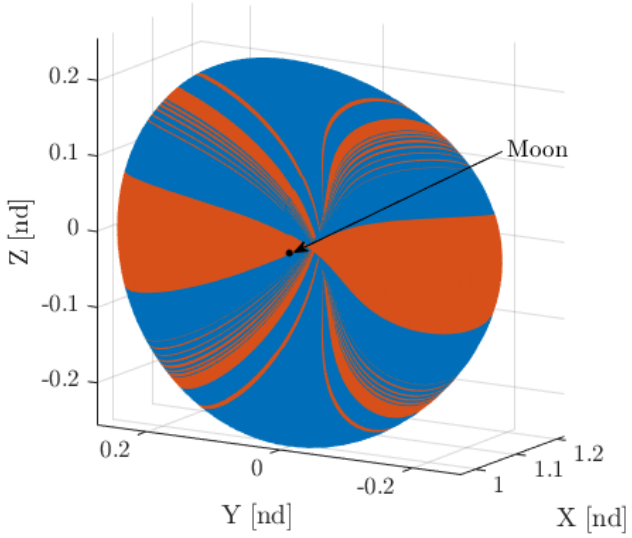

Figure 4.84.: L_2 Axial Orbits Where Red Indicates Axial Orbits with Impacting Manifolds and Blue Indicates Axial Orbits without Impacting Manifolds

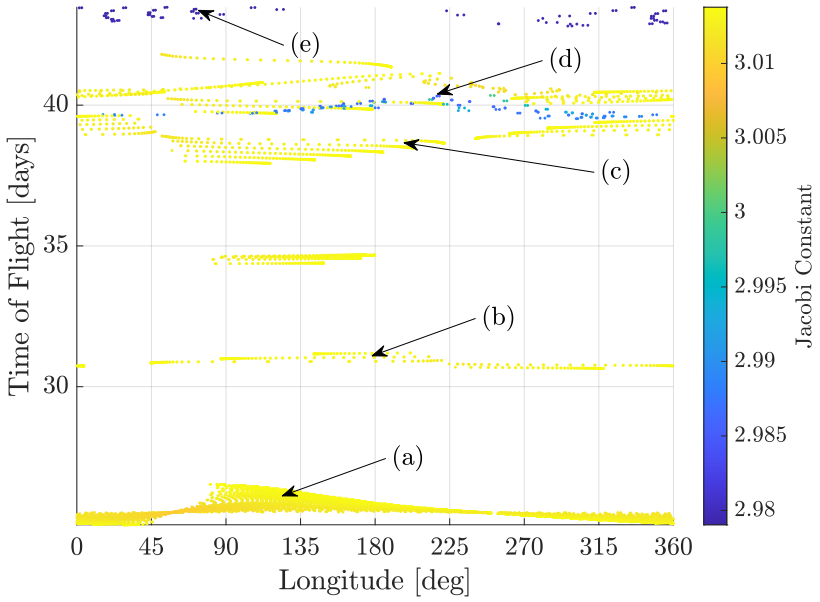

Figure 4.85.: Time of Flight as a Function of Longitude of Lunar Impact Conditions of Unstable Manifolds Associated with L_2 Axial Orbits

to the L_1 case, Figures 4.86(a), 4.86(b), and 4.86(c) present geometry groups for the nearly-planar members at lower TOFs and Figures 4.86(d) and 4.86(e) demonstrate

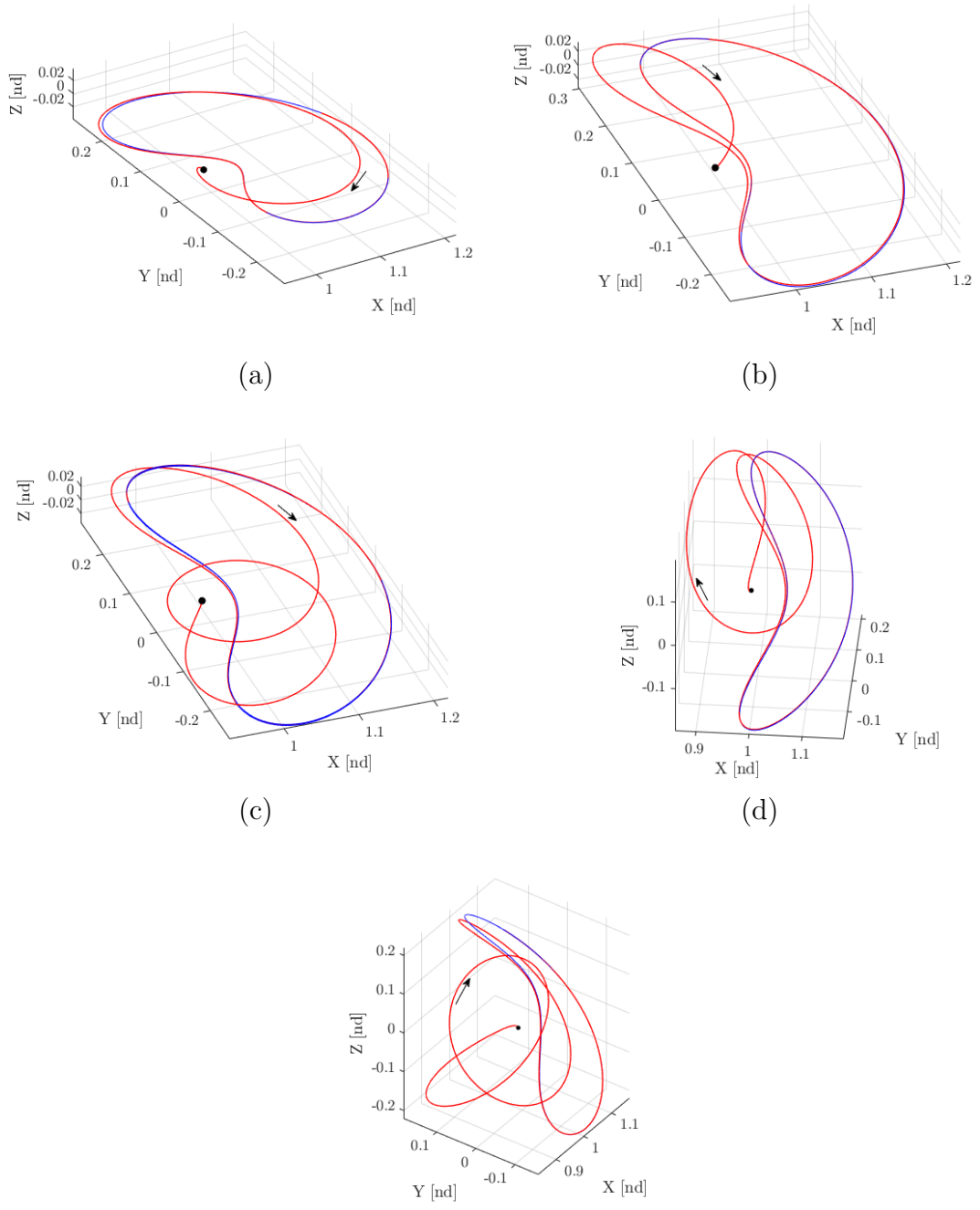

Figure 4.86.: Example Impacting Trajectories from L_2 Axial Orbits Corresponding to Marked Points in Figure 4.85

transfers from the more out-of-plane members at high TOFs. Notably, the availability of transfers originating from these out-of-plane members is limited with the transfers demonstrated in Figures 4.86(d) and 4.86(e) providing the bulk of geometry observed.

The latitude values of the L_2 axial impact conditions displayed in Figure 4.87 demonstrate the $\lambda = 0°$ symmetry observed in the L_1 axial orbits as well as the vertical families. Similar to the L_1 axial orbits, the discretization of the family mem-

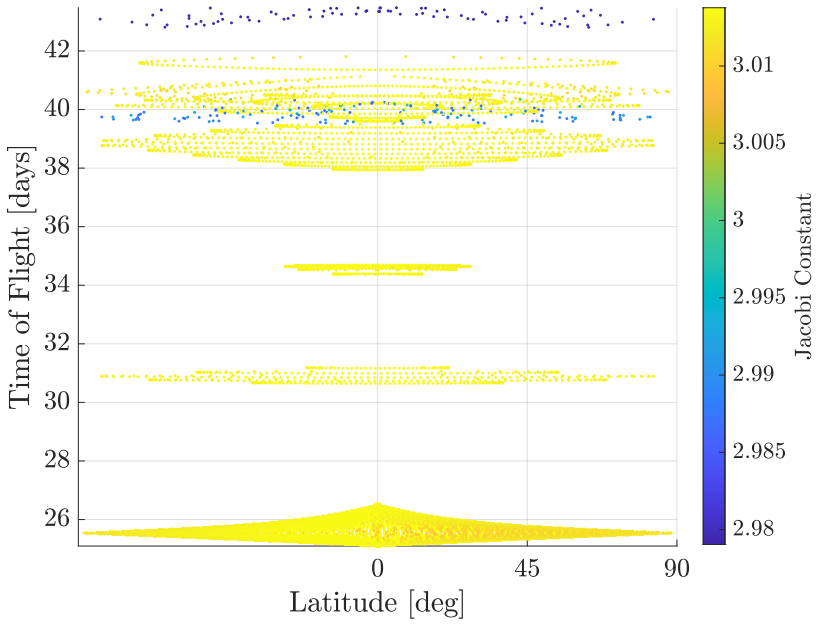

Figure 4.87.: Time of Flight as a Function of Latitude of Lunar Impact Conditions of Unstable Manifolds Associated with L_2 Axial Orbits

bers limits the perfection of the observed symmetry. Consistent with observations in Figure 4.85, low Jacobi constant impacts are not observed until around 40 days of propagation; these low Jacobi constant impacts do, however, span latitudes from $\lambda = -86°$ to $\lambda = 86°$ with no clearly preferred hemisphere. The higher Jacobi constant impacts in yellow, span latitudes until both the northern and southern poles at 25.5 days. The latitude versus longitude relation is demonstrated in Figure 4.88 for the L_2 axial orbits. Similarly to the L_1 axial family, the impact conditions span the full surface. However, the L_2 axial conditions demonstrate a sparsity of low Jacobi constant impacts with no clumped structure forming. Therefore, these low Jacobi

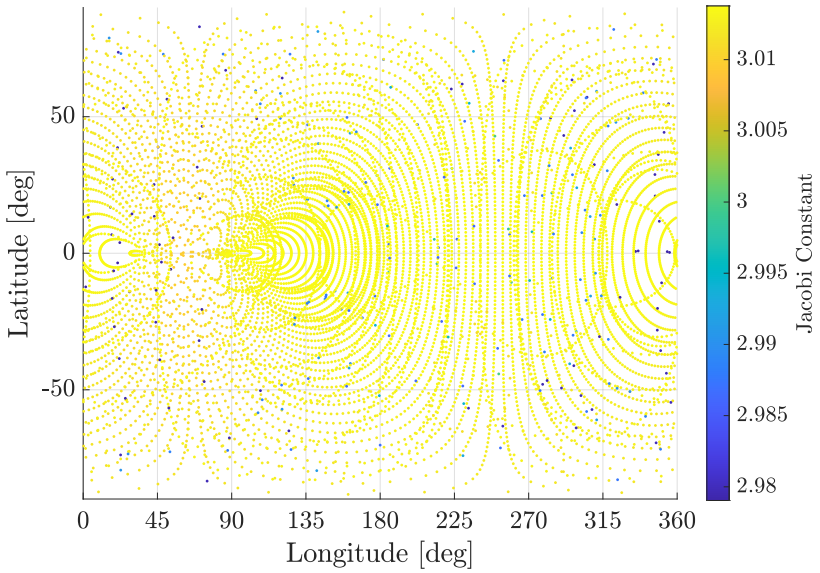

Figure 4.88.: Latitude Versus Longitude of Impact Conditions of Unstable Manifolds Associated with the L_2 Axial Orbit Family

constant trajectories, while nearby in energy and initial condition to each other, yield significantly varied impact locations. Conversely, the high Jacobi constant impacts near $\lambda = 0°$ yield tightly grouped impacts. Figures 4.89(a) and 4.89(b) display the data colored by angle and speed, respectively. The impact angles are minimize in the third quadrant and maximize in the first quadrant with smooth evolution between these extrema occurring in the second and fourth quadrants presenting relatively well structured angle behavior. The impact speeds vary only slightly throughout the impact conditions demonstrating the dominance of the lower Jacobi constant impact conditions.

The L_1 and L_2 axial orbits present substantial impact location opportunities but at significantly restricted Jacobi constant values and times-of-flight. The primary driver of this restriction is the lack of impacting conditions for the members of both families with greater out-of-plane components similar to the behavior observed in the vertical orbit families. Impacts are not observed until at least 23 days for either family and approaching 40 days for the lower Jacobi constant trajectories. The axial manifolds demonstrate similar symmetry properties to the vertical orbits, and thus

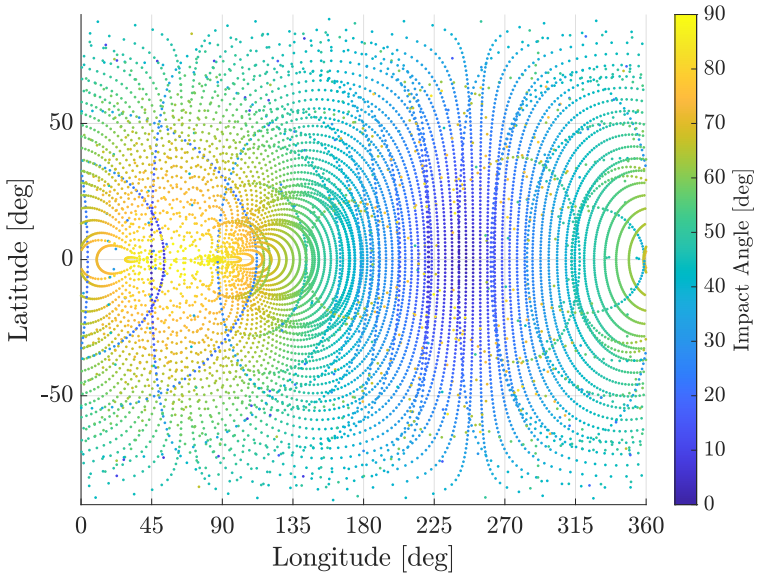

(a) Impact Angle

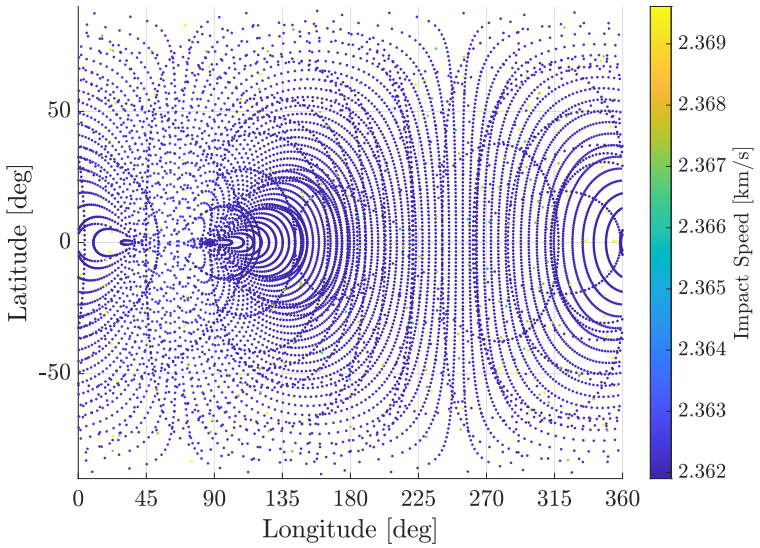

(b) Impact Speed

Figure 4.89.: Latitude Versus Longitude for Impacts of Unstable Manifolds Associated with the L_2 Axial Orbits

yield impacts spanning a large range of latitudes. The axial orbits, therefore, yield rich candidate trajectories for Lunar impact mission design.

Butterfly Orbit Family

Like the vertical and axial orbit families, the butterfly orbits maintain an unstable subspace throughout the family. However, the time constants of many butterfly orbits are greater than the 1.5 critical value cutoff point. Therefore, only a subset of the butterfly orbits are included in the Lunar surface access analysis; 125 of the 1000 orbits analyzed possess sufficiently fast manifold structures. Recall that analysis of the northern butterfly family yields identical results to that of the southern save a reflection over the xy-plane. Figure 4.90 presents representative orbits from the 125 Earth-Moon butterfly orbits with $\kappa_\tau < 1.5$. The unstable butterfly orbits span Jacobi

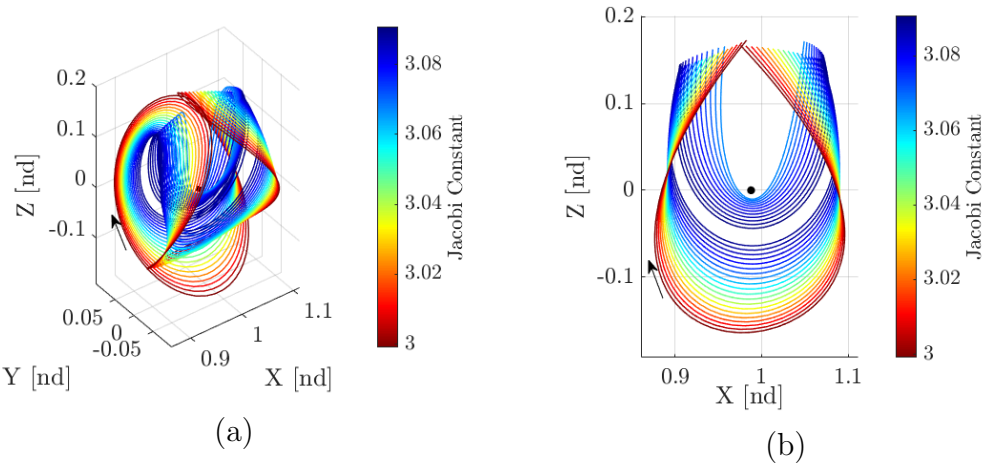

Figure 4.90.: Earth-Moon Northern Butterfly Orbits with Sufficiently Fast Manifold Departure

constants from 3.0 to slightly greater than 3.08. This range of Jacobi constants has been observed consistently across many of the unstable families analyzed. Trajectories on the unstable manifolds associated with these orbits are propagated for a maximum of approximately 43 days to determine impact characteristics.

Figure 4.91 presents the fast departure butterfly orbits colored by the existence of manifold structures impacting the Moon within the 43 day integration. A considerable number of these fast departure butterflies fail to yield impact conditions, indicated by

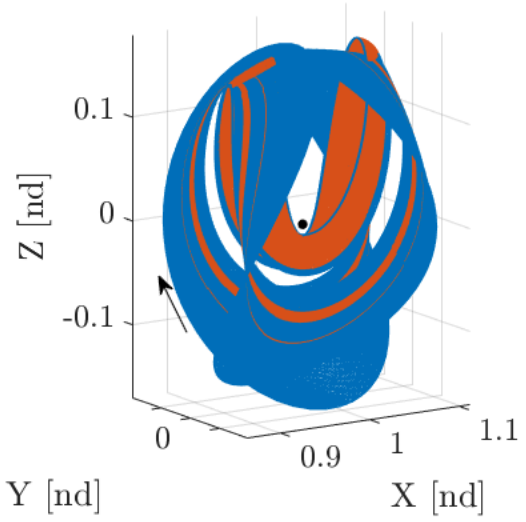

Figure 4.91.: Unstable Northern Butterfly Orbits with Manifold Structures Impacting the Moon Within 43 Days

the large number of blue orbits in the figure. Two main bands of impacting orbits are observed: a thick band in the section of butterfly orbits with smaller periapse radii and a thinner band in the high-periapse-radii butterfly orbits. Several other smaller groups exist as well, however. Of the 125 sufficiently unstable orbits analyzed, 49 are found with impacting unstable manifolds. The impacting orbits span Jacobi constants from $J = 3.058$ to $J = 3.090$ representing the upper end of Jacobi constants observed for the entirety of the butterfly orbits presented in Figure 4.90.

The impact longitudes and times-of-flight for the northern butterflies are shown in Figure 4.92. No impact are observed until after 30 days of propagation despite the proximity of the butterfly orbits to the Moon. Furthermore, the impact observed lower times-of-flight appearing as nearly vertical lines around 135° and 0° originate from the larger r_p butterfly group shown in Figure 4.90(a). These lines break near 34 days before beginning again around 36 days and continuing until the 43 day limit. Figures 4.93(a) and 4.93(b) demonstrate sample trajectories from these structures. All impacts from these linear groups present very similar geometry. Notably, these structures are the only locations where impacts from the larger r_p butterfly orbits are

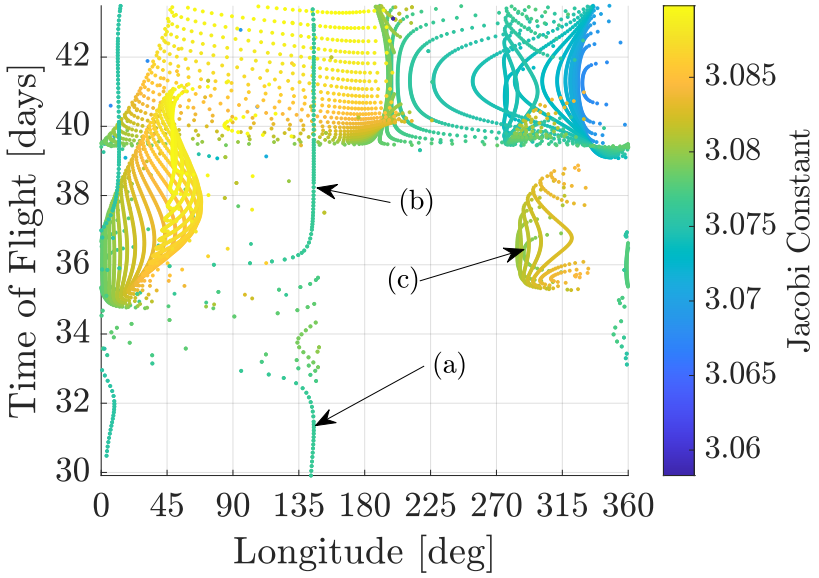

Figure 4.92.: Time of Flight and Longitude of Impact Conditions for Unstable Manifolds Associated with Northern Butterfly Orbits

observed; all remaining impact conditions in Figure 4.92 originate from the smaller r_p group of sufficiently unstable butterfly orbits. Figure 4.93(c) presents an example of these low r_p impact trajectories. While the impact locations of these low r_p trajectories span a wide range in Figure 4.92, the geometrical structure does not deviate greatly from that observed in Figure 4.93(c). Apparent in Figure 4.92, at TOFs less than 35 days, impacts are constrained to the first and second quadrants and not until approximately 40 days do a large number of impacts arise in the third and fourth quadrants congruent with the observed geometry of the butterfly orbits. Figure 4.94 displays the impact condition latitudes with the large r_p impact conditions highlighted. The large r_p impact conditions appear in the latitude figure as vertical lines at $\lambda = 30°$ and $\lambda = 45°$. Thus, the impact conditions originating from the higher periapse radius butterfly orbits present a very limited set of Lunar impact conditions despite impacting at slightly lower TOFs. The lower periapse radius impact conditions present impacts at all latitudes beyond 38 day TOF but present impacts at and below $\lambda = 45°$ at TOFs around 35 days. Therefore, as observed in Figures 4.92 and 4.94, the lower periapse radius butterfly orbits present a wide range

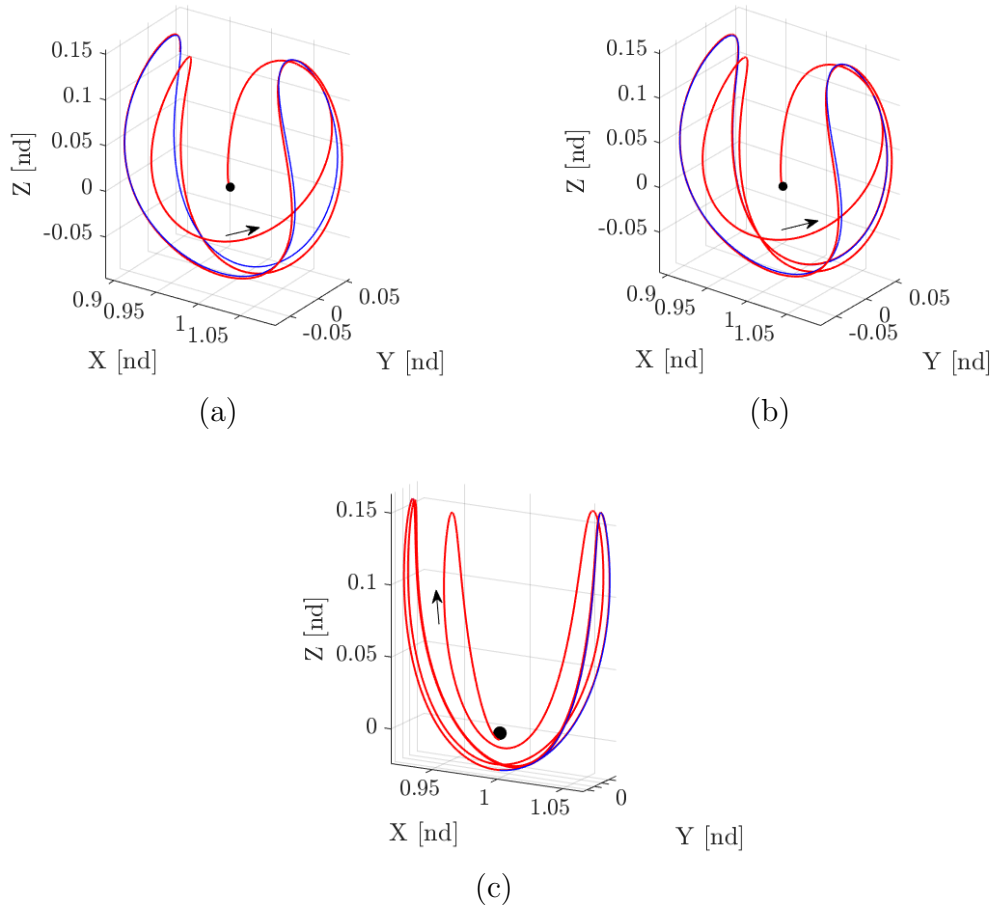

Figure 4.93.: Example Impacting Trajectories from Northern Butterfly Orbits Corresponding to Marked Points in Figure 4.92

of impact locations at higher times-of-flight despite the limited number of orbits with impacting manifolds. The latitude and longitude of the impact conditions appear in Figure 4.95. The impact conditions appear most often in the northern hemisphere of the Lunar surface with southern extensions around $\varphi = 0°$ and $\varphi = 180°$. The large r_p impacts appear as an arc in the first and second quadrants with the rest of the impact conditions originating from the lower periapse radius orbits. The higher Jacobi constant conditions yield impacts in the first two quadrants with an evolution to lower Jacobi constant impacts in the third and fourth quadrants. Two large gaps appear centered around $\varphi = 90°$ and $\varphi = 270°$ at the equator. Even considering

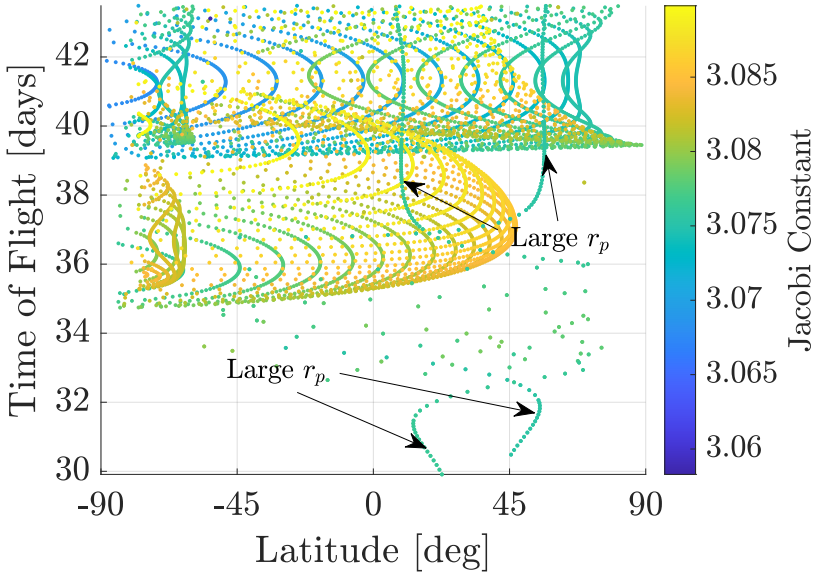

Figure 4.94.: Time of Flight as a Function of Latitude of Lunar Impact Conditions of Unstable Manifolds Associated with Northern Butterfly Orbits

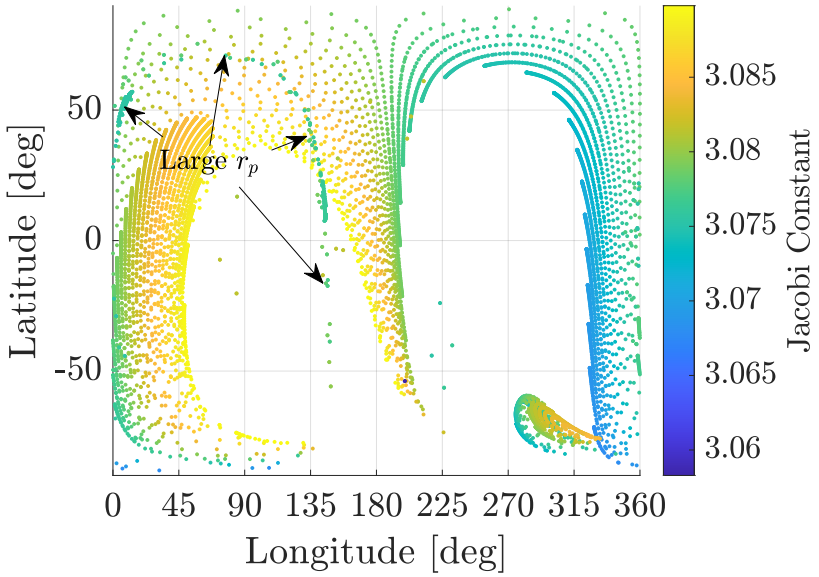

Figure 4.95.: Latitude Versus Longitude of Impact Conditions of Unstable Manifolds Associated with the Northern Butterfly Orbit Family

the southern family, these gaps indicate that near equatorial impacts are not possible around these longitudes. Figure 4.96 presents the latitude and longitude colored by impact angle and speed. The butterfly impact display strong correlation between

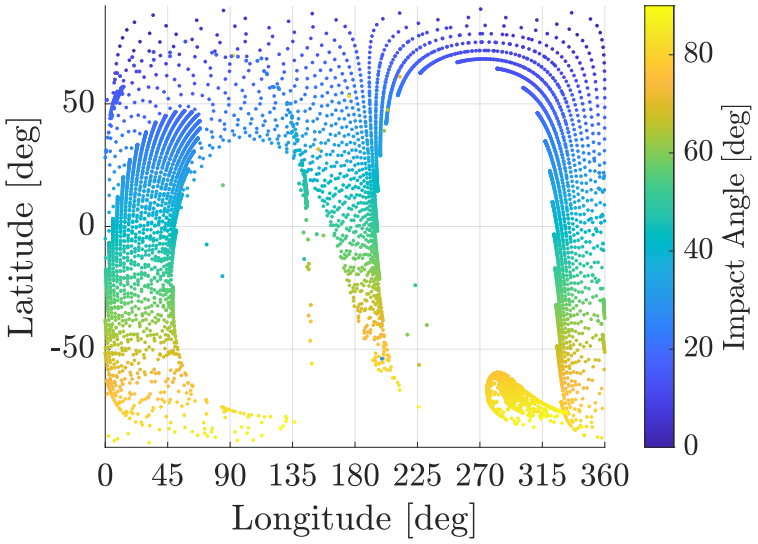

(a) Impact Angle

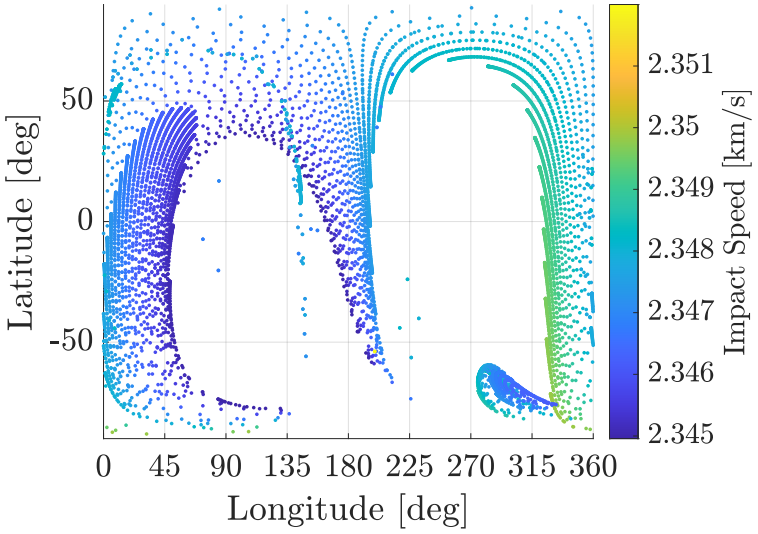

(b) Impact Speed

Figure 4.96.: Latitude Versus Longitude for Impacts of Unstable Manifolds Associated with the Northern Butterfly Orbits

impact latitude, λ, and the impact angle, ϑ. Lower latitude conditions yield nearly tangent impacts while those at high latitudes yield impacts normal to the surface. Furthermore, all impact angles between 0° and 90° are found. Reflecting the impact conditions over $\lambda = 0$ to represent the southern butterfly presents the inverse case where high latitude conditions yield high impact angles. The impact speeds show

similar quadrant dependence to that observed in the vertical and axial families, but the significantly reduced Jacobi constant range of the impacting butterflies yields total variations not exceeding 7 m/s.

Period-Four Halo Orbit Families

The period-four halo families present multi-revolution periodic orbits near the Moon and both contain unstable members with sufficiently low time constants. However, the P4HO1 family possesses significantly fewer of these sufficiently low time-constant orbits and, furthermore, all those that the P4HO1 does possess have periapse radii less than that of the mean Lunar radius evident in Figure 4.31. As a result, the manifolds associated these fast departure P4H01 orbits simply impact the Moon when the trajectories pass near the periapse of the underlying periodic orbit. Consequently, the P4HO1 orbits are not included in the impact analysis. Conversely, the P4HO2 family presents sufficiently unstable orbits with Lunar periapse radii above the Lunar surface.

The P4HO2 orbits are presented in Figure 4.97 colored corresponding to the binary indication of departure speed obtained through the time constant. Clearly, the majority of the P4HO2 family possesses sufficiently low time constants. Only a small section of the P4HO2 family near the bifurcation with the L_2 northern halo orbits yields "slow" manifold departures. The unstable manifolds associated with the fast departure orbits in Figure 4.97 are propagated for approximately 43 days and impact conditions are determined. Figure 4.98 displays the P4HO2 orbits colored based on the existence of impacting manifolds. Noticeably, many large members of the family fail to yield impact conditions due to the limitation of the TOF to 43 days. However, a large number of the P4HO2 family orbits do present impact conditions. The longitudes and times-of-flight of these impact conditions are shown in Figure 4.99. The TOFs for impacts originating from the manifolds associated with the P4HO2 orbits are higher than those observed for other Lunar region periodic orbits as the

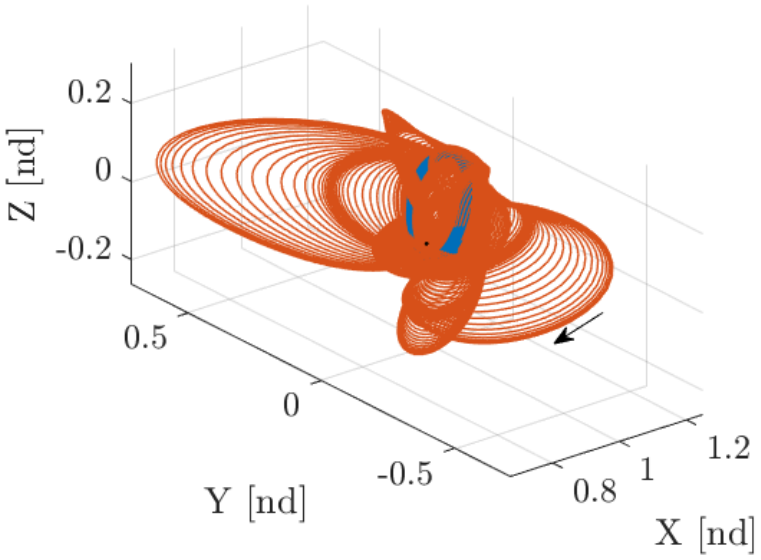

Figure 4.97.: P4HO2 Orbits where Red Indicates $\kappa_\tau < 1.5$ and Blue Indicates Otherwise

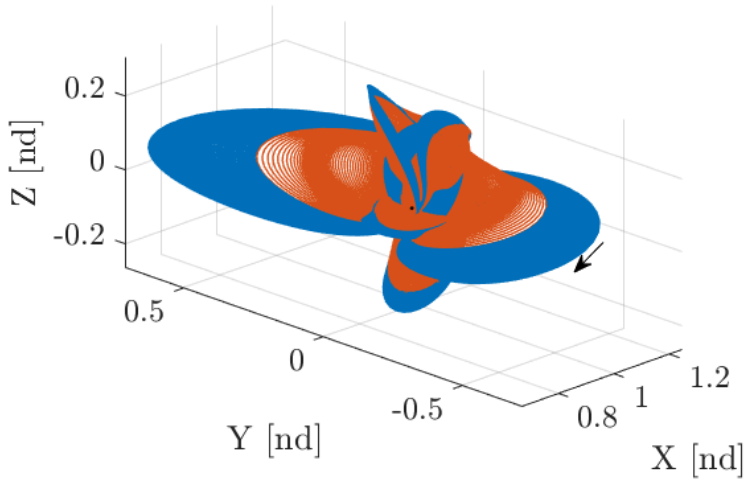

Figure 4.98.: Unstable P4HO2 Orbits with Manifold Structures Impacting the Moon Within 43 Days

first impact occurs at 25.6 days. However, impacts at all longitudes are observed. The higher Jacobi constant impacts are generally focused in the third quadrant and the lower Jacobi constant impacts are similarly focused in the first quadrant. As

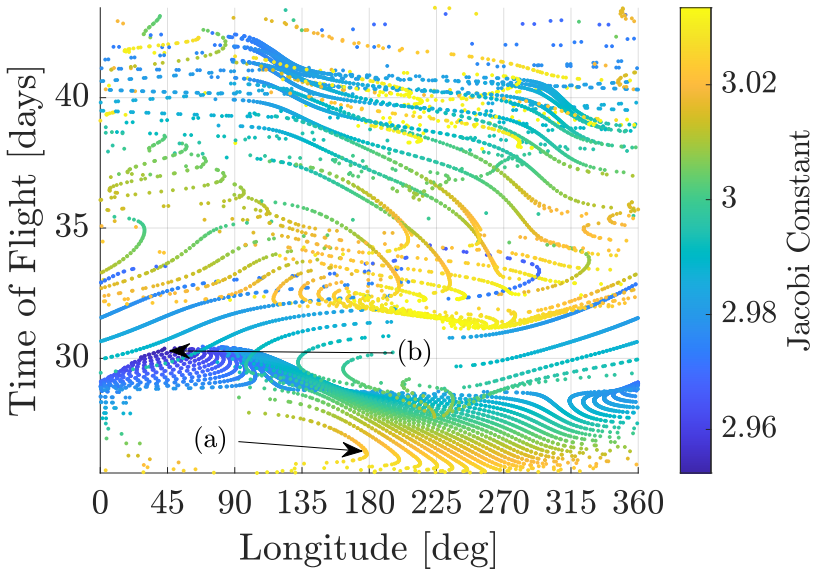

Figure 4.99.: Time of Flight and Longitude of Impact Conditions for Unstable Manifolds Associated with P4HO2 Orbits

observed in the impact patterns of other periodic orbit families, at higher TOFs, the impact conditions are less structured than those at lower times-of-flight. Figure 4.100 presents two sample impacting geometries identified in Figure 4.99. Figure 4.100(a) depicts a higher Jacobi constant impacting trajectory and, thus, is smaller than than the lower Jacobi constant orbit shown in Figure 4.100(b). The geometry of the high Jacobi constant impacts varies substantially more across impact conditions compared with the low Jacobi constant impacts. This geometry variation permits the higher Jacobi constant orbits to yield more varied impact locations as evident in Figure 4.99. The latitudes corresponding to the impact conditions in Figure 4.99 are given in Figure 4.101. The lower latitude values are dominated by the higher Jacobi constants congruent with the impact geometry shown in Figure 4.100(b). Nevertheless, impacts across all Jacobi constant values are found at all latitudes between the poles. However, the structure of the impact conditions shown in Figure 4.101 restricts the Jacobi constants available at a given TOF for a given latitude. Both the latitude and longitude are shown in Figure 4.102 colored by Jacobi constant. This figure further emphasizes the dominance of higher Jacobi constant impacts at low latitudes. How-

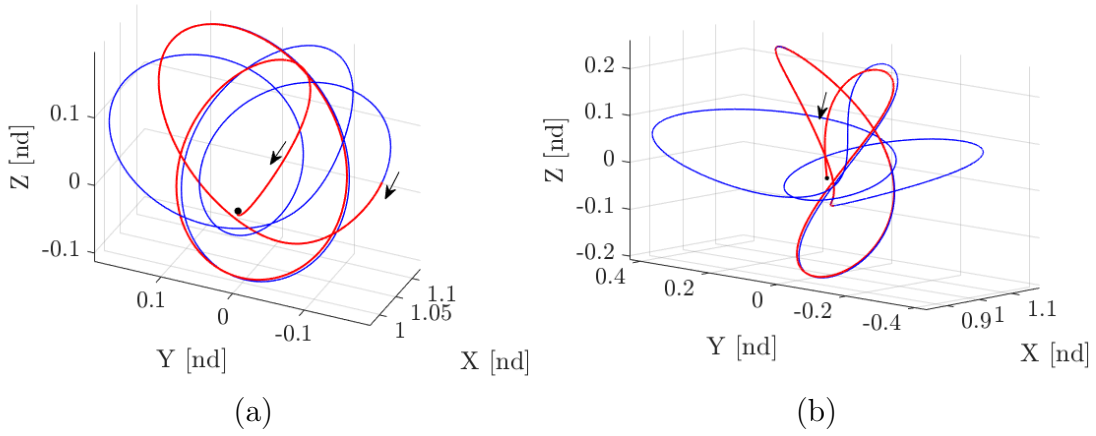

Figure 4.100.: Example Impacting Trajectories from P4HO2 Orbits Corresponding to Marked Points in Figure 4.99

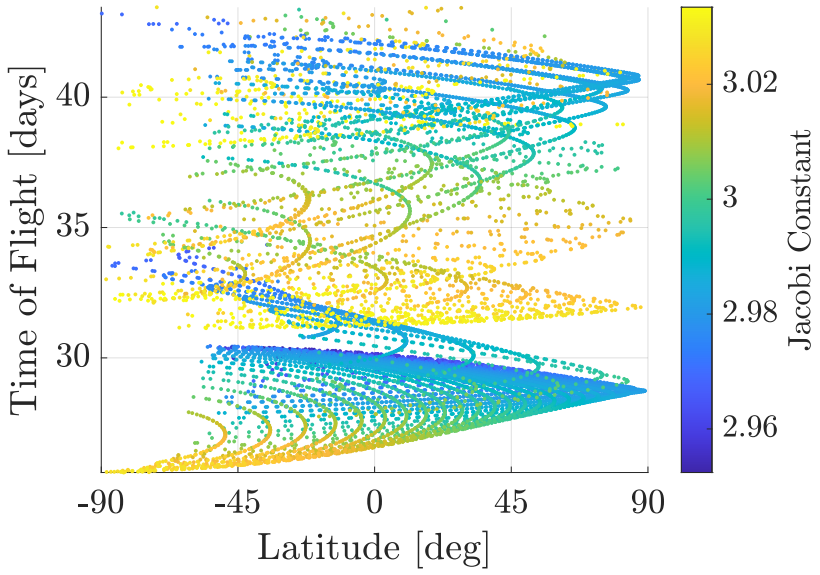

Figure 4.101.: Time of Flight and Latitude of Impact Conditions for Unstable Manifolds Associated with P4HO2 Orbits

ever, given the symmetry of the southern version of the family, a southern P4HO2 orbit at a low Jacobi constant may be used to achieve southern hemisphere impacts. However, even without incorporation of the southern family, impact conditions are found for nearly all locations on the Lunar surface. Finally, the angles and speeds of the P4HO2 impacts are investigated in Figure 4.103. As observed for the other peri-

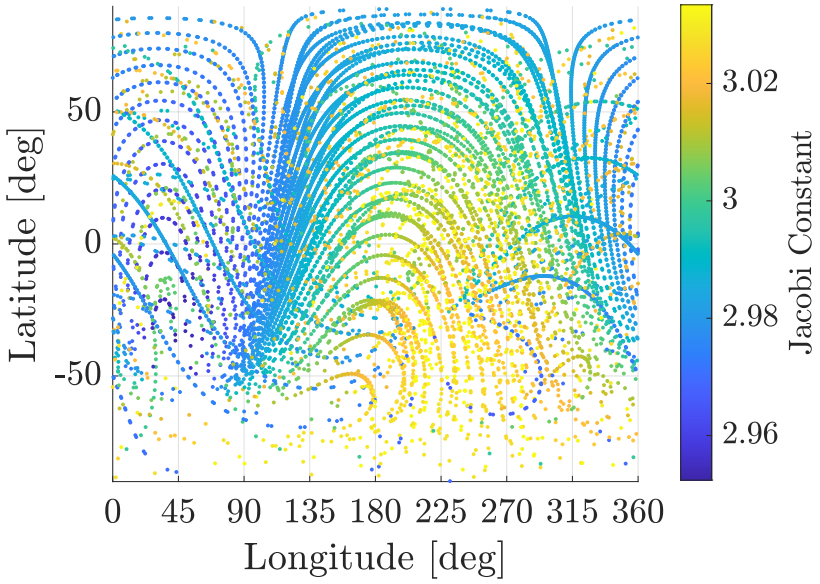

Figure 4.102.: Latitude Versus Longitude of Impact Conditions of Unstable Manifolds Associated with the Northern P4HO2 Orbit Family

odic orbit families, the impact speed shown in Figure 4.103(b) directly correlates to the Jacobi constant of the impacting trajectory. Consequently, lower impact speeds are observed in the far southern latitudes and conversely for the high latitudes. Impact angles decrease as latitude increases with nearly normal impacts occurring near $\lambda = 90°$. This behavior is evident in the impact trajectory shown in Figure 4.100(b). Similarly, Figure 4.100(a) presents an example of the high impact angles observed at low latitudes.

The P4HO2 family presents a substantial amount of impacts on the Lunar surface ranging in Jacobi constant from $J = 2.95$ to $J = 3.03$. These impacts span a significant portion of latitudes and longitudes and the existence of the southern and northern families presents a large variety of options for (J, φ, λ) combinations.

4.3.5 Low Lunar Orbit Access Characteristics of Spatial Orbit Families

Understanding of the LLO access capabilities of the spatial orbit families provides insight into the design of missions moving between periodic orbits in the Lunar re-

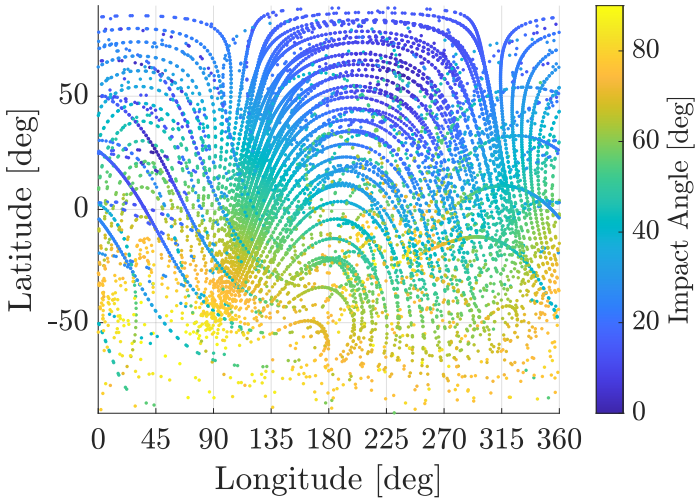

(a) Impact Angle

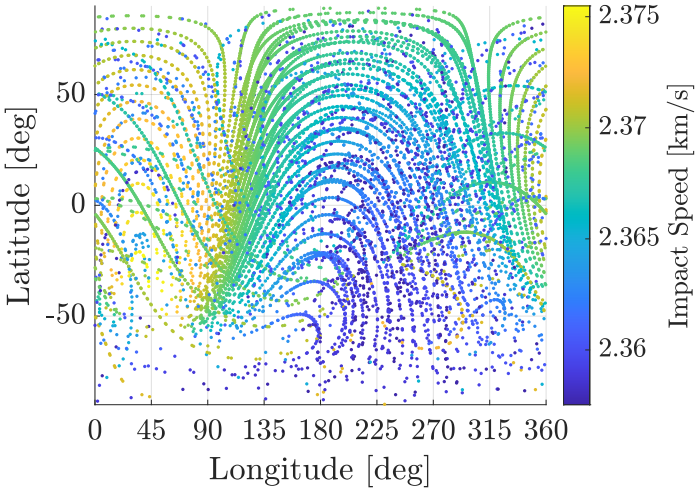

(b) Impact Speed

Figure 4.103.: Latitude Versus Longitude for Impacts of Unstable Manifolds Associated with the P4HO2 Orbits

gion and Keplerian orbits near the Moon. Therefore, periapse locations along the same unstable manifolds investigated in Section 4.3.4 are found to determine transfer geometries from Lunar region periodic orbits to LLO. Unlike the planar case, the apse conditions along the unstable manifolds associated with spatial periodic orbits contain out-of-plane components. Subsequently, the inclinations associated with the periapse locations are also determined.

Halo Orbit Families

The unstable manifolds of the halo orbits with $\kappa_\tau < 1.5$ are propagated to find periapse conditions with respect to the Moon and the inclination and altitude of these periapse conditions are recorded. As both the L_1 and L_2 halo orbits possess sufficiently fast manifold structures, both families will be investigated. Note, because of the symmetry, the northern and southern families will yield apses with the same inclinations but differing right ascensions. Figure 4.104 presents the periapse altitudes and the propagation times required to reach those apses for the L_1 Northern halo family. While gaps exist at higher altitudes, the L_1 halo orbits present periapses at

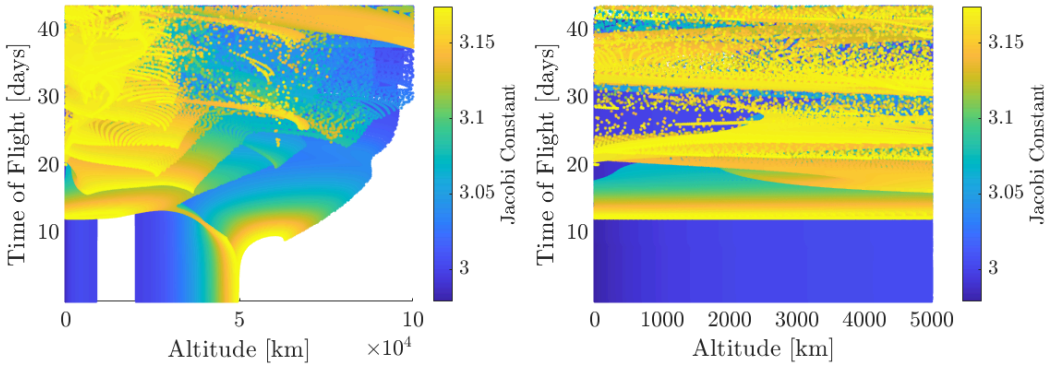

(a) Altitude $< 100,000$ km (b) Altitude $< 5,000$ km

Figure 4.104.: Time of Flight and Altitude for Periapse Conditions on Manifolds Associated with the L_1 Halo Orbit Family

all altitudes less than approximately 8600 km. However, the low time-of-flight and low Jacobi constant periapse conditions result from periapses along the low periapse orbits themselves. Higher Jacobi constant periapses do not occur until around 12 days as observed in Figure 4.104(b). At higher times of flight, periapses across all altitudes are observed for nearly all Jacobi constant values indicating a significant amount of LLO access. Figure 4.105 provides the inclinations and altitudes of the periapses at altitudes less than 5000 kilometers. Clearly, a majority of low inclinations periapse conditions occur at high Jacobi constant values. This relationship makes sense as

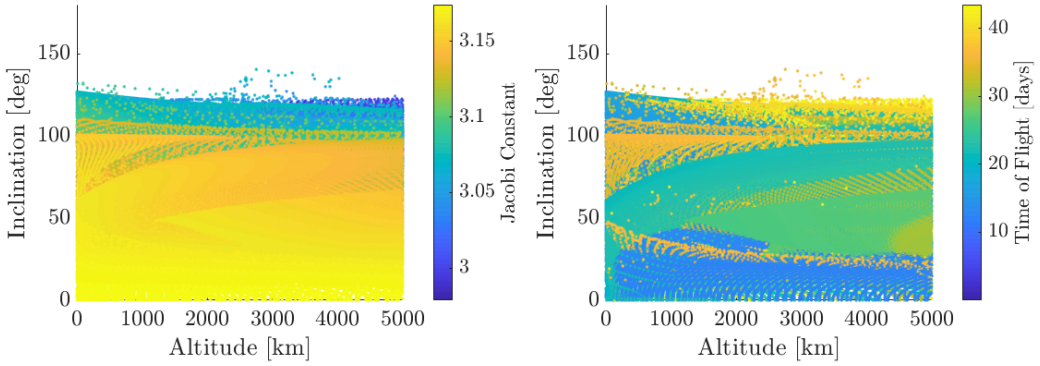

(a) (b)

Figure 4.105.: Inclinations and Altitudes of Periapse Conditions on Manifolds Associated with the L_1 Halo Orbit Family

the higher Jacobi constant halo orbits possess less of an out-of-plane component. Importantly, all inclinations below approximately 120° are feasible to reach from the L_1 halos for the given altitude range. Figure 4.106 demonstrates the times-of-flight and altitudes for the L_2 halo orbit family periapse conditions. The overall structure

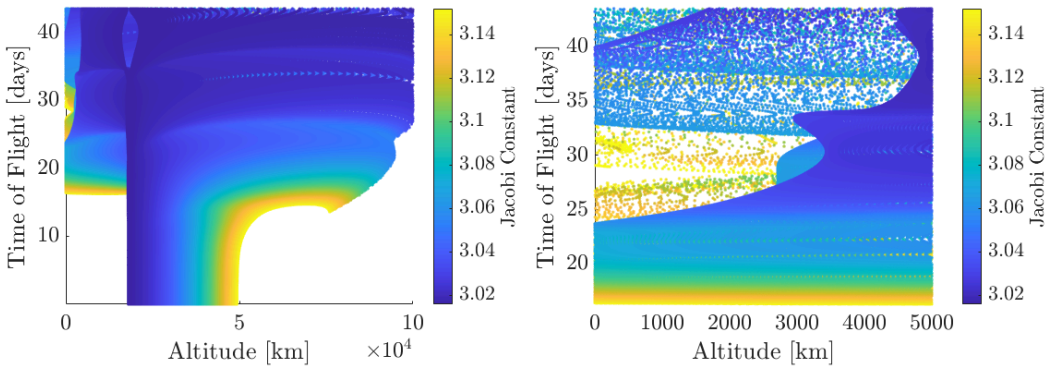

(a) Altitude $< 100,000$ km (b) Altitude $< 5,000$ km

Figure 4.106.: Time of Flight and Altitude for Periapse Conditions on Manifolds Associated with the L_2 Halo Orbit Family

is similar to that of the L_1 halo orbits. However, due to the slow manifolds of the L_2 halo orbits near the Moon, the low time-of-flight periapses observed in the L_1 case

are not found in Figure 4.106(b). As a result, below 18,000 km altitude, no apses are found until after approximately 16 days. The inclinations and altitudes colored by Jacobi constant and time-of-flight for the L_2 halo orbits are shown in Figures 4.107(a) and 4.107(b), respectively. The behavior present in these figures is similar to that of the L_1 halo orbits. All inclinations below approximately 120° are available at all altitudes shown.

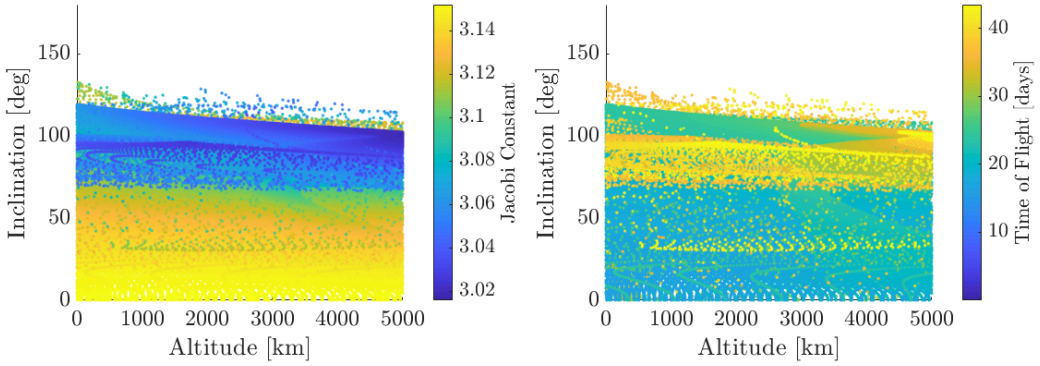

Figure 4.107.: Inclinations and Altitudes of Periapse Conditions on Manifolds Associated with the L_2 Halo Orbit Family

Vertical Orbit Families

Similar to the halo orbit families, the unstable manifolds of the sufficiently unstable members of the vertical orbit families are propagated to determine periapse conditions. The times-of-flight and altitudes of the L_1 vertical orbit manifold periapses are shown in Figure 4.108. The vertical orbit manifolds yield a substantial amount of apses at high altitudes but yield very few low altitude periapses with periapses below 1000 km not occurring until after 20 days echoing behavior observed in the impact conditions. As observed in Figure 4.108(b), all of the low altitude periapses occur at high Jacobi constant values, beneficial for access from other Lunar-region orbits. The corresponding inclinations and altitudes are shown in Figure 4.109. Clearly, a band

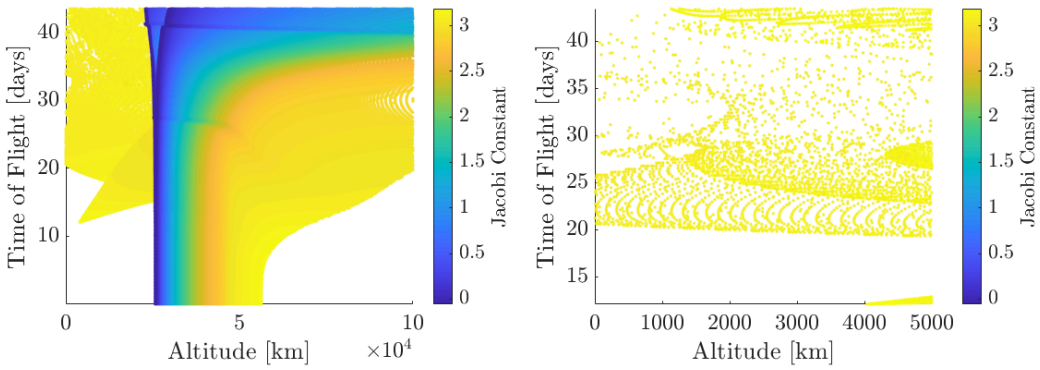

(a) Altitude $< 100,000$ km (b) Altitude $< 5,000$ km

Figure 4.108.: Time of Flight and Altitude for Periapse Conditions on Manifolds Associated with the L_1 Vertical Orbit Family

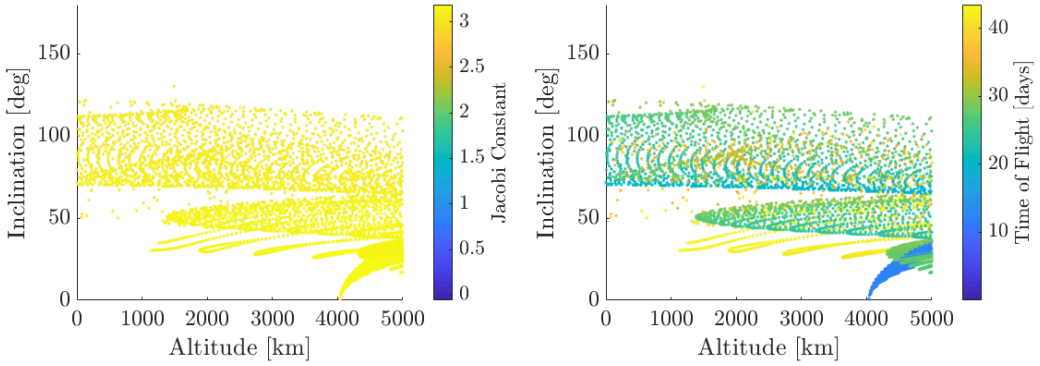

(a) (b)

Figure 4.109.: Inclinations and Altitudes of Periapse Conditions on Manifolds Associated with the L_1 Vertical Orbit Family

is observed centered around $i = 90°$ inclination consistent with the vertical nature of the orbits. Periapses are observed between $i = 75°$ and $i = 115°$ for all the altitudes given. An additional grouping occurs around $i = 50°$ at altitudes beyond 1000 km. Continuing for L_2, the periapse altitudes and times-of-flight for the L_2 vertical orbits are given in Figure 4.110. The L_2 results are very similar to those of the L_1 vertical orbits, but do demonstrate slightly higher times of flight across the board. Similarly, for the inclination and altitudes given in Figure 4.111, the band around 90° is again

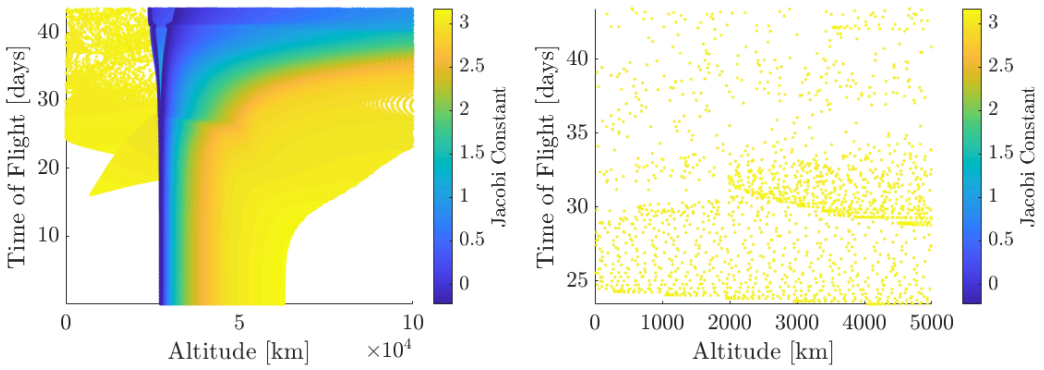

(a) Altitude $< 100,000$ km (b) Altitude $< 5,000$ km

Figure 4.110.: Time of Flight and Altitude for Periapse Conditions on Manifolds Associated with the L_2 Vertical Orbit Family

observed with another grouping occurring at altitudes beyond 2000 km. Overall, the vertical orbits present a more constrained set of periapse characteristics than the halo orbit families.

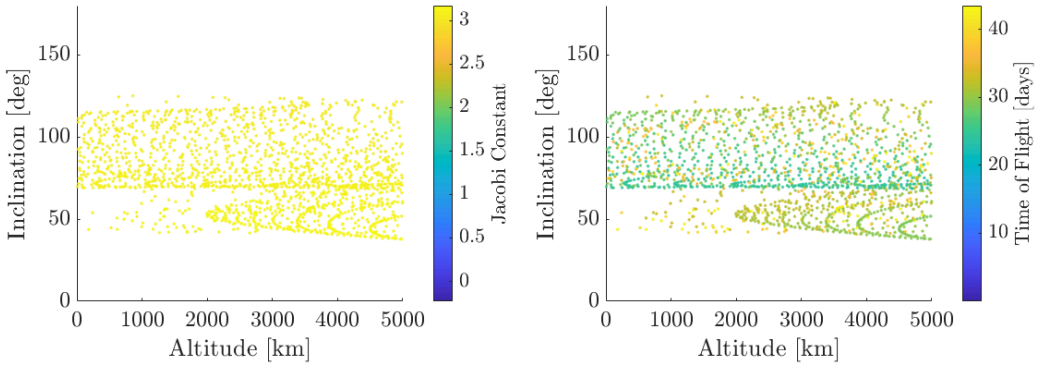

(a) (b)

Figure 4.111.: Inclinations and Altitudes of Periapse Conditions on Manifolds Associated with the L_2 Vertical Orbit Family

Axial Orbit Families

The altitudes and times-of-flight of the periapses along the unstable manifolds of the L_1 axial orbits are shown in Figure 4.112. Similar to the observations regard-

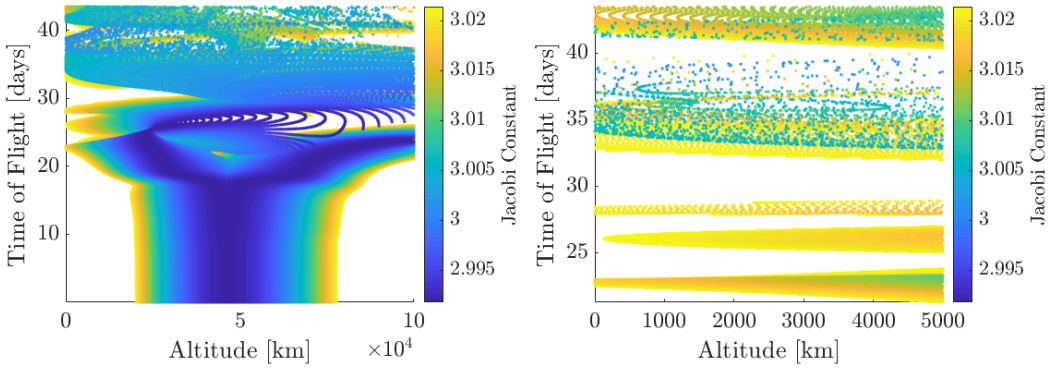

(a) Altitude $< 100,000$ km (b) Altitude $< 5,000$ km

Figure 4.112.: Time of Flight and Altitude for Periapse Conditions on Manifolds Associated with the L_1 Axial Orbit Family

ing the Lunar impacts, the axial orbits require longer times-of-flight to reach lower altitudes. The first L_1 axial periapse below 5000 km does not occur until after 20 days of propagation. However, after 20 days several groups are observed that span all altitudes below 5000 km. These bands are dominated by higher Jacobi constant periapses and very few low Jacobi constant conditions are observed at low altitudes. The inclinations and altitudes plotted in Figure 4.113 demonstrate that the L_1 axial orbit manifolds provide an exceptional amount of inclination and altitude coverage at low altitudes. The behavior observed indicates that manifolds exist that offer transfers to all inclination and altitude combinations below 5000 km altitude presenting a divergence from the capabilities observed in the halo and vertical orbit families. The L_2 axial altitudes and TOFs shown in Figure 4.114 appear very similar to that observed for L_1. Furthermore, like the L_1 axial orbits, the L_2 axial family presents complete coverage of altitudes and inclinations below 5000 km as observed in Figure 4.115. The L_1 and L_2 axial families present significant coverage of periapse locations

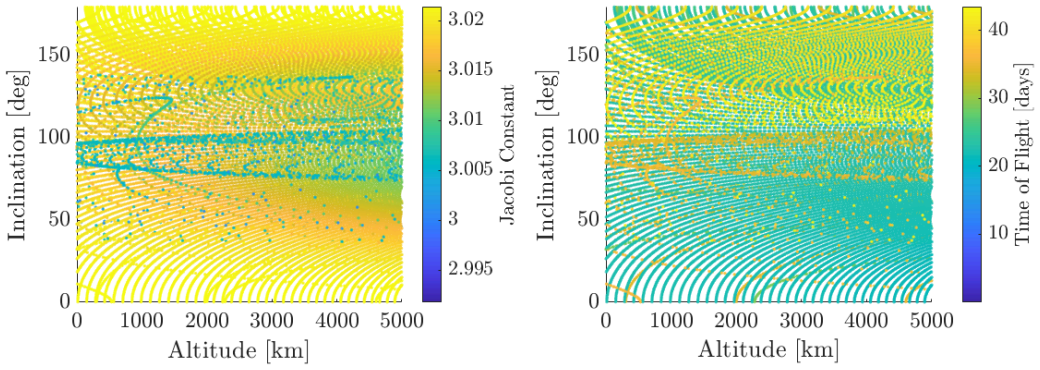

(a) (b)

Figure 4.113.: Inclinations and Altitudes of Periapse Conditions on Manifolds Associated with the L_1 Axial Orbit Family

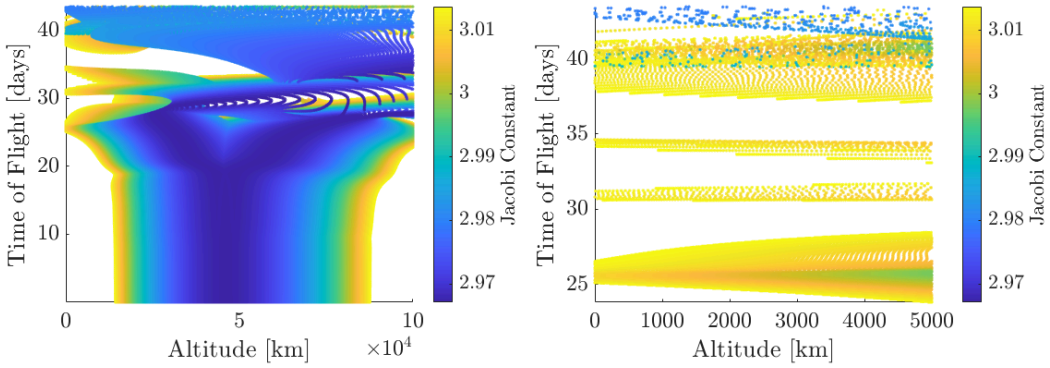

(a) Altitude $< 100,000$ km (b) Altitude $< 5,000$ km

Figure 4.114.: Time of Flight and Altitude for Periapse Conditions on Manifolds Associated with the L_2 Axial Orbit Family

at low Lunar altitudes. However, these conditions occur at lower Jacobi constants than those of the vertical and halo orbits and required longer times-of-flight. These trajectories may serve, however, as intermediate arcs between lower Jacobi constant orbits and high Jacobi constant LLOs.

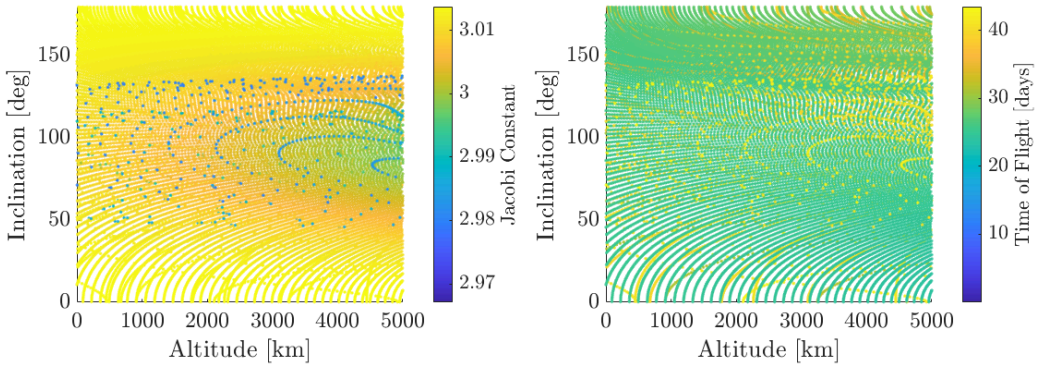

(a) (b)

Figure 4.115.: Inclinations and Altitudes of Periapse Conditions on Manifolds Associated with the L_2 Axial Orbit Family

Butterfly Orbit Family

A similar analysis is performed for the northern butterfly orbits, but recall that the number of sufficiently unstable Butterfly orbits was small. Therefore, the resulting conditions are more limited than the other Lunar region periodic orbit families. Figure 4.116 depicts the altitudes and times-of-flight of the periapse conditions. A large gap

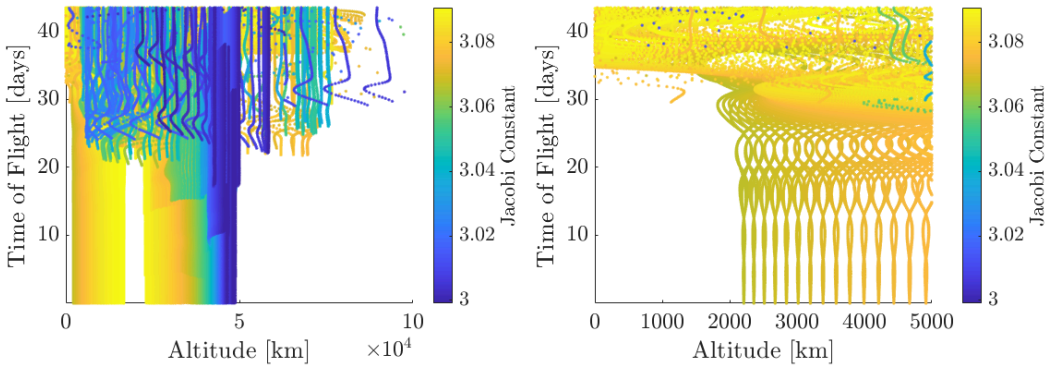

(a) Altitude $< 100,000$ km (b) Altitude $< 5,000$ km

Figure 4.116.: Time of Flight and Altitude for Periapse Conditions on Manifolds Associated with the L_2 Butterfly Orbit Family

is observed at periapse altitudes below approximately 2100 km; periapses do not

occur at these altitudes for TOFs less than nearly 30 days. Additionally, the lower altitude impacts are all at higher Jacobi constants as the low Jacobi constant orbits depart the Lunar region. Figure 4.117 demonstrates the inclinations and altitudes of these periapse conditions. Clearly, the inclinations at which the periapses occur

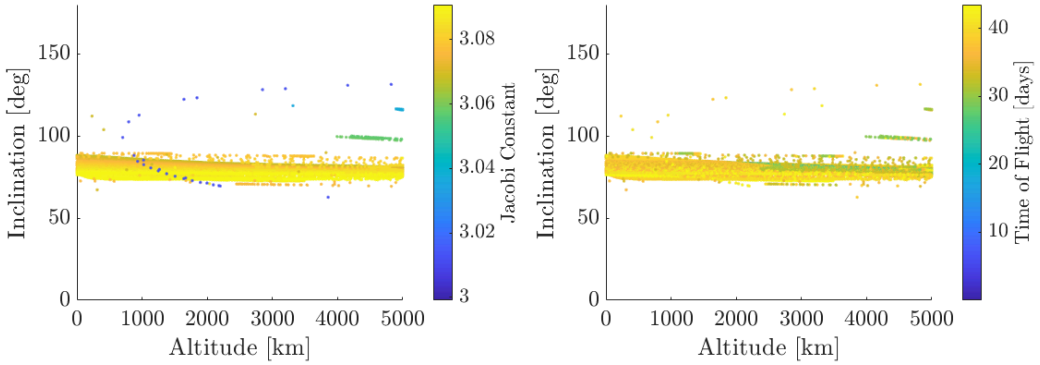

Figure 4.117.: Inclinations and Altitudes of Periapse Conditions on Manifolds Associated with the L_2 Butterfly Orbit Family

are severely limited to a thin band around 90°. While these bands do extend across all altitudes, they present a significant restriction on available insertion inclinations. Overall, the northern butterflies present higher Jacobi periapses at low altitudes, but are severely limited in the times-of-flight and inclinations available.

Period-Four Halo Orbit Families

Finally, the periapse investigation is performed for the period-four halo orbit families. As discussed in Section 4.3.4, the P4HO1 family does not yield fast manifold departures at periapse radii above the Lunar radius and, thus, is not included in the periapse investigation. Figure 4.118 presents the times-of-flight and altitudes for the P4HO2 family. While a large number of periapses are observed at high altitudes, a gap is observed at low times-of-flight for low altitudes. No periapses are observed below 5000 kilometers until after 22 days, congruent with the long periods of the un-

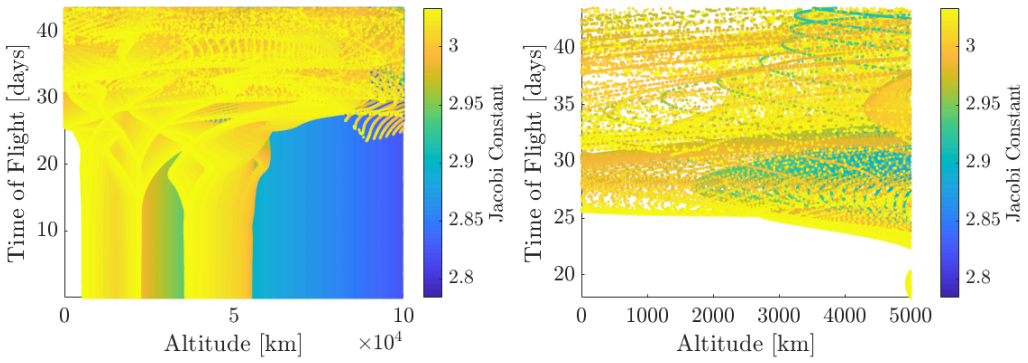

(a) Altitude $< 100,000$ km (b) Altitude $< 5,000$ km

Figure 4.118.: Time of Flight and Altitude for Periapse Conditions on Manifolds Associated with the P4HO2 Orbit Family

derlying periodic orbits. However, after 22 days, many periapses are found at higher Jacobi constants across all altitudes. Figure 4.119 shows the inclinations and altitudes of the periapse conditions. Similar to the butterfly orbits, a band is observed

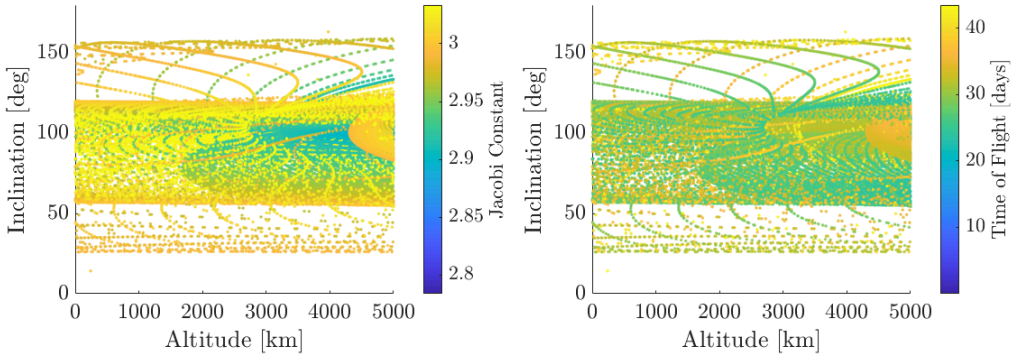

(a) (b)

Figure 4.119.: Inclinations and Altitudes of Periapse Conditions on Manifolds Associated with the P4HO2 Orbit Family

around $i \approx 90°$ but extends farther to $i \approx 60°$ and $i \approx 120°$. Despite the restriction on the inclinations of the periapses, a large number of low-altitude periapses are observed. Additionally, those at lower altitudes demonstrate higher Jacobi constant values indicating utility for transfers from other Lunar region orbits.

5. APPLICATION: LUNAR ACCESS FROM 9:2 LSR NRHO USING INTERMEDIATE PERIODIC ORBITS

The utility of intermediate periodic orbits as a method of designing transfers to the Lunar surface and LLO is investigated through the design of trajectories from the 9:2 LSR NRHO introduced in Section 3.1. Impulsive transfers are determined from the NRHO to the Shackleton crater locations in 2023 as well as from the NRHO to a circular LLO with $i = 90°$.

5.1 Shackleton Crater Impact Trajectories

A key drawback of the method presented in Section 3 is lack of variation in the types of the impacting trajectories. This bottleneck reduces the availability of trajectories with desirable impact conditions and geometries. Both types of motion in Section 3 present complex behavior. One desirable aspect for an impact trajectory is a constant line-of-sight from the impacting spacecraft to the Earth. This line-of-sight allows for the monitoring of a landing spacecraft or a view of ejecta post-impact for an impactor. The methodology offered in Section 3 does not provide a manner of obtaining trajectory geometry satisfying this line-of-sight constraint. In fact, only the low impact angle example in Figure 3.25(a) offers these desired line-of-sight characteristics, but with very little margin. Therefore, as an example, the periodic orbit information developed in Section 4 is used to determine impact trajectories with unobstructed line-of-sight to the Earth. Periodic orbits with impacting trajectories that do not violate the line-of-sight constraint are determined, then connecting transfers from the 9:2 LSR NRHO are found. Finally, impact trajectories are converged for all epochs investigated in Section 3.

The first step in design of impacting trajectories is the determination of periodic orbit families satisfying the line-of-sight requirement with impacting manifolds structures. Clearly, the L_2 axial, displayed in Figure 4.84, and vertical, displayed in Figure 4.72, families violate the line-of-sight constraint due to their passing behind the Moon as observed from the Earth and are, therefore, removed from the search space. Furthermore, because the crater locations do not cross the xy-plane, no planar families are included. Thus, the remaining families included in the analysis are the northern and southern halo orbits, the northern and southern P4HO2 families, the L_1 axial orbits, the L_1 vertical orbits, and the northern and southern butterfly orbits. The impact latitudes and longitudes of the manifolds associated with these families are shown in Figure 5.1 colored by impact angle. The figure is grouped into the northern families (e.g., northern L_1 halos), the southern families (e.g., southern P4HO2), and the axial and vertical families which lack northern and southern halves. An important observation in Figure 5.1 is the obvious trend in impact angle between the northern and southern groups. The northern families present low latitude impacts with nearly all high impact angles, i.e., nearly tangent to the surface. Consequently, due to the symmetry of the northern and southern half-families, the southern orbits present southern latitude impacts with nearly all low impact angles, i.e., nearly normal to the surface. This observation is consistent with the behavior observed in Section 3 where the trajectories with high impact angles "flip" to a northern-like motion before impacting while the low impact angle trajectories maintain their southern characteristic. Therefore, to obtain both low impact angle and high impact angle trajectories, both southern and northern family members must be leveraged. Both the axial and vertical orbit families do not present a substantial number of impacts in the $\varphi = 200^\circ$ area required for Shackleton crater. Additionally, as transfers are more readily found between the southern 9:2 LSR NRHO and other southern orbits, the search space is limited to the southern orbit families.

To begin, impact trajectories to the Shackleton crater leveraging the southern orbit families are determined. As demonstrated in Figure 5.1(b), the majority of southern

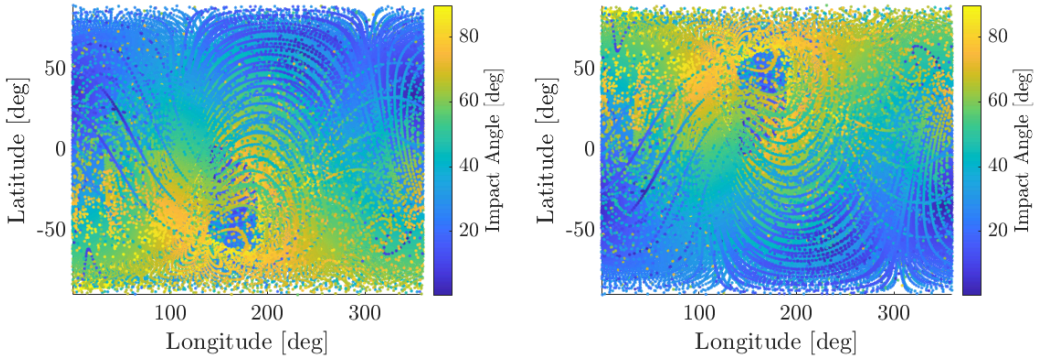

(a) Northern Orbits

(b) Southern Orbits

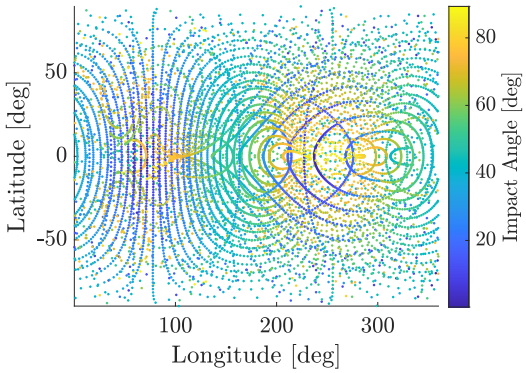

(c) Vertical and Axial Orbits

Figure 5.1.: Latitude and Longitude of Impacts for Spatial Periodic Orbits in the Lunar Region Excluding L_2 Vertical, L_2 Axial, and P4HO1 Families Separated Into Northern, Southern, and Axial/Vertical Groups

hemisphere impacts occur at a lower impact angle; however, several higher impact angle points do exist at $\lambda < 0°$. Figure 5.2 presents the impact conditions of the manifolds associated with the southern orbits near the Shackleton crater region. Very few high impact angles are observed. Figure 5.3 displays the two selected trajectories in Figure 5.2 from the southern family impact conditions near the Shackleton crater locations. Figure 5.3(b) displays an impact trajectory with a higher impact angle at $\vartheta \approx 60°$. This impact is characteristic of the highest angle impact found reasonably close to the Shackleton crater to use as an initial condition. Additionally, a low impact angle candidate trajectory, depicted in Figure 5.3(a), is selected based on its proximity to the Shackleton crater and because it possesses a Jacobi constant of $J \approx 3.03$, close

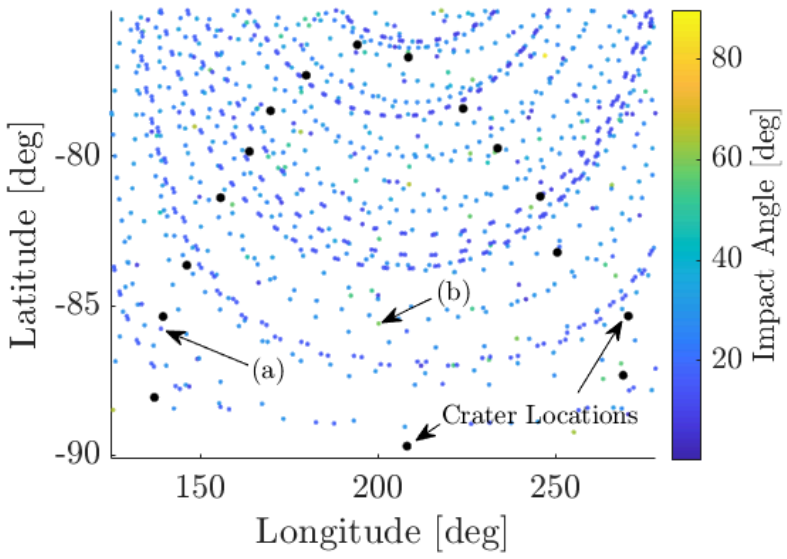

Figure 5.2.: Shackleton Crater Locations Overlaid on Unstable Manifold Impact Locations Associated with the Southern Lunar Region Orbits

to that of the 9:2 LSR NRHO ($J \approx 3.05$). The low impact angle trajectory originates from a P4HO2 orbit while the high impact angle trajectory originates from an L_2 halo orbit. Figure 5.4 demonstrates that both geometries satisfy the line-of-sight requirement. The trajectory originating from the halo orbit does, however, pass in

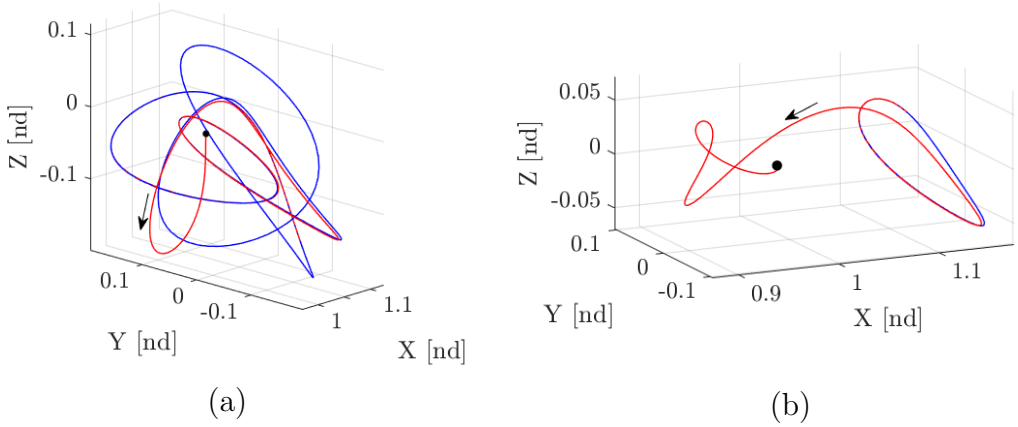

Figure 5.3.: Candidate Trajectories Selected from Southern Family Impact Conditions in Figure 5.2

between the Earth and Moon slightly. Neither of the trajectories in Figure 5.3 impact any of the Shackleton crater locations exactly. As a result, a corrections process is

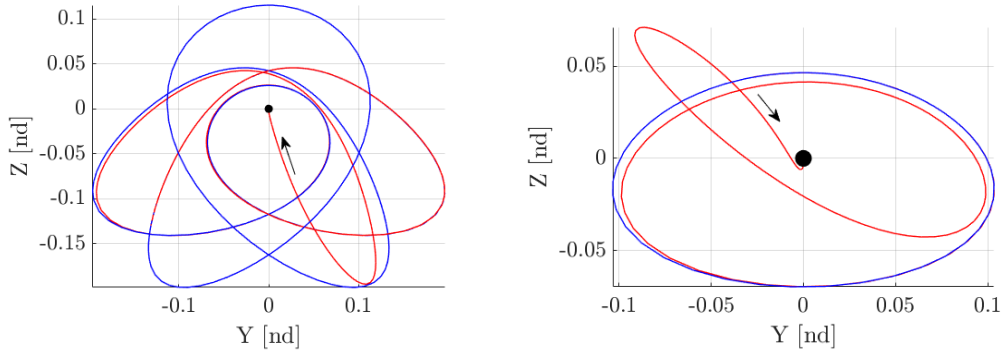

(a) Low Impact Angle

(b) High Impact Angle

Figure 5.4.: Views Down x-Axis of Candidate Trajectories Selected from Southern Family Impact Conditions in Figure 5.2

used to target these locations shown as black dots in Figure 5.2. The process is identical to that presented in Section 3.2.1 with free variable vectors of

$$\mathbf{X} = \begin{bmatrix} \tau_N & \Delta \mathrm{v} & \mathbf{x}_1^0 & \dots & \mathbf{x}_M^0 & \tau_1 & \dots & \tau_M \end{bmatrix}^{\mathrm{T}} \tag{5.1}$$

and

$$\mathbf{F}(\mathbf{X}) = \begin{bmatrix} \mathbf{r}_0^{\tau_N} - \mathbf{r}_1^0 \\ \mathbf{v}_0^{\tau_N} + \Delta\mathbf{v} - \mathbf{v}_1^0 \\ \mathbf{x}_2^0 - \mathbf{x}_1^{\tau_1} \\ \mathbf{x}_3^0 - \mathbf{x}_2^{\tau_2} \\ \vdots \\ \mathbf{x}_M^0 - \mathbf{x}_{M-1}^{\tau_{M-1}} \\ \mathbf{r}_M^{\tau_M} - \mathbf{r}_S \end{bmatrix}, \tag{5.2}$$

respectively. However, unlike the case in Section 3.2.1, the starting condition from which τ_N is referenced is on one of the two unstable orbits selected rather than the 9:2 LSR NRHO. The corrections process is run for all Shackleton crater locations and

the impacting trajectories are determined. Figures 5.5 and 5.6 display the converged results for the low and high angle impact trajectories, respectively. Clearly, the

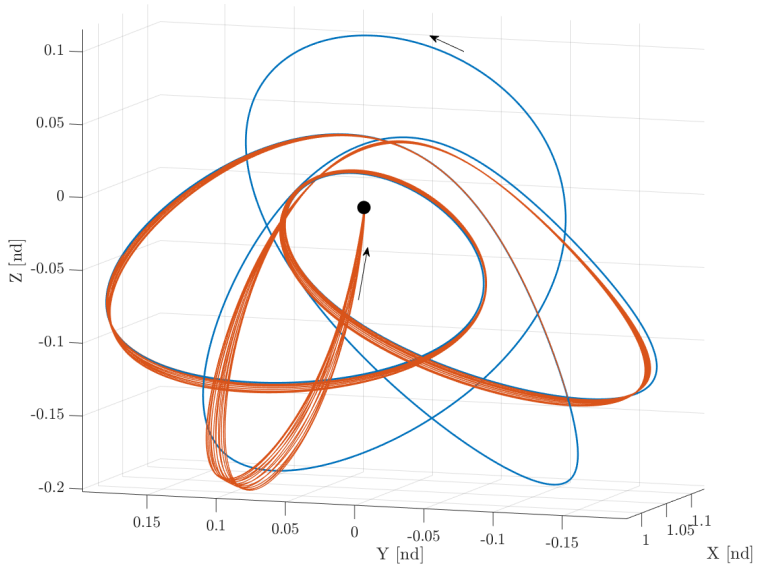

Figure 5.5.: Converged Transfers from P4HO2 Orbit To Shackleton Crater Locations in 2023 Yielding Low Impact Angle Trajectories

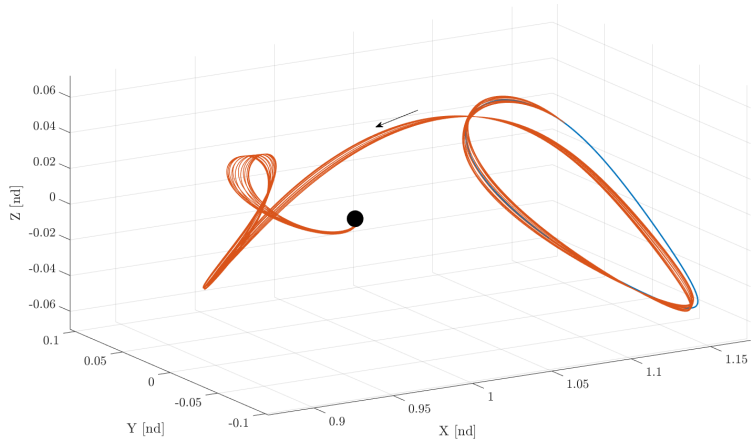

Figure 5.6.: Converged Transfers from L_2 Halo Orbit To Shackleton Crater Locations in 2023 Yielding High Impact Angle Trajectories

geometry of the initial guess is well preserved through the corrections process as neither group of transfers presents any drastic change. Furthermore, neither group of transfers violates the line-of-sight constraint. The small variation in geometry

observed is reinforced by the low required Δv magnitudes given in Figure 5.7. Neither

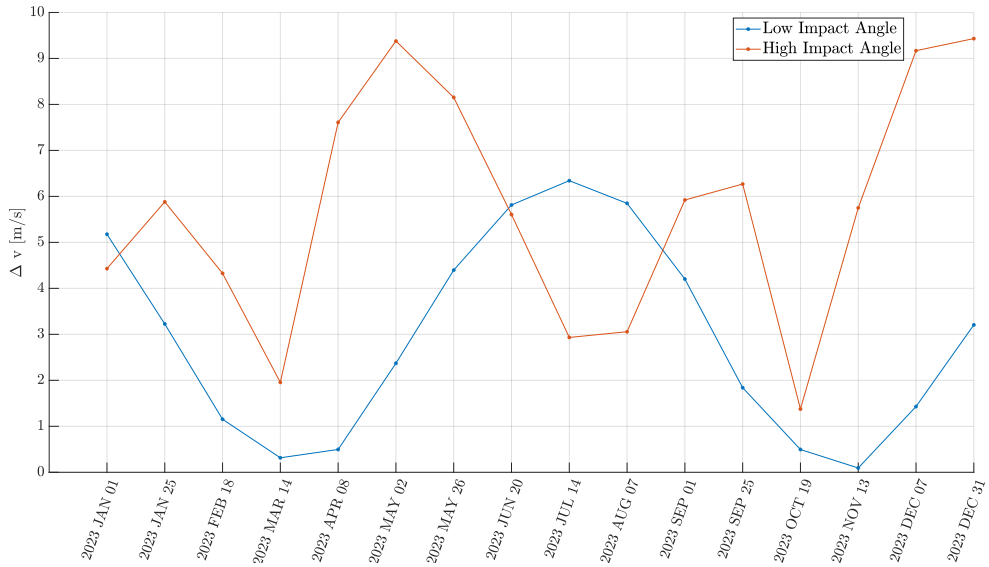

Figure 5.7.: Required Departure Δv of Impact Trajectories at Epochs Associated with Shackleton Crater Locations

transfer geometry requires more than 9.5 m/s to depart the periodic orbit on the desired impacting trajectory. The times-of-flight and impact angles given in Figures 5.8 and 5.9, respectively, similarly show little variation. Both the low and high impact trajectories have times-of-flight around 30 days. Comparing these values with the 47 and 61 day transfers found in Section 3.2.1, a difference of 20 to 30 days exists, but a transfer trajectory to the intermediate periodic orbit from the 9:2 LSR NRHO is still required.

The transfers to the selected P4HO2 and L_2 southern halo orbits are found via a $y = 0$ Poincaré map. The stable manifolds of the periodic orbits are propagated in negative time and the $y = 0$ crossings are found. Additionally, maneuvers in the velocity direction at points along the 9:2 LSR NRHO are applied and the resulting trajectories are propagated forward in time and the $y = 0$ crossings are found. The magnitudes of these maneuvers are such that the Jacobi constant of the resulting trajectory is equal to that of the targeted periodic orbit. Following the determination of a sufficiently close connection, the arcs are converged through a multiple shooting

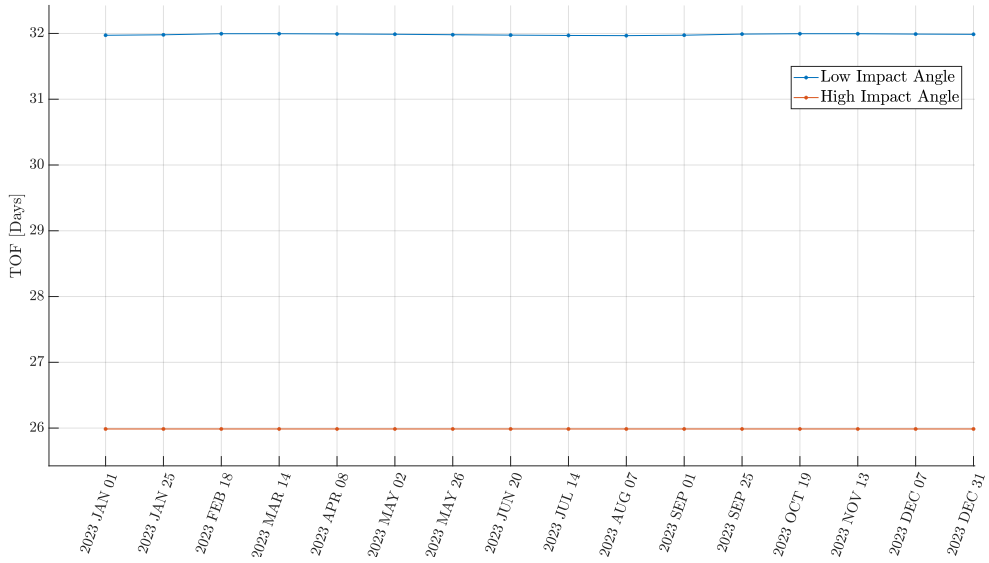

Figure 5.8.: Time of Flight Along Impact Trajectories at Epochs Associated with Shackleton Crater Locations

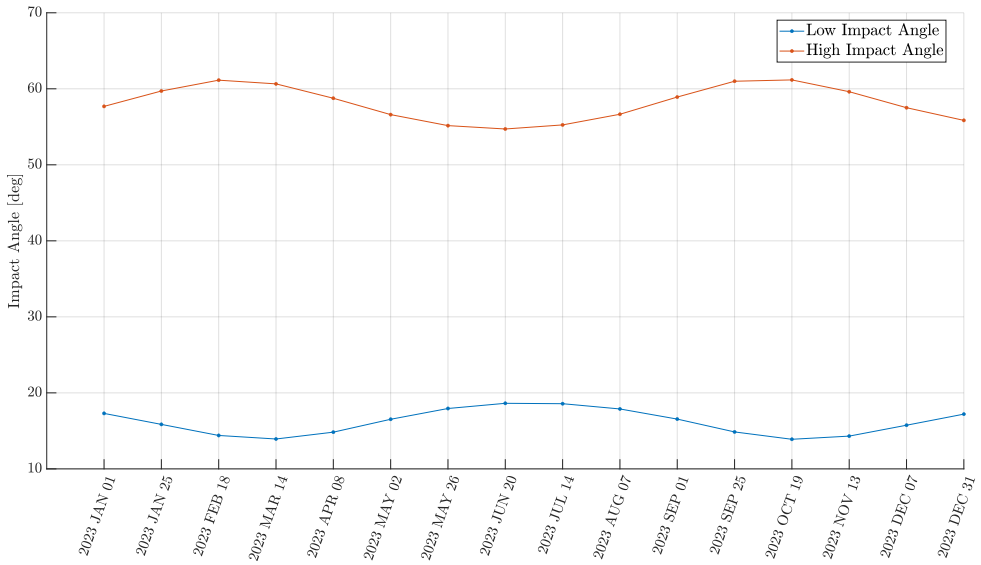

Figure 5.9.: Impact Angle of Trajectories at Epochs Associated with Shackleton Crater Locations

algorithm. Three maneuvers are permitted along the transfer: a maneuver to depart the NRHO, a maneuver at the connection of the arc departing from the NRHO and the arc arriving at the target orbit, and a maneuver at the insertion point along the target orbit. These maneuvers are modeled as impulsive burns and are, therefore, in-

corporated into the shooting scheme via the removal of velocity continuity constraints at the burn locations. Therefore, the free variable vector is

$$\mathbf{X} = \begin{bmatrix} \tau_0 \\ \mathbf{x}_1^0 \\ \mathbf{x}_2^0 \\ \vdots \\ \mathbf{x}_M^0 \\ \mathbf{x}_{M+1}^0 \\ \mathbf{x}_{M+2}^0 \\ \vdots \\ \mathbf{x}_{M+N}^0 \\ \tau_1 \\ \tau_2 \\ \vdots \\ \tau_M \\ \tau_{M+1} \\ \tau_{M+2} \\ \vdots \\ \tau_{M+N} \\ \tau_f \end{bmatrix}, \tag{5.3}$$

where τ_0 and τ_f are the times-of-flight along the 9:2 LSR NRHO and the target periodic orbit, respectively, and there are M segments along the arc departing the NRHO and N segments along the arc arriving at the target periodic orbit. The

constraint vector is updated to take into account the allowed velocity discontinuities and the second periodic orbit arrival as

$$\mathbf{F}\left(\mathbf{X}\right) = \begin{bmatrix} \mathbf{r}_0^{\tau_0} - \mathbf{r}_1^0 \\ \mathbf{x}_2^0 - \mathbf{x}_1^{\tau_1} \\ \vdots \\ \mathbf{x}_M^0 - \mathbf{x}_{M-1}^{\tau_{M-1}} \\ \mathbf{r}_{M+1}^0 - \mathbf{r}_M^{\tau_M} \\ \mathbf{x}_{M+2}^0 - \mathbf{x}_{M+1}^{\tau_{M+1}} \\ \vdots \\ \mathbf{x}_{M+N}^0 - \mathbf{x}_{M+N-1}^{\tau_{M+N-1}} \\ \mathbf{r}_f^{\tau_f} - \mathbf{r}_{M+N}^{\tau_{M+N}} \end{bmatrix}. \tag{5.4}$$

Finally, the total required Δv is calculated as the sum of the velocity discontinuity magnitudes at each of the specified maneuver locations.

Beginning with the low impact angle trajectory, the $y = 0$ Poincaré map is displayed in Figure 5.10. The selection, shown in Figure 5.10(b), represents the two map points with the minimal velocity discontinuity. The trajectories associated with

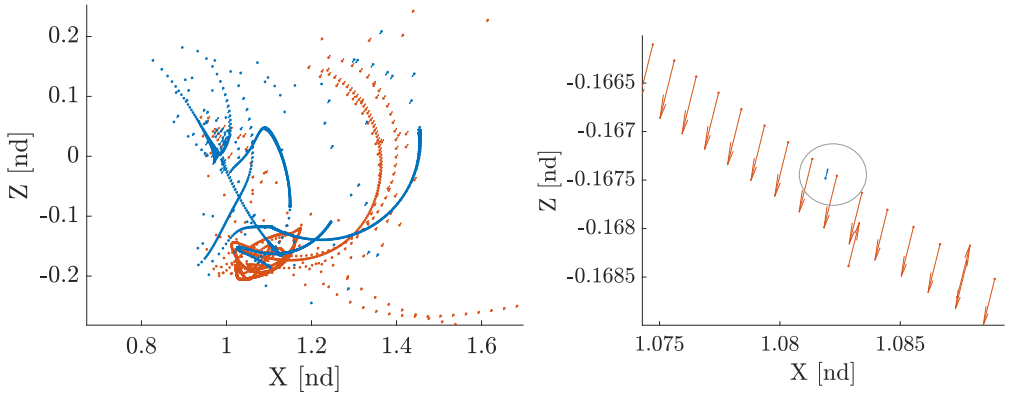

(a) Entire Lunar Region (b) Close Up On Selected Points

Figure 5.10.: Poincaré Map For Connections Between the 9:2 LSR NRHO in Red and the Selected P4HO2 Orbit in Blue

these points are corrected using the multiple shooting algorithm outlined. The resulting corrected transfer is given in Figure 5.11. The time-of-flight of the converged

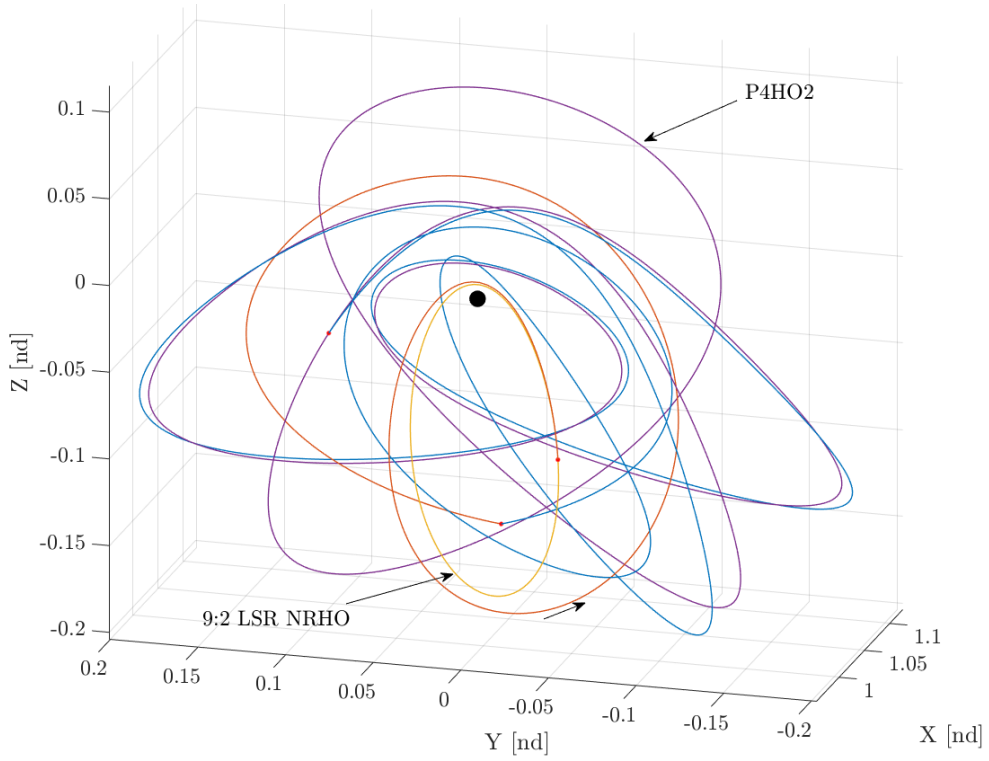

Figure 5.11.: Corrected Transfer from 9:2 LSR NRHO to P4HO2; Δv = 140.4 m/s, TOF = 60.6 days

transfer is high, but the line-of-sight constraint is not violated due to the transfer geometry remaining close to the geometries of the NRHO and P4HO2 orbits. This geometry is similar to that obtained by Zimovan-Spreen et al. in [25], but requires a higher time-of-flight to achieve a lower transfer cost as Zimovan-Spreen et al. present transfers requiring 260 m/s but taking only 16 days. The converged transfer in Figure 5.11 is combined with the impact transfers to build the complete mission design, displayed in Figure 5.12. The transfer from the NRHO to the P4HO2 orbit inserts into the orbit approximately 22 days behind the impact trajectory resulting in the higher time-of-flight given in Figure 5.12. The result given in Figure 5.12 presents a NRHO to Shackleton crater transfer geometry without violating the line-of-sight con-

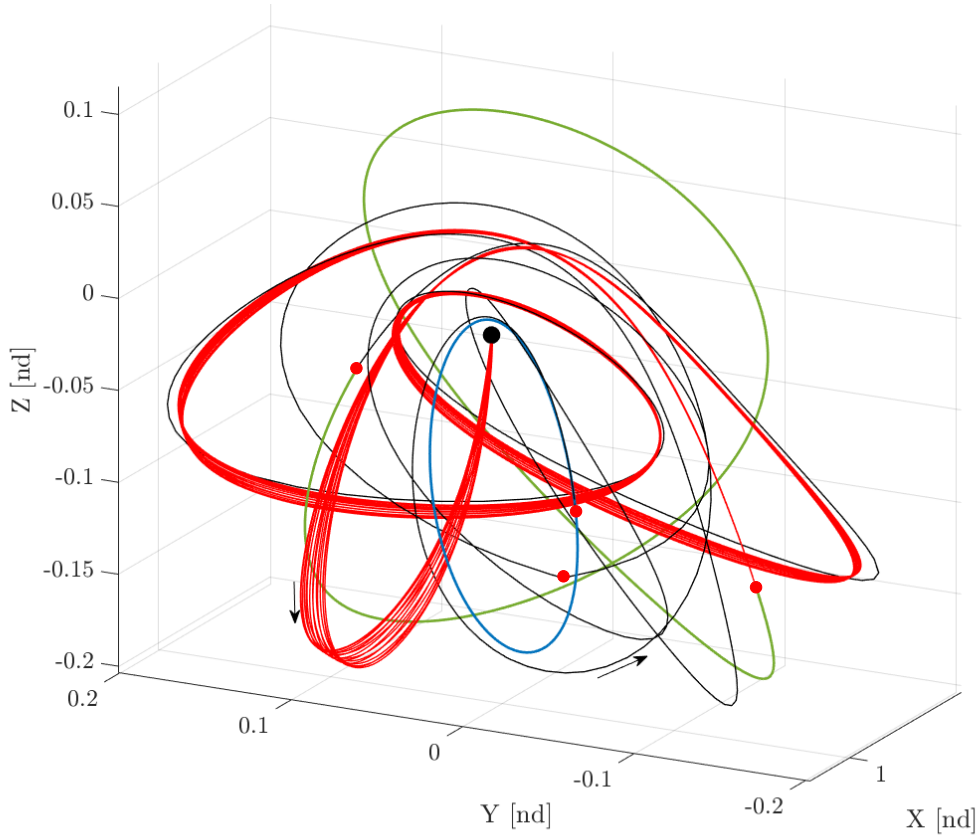

Figure 5.12.: Complete Transfer From 9:2 LSR NRHO to Shackleton Crater Location Using Intermediate P4HO2; Δv_{max} = 145.9 m/s, TOF_{Avg} = 115.0 days (Maneuver Locations Marked with Red Dots)

straint and is obtained without requiring explicit implementation of the line-of-sight constraint.

A similar process is followed for the determination of transfer geometry to the L_2 halo orbit yielding the high impact angle conditions, given in Figure 5.6. The corrected transfer geometry is shown in Figure 5.13. The required Δv magnitude is around 200 m/s larger than the P4HO1; however, the Jacobi constant of the L_2 halo (J = 3.13) is significantly farther from that of the NRHO compared to the P4HO1 orbit. It is likely that the transfer cost would be reduced significantly if an optimization algorithm was applied. However, the time-of-flight of the NRHO to halo orbit transfer is nearly 30 days shorter than that of the P4HO1. Similarly to the low impact angle case, the NRHO to halo transfer is combined with the halo to Shackleton

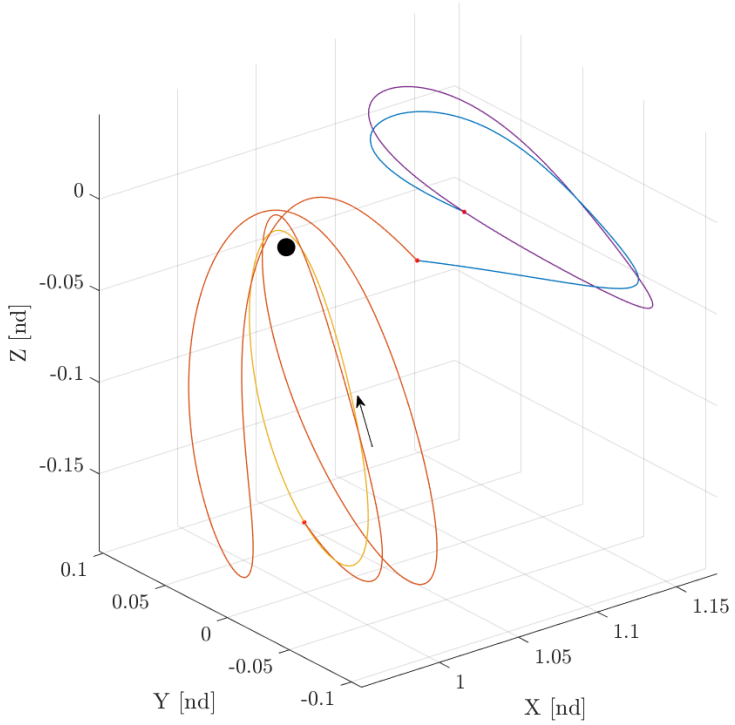

Figure 5.13.: Corrected Transfer from 9:2 LSR NRHO to L_2 Halo; Δv = 307.0 m/s, TOF = 34.5 days

crater transfer results to obtain the full mission design. Thus, the full mission design using the high impact angle L_2 halo intermediate orbit is given in Figure 5.14. Like the P4HO1 intermediate orbit, the L_2 halo intermediate orbit mission does not violate the line-of-sight constraint. While the required Δv is greater than that of the P4HO1 case, the time-of-flight is around 30 days shorter, putting the transfer in a similar range to those given in Section 3.2.1.

5.2 Transfers from 9:2 LSR NRHO to LLO

In addition to leveraging intermediate periodic orbits for impact missions, the apse conditions of the unstable manifolds associated with the periodic orbits may be used to find transfers to Low Lunar Orbit (LLO). Polar ($i = 90°$) 100 km altitude LLOs are of particular interest for Lunar south pole operations [2]. Therefore, a transfer

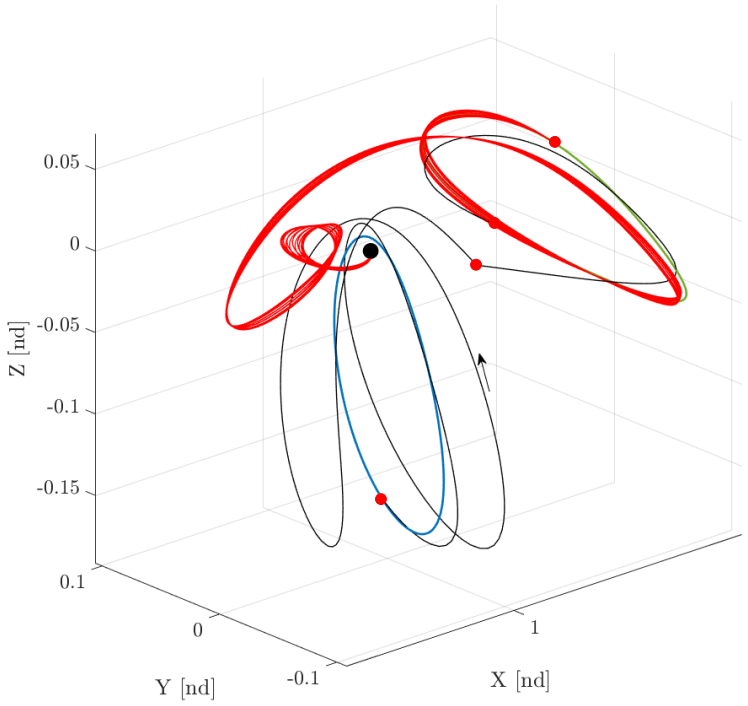

Figure 5.14.: Complete Transfer From 9:2 LSR NRHO to Shackleton Crater Location Using Intermediate L_2 Halo; Δv_{max} = 316.8 m/s, TOF_{Avg} = 82.3 days (Maneuver Locations Marked with Red Dots)

from the 9:2 LSR NRHO to a 90° inclination polar orbit is sought. Whitley et al. present step-off methods for determining these transfers; intermediate periodic orbits are used in this investigation to determine possible advantages and disadvantages in comparison. Periodic orbits are determined with the desired apse condition with respect to the Moon (i = 90°, Altitude = 100 km). A transfer from the 9:2 LSR NRHO is then determined similarly to the process in Section 5.1.

Potential intermediate orbits are determined via the inclinations, altitudes, and Jacobi constants of the apse conditions along their associated periodic orbits. Clearly, apse conditions are desired that have inclinations and altitudes close to 90° and 100 km, respectively. However, transfers are also desired that are at Jacobi constants near that of the 9:2 LSR NRHO to reduce the required energy change at the maneuver

location. In order to determine trajectories yielding these desirable conditions, the nondimensional quantity Λ is introduced as

$$\Lambda = \sqrt{\left(\frac{\text{Alt} - 100 \text{ km}}{100 \text{ km}}\right)^2 + \left(\frac{i - \pi/2}{\pi/2}\right)^2}, \tag{5.5}$$

where i is written in radians. Therefore, a condition where $\Lambda = 0$ produces a 90° apse at 100 km altitude. The relative differences in Jacobi constant, $\tilde{J}$ between the 9:2 LSR NRHO and the apse conditions, i.e.

$$\tilde{J} = \frac{J - J_{9:2}}{J_{9:2}}, \tag{5.6}$$

are plotted against the corresponding Λ values in Figure 5.15 for all of the spatial periodic orbits included in the analysis. Note, only the region near $(0, 0)$ is pictured. The indicated point in Figure 5.15 presents a condition on the Pareto front that

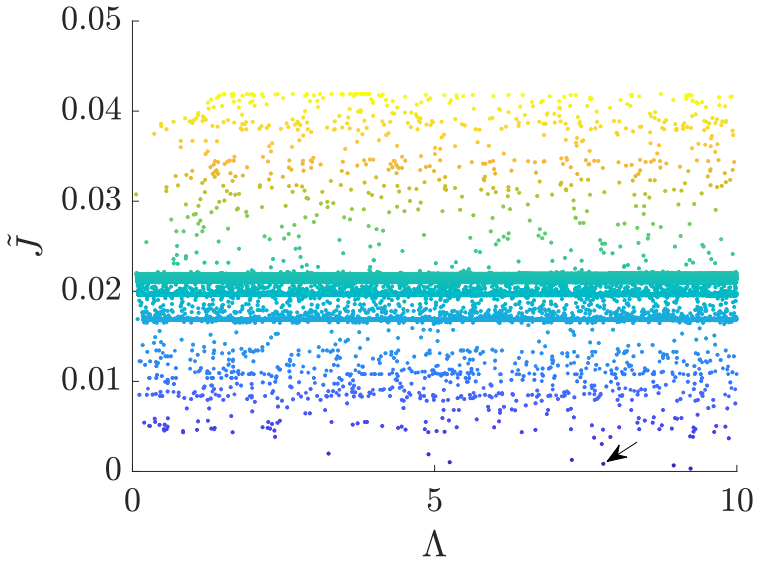

Figure 5.15.: Difference in Jacobi Constant from 9:2 LSR NRHO Versus Λ for Periodic Orbit Apse Conditions

favors the energy differential chosen in an attempt to reduce the transfer cost from the NRHO. Figure 5.16 displays the geometry corresponding to this selected point. Clearly, the underlying periodic orbit is an L_2 northern halo orbit. The time-of-flight

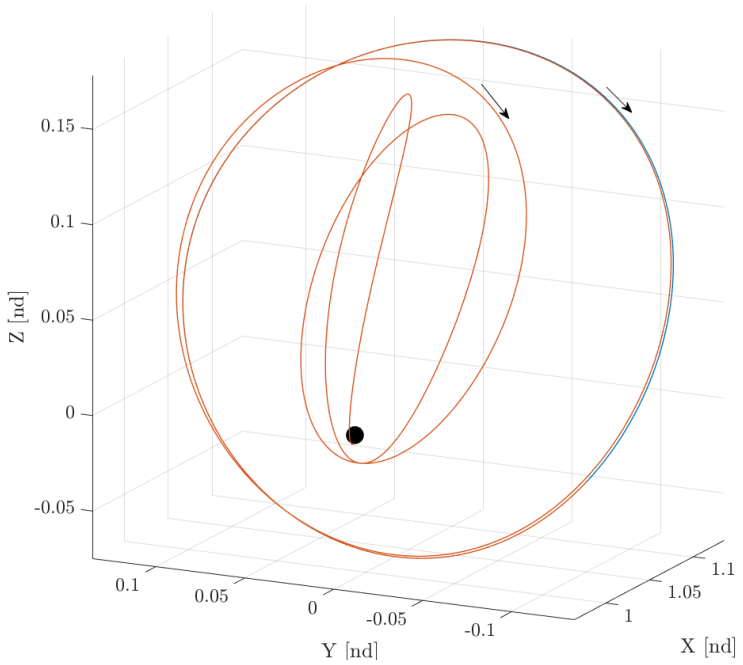

Figure 5.16.: Manifold from L_2 Northern Halo Yielding Apse Condition Selected in Figure 5.15. TOF = 37.3 Days

of the manifold transfer to the apse condition is approximately 37 days displaying a similar time to that required by the impact transfer from the L_2 southern halo orbit observed in Figure 3.26. The depicted trajectory does not provide an exact 100 km altitude, 90° inclination apse condition, however. Therefore, a corrections process is applied to determine the required maneuver at the halo departure to achieve the desired apse condition. A single maneuver is allowed at the halo departure and the final inclination and altitude are fixed while also ensuring the final location is an

apse. The free variable vector includes the initial time-of-flight along the orbit and the initial states and times-of-flight of the departure trajectory segments, i.e.,

$$\mathbf{X} = \begin{bmatrix} \tau_0 \\ \mathbf{x}_1^0 \\ \mathbf{x}_2^0 \\ \vdots \\ \mathbf{x}_N^0 \\ \tau_1 \\ \tau_2 \\ \vdots \\ \tau_N \end{bmatrix}, \tag{5.7}$$

where N is the number of segments used on the departure trajectory. Constraints on the final inclination, altitude, and apse condition are applied in addition to the continuity constraints. The constraint vector is, thus, written,

$$\mathbf{F} = \begin{bmatrix} \mathbf{r}_0^{\tau_0} - \mathbf{r}_1^0 \\ \mathbf{x}_2^0 - \mathbf{x}_1^{\tau_1} \\ \vdots \\ \mathbf{x}_N^0 - \mathbf{x}_1^{\tau_1} \\ i_f - 90^\circ \\ \left(r_{23}^f - \frac{R_{Moon}}{l^*}\right) - \frac{100 \text{ km}}{l^*} \\ \mathbf{r}_{23}^f \cdot \mathbf{v}_N^F \end{bmatrix}, \tag{5.8}$$

where $\mathbf{r}_{23}^f$ is the position vector of the spacecraft at the final time with respect to the Moon and i_f is the inclination in the inertial frame with respect to the Moon at the final state. The trajectory in Figure 5.16 is corrected using this scheme and the resultant trajectory is shown in Figure 5.17. Some noticeable change in the geometry is observed in Figure 5.17 compared to Figure 5.16. The majority of this variation is

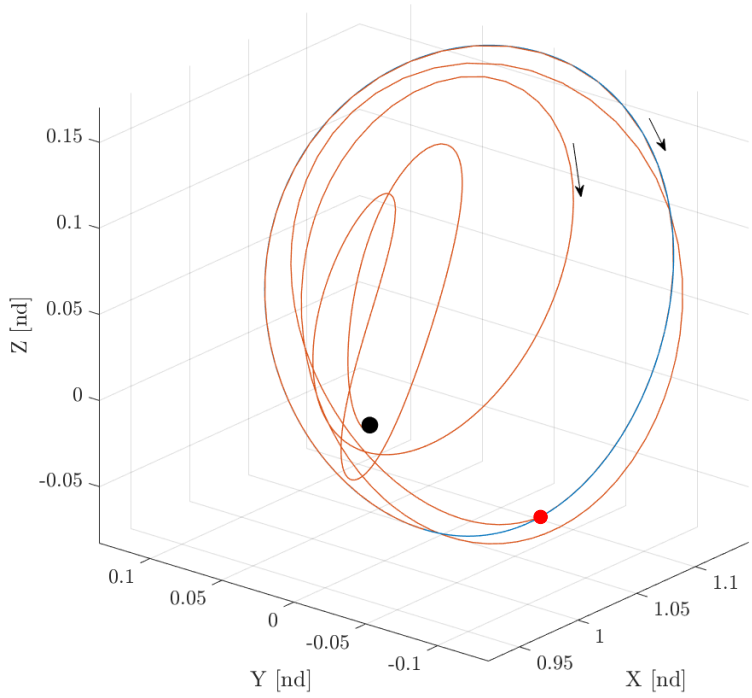

Figure 5.17.: Manifold from L_2 Northern Halo Yielding Apse Condition Selected in Figure 5.15 Corrected to $i = 90°$, Altitude = 100 km. Δv = 77 m/s, TOF = 37.4 Days

caused by the forcing the trajectory to reach an apse at exactly 90°, the sensitivity of the solutions to desired inclination is also noted by Whitley et al. [2]. Along with the slight variation in geometry, the required maneuver magnitude is around 77 m/s compared with the 0 m/s required in the unconstrained case; this increase in maneuver cost is caused similarly by the inclination constraint. Despite the geometry and $\Delta\mathbf{v}$ changes, the time-of-flight observed changed by only a tenth of a day from the original uncorrected trajectory.

Given the selected L_2 northern halo with desired apse conditions, a transfer from the 9:2 LSR NRHO is required. The transfer is determined in the same manner as the impact cases, i.e. a Poincaré map is determined using stable manifolds originating from the halo orbit and step-off trajectories from the NRHO. The corresponding map is shown in Figure 5.18(a) with a closer view on the selected conditions in Figure 5.18(b). A large number of potential connections are found, but the connection with

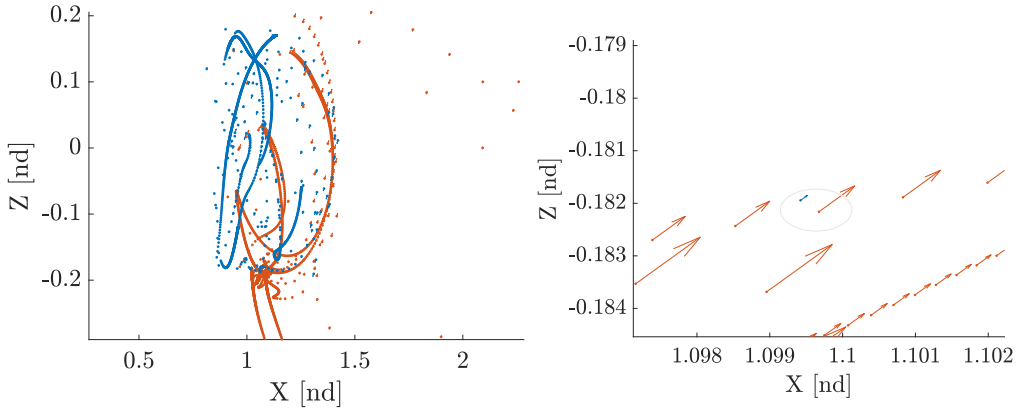

(a) Entire Lunar Region (b) Close Up On Selected Points

Figure 5.18.: Poincaré Map For Connections Between the 9:2 LSR NRHO in Red and the Selected Halo Orbit in Blue

minimal velocity discontinuity is selected (shown in Figure 5.18(b)). This connection is corrected with the same methodology as used in the impact connections, i.e. using the free variable and constraint vectors in Equations (5.3) and (5.4), respectively. The resulting transfer from the 9:2 LSR NRHO to the L_2 halo is depicted in Figure 5.19. The $\Delta\mathbf{v}$ magnitude determined for this transfer is 164 m/s with a time-of-flight of 65.6 days. These quantities are similar to those required to transfer from the 9:2 LSR NRHO to the P4HO2 orbit identified in the impact trajectory design.

The transfer to the L_2 halo from the NRHO is combined with the halo to apse transfer to form the full mission design from the NRHO to the apse condition. Additionally, because the final location occurs at an apse, the circularization maneuver magnitude, $\Delta \mathrm{v}_{\mathrm{circ}}$ is determined as

$$\Delta \mathrm{v}_{\mathrm{circ}} = \mathrm{v}_{\mathrm{Inert}} - \sqrt{\frac{\mathrm{GM}_{Moon}}{\mathbf{r}_{23}^{f}}}, \tag{5.9}$$

where $\mathrm{v}_{\mathrm{Inert}}$ is the final velocity magnitude in the *inertial* frame. As described by Whitley et al., the minimal transfer cost between the NRHO and the LLO can be

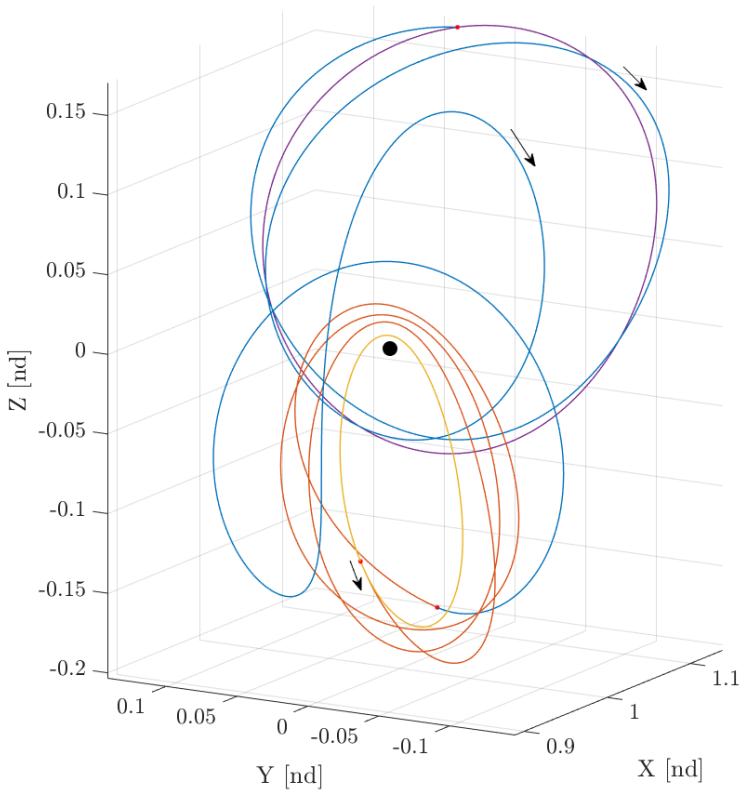

Figure 5.19.: Transfer from NRHO to L_2 Northern Halo. Δv = 164.0 m/s, TOF = 65.6 Days

calculated via the difference in Jacobi constants and noting that the minimal maneuver magnitude to change between two Jacobi constants is

$$\Delta \mathrm{v} = \sqrt{(2\Omega_1 - J_1) - (2\Omega_0 - J_0)}, \tag{5.10}$$

where J_0 and Ω_0 are the initial Jacobi constant and pseudopotential and J_1 and Ω_1 are the final Jacobi constant and pseudopotential [2]. The minimal transfer cost between the 9:2 LSR NRHO and the 100 km altitude polar LLO is, thus, calculated to be approximately 655 m/s. The cost of insertion into the LLO for the transfer in Figure 5.19 is 673.8 m/s. Therefore, the insertion Δv is 20 m/s greater than the theoretical minimum due to the maneuvers performed. Combining the NRHO to halo orbit transfer, the departure from the halo, and the LLO insertion, the complete

design is shown in Figure 5.20. This unoptimized trajectory is around 250 m/s more expensive than the optimal results obtained by Whitley et al. [2]. However, because the intermediate halo is used, the geometry is restricted to the Lunar region.

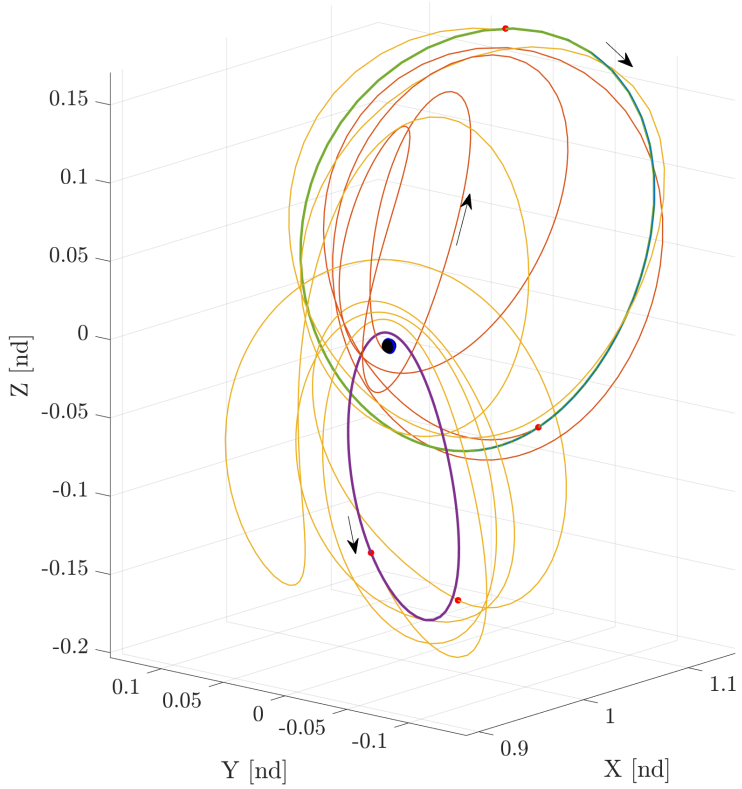

Figure 5.20.: Transfer from NRHO to LLO with $i = 90°$, Altitude = 100 km. Δv = 914.8 m/s (Including 673.8 m/s Insertion into LLO), TOF = 110.2 Days

6. CONCLUDING REMARKS

6.1 Summary

The current investigation seeks to understand the Lunar access characteristics of periodic orbits in the Lunar region including the access to the surface of the Moon and Low Lunar Orbit (LLO). These access characteristics of departure trajectories at various maneuver magnitudes from the 9:2 Lunar Synodic Resonant (LSR) Near Rectilinear Halo Orbit (NRHO) determined and used to design NRHO to Shackleton crater impact transfers as a motivating example for the incorporation of intermediate periodic orbits in the design process. A selection of planar (low prograde orbits, distant retrograde orbits, and Lyapunov orbits) and spatial (halo orbits, vertical orbits, axial orbits, butterfly orbits, and period-four halo orbits) periodic orbit families in the Lunar region are identified. The stability index and time constant are introduced to quantify stability and manifold departure rate. These metrics are used to determine suitably unstable members of the identified periodic orbit families. Impact and apse conditions including impact location, impact speed, impact angle, apse altitude, and apse inclination of the unstable manifold structures associated with these unstable periodic orbits are determined through explicit propagation. These access characteristics are then used in the design of two different impulsive propulsion access transfer scenarios from the NRHO. First, periodic orbit manifold structures that impact at the Shackleton crater locations are determined and two separate families of geometries are converged yielding impact trajectories at various epochs. Transfers from the NRHO to the underlying periodic orbits associated with these structures are found and end-to-end feasible mission designs leveraging impulsive maneuvers are then presented. Second, periodic orbits with manifold structures yielding desirable apse conditions are determined and a selected orbit and manifold structure are cor-

rected for transfer design into a circular polar 100 km altitude LLO. Similar to the impact design, a transfer from the NRHO to the selected orbits is then corrected and a complete NRHO to LLO impulsive mission design is established. Fundamentally the conclusions of the current work are:

1. Lunar access trajectories from periodic orbits without fast departure manifolds such as the 9:2 LSR NRHO can be effectively obtained by applying a series of impulsive maneuvers around the orbit and determining the impact conditions of the resulting trajectories. However, this method of transfer generation does not offer a large amount of control over the geometries obtained especially when constraints are applied to impact conditions due to the limited variation of impact trajectories. Conversely, this method of trajectory generation often produces lower Δv requirements and requires fewer maneuvers due to the reduced complexity.

2. Many of the Lunar region periodic orbit families present periodic orbits with sufficiently fast departing manifold structures yielding impact conditions over the Lunar surface and apse conditions in the LLO region. The planar families present Lunar impacts spanning all locations in the xy-plane at Jacobi constant values near that of the NRHO as well as many other periodic orbits in the Lunar region. Furthermore, the apse conditions of the Lunar region periodic orbits present apses at all altitudes close to the Moon. Similarly, the manifolds associated with the spatial orbits present considerable Lunar access characteristics. However, in any particular families, trades exist between the impact location and the speed, time-of-flight, and Jacobi constant. Additionally, northern and southern families present large variations in the impact location with southern Lunar latitudes impacted primarily by northern orbits and vice-versa. The apse conditions are closely connected with the Jacobi constant of the underlying periodic orbit as higher Jacobi constants yield a greater number of low altitude apses but require larger times-of-flight.

3. The Lunar access characteristics of the Lunar region periodic orbits provide baseline geometry that can effectively be included in mission design applications regarding transferring from stable (as well as unstable) periodic orbits to the Lunar surface and LLO. The primary advantage of this methodology is the ability to influence the geometry of the resulting transfers. However, the incorporation of intermediate periodic orbits is shown to increase the required Δv and TOF required for a mission in the cases analyzed. These increases in cost may be further reduced with optimization routines.

The current investigation demonstrates the significant amount of Lunar access capability presented by the Lunar region periodic orbit families. While increases in maneuver cost and TOF are observed, these unstable periodic orbits can be leveraged as intermediate steps in a trajectory design process to influence geometry of the resulting mission in the context of an impulsive propulsion spacecraft.

6.2 Recommendations for Future Work

The current investigation produces transfers to LLO and the Lunar surface using propulsion systems modeled with impulsive Δv maneuvers. However, the long times-of-flight observed indicates that the transfers may benefit from analysis in the context of a low thrust propulsion system. Low thrust transfers could more efficiently leverage the multi-revolution geometry and Lunar flybys. Finally, the incorporation of the non-spherical Lunar gravity, solar gravity perturbations, and solar radiation pressure in the dynamical model could further refine the results in the low Lunar region. Transferring the resultant solutions into a higher-fidelity ephemeris model and optimizing may further indicate the usefulness of the obtained solutions. These additional avenues of investigation may provide more complete understanding of the Lunar access characteristic in the region.

REFERENCES

[1] Ryan Whitley and Roland Martinez. Options for Staging Orbits in Cislunar Space. Big Sky, Montana, March 2016.

[2] Ryan Whitley, Diane Davis, Laura Burke, Brian McCarthy, Rolfe Power, Melissa McGuire, and Kathleen Howell. Earth-Moon Near Rectilinear Halo and Butterfly Orbits for Lunar Surface Exploration. Snowbird, Utah, August 2018.

[3] Max Caspar and Clarisse Doris Hellman. *Kepler*. Dover Publications, New York, New York, 1993.

[4] Isaac Newton. *Philosophiae naturalis principia mathematica.* Jussu Societatis Regiae ac Typis Josephi Streater. Prostat apud plures Bibliopolas., Londini, 1687.

[5] Victor Szebehely. *Theory of Orbits: The Restricted Problem of Three Bodies*. Academic Press, New York, New York, 1967. OCLC: 870329834.

[6] Florin Diacu. The solution of the n-body problem. *The Mathematical Intelligencer*, 18(3):66–70, June 1996.

[7] A. E. Roy and M. W. Ovenden. On the Occurrence of Commensurable Mean Motions in the Solar System: The Mirror Theorem. *Monthly Notices of the Royal Astronomical Society*, 115(3):296–309, June 1955.

[8] Lawrence Perko. *Differential Equations and Dynamical Systems*, volume 7 of *Texts in Applied Mathematics*. Springer, New York, New York, 2001.

[9] Jacob Palis and Welington de Melo. *Geometric theory of dynamical systems: an introduction.* Springer, New York, New York, 2012. OCLC: 968650107.

[10] Amanda Haapala. *Trajectory Design in the Spatial Circular Restricted Three-Body Problem Exploiting Higher-Dimensional Poincaré Maps*. Ph.D. Dissertation, Purdue University, West Lafayette, Indiana, December 2014.

[11] Thomas S. Parker and Leon O. Chua. *Practical Numerical Algorithms for Chaotic Systems*. Springer, New York, New York, 1989.

[12] Diane Davis, Kenza Boudad, Rolfe Power, and Kathleen Howell. Heliocentric Escape and Lunar Impact from Near Rectilinear Halo Orbits. Portland, Maine, August 2019.

[13] Lucia Capdevila, Davide Guzzeetti, and Kathleen Howell. Various Transfer Options from Earth into Distant Retrograde Orbits in the Vicinity of the Moon. Santa Fe, New Mexico, January 2014.

[14] Matthew Wittal and Rolfe Power. Spaceflight Hazards of Escape-Velocity-Domain Impact Ejecta in the CR3BP. Portland, Maine, August 2019.

[15] Daniel Andrews. LCROSS lunar impactor - Lessons learned from a small satellite mission. In *61st International Astronautical Congress 2010, IAC 2010*, volume 11, pages 9470–9478, 2010.

[16] Diane Davis. *Multi-Body Trajectory Design Strategies Based on Periapsis Poincare Maps*. Ph.D. Dissertation, Purdue University, West Lafayette, IN, August 2011.

[17] Elyse J. Allender, Csilla Orgel, Natasha V. Almeida, John Cook, Jessica J. Ende, Oscar Kamps, Sara Mazrouei, Thomas J. Slezak, Assi-Johanna Soini, and David A. Kring. Traverses for the ISECG-GER Design Reference Mission for Humans on the Lunar Surface. *Advances in Space Research*, 63(1):692–727, January 2019.

[18] B.A.E. Lehner, J. Schlechten, A. Filosa, A. Canals Pou, D.G. Mazzotta, F. Spina, L. Teeney, J. Snyder, S.Y. Tjon, A.S. Meyer, S.J.J. Brouns, A. Cowley, and L.J. Rothschild. End-to-End Mission Design for Microbial ISRU Activities as Preparation for a Moon Village. *Acta Astronautica*, 162:216–226, September 2019.

[19] Maria T. Zuber, James W. Head, David E. Smith, Gregory A. Neumann, Erwan Mazarico, Mark H. Torrence, Oded Aharonson, Alexander R. Tye, Caleb I. Fassett, Margaret A. Rosenburg, and H. Jay Melosh. Constraints on the Volatile Distribution Within Shackleton Crater at the Lunar South Pole. *Nature*, 486(7403):378–381, June 2012.

[20] National Aeronautics and Space Administration. Spaceflight Demonstration of a Power and Propulsion Element (PPE), November 2017.

[21] Charles Acton, Nathaniel Bachman, Boris Semenov, and Edward Wright. A Look Towards the Future in the Handling of Space Science Mission Geometry. *Planetary and Space Science*, 150:9–12, January 2018.

[22] Daniel Grebow. *Trajectory Design in the Earth-Moon System and Lunar South Pole Coverage*. Ph.D. Dissertation, Purdue University, West Lafayette, Indiana, May 2010.

[23] Emily Zimovan. Characteristics and Design Strategies for Near Rectilinear Halo Orbits Within the Earth-Moon System. Master's thesis, Purdue University, West Lafayette, Indiana, August 2017.

[24] Daniel D. Mazanek, Raymond G. Merrill, John R. Brophy, and Robert P. Mueller. Asteroid Redirect Mission Concept: A Bold Approach for Utilizing Space Resources. *Acta Astronautica*, 117:163–171, December 2015.

[25] Emily Zimovan-Spreen and Kathleen Howell. Dynamical Structures Nearby NRHOs with Applications in Cislunar Space. Portland, Maine, August 2019.